DISS. ETH NO. 24035

In Situ X-ray Absorption Spectroscopy and X-ray Diffraction of Non-stoichiometric Ceria-based Oxides for Two-step Solar Thermochemical Fuel Production

A thesis submitted to attain the degree of
DOCTOR OF SCIENCES of ETH ZURICH
(Dr. sc. ETH Zurich)

presented by
MATTHÄUS ROTHENSTEINER
Dipl.-Ing. in Technical Chemistry, Technische Universität Wien

born on September 28, 1985
citizen of Austria

accepted on the recommendation of
Prof. Dr. Jeroen A. van Bokhoven, examiner
Prof. Dr. Alexander Wokaun, co-examiner

2017

Contents

Abstract

The adverse effects of anthropogenic climate change and the detrimental environmental impact of fossil fuels urge a transition to sustainable, environmentally benign primary energy supplies. Solar power has the highest potential of all renewable energy sources for the production of clean energy vectors. However, solar radiation is a rather dilute energy source, that is intermittent and unevenly distributed on the surface of the earth. The energy-efficient conversion and the storage of solar energy in chemical bonds by driving two-step thermochemical cycles with high-temperature heat from concentrated solar radiation requires new high-performance oxygen storage materials.

Two-step thermochemical cycles enable the dissociation of water or carbon dioxide and the production of hydrogen, carbon monoxide or synthesis gas, which can be further processed to hydrocarbons. State-of-the-art solar thermochemical reactors require stable, solid, non-volatile materials with a high oxygen storage capacity and favorable thermodynamics. Thermochemical looping of non-stoichiometric ceria-based oxygen storage material is performed at a typical reaction temperature of up to 1773 K, which makes the determination of structure-property relationships under relevant conditions very challenging. The focus of this thesis is the in situ characterization of non-stoichiometric ceria-based materials under relevant reaction conditions using hard X-rays and the experimental capabilities of beamline BM01B at the European Synchrotron Radiation Facility in Grenoble, France.

A suitable setup for fast thermochemical cycling, consisting of an automated gas and vapor dosing system, a high-temperature furnace and a quadrupole mass spectrometer for the quantification of oxygen and hydrogen was built and optimized. A cell for in situ X-ray absorption spectroscopy and a cell for quasi-simultaneous in situ X-ray absorption spectroscopy and X-ray diffraction in transmission mode were developed.

In situ X-ray absorption spectroscopy at the Ce K edge enables time-resolved determination of the average electronic structure of cerium by measuring the shift in the energy of the absorption edge, which is proportional to the non-stoichiometry of a com-

pound. At relevant process conditions – reduction at 1773 K and oxidation at 1073 K – analysis of the X-ray absorption fine structure is limited to the near edge region due to strong thermal damping of the extended X-ray absorption fine structure.

X-ray absorption spectroscopy in transmission mode gives access to the absorption edges of heterocations that are introduced into the material to tune its properties with the aim to improve the overall efficiency of the process. Structural changes in equimolar ceria-zirconia were determined by Ce K and Zr K edge X-ray absorption near edge structure at isothermal carbon dioxide splitting conditions at 1773 K. Features of the Zr K edge X-ray absorption near edge structure indicated changes to a more centrosymmetric oxygen coordination upon reduction of the initial structure of the mixed oxide obtained by sintering at 1873 K in air.

Time-resolved in situ X-ray diffraction of equimolar ceria-hafnia indicated the formation of the pyrochlore-type structure, an ordered arrangement of the cations by reducing pressed pellets of powders prepared by polymerized-complex method and calcination. Under isothermal carbon dioxide splitting conditions, cation ordering was not stable, the ordered phase gradually disappeared and a secondary phase, monoclinic hafnia formed in the oxidation step. Hf K edge X-ray near edge absorption spectroscopy of equimolar ceria-hafnia indicated structural changes and Hf K edge extended X-ray absorption fine structure of the reduced material at room temperature agreed with the pyrochlore-type structure.

The possibility of direct production of hydrocarbons in a two-step solar driven thermochemical cycle using rhodium-ceria and nickel-ceria was evaluated in durability tests. While rhodium-ceria converted water and carbon dioxide into oxygen, hydrogen, carbon monoxide and traces of methane, nickel-ceria was not stable under thermochemical looping conditions with reduction at 1673 K and oxidation at 773 K.

Diffraction is the method of choice for the determination of the bulk properties and crystal structure of oxygen storage materials at high temperature. X-ray absorption spectroscopy provides valuable complementary information of the average oxidation state of cerium and the electronic and local geometric structure of heterocations. New materials for solar-driven thermochemical fuel production and the opportunities of in situ X-ray absorption spectroscopy and X-ray diffraction as well as alternative characterization techniques are discussed.

Zusammenfassung

Die negativen Auswirkungen des anthropogenen Klimawandels und der schädliche Umwelteinfluss von fossilen Brennstoffen fordern die Hinwendung zu nachhaltigen, umweltfreundlichen Primärenergiequellen. Solarenergie hat das höchste Potential aller erneuerbaren Energiequellen für die Herstellung sauberer Energieträger. Sonnenstrahlung weist jedoch eine niedrige Energiedichte auf und ist nur zeitweise verfügbar und ungleich über die Erdoberfläche verteilt. Die energieeffiziente Umwandlung und Speicherung von Solarenergie in chemischen Bindungen durch das Antreiben von zweistufigen thermochemischen Kreisprozessen mit der Hochtemperaturwärme konzentrierter Sonnenstrahlung werden Hochleistungs-Sauerstoff-Speicher-Materialien benötigt.

Zweistufige thermochemische Kreisprozesse ermöglichen die Dissoziation von Wasser oder Kohlendioxid und die Herstellung von Wasserstoff, Kohlenmonoxid oder Synthesegas, welches zu Kohlenwasserstoffen weiterverarbeitet werden kann. Moderne thermochemische Solarreaktoren benötigen stabile, feste, nicht flüchtige Materialien mit hoher Sauerstoff-Speicher-Kapazität und günstigen thermodynamischen Eigenschaften.

Thermochemische Kreisprozesse mit nicht-stoichiometrischen Ceroxid-basierten Materialien werden bei Reduktionstemperaturen bis zu typischerweise 1773 K durchgeführt, was die Bestimmung von Struktur-Eigenschaftsbeziehungen unter relevanten Reaktionsbedingungen erheblich erschwert.

Der Fokus dieser Arbeit liegt auf der in situ Charakterisierung von nicht-stoichiometrischen, Ceroxid-basierten Materialien unter relevanten Reaktionsbedingungen mithilfe harter Röntgenstrahlung und den experimentellen Möglichkeiten der Strahllinie BM01B an der Europäischen Synchrotron-Lichtquelle in Grenoble, Frankreich.

Eine geeignete Apparatur für schnelles thermochemisches Zyklieren, welche aus einer automatisierten Dosiervorrichtung für Gase und Wasserdampf, einem Hochtemperaturofen und einem Quadrupol Massenspektrometer für die Quantifizierung von Sauerstoff und Wasserstoff besteht, wurde gebaut und optimiert. Eine Messzelle für in situ Röntgen-Absorptions-Spektroskopie und eine Messzelle für quasi-simultane in situ

Röntgen-Absorptions-Spektroskopie und Röntgen-Diffraktion in Transmission wurden entwickelt.

In situ Röntgen-Absorptions-Spektroskopie an der Ce K Kante ermöglicht die zeitaufgelöste Bestimmung der mittleren elektronischen Struktur von Cer durch Bestimmung der Änderung der Energie der Absorptionskante, die proportional der Nichtstoichiometrie einer Verbindung ist. Bei relevanten Prozessbedingungen - Reduktion bei 1773 K und Oxidation bei 1073 K - ist die Analyse der Röntgen-Absorptions-Feinstruktur durch thermische Dämpfung auf den Nahkantenbereich beschränkt.

Röntgen-AbsorptionsSpektroskopie in Transmission ermöglicht die Strukturbestimmung von Heterokationen in Ceroxid, welche mit dem Ziel eingebracht werden, die Materialeigenschaften so einzustellen, dass sich die Effizienz des Gesamtprozesses erhöht. Strukturelle Veränderungen in equimolarem ceroxid-Zirconoxid wurden mit Röntgen-Nahkanten-Spektrosopie an der Ce K und Zr K Kante unter den Bedingungen der isothermalen zweistufigen Spaltung von Kohlendioxid bei 1773 K bestimmt. Besondere Merkmale an der Zr K Nahkanten-Absorptions-Feinstruktur zeigten Veränderungen zu einer zentrosymmetrischen Koordination von Sauerstoff nach Reduktion des Mischoxids, welches durch Sintern bei 1873 K erhalten wurde. Zeitaufgelöste in situ Röntgendiffraktion von equimolarem Ceroxid-Hafniumoxid zeigte die Bildung der Pyrochlorstruktur, eine geordnete Anordung der Kationen, bei der Reduktion von Presslingen aus Pulver, welche durch eine Polymerkomplexierungs-Methode und Kalzinierung hergestellt wurden. Im Oxidationsschritt der isothermalen Spaltung von Kohlendioxid bei 1773 K war die Anordnung der Kationen nicht stabil und verschwand allmählich, während sich eine monokline Hafniumoxid-Phase bildete. Die Röntgen-Nahkanten-Absorptions-Feinstruktur an der Hf K Kante zeigte strukturelle Veränderungen durch die Reduktion von equimolarem Ceroxid-Hafniumoxid an und bei Raumtemperatur stimmte die Röntgen-Absorptions-Feinstruktur gut mit einem theoretischen Modell der Pyrochlorstruktur überein.

Die Möglichkeit der direkten Herstellung von Kohlenwasserstoffen in einem zweistufigen thermochemischen Kreisprozess mittels Rhodium-Ceroxid und Nickel-Ceroxid wurde in Stabilitätstests evaluiert. Während Rhodium-Ceroxid Wasser und Kohlendioxid in Sauerstoff, Wasserstoff, Kohlenmonoxid und Spuren von Methan umwandelte, war Nickel-Ceroxid bei thermochemischer Reduktion bei 1673 K und Oxidation bei 773 K nicht stabil.

Diffraktion ist die Methode der Wahl für die Bestimmung der Festkörpereigenschaften und der Kristallstruktur von Sauerstoff-Speicher-Materialien bei hohen Temperaturen.

Röntgen-Absorptions-Spectroskopie liefert wertvolle komplementäre Information über den mittleren Oxidationszustand von Cer und die elektronische und lokale geometrische Struktur von Heterokationen. Neue Materialien für die thermochemische Herstellung von Solartreibstoffen sowie die Möglichkeiten von in situ Röntgen-Absorptions-Spektroskopie und Röntgen-Diffraktion sowie alternative Charakterisierungsmethoden werden besprochen.

Chapter 1

Introduction

1.1 Solar energy conversion and storage

Solar energy has the highest potential of all renewable energy sources and the sun has already become an important ecologically benign energy source. Estimates show that at a conversion efficiency of about 20 %, an area of only 0.1 % of the solid surface of the earth is sufficient to supply the current primary energy needs of the whole planet. At present, however, the global total primary energy supply (about 13 700 Mtoe) is dominated by fossil fuels: coal (29 %), oil (31 %) and natural gas (21 %) according to the latest statistics.[1] Scientists have recommended the de-carbonization of the energy system to keep the potentially disastrous consequences of anthropogenic climate change[2] at bay. Economically viable technologies that enable efficient conversion, storage and transport of solar energy represent the key to a clean and carbon-neutral energy future. There are three main challenges in harnessing solar energy: Firstly, the solar energy flux is rather dilute - the solar irradiation on the surface of the earth is about 1 kWm^{-2}. Secondly, the sun is an intermittent energy source - it is only available during day-time and its power varies considerably due to local and seasonal changes in the absorption and scattering properties of the atmosphere. Thirdly, solar irradiation is unequally distributed over the surface of the earth. The highest solar irradiation occurs between 30° northern and 30° southern latitude. The map of solar energy potential does not match well the map of the energy demand. Figure 1.1 depicts the distribution of the direct normal solar irradiation on the surface of the earth.

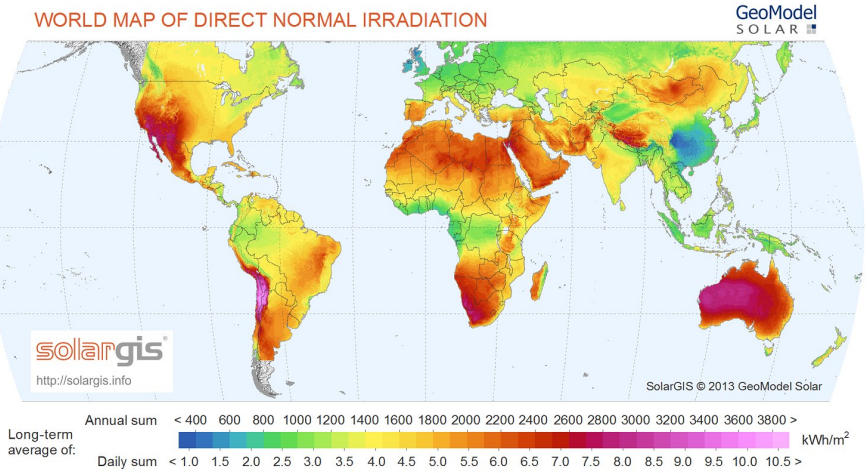

Figure 1.1 World map of long term average direct normal solar irradiation.[3]

Silicon-based photovoltaic solar panels and solar thermal power plants have already gained a significant share in the electricity markets of a few countries. Dye-sensitized

solar cells such as Grätzel cells[4,5] and similar technologies promise revolutionary changes towards a decentralized energy system by facilitating the conversion of solar energy. Solar energy can be stored by synthesizing energy carriers and fuels, such as hydrogen and hydrocarbons from their combustion products water and carbon dioxide. Research on artificial photosynthesis aims to capture solar energy and to store it in the chemical bonds of a fuel by means of photo- and electrochemical devices. A typical example of this strategy is the concept of the artificial leave.[6] Many strategies to harness solar radiation at high efficiency involves devices to concentrate solar radiation. High temperature process heat from concentrated solar radiation is also an attractive primary energy source.[7,8] Systems for heat storage enable continuous power generation.[9,10] The first commercial solar thermal power stations that use steam generated by heat from concentrated solar power (CSP) to drive turbines for the production of electricity, such as PS10 in Andalusia, Spain[11] or the Ivanpah Solar Electric Generating System in the California Mojave Desert[12] have been installed in the last decade. The energy of high temperature heat provided by concentrated solar radiation can drive highly endothermic chemical reactions. The thermochemical dissociation of water and carbon dioxide, which allows to produce hydrogen, carbon monoxide and oxygen is an interesting alternative to photo- and photo-electrochemical solar energy conversion. While solar hydrogen can be directly used as energy vector, syngas, a mixture of hydrogen and carbon monoxide, can be further processed to hydrocarbon fuels by means of large-scale industrially proven technologies, such as Fischer-Tropsch synthesis.[13] Eventually, a carbon-neutral fuel cycle could be created by combining carbon capture and storage (CCS) technology[14,15] with solar fuel production. Essentially, solar thermochemical technology is still in an early stage of development.[8,16–30] First pilot-scale plants have been realized (e.g.[31]), however industrial applications are not expected in the near future.[26,32,33] The development of reliable high-temperature process technology faces many engineering and associated material-related challenges. The most important challenge for economically viable production of solar fuels is the development of an oxygen storage material that enables solar-driven two-step thermochemical cycles for the dissociation of water and carbon dioxide with competitive solar-to-fuel conversion efficiency. Non-stoichiometric ceria-based materials are promising candidates for this mode of solar energy conversion and storage. The determination of the electronic and geometric structure of these materials under relevant reaction conditions is the main goal of this thesis.

1.2 Thermochemical cycles for the dissociation of water and carbon dioxide

Direct thermolysis

A straightforward method to produce hydrogen from water is direct thermolysis, i.e. removing hydrogen from the equilibrium mixture of the dissociation products of water[34–38] at very high temperature. In the same way, carbon monoxide can be obtained from carbon dioxide.[39]

This brute-force approach requires a reactor temperature well above 2500 K and a method to separate the fuel and oxygen at high temperature. ΔG of the dissociation of water reaches zero at about 4300 K.[19] Although solar furnaces can quite easily produce the temperature required for a sufficient degree of dissociation in direct thermolysis, thermal losses due to re-radiation, the requirement of a gas separation method that works at very high temperature, the availability of suitable and stable reactor materials and safety concerns make it highly desirable to lower the temperature of operation and to temporary or spatially separate oxygen and fuel formation. This can be achieved by thermochemical cycles.

Two-step thermochemical cycles

A thermochemical cycle divides a thermodynamically unfavorable reaction into a number of reactions that can be carried out at significantly lower temperature and add up to the thermodynamically unfavorable reaction. The reactants of the individual reactions are recovered and reused. Thermochemical cycles for the dissociation of water or carbon dioxide can be based on two or more individual reactions that add up to the dissociation of water or carbon dioxide (Equations 1.1, 1.2).

$$\mathrm{H_2O} \rightarrow \mathrm{H_2} + \frac{1}{2}\mathrm{O_2} \tag{1.1}$$

$$\mathrm{CO_2} \rightarrow \mathrm{CO} + \frac{1}{2}\mathrm{O_2} \tag{1.2}$$

A large number of thermochemical cycles for water-splitting have been identified.[21,40–42] While many thermochemical cycles with three or more steps for hydrogen production have been developed for the utilization of heat with a maximum temperature below about 1200 K generated by nuclear reactors, such as the sulfur-iodine cycle,[43] the higher temperature attainable with CSP facilitates cycles with only two steps based on reactions

with high entropy changes. The main advantages of high-temperature two-step cycles are a higher theoretical solar-to-fuel energy conversion efficiency and fast reaction kinetics. Figure 1.2 illustrates a two-step thermochemical cycle based on non-stoichiometric ceria and the fuel cycle.

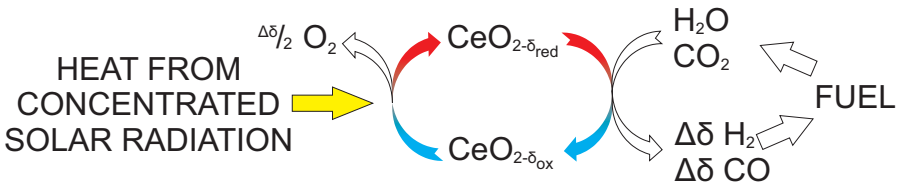

Figure 1.2 Schematic of solar fuel production using non-stoichiometric ceria as redox intermediate in a two-step thermochemical redox cycle driven by high temperature process heat provided by concentrated solar radiation.

Thermodynamic framework

The temperature and pressure ranges that are thermodynamically favorable for the thermal reduction and gas splitting reactions can be determined from basic thermodynamic considerations.[36,44–48] A two-step thermochemical cycle consists of the endothermal autoreduction of an oxygen exchange material, typically a metal oxide at high temperature (Equation 1.3a) and its subsequent re-oxidation at the same or at a lower temperature with water (Equation 1.3b) or carbon dioxide (Equation 1.3c).

$$\mathrm{MO}_{\alpha} \longrightarrow \mathrm{MO}_{\alpha-\beta} + \frac{\beta}{2}\mathrm{O}_2 \tag{1.3a}$$

$$\mathrm{MO}_{\alpha-\beta} + \beta\mathrm{H}_2\mathrm{O} \longrightarrow \mathrm{MO}_{\alpha} + \beta\mathrm{H}_2 \tag{1.3b}$$

$$\mathrm{MO}_{\alpha-\beta} + \beta\mathrm{CO}_2 \longrightarrow \mathrm{MO}_{\alpha} + \beta\mathrm{CO} \tag{1.3c}$$

Thermodynamics sets the boundary conditions for the feasibility of a cycle and provides design rules for oxygen exchange materials: Both the autoreduction (Equation 1.3a) and oxidation (Equations 1.3b 1.3c) of the oxygen carrier should be spontaneous, i.e. exergonic, with the Gibbs free energy $\Delta G \leq 0$, at the reaction temperature. Thus, the overall energy input and entropy gain of the thermochemical cycle must be equal or higher than that of the direct dissociation reactions (Equations 1.1 and 1.2). In the case of water splitting (Equation 1.1) Δ H $\geq$ 286 kJmol^{-1} and Δ S $\geq$ 44.4 Jmol^{-1}K^{-1} and carbon dioxide splitting (Equation 1.2) 284 $kJmol^{-1}$ reduction enthalpy and 43.3 Jmol^{-1}K^{-1}, respectively. The Gibbs free energies of the two-step dissociation of one mole

of water or carbon dioxide ($\beta = 1$ in equations 1.3) are given by:[44,45]

$$\Delta G_{\mathrm{red},T_{\mathrm{red}}} = \Delta H_{\mathrm{red}} - T_{\mathrm{red}} \left(\Delta S_{\mathrm{red}} + \frac{1}{2} S^{\mathrm{O_2}}_{T_{\mathrm{red}}} \right) \leq 0 \tag{1.4a}$$

$$\Delta G_{\mathrm{ox},T_{ox}} = -\Delta H_{\mathrm{red}} - \Delta H^{\mathrm{H_2O}}_{\mathrm{f},T_{ox}} - T_{\mathrm{ox}} \left(-\Delta S_{\mathrm{red}} + S^{\mathrm{H_2}}_{T_{\mathrm{ox}}} - S^{\mathrm{H_2O}}_{T_{\mathrm{ox}}} \right) \leq 0 \tag{1.4b}$$

$$\Delta G_{\mathrm{ox},T_{ox}} = -\Delta H_{\mathrm{red}} - \Delta H^{\mathrm{CO_2}}_{\mathrm{f},T_{ox}} + \Delta H^{\mathrm{CO}}_{\mathrm{f},T_{ox}} - T_{\mathrm{ox}} \left(-\Delta S_{\mathrm{red}} + S^{\mathrm{CO}}_{T_{\mathrm{ox}}} - S^{\mathrm{CO_2}}_{T_{\mathrm{ox}}} \right) \leq 0 \tag{1.4c}$$

T_{red} and T_{ox} are the temperature of the reduction and oxidation reaction. ΔH_{red} and ΔS_{red} denote the enthalpy and entropy changes in the oxygen storage material. This entropy change is negative in most elemental oxides and counter-acts the positive entropy change of the release of gaseous oxygen, which is the major driving force. The influence of the oxygen partial pressure in the reduction step is accounted for by adding a term $-\frac{1}{2} R T_{\mathrm{red}} \ln p_{\mathrm{O_2}}$ in equation 1.4a. The lower the oxygen partial pressure, the lower the temperature required for auto-reduction (see also Figure 1.3).

Figure 1.3 plots the Gibbs free energy of a two-step carbon dioxide splitting cycle as a function of temperature. The oxygen partial pressure affects the slope of the line representing the auto-reduction reaction. At temperatures lower than T_{ox} the oxidation reaction and at temperatures higher than T_{ox} the reduction reaction are exergonic. Adding equations 1.4a and 1.4b, defining the temperature swing $\Delta T = T_{\mathrm{red}} - T_{\mathrm{ox}}$ and ΔS as the entropy term $S^{\mathrm{O_2}}_{T_{red}} - S^{\mathrm{H_2}}_{T_{ox}}$ in equation 1.5a and the corresponding term for carbon dioxide in 1.5b describe the boundary condition of $\Delta G \leq 0$ for each reaction in the thermochemical cycle:

$$\Delta T \geq \frac{-2\Delta G^{\mathrm{H_2O}}_{\mathrm{f},T_{ox}} - T_{\mathrm{ox}} \Delta S}{S^{\mathrm{O_2}}_{T_{\mathrm{red}}} + 2\Delta S_{\mathrm{red}}} \tag{1.5a}$$

$$\Delta T \geq \frac{-2(\Delta G^{\mathrm{CO_2}}_{\mathrm{f},T_{ox}} - \Delta G^{\mathrm{CO}}_{\mathrm{f},T_{ox}}) - T_{\mathrm{ox}} \Delta S}{S^{\mathrm{O_2}}_{T_{\mathrm{red}}} + 2\Delta S_{\mathrm{red}}} \tag{1.5b}$$

By neglecting the material-dependent contributions ΔS_{red} and Δ S it follows that the term $\Delta T S^{\mathrm{O_2}}_{T_{\mathrm{red}}}$ must be equal or greater than twice the free energy of formation of water $-2\Delta G^{\mathrm{CO_2}}_{\mathrm{f},T_{ox}}$ at the oxidizing temperature. Low values of ΔT are desirable to minimize heat losses from a solar reactor. The main thermodynamic driving force is the entropy of oxygen at high temperature, $S^{\mathrm{O_2}}_{T_{\mathrm{red}}}$, which explains that two-step thermochemical cycles feasible below a certain temperature (ca. 1250 K) have not yet been identified. The solid state entropy change ΔS_{red} is comparatively small, however positive values of ΔS_{red} reduce ΔT and enlarge the temperature range in which both reactions of the cycle are exergonic. The solid state entropy change upon reduction of most binary

oxides is negative.[44] Because the formation of hydrogen and oxygen from water has a positive entropy, the oxidation reaction has to be exothermic. In general, the dissociative reduction of a metal oxide is an endothermic process with a positive enthalpy of reduction ΔH_{red}. Oxides that have a sufficiently high ΔH_{red} and a positive or moderately negative ΔS_{red} are thus interesting candidates. In the case of Co_3O_4 or CdO, the requirements for an exergonic two-step water splitting cycle are not given.[50]

Figure 1.4 illustrates a screening of binary oxides based on thermodynamic properties. The changes in enthalpy of reduction ΔH_{red} and entropy of reduction ΔS_{red} were calculated at 1773 K for thermal reduction at 2000 K and re-oxidation at 1000 K. Cerium dioxide and zincoxide are both promising materials because their reduction reactions have high changes in enthalpy and entropy.

Isothermal operation with $T_{\mathrm{red}} = T_{\mathrm{ox}}$ is possible when switching from reducing (inert sweep gas or vacuum) to oxidizing conditions can provide enough thermodynamic driv-

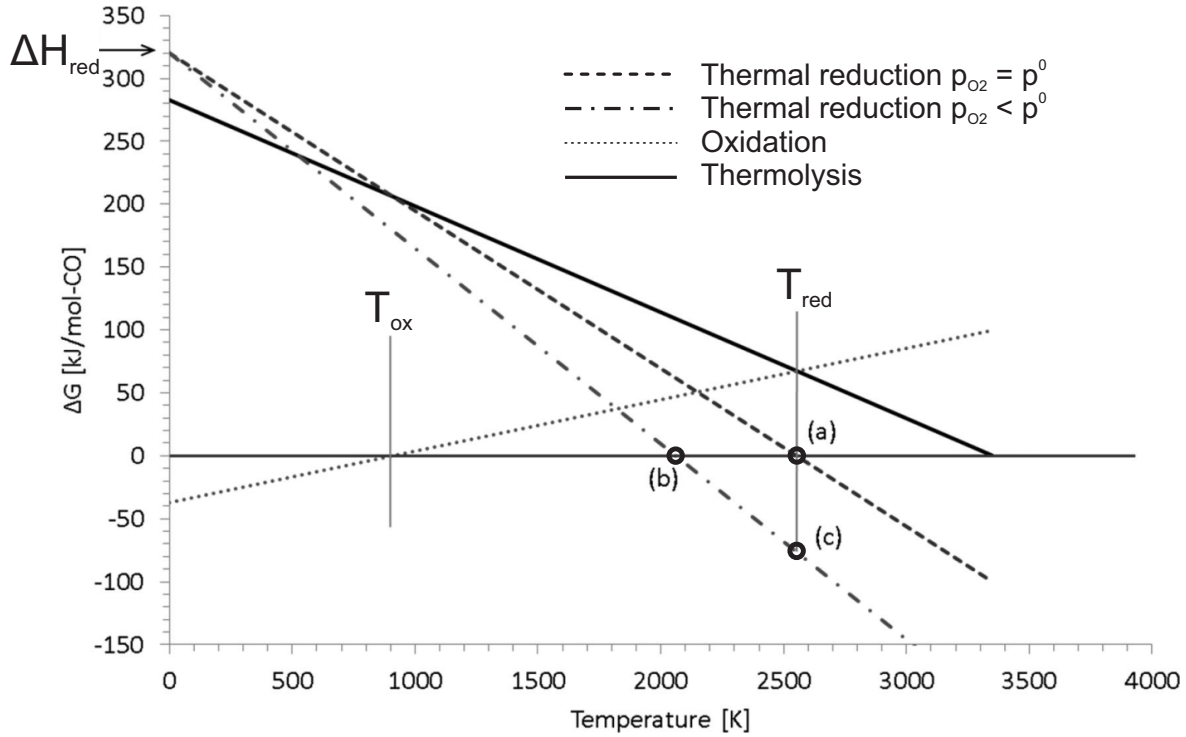

Figure 1.3 The thermodynamics of carbon dioxide splitting from Siegel et al.[49] The thermal reduction is shown at standard (dashed line) and reduced oxygen pressure (dash-dotted line). The re-oxidation reaction are represented by a dotted line and the thermolysis reaction by a solid line. A decrease of the oxygen pressure enables lowering the temperature above which the thermal reduction is exergonic (at point b) instead of a). Point c) indicates the equilibrium at T_{red}.

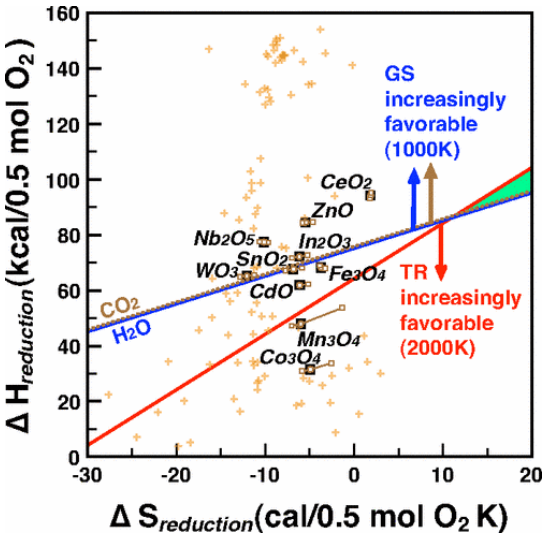

Figure 1.4 Screening of binary oxides by Meredig et al.[44] showing ΔS_{red} and ΔH_{red} with T_{red} = 2000 K and T_{ox} = 1000 K at 1 bar. The small temperature-dependence of the thermodynamic values is indicated by brackets, indicating deviations of ±200 K from the intermediate temperature 1500 K used in the calculation based on literature data.

ing force. Thermochemical looping without a temperature swing has been demonstrated for hercynites[51,52] and non-stoichiometric ceria.[53–57] Low oxygen partial pressures during reduction and a high water/hydrogen ratio during oxidation are desirable.[52] Examples of two-step cycles based on metal/metal oxides that have been investigated experimentally are the zinc-zincoxide system,[16,58–60] the tinoxide-tindioxide system[61,62] or the tungsten-tungstentrioxide system.[63] The formation of liquid or gaseous redox intermediates, such as zinc or tinoxide is entropically favorable but phase changes in the oxygen exchange material are impractical because they complicate reactor design. Quenching might be required to separate the metal vapor and oxygen. Thus, non-volatile oxides such as ferrites,[36,64,65] ceria,[66,67] hercynites[50,52] and perovskites[68,69] are more promising oxygen exchange materials.[70]

Figure 1.5 depicts the most simple design of a solar thermochemical reactor: a cavity receiver reactor that contains no moving parts. Solar radiation enters through a window into a container that is filled with a porous monolith of the redox material. The reactants and products are introduced and removed via the gas phase by flushing the reactor with inert gas or the reactants. To maintain a morphology for fast mass and heat transfer during fast changes in temperature and reaction conditions over a large number of cycles, it is advantageous to use non-volatile, non-stoichiometric compounds such as perovskites and ceria-based oxides that do not undergo phase changes during

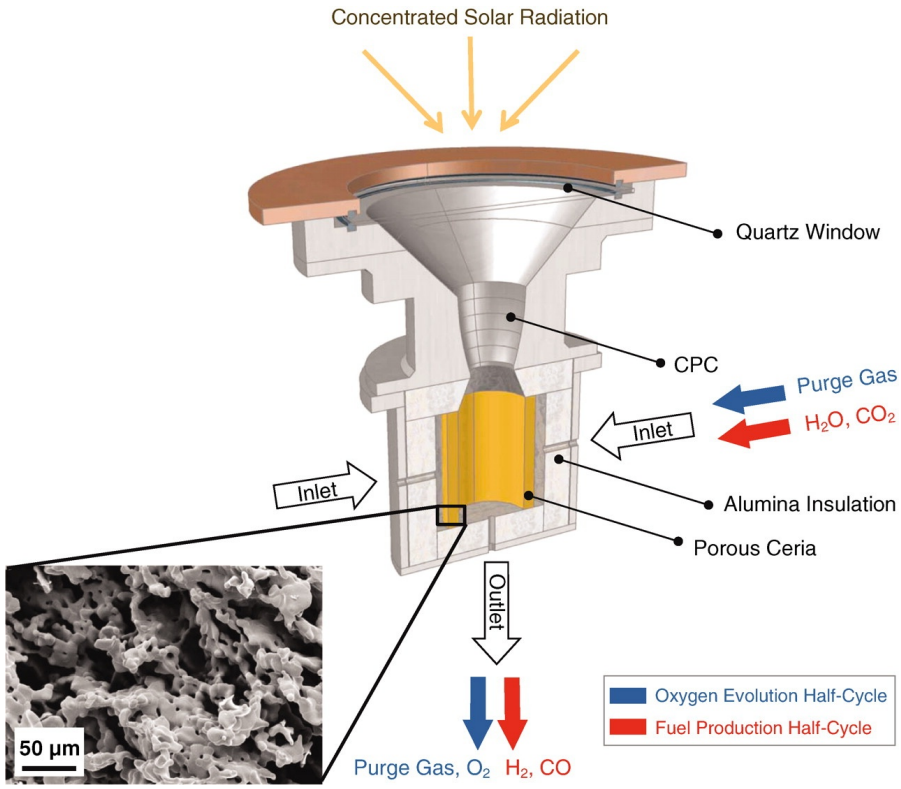

Figure 1.5 Cavity receiver reactor containing a porous monolith of ceria for two-step thermochemical water or carbon dioxide splitting.[67] Concentrated solar radiation enters through a transparent window. Reactants and products are introduced and removed via the gas phase. The reactor contains no moving parts.

thermochemical cycling. A disadvantage of non-stoichiometric materials is their rather small oxygen storage capacity – i.e. energy density in the reduced state – compared to stoichiometric oxygen exchange materials.

1.3 Non-stoichiometric ceria as oxygen storage material for two-step solar thermochemical cycles

At elevated temperatures and under reducing conditions, cerium dioxide exhibits a high level of non-stoichiometry $CeO_{2-\delta}$ while maintaining its fluorite-type crystal structure.[71–76] Figure 1.6 displays the unit cell of the crystal structure of ceria. In cerium(IV)oxide, oxygen ions are arranged in planes and oxygen vacancies exhibit high mobility. The capacity to transport oxygen via these vacancies and to reversibly bind and release oxygen

with fast kinetics means that ceria is of great importance for a large number of applications in which oxygen needs to be activated, transported or stored. Ceria-based materials are applied on a large scale in three-way catalytic converters for the abatement of combustion engine exhaust gas as reducible supports for oxygen storage and activation. Other applications in heterogeneous catalysis[77] include preferential oxidation of carbon monoxide in a stream of hydrogen. In electrochemical devices, ceria-based material are used as electrolytes[78–80] for example in solid oxide fuel cells (SOFCs).[81,82] Hydrogen production by exploiting the oxygen storage capacity $\Delta\delta = \delta_{red} - \delta_{ox}$ of $CeO_{2-\delta}$

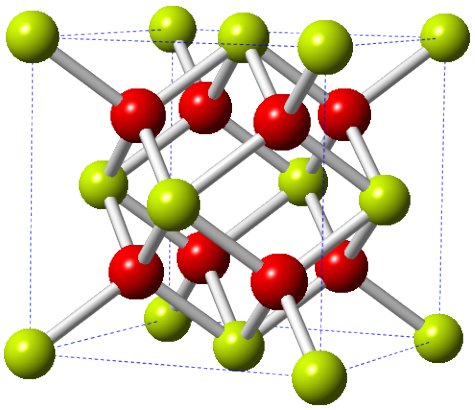

Figure 1.6 The fluorite-type structure ($Fm\bar{3}m$, No. 225) of ceria. The cerium cations form a face-centered cubic lattice and are coordinated by eight oxygen anions that occupy all tetrahedral sites. The lattice constant 5.412 Å and the cerium-oxygen bond length is 2.343 Å.

was first desribed by Otsuka et al.[83] The Ce^{3+}/Ce^{4+} redox cycle can be driven by high-temperature heat from concentrated solar radiation and enables water and carbon dioxide splitting. The stoichiometric conversion of cerium(IV)oxide to cerium(III)oxide was first proposed and demonstrated experimentally by Abanades et al.[42,66] which was soon followed by a demonstration of the cycle utilizing non-stoichiometric ceria.[67,84] It is vital to perform the redox cycle at very low oxygen partial pressure, which is achieved using an inert sweep gas such as argon or by applying vacuum. The first step of the thermochemical looping process is the endothermic partial reduction of ceria (equation 1.6a), which is usually performed at 1773 K. The second step – closing the redox cycle – is the exothermic oxidation of partly reduced ceria (equations 1.6b and 1.6c). The thermochemical cycle can be performed with a temperature swing with the oxidation reaction typically performed at 1073 K, however isothermal operation (at the temperature

of the reduction reaction) is also possible.[53–56]

$$CeO_{2-\delta_{ox}} \longrightarrow CeO_{2-\delta_{red}} + \frac{\Delta\delta}{2}O_2 \tag{1.6a}$$

$$CeO_{2-\delta_{red}} + \Delta\delta H_2O \longrightarrow CeO_{2-\delta_{ox}} + \Delta\delta H_2 \tag{1.6b}$$

$$CeO_{2-\delta_{red}} + \Delta\delta CO_2 \longrightarrow CeO_{2-\delta_{ox}} + \Delta\delta CO \tag{1.6c}$$

Oxygen vacancies

The release of dioxygen and the formation of oxygen vacancies ($\ddot{V_O}$) and Ce^{3+} polaron defects ($Ce^{'}_{Ce}$) from Ce^{4+} at regular cerium lattice sites (Ce_{Ce}) and O^{2-} anions on regular oxygen sites (O_O) is written in Kröger-Vink notation[85] in equation 1.7. Polarons, localized electrons $Ce^{'}_{Ce}$, and oxygen vacancies $\ddot{V_O}$ are the major type of defects in the material.[75] Polarons reside in the narrow, localized 4f level in the band gap of ceria.[86,87] Figure 1.7 shows the equilibrium non-stoichiometry of ceria determined by Panlener et al.[71] in the ranges of temperature and oxygen partial pressure relevant for solar thermochemical cycles.

$$2Ce_{Ce} + O_O \longrightarrow 2Ce^{'}_{Ce} + \ddot{V_O} + \frac{1}{2}O_2(g) \tag{1.7}$$

The relations between temperature, oxygen partial pressure and non-stoichiometry of pure ceria are well known.[71,75,76,88–91] The charge compensation relation $[Ce^{'}_{Ce}] = 2[\ddot{V_O}]$ and the law of mass action relate the oxygen partial pressure and the non-stoichiometry δ.

$$[Ce^{'}_{Ce}]^2[\ddot{V_O}]p_{O_2}^{\frac{1}{2}} = K \tag{1.8}$$

$$\delta \propto p_{O_2}^{-\frac{1}{6}} \tag{1.9}$$

A slope of 1/6 in a double-logarithmic plot of oxygen partial pressure and non-stoichiometry is, however only observed in pure ceria at very low non-stoichiometry. Deviations at higher non-stoichiometry have been explained by defect interactions - defect association, ordering and the formation of intermediate phases.[75,76,90,92–95] Defect models are based on defect reactions, electroneutrality and site conservation. The association of a fraction of the defects to 'defect trimers' according to Equation 1.10 and the law of mass action were successfully applied to model the non-stoichiometry of pure and doped ceria when exposed to solar-driven thermochemical cycles.[96–98]

$$2Ce^{'}_{Ce} + \ddot{V_O} \longrightarrow (Ce^{'}_{Ce}\ddot{V_O}Ce^{'}_{Ce})^{\times} \tag{1.10}$$

Non-stoichiometry and partial thermodynamic quantities

The partial free energy, enthalpy and entropy of formation (per mole of dioxygen) of non-stoichiometric ceria can be determined by measuring the relation between the oxygen partial pressure p_{O_2}, temperature and non-stoichiometry and applying Equation 1.11 for values of constant non-stoichiometry δ.

$$\ln p_{O_2} = \frac{\Delta h_{O_2}}{RT} - \frac{\Delta s_{O_2}}{R}|_{\delta=\text{const}} \tag{1.11}$$

The standard Gibbs free energy change Δg_{red} of the reduction of ceria (Equation 1.6a) can be determined by integrating over the non-stoichiometry:[92,97]

$$\Delta g_{red} = \frac{1}{2}\int_{\delta_{red}}^{\delta_{ox}} \Delta g_{O_2} d\delta \tag{1.12}$$

Intrinsic material properties can be related to the efficiency of the overall process. The non-stoichiometry and related partial molar quantities are pivotal parameters for the rational design of tailored oxygen storage materials to optimize the energy conversion efficiency of solar thermochemical devices.

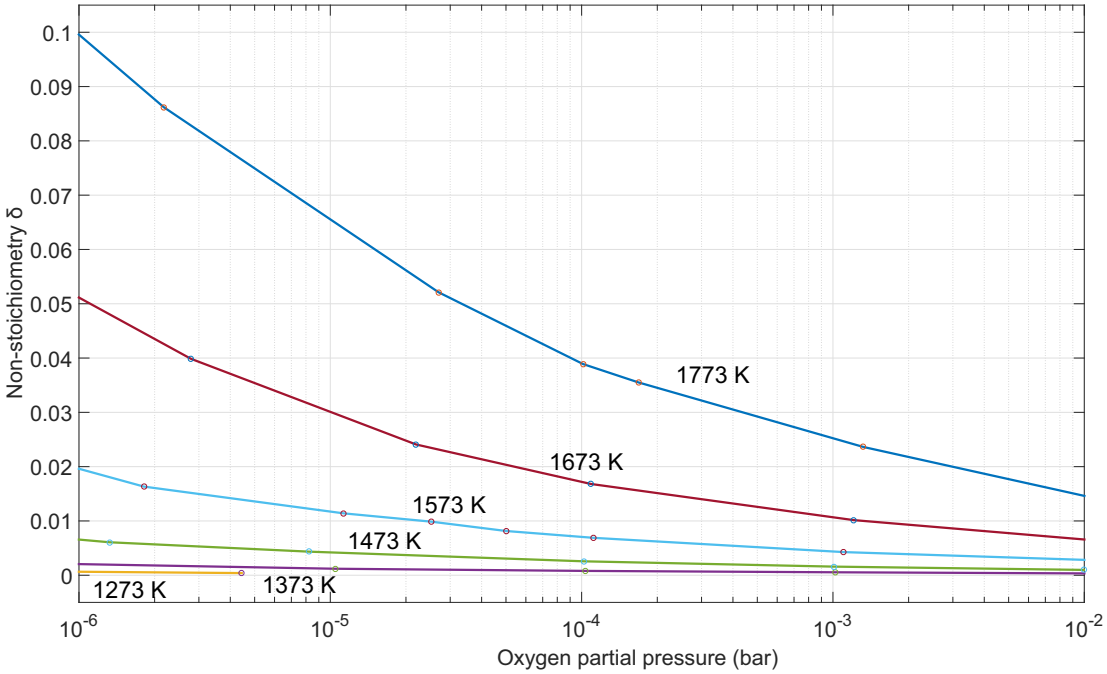

Figure 1.7 The equilibrium non-stoichiometry of ceria[71] in the range of temperature and oxygen partial pressure relevant for solar thermochemical cycles.

Configuration entropy

In models based on statistical thermodynamics, the configuration entropy is introduced.[98] The partial entropy change of vacancy formation is described as the sum of the contributions of the oxygen gas, the change in lattice vibrational entropy and the configuration entropy. If $\Delta\delta$ vacancies are formed in cerium(IV)oxide according to equation 1.6a, the partial molar entropy changes are given by:

$$\Delta s_{\mathrm{vac}} = \Delta\delta\left(\frac{1}{2}s_{\mathrm{O}_2} + \Delta s_v\right) + \Delta s_{\mathrm{con}} \tag{1.13}$$

The general form of the configuration entropy Δs_{con} is the sum over the number of configurations, i.e. the number Ω_{con} of distinct ways all species (vacancies, cations and anions) can be arranged in the material and the corresponding probabilities At very low vacancy concentrations the configurations have the same probability (microcanonical ensemble):

$$\Delta s_{\mathrm{con}} = k_B \ln \Omega_{\mathrm{con}} \tag{1.14}$$

However, as described above, at relevant non-stoichiometry, vacancy clusters form, which decreases the contribution of the configuration entropy.

Ordered arrangements of oxygen vacancies in ceria

In addition to the cubic, fluorite-type structure of cerium(IV)oxide and the hexagonal structure of cerium(III)oxide many intermediary phases that exhibit a long-range order of oxygen vacancies have been identified in the cerium-oxygen system. These discrete compounds, commensurate superstructures of the fluorite-type structure have a composition $\mathrm{Ce_nO_{2(n\text{-}m)}}$, with the integers $n > m$, such as $\mathrm{Ce_7O_{12}}$ and $\mathrm{Ce_9O_{16}}$.[76] Ordering phenomena involving oxygen vacancies have been studied by neutron diffraction of powders and single crystals.[74,99,100] Oxygen vacancies preferentially align as pairs in the [111] cubic directions as the degree of non-stoichiometry increases.[100] The structure of $\mathrm{Ce_7O_{12}}$ consists of a rhombohedral super-cell (space group $R\bar{3}$,148) and can be derived from the fluorite-type structure by placing strings of oxygen vacancies along the [111] direction, with one seventh of cations placed in the strings and six-fold coordinated to oxygen and the remaining cations as nearest neighbors with seven-fold oxygen coordination.[99] $\mathrm{Ce_7O_{12}}$ decomposes at 1321 K into $\mathrm{Ce_3O_{5\pm x}}$ (cubic, $Ia\bar{3}$, 206) and fluorite-type $\mathrm{CeO_{2-\delta}}$.[76]

1.4 The solar-to-fuel energy conversion efficiency

The theoretical efficiency limit of solar thermochemical energy conversion is given by the solar-to-heat energy conversion efficiency of the absorber and the efficiency of the Carnot cycle of the thermochemical cycle.[20,35] The solar-to-heat energy conversion coefficient is given by re-radiation losses of a black body, with σ the Stefan-Boltzmann constant, I the normal beam insolation and S the concentration ratio. Re-radiation scales with the fourth power of temperature. The theoretical efficiency stagnates when re-radiation losses are higher than the increase in the Carnot efficiency. In a real system, the efficiency is determined by the fraction of the higher heating value of hydrogen $\mathrm{HHV(H_2)}$ (285.5 $kJmol^{-1}$) and the energy Q_{cycle} required to produce hydrogen.

$$\eta_{\text{solar-to-fuel,ideal}} = \eta_{\text{abs,ideal}} \cdot \eta_{\text{Carnot}} = \frac{IS - \sigma T^4}{IS} \cdot \frac{T_H - T_L}{T_H} \tag{1.15}$$

$$\eta_{\text{solar-to-fuel}} = \frac{Q_{\text{out}}}{Q_{\text{in}}} = \eta_{\text{abs}} \frac{\mathrm{HHV(H_2)}}{Q_{\text{cycle}}} \tag{1.16}$$

The heat required for producing one mole of hydrogen in a thermochemical water-splitting utilizing non-stoichiometric ceria as redox intermediate, Q_{cycle} consists of the heat needed to increase the temperature of the required amount of water $n_{\mathrm{H_2O}}$ to the lower temperature of the cycle, T_L, the heat to increase the temperature of oxidised ceria from T_L to T_H, with HR the fraction of sensible heat that is recovered, and the enthalpy of reduction of ceria from δ_{ox} to δ_{red}. The expression in Equation 1.17 does not include auxiliary power needed for pumping and gas separation.

$$\begin{aligned} Q_{\mathrm{cycle}} = \Bigg[n_{\mathrm{H_2O}} \left(\Delta H^{298K \rightarrow 373K}_{\mathrm{H_2O}(l) \rightarrow (g)} + \int_{373K}^{T_L} \mathrm{C_{p,H_2O(g)}dT} \right) \\ + \frac{1}{\Delta\delta} \int_{T_L}^{T_H} \mathrm{C_{p,CeO_2}dT} \Bigg] \cdot (1 - \mathrm{HR}) + \Delta H_{\mathrm{red}}(T_H) \end{aligned} \tag{1.17}$$

Thermodynamic process analysis and reactor design

A large number of studies addressed considerations on the ideal material properties, design and mode of operation of thermochemical looping reactors based on thermodynamic analysis of model systems,[24,47,51–53,96,97,101–108] most of them include efficiency calculations and conclusions based on projected system efficiencies. Efficiency calculations were recently reviewed by Muhich.[48] The predictions of the solar-to-fuel efficiencies span a large range and reflects both the potential improvements of the process and the importance of accounting for reaction kinetics as well as the transient nature of heat and mass transfer. Optimistic assumptions suggest that the process has the potential to

outperform the 'state-of-the-art' benchmark[24,49] of hydrogen production using renewable energy: the combination of photovoltaics and electrolysis, which reaches a solar-to-fuel energy conversion efficiency of about 20 %.

Heat recovery from gases and solids, efficient operation at low oxygen partial pressure and the reduction of thermal re-radiation losses have been identified as the major technical challenges in reactor design and operation. The most critical limitations on the efficiency of solar thermochemical cycles have recently been reviewed by Jarret et al.[109]

The high temperature of typically 1773 K required to reach sufficient non-stoichiometry in ceria represents an unsolved engineering challenge. Concerning structural materials, it is essential to reduce the operation temperature. Alternatives to reduce the oxygen partial pressure were explored[110] and it is still not entirely clear if the use of sweep gas or pumping, for example optimized multiple pumping stages,[111] are the better option.[98,109] The problem of mechanical failure of porous ceria-based ceramics upon cycling can be eliminated in aerosol reactors.[112,113] Hybrid thermochemical cycles, such as the combination of solar methane reforming (methane-driven reduction of ceria) and thermochemical conversion of water and carbon dioxide represent an option to both lower operation temperature and increase energy conversion efficiency.[114–116] The comparatively low oxygen storage capacity of ceria is equivalent to a low energy density, which might explain the rather low experimental solar-to fuel conversion efficiency in state-of-the-art solar cavity reactors. Performing solar-heat and heat-chemical energy conversion in two separate steps using a liquid metal as heat transfer fluid might help to reduce re-radiation losses and overcome the power-density mismatch of state-of-the art cavity receiver reactors and substantially improve the overall energy conversion efficiency.[117]

Efficiency - experimental results

Contrarily to the number of projections and estimations of the efficiency based on theoretical models, few experimental data on the efficiency of thermochemical reactors are available. Chueh et al.[67] reported 0.8% and 0.7%, peak efficiencies for carbon dioxide and water splitting, respectively. Furler et al. reported a solar-to-fuel efficiency of 1.73 % average and 3.53 % peak efficiency for carbon dioxide splitting.[118] Venstrom[55] reported a projected efficiency of 4% of isothermal carbon dioxide splitting, and Hathaway an efficiency of 0.72 % of a reactor optimized for isothermal carbon dioxide splitting. There is a strong mismatch between the predicted efficiency and experimental results.

Isothermal operation vs temperature-swing

In the case of ceria[53–56] and hercynites,[51,52] also isothermal operation of the thermochemical cycle is feasible, which has some advantages for reactor design: Isothermal operation provides faster reaction kinetics, eliminates the need of solid-solid heat recovery, and reduces the mechanical stress on the redox material. In the case of operation with a temperature swing, the efficiency of the process is mainly reduced due to thermal losses and the redox material has to withstand fast changes in temperature. Heat recuperation from both the gas and the solid phase are desirable, with the former a technologically easier task than the latter. Which of the two is more important depends on the the design of the reactor and its operation. Bader et al.[54] modeled an isothermal reactor and concluded that introducing a modest temperature swing improves efficiency. Based on experimental data, a projected reactor efficiency of 4% was reported for carbon dioxide splitting.[55] Hathaway et al.[56] reported a 4.4 kW solar cavity carbon dioxide splitting reactor with a solar-to-fuel efficiency of 0.72% despite 95% gas phase heat recovery and an concluded that the experimental efficiency limit of isothermal cycling is about 2%. It was concluded that isothermal operation, i.e. reducing ΔT in many cases results in lower efficiency due to low fuel yields and high costs for oxygen partial pressure reduction.[47,54,104,108]

Surface reaction kinetics and bulk diffusion

The release and uptake of oxygen can be limited by the kinetics of the surface reaction or the diffusion of oxygen and oxygen vacancies in the bulk. The rate limiting process is the reaction on the surface rather than the transport of oxygen atoms and vacancies by ambipolar diffusion in the bulk.

Bulk diffusion

In the random-walk diffusion model, the mean squared displacement $\langle x^2(t)\rangle$ in one dimension is proportional to time t and the chemical (ambipolar) diffusion coefficient of oxygen $\widetilde{D}$:

$$\left\langle x^2(t)\right\rangle = 2\widetilde{D}(T)t \tag{1.18}$$

The ambipolar diffusion coefficient of ceria $\widetilde{D}$ is about $[10^{-6}, 10^{-4}]$ cm^2s^{-1} at 1073 K.[119] In 15% samarium doped ceria $\widetilde{D}$ falls in the range $1.7 \cdot 10^{-5}$ to $1.1 \cdot 10^{-4}$ cm^2s^{-1} at 1073 K and within $2.1 \cdot 10^{-4}$ to $3.6 \cdot 10^{-4}$ cm^2s^{-1} at 1773 K.[84] Thus, the diffusion time is in the order of magnitude of microseconds for a typical diffusion length of 5 μm. Unless

very unfavorable geometries with large diffusion lengths are used, the surface process is the bottleneck and rate-limiting step.

Surface area and surface reaction kinetics

Maintaining an open, porous morphology is indispensable for achieving high rates of mass and heat transfer.[120] Long-term stability of porous structures under realistic conditions has not yet been demonstrated. Many different morphologies have been tested, such as ceria felt,[121] cast monoliths,[46] electrospun fibers,[122] reticulated porous structures,[118] reticulated porous structures with a dual-scale porosity[123] and wood-templated porous structures.[124]

In cycling experiments with constant re-oxidation time, a gradual decrease in the fuel yield is mostly caused by incomplete oxidation due to loss of surface area. Call reported a decrease in the fuel yield due to sintering of $Ce_{0.85}Zr_{15}O_{2-\delta}$ from a characteristic length of one to 50 μm after 100 cycles with thermal reduction in a flow of inert gas at a temperature of 1673 K[125] In long time durability tests, after 100 cycles the hydrogen productivity had stabilized at about 75 % of the initial productivity[67] and under slightly different conditions, after 2000 cycles, a steady decline to 86 % of the initial productivity was reported.[126]
Even in the case of very 'mild' thermochemical looping conditions with very short exposure to 1473 K during reduction, only macropores ($d > 50nm$, IUPAC definition) were stable and after only 50 cycles (of 5 min each), the specific surface area (determined by nitrogen adsorption and the BET isotherm) decreased by a factor of more than 10 to about 4 m^2g^{-1}.[127] Cycling between 1473 and 1273 K decreased the specific surface area of magnesium and calcium stabilized ceria-zirconia from 80-100 m^2g^{-1} to about 1 m^2g^{-1}.[128] A similar drop in the BET specific surface areas of nano-structured ceria prepared by a flame-spray synthesis after only ten cycles of isothermal partial oxidation of methane and carbon dioxide splitting at 1173 K.[116] In materials that were exposed to the most common reduction temperature of 1773 K, the characteristic lengths required to maintain an open porosity are several micrometers and the specific surface area of the materials are smaller than 1 m^2g^{-1}. Further material degradation can be caused by the sublimation of ceria at temperatures above 1773 K,[66] for example as a consequence of direct exposure to concentrated radiation in solar simulators with limited temperature control.[129]

The structural features, interactions and dynamics of the defects involved in the

dissociation of water or carbon dioxide at the oxide-gas interface of reduced ceria are not well known. The most stable surface facet of ceria is the oxygen termination of the (111) crystal plane.[94,130] Along the [111] direction, oxygen-cerium-oxygen layers are stacked. Surface and sub-surface oxygen vacancy associations were visualized by means of scanning tunneling microscopy (STM),[94] however there are indications that oxygen vacancies might have been confused with fluorine impurities.[131] The concentration of Ce^{+3} on the (100) surface of samarium doped ceria was significantly higher than in the bulk and independent of the oxygen partial pressure in the range 10^{-34} to 10^{-21} atm.[132] It was speculated that the electron transfer between cerium cations and surface hydroxyl-ions might be the rate-determining step on the surface of reduced ceria.[130,133–135] In cycling experiments using very small ceria particles, the kinetics of the oxidation step of water splitting (hydrogen production rate) was weakly temperature-dependent and the reduction reaction carried out with hydrogen was the rate limiting step of the overall process.[135] The mechanism of water dissociation and hydrogen formation involves more steps than the dissociation of carbon dioxide. An electrical conductivity relaxation study found that carbon dioxide reacts significantly faster than water on the surface of reduced ceria[136] which might be due to a 'poisoning effect' of hydroxyl groups on the surface in case of the water splitting reaction. The exceptionally high reaction rates of ceria at high temperature can lead to the observation of apparent reduction kinetics, because of gas-flow limited behavior.[137] In the design of materials for use at 1773 K, thermodynamic properties can be prioritized because reaction kinetics are very fast.[57]

1.5 Vacancy engineering in ceria-based oxides

Many efforts have been made to boost the performance of ceria-based materials in solar thermochemical cycles by improving the oxygen storage capacity $\Delta\delta$. An ideal oxygen storage material is composed of non-toxic, abundant and cheap chemical elements, has favorable thermodynamic properties (see Section 1.2) that enable operation at reasonable temperature, exhibits high oxygen storage capacity, high oxygen bulk diffusion rates, fast surface reaction kinetics and is resistant to degradation and thermal shock.

The exchange of cerium cations with iso- or aliovalent cations has a strong impact on the concentration, stability and mobility of oxygen vacancies, which enables tuning of intrinsic material properties for specific applications. Heterocations are often referred to as 'dopants'. For single-phase materials (solid solutions), the typical hetero-cation concentration is in the range $x \leq 0.2$ in $Ce_{1-x}M_xO_{2-\delta}$. The solubility limits vary strongly.[75,78]

Improved mechanical stability and higher resistance against sintering can be positive side-effects of doping. A large number of ceria-based materials containing mono-, di-, tri-, tetra- and pentavalent hetero-cations have been tested in thermochemical water and carbon dioxide splitting cycles.[125,128,138–160]

Introducing tetravalent hetero-cations decreases the energy barrier of oxygen release, which can lead to higher fuel yields (per mass of material). Higher fuel yields do not necessarily imply an increase in efficiency. Lowering the barrier for oxygen release also decreases the thermodynamic driving force of the re-oxidation reaction and shifts the equilibrium non-stoichiometry to higher oxygen partial pressure. This requires higher water or carbon dioxide pressure or a larger temperature swing to oxidize the material. As discussed in section 1.4, the amounts of reactants that have to be heated to the reaction temperature represent an important energy penalty. A material that performs effectiviely better than the 'benchmark' pure ceria[96,103] will yield more fuel at a lower temperature without a decrease in the thermodynamic driving force.

Di- and trivalent cations

Replacing Ce_{Ce} with di- or trivalent cations, stable extrinsic, charge compensating oxygen vacancies are created. In the case of a trivalent cation of elements such as scandium, lanthanum, praseodymium, samarium or gadolinium, this formally corresponds to replacing Ce'_{Ce} by M'_{Ce} in Equation 1.7, also referred to acceptor-doped ceria. While extrinsic oxygen vacancies in ceria doped with trivalent cations improve the ambipolar transport of oxygen, influence the electrical conductivity and may change the surface reactivity, there is no compelling evidence that they significantly improve the oxygen storage capacity $\Delta\delta$ per gram of material.[70]

Mixed valence cations

Some cations have more than one stable oxidation state. For example, praseodymium can substitute Ce^{4+} as Pr^{4+} or Pr^{3+}. At high oxygen partial pressure, Pr^{4+} is formed.[161] In thermochemical carbon dioxide splitting cycles, $Ce_{1-x}Pr_xO_{2-\delta}$ with x = 0.05 and 0.1, Pr^{4+} was converted to Pr^{3+} in the first cycle in a flow of argon at 1773 K and was not oxidised in 0.5 atm carbon dioxide/argon at 1273 K.[157]

Pentavalent cations

In donor-doped ceria containing cations, such as Ta^{5+} and Nb^{5+}, the prevalent charge compensation mechanism at high temperature and low to medium oxygen partial pressure is the formation of polarons Ce'_{Ce}. At low temperature and high oxygen partial pressure, oxygen interstitial defects form.[162] Under thermochemical water splitting conditions, the reducibility of $Ce_{1-x}Ta_xO_{2-\delta}$ increased but a detrimental, inert secondary phase formed.[149]

Tetravalent cations - ceria-zirconia and ceria-hafnia

The lower energy barrier for oxygen release in the case of tetravalent hetero-cations was explained by simple geometry.[148,155] The smaller size of the hetero-cations reduce strain of the chemical expansion of the crystal lattice caused by non-stoichiometry.[75,95,163,164] The Ce^{3+} ion (1.14 Å) is larger than the Ce^{4+} ion (0.97 Å). The preferred oxygen coordination number of Zr^{4+} (0.84 Å) is seven. In the monoclinic crystal structure of zirconia that is stable below 1343 K, seven oxygen anions coordinate around zirconium.

Compared to pure ceria, the changes in the thermodynamic quantities of ceria-zirconia are less favorable for water- or carbon dioxide splitting.[70] Statistical thermodynamics suggests that the increase in the stability of oxygen vacancies is related to the configuration entropy (see Section 1.3). Heterocations block lattice sites of polarons and decrease the configuration entropy.[98] Changes in the properties of non-stoichiometric tetragonal ceria-zirconia materials related to the thermochemical history of samples have been ascribed to ordering phenomena by Kuhn et al.[165] These were partly reversible by oxidation at 1273 K. In thermochemical cycling, ceria-zirconia and ceria-hafnia showed similar behavior,.[153] Zirconium and hafnium have a very similar chemistry and their oxides are isomorphs. Tabulated cation radii in crystals of Zr^{4+} and Hf^{4+} in 6-fold (0.72 and 0.71) and 8-fold coordination (0.84 and 0.83), respectively, are very similar. The tabulated cation radii of Ce^{3+} and Ce^{4+} in 6-fold coordination are 1.01 and 0.87 and they are 1.14 and 0.97 Å in 8-fold coordination.[166] With increasing temperature, the structures of zirconia and hafnia transform from the monoclinic to the tetragonal phase at moderate temperatures and to a cubic structure at high temperatures. Although only minute differences between monoclinic zirconia and hafnia have been found, the monoclinic-tetragonal phase transition in hafnia occurs at significantly higher temperature than in zirconia. The monoclinic-tetragonal inversion of hafnia occurs at about 600 K higher than that of zirconia.[167,168]

Ceria-zirconia and ceria-hafnia solid solutions maintain a fluorite-type structure over a large temperature range and up to high non-stoichiometry δ. The equilibrium ceria-zirconia phase diagram consists of monoclinic, cubic (fluorite type) and tetragonal phases.[169–172] Allotropic phases in the ceria-zirconia system are essentially distorted fluorite-type phases, the most prominent being the tetragonal (space group P42/nmc, 137) t, t' and t" phases. They are closely related to and can be easily deduced from the fluorite-type structure. A large number of other ceria-zirconia phases have been identified.[173] The arrangement of hetero-cations is random in fluorite-type solid solutions with fluorite-type and tetragonal structures. Heterogeneity due to local differences in the composition can affect material properties.[145,174] Under reducing conditions, ordering of cations and oxygen vacancies of the solid solution with an equimolar composition leads to the formation of the pyrochlore structure (space group $Fd\bar{3}m$, No. 227). Figure 1.8 visualizes the oxygen coordination of zirconium and cerium in monoclinic zirconia, tetragonal t' ceria and in the cation-ordered pyrochlore structure.

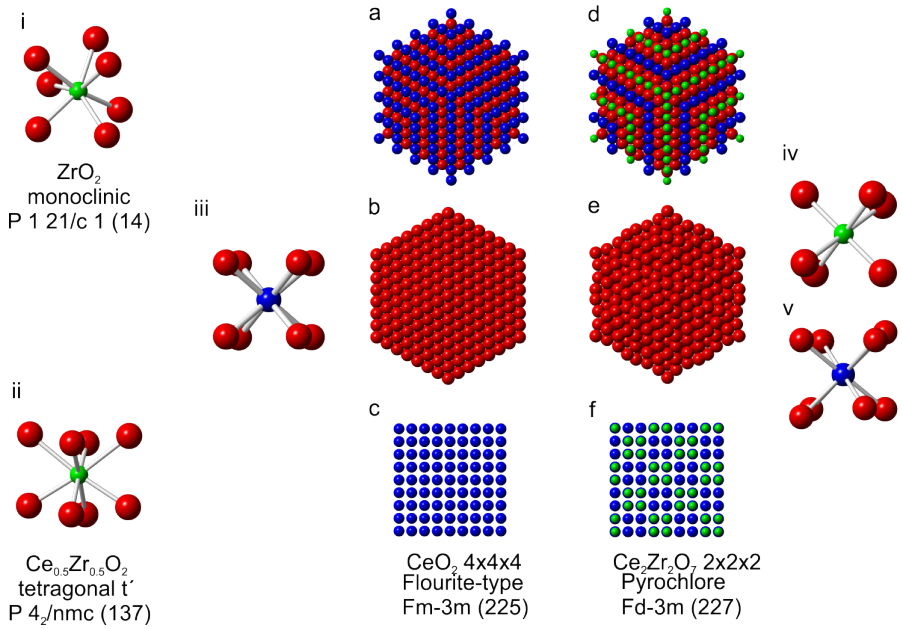

Figure 1.8 Arrangement of cerium (blue), oxygen (red) and zirconium (green) ions in the cubic fluorite-type (a-c) and pyrochlore (d-f) structures. Views of supercells in direction of the diagonal [111] direction in a,b,d and e) and the x axis N(100) in c) and f), illustrating the ordered arrangement of cations in the pyrochlore-type structure. In addition the oxygen coordination geometry in monoclinic zirconia (i), tetragonal ceria-zirconia (ii), fluorite-type ceria (iii) and the pyrochlore phase (iv and v).

The pyrochlore structure in ceria-zirconia and ceria-hafnia

In the ideal pyrochlore structure, $A_2B_2O_6O$, space group Fd3m, A^{3+} ions are coordinated to 8 oxygen atoms and B^{4+} ions are surrounded by 6 oxygen atoms. The ratio of the ionic radii of the A and B cations are typically found in the range $1.46 \leq \frac{r_A}{r_B} \leq 1.8$.[175] The pyrochlore structure can be derived from a fluorite-type structure with an ordered arrangement of cations such as Ce^{3+} and Zr^{4+} by removing and displacing oxygen atoms from their original lattice positions. Variations in the oxygen stoichiometry causes distortions and changes in symmetry.[176] Upon oxidation, cation ordering can be maintained and the cubic κ-$Ce_2Zr_2O_8$ phase, is formed. Intermediate oxygen-rich phases, such as the $Ce_2Zr_2O_{7.5}$ phase[176–179] exhibit an ordered arrangement of cations, while the anion sub-lattice is defective. The extent of order/disorder in the arrangement of cations and oxygen vacancies strongly affects the capacity and dynamics of the oxygen release and uptake.[180–185]

Similar to ceria-zirconia, relatively wide concentration ranges of solid solutions with pyrochlore structure exist in ceria-hafnia. Homogeneity ranges become narrower as the stability of the pyrochlore phase decreases with increasing temperature and decreasing rare earth cation radius. Unlike the fluorite-type phases, the pyrochlore hafnates are more stable than the corresponding zirconates. The formation of pyrochlore structures with Ce^{4+} ions has not been observed.[186,187]

The case of ceria containing pyrochlores, such as hafnates containing cerium in a 3+ oxidation state, was not considered in many studies because their preparation requires vacuum or more reducing conditions and high temperatures. Experimental evidence about structural changes in ceria-hafnia materials under reducing conditions at elevated temperatures is scarce. Andrievskaya et al.[188,189] determined ceria-hafnia-zirconia phase equilibria at 1773 K in air. Stanek et al.[190] had no data on ceria-hafnia at hand for use in their predictive study of hafnia-containing pyrochlore phase fields.

Baidya et al.[191] compared the chemical reduction of fluorite-type $Ce_{0.5}Hf_{0.5}O_2$ and $Ce_{0.5}Zr_{0.5}O_2$ prepared by a solution combustion route. Temperature-programmed reduction in dry hydrogen up to 1073 K indicated that the hydrogen uptake profile of ceria-hafnia was different and shifted to higher temperatures compared to ceria-zirconia. While ceria-zirconia was reduced to $Ce_{0.5}Zr_{0.5}O_{1.75}$ and even beyond that, ceria-hafnia could only be reduced to a composition of $Ce_{0.5}Hf_{0.5}O_{1.77}$ and the pyrochlore crystal structure was not detected. Bonk et al.[164] prepared ceria-hafnia powders containing up to 20 mol% hafnia ($Ce_{0.8}Hf_{0.2}O_2$) using a Pechini-type synthesis and obtained ceramic bodies by sintering at 1873 K in air. The lattice expansion was related to the non-

stoichiometry of fluorite-type phases using in situ XRD during a switch from vacuum to 2 bar hydrogen at 873 K. Weak reflections of other phases emerged during chemical reduction in hydrogen at 873 K. However, indications of the formation of a pyrochlore phase are absent. The pyrochlore structure and cation ordering have not been reported in ceria-zirconia or ceria-hafnia nanoparticles. Zhou and Gorte[192] reported single phase $Ce_{0.5}Hf_{0.5}O_2$ nanoparticles and Raitano et al.[193] reported on the phase boundary of the cubic domain of nanocrystals, which was found close to x = 0.5 in $Ce_{1-x}Hf_xO_2$. Sharma et al.[194] performed XANES (at the O K and Ce M_5 edges) and EXAFS (at the Ce K, Zr K and Hf L_3 edges) of nanoparticles with composition $Ce_{0.5}Zr_{0.5}O_2$, $Ce_{0.5}Hf_{0.5}O_2$ and $Ce_{0.5}Hf_{0.25}Zr_{0.25}O_2$. Fujimori et al.[195] confirmed the existence of the tetragonal t" phase in compounds with up to 20 mol% hafnia using synchrotron X-ray diffraction and Raman scattering.

1.6 Characterization of non-stoichiometric ceria-based materials

A comprehensive picture of the relevant properties of oxygen storage materials for solar thermochemical looping is obtained by the accurate determination of the geometric arrangements of atoms as a function of the oxygen content and how it is related to the oxygen partial pressure and temperature. The determination of these structure-property relationships requires a combination of several characterization methods of bulk properties. For the elucidation of the mechanism of surface reactions, surface-sensitive methods such as X-ray photoelectron spectroscopy (XPS), (polarization-modulated) Fourier transform infrared spectroscopy (FTIR), scanning tunneling microscopy (STM), atomic force microscopy (AFM), low energy electron diffraction (LEED), ion scattering spectroscopy (IS), sum-frequency generation spectroscopy or grazing incidence X-ray diffraction (GI-XRD) or gracing incidence small angle X-ray scattering (GI-SAXS). The named surface science techniques typically require vacuum with a lower oxygen partial pressure than relevant for solar thermochemical cycles and are in most cases not applicable at relevant temperature.

X-ray based methods

Ceria-based materials have been extensively studied using XAS, mainly in the context of heterogeneous catalysis and nano science. XAS of ceria compounds was performed

at the Ce K, Ce L_{III}, Ce $M_{5,4}$ and O K edges. XAS at absorption edges of heterocations such as the Zr K, Zr L_{III}, , Hf L_3, Co K edges have also been carried out. Paun and Safonova et al.[196] determined the concentration of Ce^{3+} in ceria nanoparticles with narrow size distributions by means of cerium K edge XANES. A shift in the edge position of a Ce^{3+} reference compound by -6.2 eV relative to a Ce^{4+} reference compound illustrates that K edge XAS is a sensitive tool for the determination of the electronic structure. HERFD-XAS at the cerium L_{III} edge revealed the dependence of spectral features on particle size. Kaneko et al.[144] reported Ce L_{III} edge XAS data of reduced and oxidised ceria mixed oxides before and after exposure to thermochemical cycling. Yamamoto et al.[180] reported Ce L_{III} and Zr K-edge time-resolved energy-dispersive in situ XAS of a ceria-zirconia supported Pt catalyst under reducing (hydrogen) and oxidising (oxygen) conditions up to 773 K. Rodriguez et al.[197] reported cerium L_{III} and Zr K edge XAS of this system. The tetragonal-to-cubic transition of ceria-zirconia solid solutions was investigated by EXAFS analysis up to 1073 K by Acuna et al.[198] The distribution of oxygen vacancies doped ceria materials was investigated by XRD, K and L edge EXAFS by Deguchi et al.[199] and Nitani et al.[200] Lee et al.[201] described typical margins of error for the first oxygen shell by fitting Ce K edge EXAFS data, whereas Zhang et al.[202] compared results of XPS and L edge XAS and determined the Ce^{3+} concentration in ceria nanocrystals. Sharma et al. collected O K edge, Ce $M_{5,4}$ edge XANES and Ce K, Zr K and Hf L_{III} edge EXAFS of ceria-zirconia and ceria-hafnia nanoparticles.[194] Zr K and Ce L_{III} edge XAS was reported by Fornasiero et al.,[203] EXAFS analysis of the anharmonic pair distribution function in Zr K edge EXAFS by Lemaux et al.[204] Rodriguez et al.[197] performed XAS at the O K, Ce and Zr L_{III} edges and time-resolved XRD of nano-particles. In many studies materials were characterized under relevant process conditions. Yamamoto et al.[180] collected in situ XAS of ceria-zirconia materials under conditions relevant for automotive catalytic converters and Kopelent et al.[205] performed in situ XES of Pt/ceria catalysts at room temperature and up to 317 K at the Ce L_{III} edge and determined the Ce^{3+} concentration in transient experiments at sub-second time resolution,[205] Bessa et al.[206] determined the oxidation state of cerium in a catalyst for methane steam reforming from Ce L_{III} edge XANES spectra acquired in situ in fluorescence mode. They found a larger amount of Ce^{3+} due to the presence of samarium(III)ooxide in a Rh/samarium(III)oxide-ceria-alumina catalyst. Acuna et al.[198,207,208] reported synchrotron XRD and Zr K edge XAS of ceria-zirconia up to 1123 K. The crystal structure of the phases and phase changes in oxygen-storage materials can be determined under reaction conditions using laboratory

X-ray diffractometers.[50,159,164,209] Bork et al.[209] determined the structure of the perovskite $La_{0.6}Sr_{0.4}Cr_{0.8}Co_{0.2}O_{3-\delta}$ at up to 1473 K under relevant thermochemical carbon dioxide splitting conditions with a laboratory X-ray diffractometer. X-ray photoelectron spectroscopy is a surface-sensitive method[210] that enables determination of the Ce^{3+} concentration,[86,160,202,211–213] recently also in situ measurements at near-ambient pressure and at elevated temperature, for surface-sensitive in situ characterization and depth-profiling have been performed,[132–134,214] aiming at better understanding of the surface reaction mechanisms.

Other Methods

The main tool to determine the non-stoichiometry of materials at high temperature and low oxygen partial pressure is thermogravimetric analysis.[123,125,126,153,157,160,165,177,209,215–218] Other methods for structural characterization of ceria-based materials include neutron diffraction of powders and single crystals,[100,183,184,219–224] Raman spectroscopy,[128,165,195,225–227] dilatometry,[73,95] electrical conductivity measurements[136,137] determination of the heat capacity,[72,228] scanning electron microscopy (SEM) and transmission electron microscopy (TEM) for morphological and structural characterization. Wang et al.[182] performed time- and temperature-resolved environmental transmission electron microscopy (TEM) and electron energy loss spectroscopy (EELS) to investigate the redox properties of ceria nano-particles at up to 1073 K in 0.5 Torr hydrogen and used the integrated white line ratio (M_5/M_4 ratio) to determine the Ce^{3+} concentration of individual particles. Mössbauer spectroscopy performed at room temperature by quenching iron-substitued ceria at different stages of the thermochemical cycle showed that iron does not change its oxidation state, i.e. that only the cerium redox pair is active for thermochemical water splitting.[141] Positron annihilation lifetime spectroscopy (PALS) was applied to characterize neodymium-doped ceria[229] and europium-doped ceria.[230] Notably, this is the only characterization method that uses a probe (positrons) that directly interacts with oxygen vacancies.

1.7 Scope of the thesis

Few attempts have been made to determine material properties under the harsh conditions of solar thermochemical looping. This thesis describes efforts in the synchrotron X-ray-based determination of the electronic and geometric structures of ceria-based oxygen storage materials under the extreme conditions of the two-step thermochemical dis-

sociation of water or carbon dioxide, exploiting the experimental capabilities of beamline BM01B at the European Synchrotron Radiation Facility (ESRF) in Grenoble, France. Equipment suitable for high-temperature in situ/operando XAS and XRD measurements in transmission mode was developed. The same setup was used for thermochemical looping experiments in the laboratory (ETH Zurich).
The thesis is organized as follows:

Chapter 2 introduces the principles of XAS and XRD with a focus on the effects of high temperature and high photon energy. Chapter 3 presents the high-temperature setup and the in situ cells, including typical results obtained with the in situ cell for combined XAS and XRD experiments and XRD with a focused beam.

Chapter 4 presents estimations of changes in the spectral features of the Ce K edge and demonstrates the extraction of structural information, i.e. the non-stoichiometry δ from in situ XANES data collected in oxidizing and reducing conditions up to 1773 K. Structural changes and temperature effects in the XANES and the possibility of high-temperature EXAFS analysis are discussed.

Chapter 5 presents in situ Ce K and Zr K edge XANES of an equimolar ceria-zirconia compound under isothermal carbon dioxide splitting conditions at 1773 K. Changes in the geometry of the oxygen coordination of zirconium and cerium are discussed and Zr K edge XANES spectra are compared with those of $Ce_{0.8}Zr_{0.2}O_{2-\delta}$. The average oxidation state of cerium in the compound is related to the phase diagram at 1773 K.

Chapter 6 presents in situ Ce K and Hf K edge XAS and XRD data of the formation of the pyrochlore ceria-hafnia phase. The dynamics of structural changes under isothermal carbon dioxide splitting at 1773 K were determined by time-resolved XRD. The pyrochlore structure with an ordered arrangement of cations was not stable under oxidizing conditions.

In Chapter 7, the direct formation of methane upon thermochemical water- and carbon dioxide splitting over Rh-decorated ceria is demonstrated. A durability test over 58 cycles was carried out. The oxygen and hydrogen production was quantified and traces of methane were detected in the product gas stream by quadrupole mass spectrometry.

Chapter 8 contains general conclusions about the characterization methods used in this project and presents an outlook.

Chapter 2

Methods

2.1 Interaction of X-rays with matter

X-radiation is electromagnetic radiation with a wavelength of about 0.01 to 10 nm. The interaction of electromagnetic radiation with matter occurs in different processes depending on the photon energy - scattering, absorption and pair production contribute to different extent. X-radiation interacts with electrons and is thus useful to obtain information about the electronic structure of materials. Photons can be scattered by an electron in an elasic or inelastic manner. These scattering phenomena are referred to as Thomson scattering and Compton scattering, respectively. In the photoelectric absorption process, a photon interacts with an electron bound in an atom. The interaction involves the annihilation of the photon and the transfer of its energy to the electron that leaves its bound state, resulting in the formation of an excited state of an ionized atom with an electron hole. This instable, excited state then decays via different mechanisms.

The attenuation of an X-ray beam passing through a material is proportional to the initial intensity I_0 and the distance z of the material according to the Beer-Lambert law. The linear attenuation coefficient $\mu(E)$ strongly depends on the photon energy.

$$dI = -\mu(E) I dz \tag{2.1}$$

$$\frac{I}{I_0} = e^{-\mu(E)z} \tag{2.2}$$

Over a wide energy range, the photoelectric absorption of electrons is the dominating process in the interaction of X-rays with matter. In elements of very low atomic number, Compton scattering can become a significant contribution at photon energies above the absorption edges. Electron pair production and nuclear pair production occur only at very high photon energies. Elastic (Thomson) scattering is significantly stronger than inelastic (Compton) scattering at low photon energies and elastic and inelastic scattering cross sections become comparable only at high photon energy. Figure 2.1(a) shows the contributions to the total interaction cross sections of photons with barium. When the electromagnetic radiation can couple with the bound electrons, photons are absorbed. Sharp increases in the photoelectric absorption cross section occur when the energy of the incident photon beam matches the binding energy of an electron. Figure 2.1(b) shows an energy diagram of core electrons and the X-ray absorption edges, which are named after the origin of the excited electron.

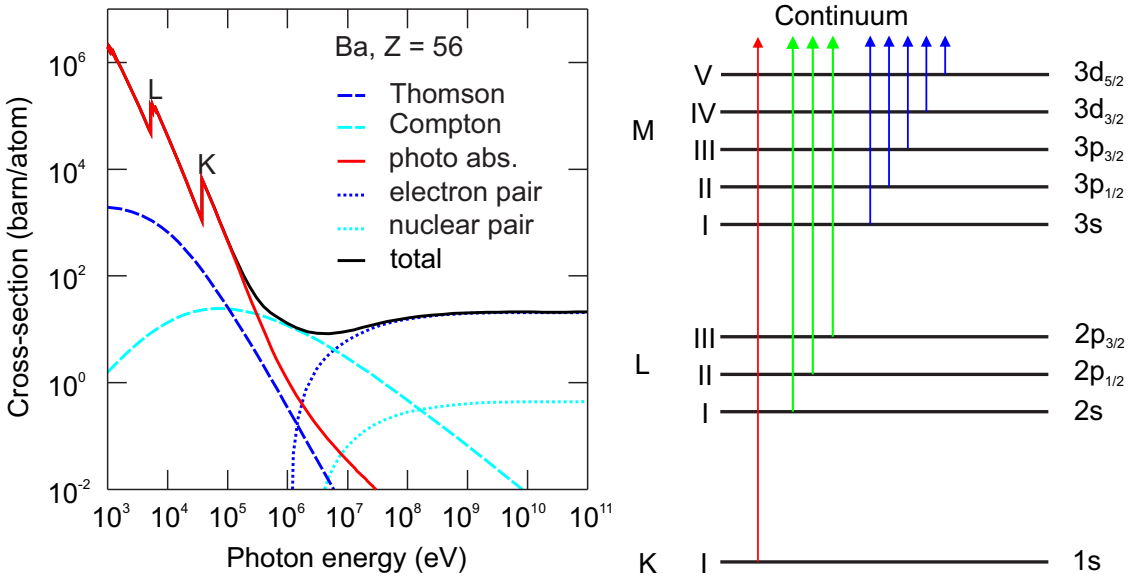

(a) (b)

Figure 2.1 Interaction of X-rays with matter, exemplified with data showing photon-matter interaction cross sections of barium[231] (a). Core electron energy diagram and nomenclature of absorption edges.[232] The electronic shells are labelled as nl_j, with n the principal, l the orbital angular momentum and j the total angular momentum quantum numbers (b).

The linear absorption coefficient is related to the atomic density ρ_a and the atomic absorption cross section σ_a

$$\mu(E) = \rho_a \sigma_a(E) \tag{2.3}$$

At most photon energies, the atomic absorption cross section $\sigma_a(E)$ is a smooth function and the variation of $\sigma_a(E)$ is approximately proportional to the fourth power of its atomic number and inversely proportional to the third power of the photon energy E. The absorption cross section is an indicator of the electron density and the binding energies of the electrons in a material.

$$\sigma_a \propto \frac{Z^4}{E^3} \tag{2.4}$$

The relaxation of the excited state created by photoelectric absorption can occur by way of two competing processes, fluorescent X-ray emission or Auger electron emission. In the mechanism leading to fluorescent X-ray emission, an electron from a higher shell relaxes and fills the core hole, thereby emitting a photon with an energy given by the difference between the initial and final states of the transition. For example, the transition of an electron from the L_3 to the K shell gives rise to the element-specific $K_{\alpha 1}$ radiation. In Auger electron emission, the relaxation involves the liberation of another electron when an electron from a higher shell relaxes and fills the core hole. For example, in a $KL_1L_{2,3}$ Auger transition, an electron relaxes from the L_1 state to the K state and an electron from the $L_{2,3}$ states is emitted. At small energy transitions in light elements, the Auger yield is high and the X-ray yield is low. The reverse is the case in heavy elements.

2.2 X-ray absorption spectroscopy

The step-like increase in the absorption cross section at absorption edges is only true for isolated atoms. The absorption cross section close to the absorption edge exhibits features that depend on the environment of the absorbing atom and thus gives access to invaluable, element-specific information about its electronic and geometric local environment. The position of an absorption edge is related to the oxidation state because the expulsion of another electron requires more energy from a positively charged ion. Absorption spectra are conventionally divided in two regions: the X-ray absorption near edge structure (XANES) and the extended X-ray absorption fine structure (EXAFS). In most cases XANES is a bigger signal than EXAFS. Figure 2.2 illustrates typical absorption spectra measured at the Ce L_{III} and Ce K edges.

X-Ray Absorption Near Edge Structure (XANES)

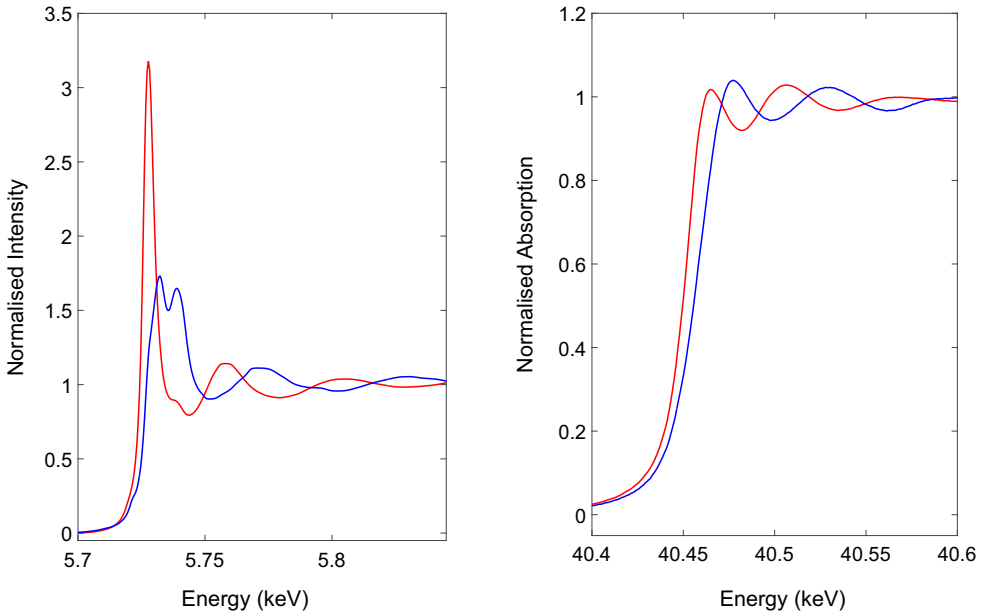

(a) (b)

Figure 2.2 XANES spectra of Ce^{3+} and Ce^{4+} compounds. Ce L_{III} edge spectra of $Ce(NO_3)_3$ (red) and CeO_2 (blue) recorded in emission mode (a). Ce K edge spectra of $Ce_2(CO_3)_3$ (red) and CeO_2 (blue) recorded in transmission mode (b). Courtesy of C. Paun, O. Safonova and R. Kopelent.[196,205]

Because a core electron can only be excited to an electronic state that is unoccupied, XAFS probes the unoccupied density of states in a material. The possibility of such a transition is given by the overlap of the wave-functions of the initial and final states, which is determined by the symmetry and parity of the involved orbitals. Fermi's golden rule in Equation 2.5 states that the probability of a transition depends on the square of the absolute value of the transition matrix element, with H' the perturbation Hamiltonian, i and f the wave functions of the initial and final states, respectively and ρ the density of states of the final state.

$$P_{i,f} = \frac{2\pi}{\hbar} \left|\langle f \left| H' \right| i \rangle\right|^2 \rho \tag{2.5}$$

Within the dipole approximation, only one-electron transitions that follow the selection rule are allowed. l is the orbital quantum number.

$$\Delta l = \pm 1 \tag{2.6}$$

The low spatial extension of orbitals makes XANES very sensitive to the local, short-range geometric arrangement of atoms adjacent to the absorbing atom. The intensity and energy of spectral features can be related to the occupancy of states below the Fermi-level, bond lengths, angles and specific coordination geometries. XANES enables semi-quantitative analysis of chemical species by linear combination fitting or spectral analysis methods such as principal component analysis.

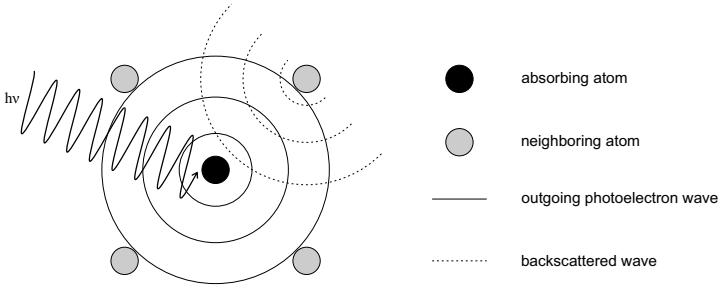

Figure 2.3 The EXAFS originates in the constructive and destructive interference of photo-electron waves due to scattering at adjacent atoms.

Extended X-ray Absorption Fine Structure (EXAFS)

The EXAFS signal χ is defined as the deviation of the absorption coefficient μ above the edge from the smooth background μ_0 of an isolated atom.

$$\mu = \mu_0(1 + \chi) \tag{2.7}$$

Backscattering of the outgoing electron at adjacent atoms modifies the wave function of the photo-electron Ψ_{final}, which gives rise to an interference pattern characteristic of the scattering properties and geometric arrangement of these atoms. Figure 2.3 shows a schematic representation of the origin of the EXAFS.

$$\Psi_{final} = \Psi_{outgoing} + \Psi_{backscattered} \tag{2.8}$$

The kinetic energy of the photo-electron is the difference between the photon energy E and the binding energy of the excited electron E_0 and relates to the wave vector (defined as $k = \frac{2\pi}{\lambda}$) according to

$$k = \sqrt{\frac{2m_e(E - E_0)}{\hbar^2}} \tag{2.9}$$

Equation 2.10 gives the customary notation of the EXAFS signal as the sum of all scattering contributions. Several terms and parameters account for the damping of the amplitude.

$$\chi(k) = S_0^2 \sum_j \frac{N_j F_j(k)}{k r_j^2} e^{-2\sigma_j^2 k^2} e^{\frac{-2r_j}{\lambda(k)}} \sin(2kr_j + \phi_j) \tag{2.10}$$

A number of N_j atoms of type j located at a distance r_j from the absorbing atom scatter with an amplitude F_j and a scattering phase shift of ϕ_j. Losses in the EXAFS amplitude due to many-body effects and shake-up or shake-off processes in the absorbing atom are accounted for by the amplitude reduction factor S_0^2. The nature of the photo-electron wave makes EXAFS a local probe. The contributions of a scatterer decreases by the square of the distance r_j. The amplitude is further reduced by the finite lifetime of the core hole and the photo-electron. The corresponding damping term contains the path traveled by a scattered electron $2r_j$ and the photo-electron mean free path $\Lambda(k)$. Moreover, the amplitude of the fine structure is damped by thermal motion or structural disorder, which is accounted for by adding the Debye-Waller factor $e^{-2\sigma_j^2 k^2}$, with σ^2 a measure for the average deviation of the absorber-scatterer distance due to vibrations or disorder. Data analysis is conventionally performed by Fourier-transform (FT) of the k-space data. The modulus of the FT can be interpreted as a pseudo-radial distribution function of scattering atoms around the absorbing atom. At low k, multiple scattering contributes significantly to the signal. Multiple scattering paths allow the determination of bonding angles. The dominant contributions are single scattering paths. The dependence of scattering factors on k leads to increasing contribution of heavy scatterers to the amplitude of the EXAFS at higher values of k. The accuracy of EXAFS analysis depends to great extent on the quality of the data and the theoretical model used for fitting. Absolute errors as small as ±1 for coordination numbers and ±0.2 pm for inter-atomic distances can be achieved.

XAFS at high temperatures

Disorder caused by thermal vibrations attenuates the amplitude of the EXAFS oscillations. The XAS signal represents the average position of a large number of atoms, averaged over time. Deviations from the average positions of the scatterers due to thermal motion or structural disorder smear the signal and reduce the amplitude of the EXAFS. In the small displacement approximation of the customary description of the EXAFS (Equation 2.10), a Gaussian-like exponential damping term $e^{-2k^2\sigma^2}$ is obtained.

The EXAFS Debye-Waller factor is related to the mean square relative displacement of the absorber and scatterer(s) of a scattering path. The total reduction of the amplitude due disorder consists of static and temperature-dependent vibrational contributions:

$$\sigma^2 = \sigma^2_{stat} + \sigma^2_{dyn} \tag{2.11}$$

Neglecting anharmonic effects, at high temperature the Debye-Waller factor can be described by Equation 2.12, with σ^2 the mean squared relative displacement that is proportional to the temperature T, the Boltzmann constant k_B and an effective spring constant k:[233]

$$\sigma^2 \approx \frac{k_B T}{k} \tag{2.12}$$

Reduction of the EXAFS amplitude due to dynamic, (vibrational) and static effects can be separated by recording temperature-dependent data, which can also give insights into the lattice dynamics and the vibrations of individual bonds. Figure 2.4 shows the temperature dependence of the pseudo-radial distribution function and changes of the Debye-Waller factors using a fitting model with coordination numbers N_i fixed to the crystallographic values.[234] At increased temperature, in this case at 300 K, strong damping of the EXAFS signal is observable. The effect on the scattering amplitude and phase shift accounted for in a more general representation of the distances r_j using a probability distribution function. A more detailed description of the distribution of inter-atomic distances and how it affects scattering is given by the cumulant expansion model. Expansion in a cumulant series around $k = 0$ (Equation 2.13) leads to a representation of the scattering amplitude with additional parameters, which are a measure of disorder-related deviations in the radial distribution function. Eventually, at very high temperature, very strong damping reduce the k-range, which reduces the statistical robustness of the fitting model, particularly when it contains a large number of parameters.

$$\int_{-\infty}^{\infty} \Phi(r) e^{2ikr} dr = exp\left[\sum_{n=0}^{\infty} (2ik)^n \frac{C^n}{n!}\right] \tag{2.13}$$

Cumulants with even n affect the amplitude and odd n the phase. For one scattering path, the cumulant expansion is

$$\begin{aligned}\chi(k) = \frac{S_0^2}{k} \frac{e^{\frac{-2C_1}{\Lambda(k)}}}{C_1^2} F_j(k) N exp\left[-2k^2 C_2 + \frac{2}{3}k^4 C_4 + ...\right] \cdot \\ sin\left[2kC_1 - \frac{4}{3}k^3 C_3 + ... + \phi(k)\right]\end{aligned} \tag{2.14}$$

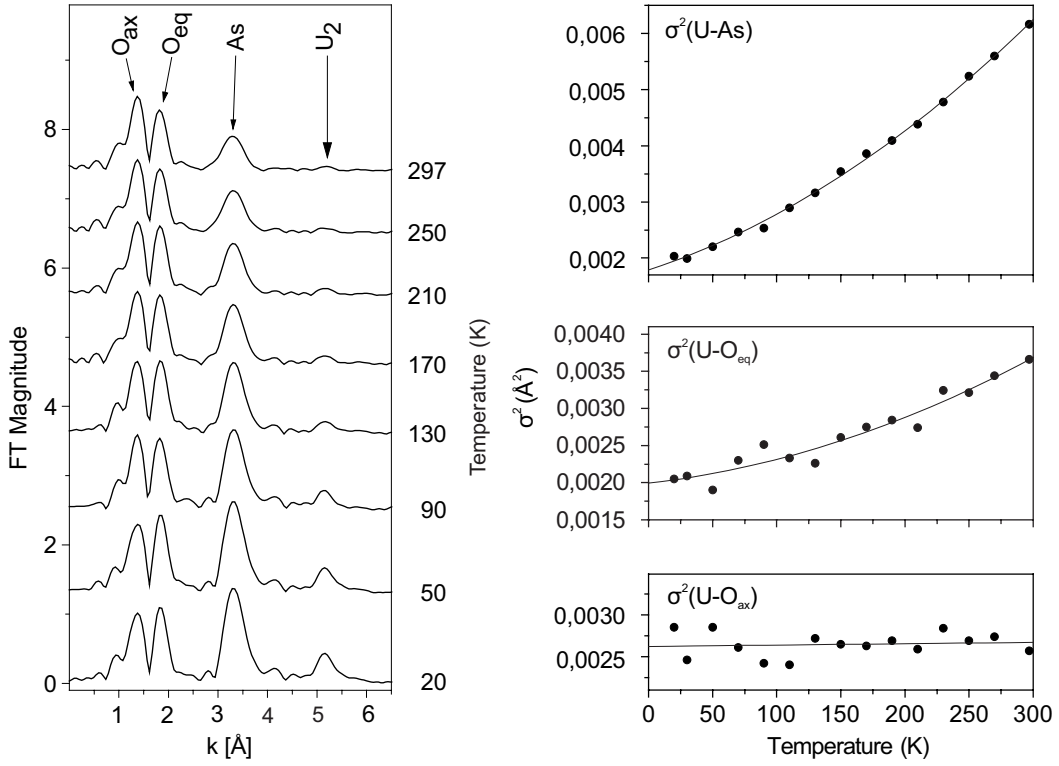

Figure 2.4 The effect of temperature in U L_{III} edge EXAFS of $H[UO_2AsO_4]\cdot 4\,H_2O$ from 20 to 297 K.[234] Reduction of the amplitude and broadening of the pseudoradial distribution function. FT magnitude of k^3-weighted EXAFS in the range 3.2 ≤ k ≤ 15.7 Å^{-1} (a) and fitting results for Debye-Waller factors σ^2 in a fit to a model with coordination numbers fixed to the crystallographic values (b).

where C_1 corresponds to r and C_2 to the scattering path length and σ^2, respectively, in the customary description of the EXAFS (Equation 2.10). The first cumulant is the mean value, the second the variance, the third the asymmetry and the fourth the flatness of the probability function describing the inter-atomic distance of a scattering path.

XAFS at high photon energies

The finite lifetime of the core hole following the Heisenberg uncertainty relation between time and energy given in Equation 2.15 leads to significant broadening of spectral features. The finite lifetime modifies both the amplitude and the phase of the EXAFS. This effect smears out the oscillations and is stronger at higher photon energies. A value of 15.1 eV of the full width at half maximum (FWHM) was reported for the natural line width of the Ce K state. The X-ray fluorescence yield is above 90 % at the Ce K

edge; At the Hf K edge, a value of 35.7 eV at FWHM for the natural level width was reported.[235]

$$\Delta t \Delta E \leq \frac{\hbar}{2} \tag{2.15}$$

Absorption of an electron of the K-shell probes p-states. This can be an advantage as in many transition metals, changes in the electronic structure happen mostly in the d band, while the little changes show up in transitions to the p states, which remain unoccupied. In many cases, this makes K-edge XAFS a less sensitive tool than L-edge XAFS. On the other hand, a much larger EXAFS data range can be collected due to larger differences in the energies of electronic states in heavy elements. At lower energies, this is not possible due to interference of a large number of resonances, particularly when many elements are present. In many elements, the k-range range of L_{III} edge EXAFS is limited by interference of the L_{II} edge. In the case of cerium, the L_{II} (6.164 keV) is only 441 eV above the L_{III} edge (5.723 keV). At the Ce K edge (40.443 keV) the accessible EXAFS data range is much larger and only limited by the damping of the signal. The Ce K edge EXAFS can be recorded over a wide range, as the only edge that could potentially interfere is the Pr K edge (41.991 keV) which is 1548 eV higher in energy. The penetration depth of high energy X-rays allows access to a wide range of experimental conditions. X-ray transparent reaction chambers such as quartz capillaries enable to collect structural data of functional materials such as heterogeneous catalysts in situ, i.e. under realistic conditions and at relevant temperature and pressure.

Experimental aspects

X-ray absorption spectroscopy requires a tunable X-ray source. Such radiation sources are provided in dedicated synchrotrons and storage rings at large scale research facilities such as the Swiss Light Source (SLS) at Paul Scherrer Institute, Switzerland or the European Synchrotron Radiation Facility (ESRF) at the European Photon and Neutron Science Campus in Grenoble, France. Recently, free electron lasers operating in the X-ray regime have become available. Figure 2.5 illustrates a typical X-ray absorption experiment. The X-rays produced by an insertion device or bending magnet passes through a monochromator, typically made of silicon single crystals. The energy of the electrons in the storage ring of ESRF is 6 GeV. The beamline BM01B (now recently established as BM31) at ESRF was dedicated to combined XRD/XAFS/Raman measurements and was optimized for quasi-simultaneous XAS in transmission and fluorescence modes and high-resolution powder XRD measurements in situ. The radiation source of the beam-

line was a bending magnet. The beamline provided sufficient photon flux from 5 to 80 keV covered by a single Si(111) double crystal monochromator.[236,237]

The intensities of the X-ray beam before and after it passing through the sample are measured with ion chambers. In addition to simple absorption measurements in transmission mode, X-ray emission (XES) techniques that are based on the detection of the emitted X-ray photons are of growing importance. A good signal can only be

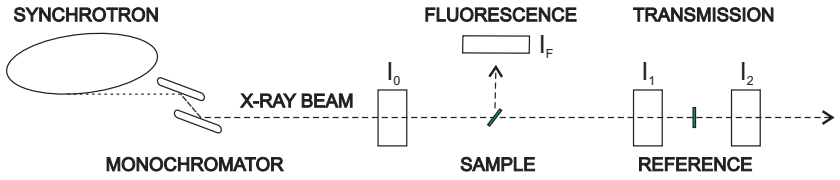

Figure 2.5 Schematic layout of an X-ray absorption experiment using X-rays from a bending magnet of a synchrotron's storage ring. The intensities of the X-ray beam is measured as a function of the incoming photon energy before and after passing through the sample. In addition, a reference channel is measured. It is also possible to measure absorption spectra by collecting the fluorescence signal.

obtained if the absorbing object is homogeneous. Variations in sample thickness or pinholes significantly decrease the quality of the spectrum. The absorbance of an X-ray that passes through a homogeneous, prism-shaped sample with thickness z, base area A_{pellet} and mass m_{sample} of a compound consisting of chemical elements of type i with molar mass M_i, and coefficients c_i in the empirical formula are related according to

$$\mu(E) = \frac{\rho_{sample}}{\sum_i M_i c_i} \sum_i M_i c_i \sigma_{m,i} \tag{2.16}$$

$$\mu z(E) = \frac{m_{sample}}{\sum_i M_i c_i A_{pellet}} \sum_i M_i c_i \sigma_{m,i} \tag{2.17}$$

The edge jump $\Delta\mu$ the mass and geometry of the sample can then be adjusted using tabulated values at energies right below and above the edge position. In the case of small concentrations of the absorbing atom of interest, an optimum of the sample thickness has to be found. If the sample is very thin, the transmitted intensity I leads to high transmitted intensity and good counting statistics but a small signal because the edge jump is very small. If the sample is very thick, the noise in the data increases. The sample has to be homogeneous over the complete cross section of the X-ray beam to obtain a useful signal. Ideally, an absorption jump by 1.0 is achieved in a transmission experiment. Experimentally, particularly when heavy elements are present in a sample,

a compromise between the transmitted intensities and the edge jump has to be found for acceptable signal/noise and/or time resolution. Small relative spectral changes or shifts of the edge energy can best be detected by alignment of spectra recorded in the reference channel to correct possible drifts in the photon energy over time. If available, a metal foil is placed between I_1 and I_2 to correct these drifts and to calibrate the photon energy to tabulated values.

$$\Delta\mu = z[\mu(E_{post}) - \mu(E_{pre})] \tag{2.18}$$

Energy resolution

For relatively low X-ray energies it is found that the energy resolution provided by the Si(111) reflection is mostly adequate, whereas at higher energies the Si(311) or (511) may be needed. Here, we describe the calculation of the energy resolution for the XAS spectrometer at BM01, Swiss-Norwegian Beamlines at the ESRF at 40 keV.

At 40 keV, the intrinsic energy resolution of parallel beams reflected on a Si(111) monochromator crystal oriented orthogonally to the polarization plane reported by Sanchez del Rio and Mathon[238] is $\Delta E = 0.135 \cdot 40 = 5.4$ eV. The angular range over which total reflection occurs is described by the Darwin width ω_D of the crystal in the dynamical theory of diffraction. The Darwin width is defined as the FWHM of the reflex of a divergent beam.

$$\omega_D = \frac{2\lambda^2 r_e C\sqrt{|\gamma|}}{\pi V}\frac{|F_{hkl}|}{\sin 2\theta_B} \tag{2.19}$$

λ is the photon wavelength, r_e the classical electron radius, C the polarization factor, γ the asymmetric ratio, V the volume of the crystal unit cell, and $|F_{hkl}|$ the structure factor for the selected crystal reflection. For a polarized beam and symmetric Bragg reflection, C and γ are equal to 1. For Cu K_α radiation with $\lambda = 1.54$ Å, $\theta_B = 14.22°$, $\omega_{D,Cu} = 3.4{\cdot}10^{-5}$ rad. At high photon energies, the structure factor $|F_{111}|$ can be considered as weakly energy dependent, which extrapolates for $\omega_{D,40}$ to:

$$\omega_{D,40} = \omega_{D,Cu} \cdot \frac{\lambda_{40}^2}{\lambda_{Cu}^2}\frac{\sin 2\theta_{B,Cu}}{\sin 2\theta_{B,40}} = 6.6 \cdot 10^{-6} rad \tag{2.20}$$

A beam with 0.5 mm height at the sample position located 40 m from the source leads to a divergence $\psi = \frac{0.375mm}{30m} = 1.25 \cdot 10^{-5}$ rad at the monochromator, which is located 30 meters away from the source. In the present case, the divergence ψ is thus about two times as large as the Darwin width. Considering the intrinsic resolution of the crystal a constant ΔE can be calculated from Equation 2.21: R_T is a measure for the efficiency

of the reflection on two crystals and defined as $R_T = R_1 R_2 p_0$, the product the ratios of the source and reflected bandwiths R_1 and R_1 and a coefficient p_0 describing the peak value of the rocking curve.

$$R_T = 1 \cdot \left(\frac{\Delta E}{E}\right)_{intr} \cdot 10^3 \tag{2.21}$$

According to Table 1 in the work of Sanchez del Rio and Mathon[238] even at $\psi = 5\omega_D$ the value for R_T changes by less than 2%.
$\Delta E_1 = E \cdot R_T \cdot 10^{-3} = 40 \cdot 1346 \cdot 10^{-7} = 5.38$ eV
$\Delta E_{\psi=5\omega_D} = E \cdot R_T \cdot 10^{-3} = 40 \cdot 1373 \cdot 10^{-7} = 5.49$ eV
We can therefore conclude that at 40 keV the energy resolution ΔE of the Si(111) double crystal monochromator with flat crystals is better or equal to 6.0 eV.

Data processing

The edge jump of absorption spectra are conventionally normalised to unity. In this work, the inflection point at the edge was defined as the edge position. A linear background was fit to the pre-edge region and a second-order polynomial to the post-edge region, and the normalised spectra were obtained by applying Equation 2.23.

$$\chi(E) = \frac{\mu(E) - \mu_0(E)}{\mu_0(E)} \tag{2.22}$$

$$\chi_{parallel}(E) = \frac{\mu(E) - \mu_{pre}(E)}{\mu_{post}(E) - \mu_{pre}(E)} \tag{2.23}$$

Determination of the non-stoichiometry of ceria

The formation of an oxygen vacancy described in Equation 1.7 leads to an energy shift in the edge position and a reduction of the Ce-O coordination number. Paun and Safonova et al.[196] found that the energy of the Ce K edge of $Ce_2(CO_3)_2 \cdot xH_2O$ is 6.2 eV higher than that of CeO_2. Braglia et al. determined changes in the non-stoichiometry with principal component analysis of Ce K edge XANES recorded at 423 K. Two components were found and assigned to the reduced and oxidized species. The Ce^{3+} concentration (0 - 25%) was determined with reference spectra of $Ce_2(CO_3)_2$ and the pristine Pt/CeO_2 material as references.[239]

The valence of cerium and the corresponding non-stoichiometry δ can be determined from the relative energy shift in the edge position. A simple but effective method to capture these energy shifts is to measure the energy of the spectra at constant normalized

absorption. The energy shift in the edge position ΔE was extracted by spline interpolation of golay-filtered normalized spectra at the absorption value of the edge position of the first spectrum. Geometrically, this corresponds to the intersection of the rising absorption curves with a line parallel to the energy axis. The non-stoichiometry δ was calculated by assuming a linear relationship between ΔE and the Ce^{3+} concentration, and that hafnium or zirconium are consistently present as Hf^{4+} or Zr^{4+}, respectively.

Table 2.1 summarizes the relationship between the non-stoichiometry δ in fluorite-type ceria and expected cerium K edge XAFS features upon reduction. These data indicate that even at the highest non-stoichiometry relevant for a solar thermochemical looping process, the corresponding spectral changes are small in both the XANES and the EXAFS. It is thus very difficult to detect and quantify related structural changes, particularly under non-ambient conditions.

The main experimental challenge is the accuracy of the mechanical movement of the monochromator crystals: At high photon energies such as the Ce K edge, an energy scan from 40 to 41 keV requires a mere 0.07° change in the Si(111) Bragg angle.

Equation	value at 10^{-6} bar oxygen, 1773 K ($\delta = 0.1$)
$\Delta N^{1}_{Ce-O} = -4 \cdot \delta$	−0.4
$\Delta E = -6.2 \cdot 2\delta$ eV	−1.24 eV

Table 2.1: Expected changes in cerium K edge XAFS features related to non-stoichiometry in fluorite-type $CeO_{2-\delta}$.

Equation 2.24 gives the relationship between the fraction of reduced cerium cations, the shift in edge energy ΔE (in eV), and the non-stoichiometry δ in $Ce_{0.5}Zr_{0.5}O_{2-\delta}$.

$$\frac{[Ce^{3+}]}{[Ce^{3+}] + [Ce^{4+}]} = \frac{-\Delta E}{6.2} = 4\delta \tag{2.24}$$

An error smaller than 5% was found when the temperature was changed by about 1500 K from 1773K to room temperature in a flow of argon (see chapter 4).[240] Application of our method to determine the edge shift on the aligned reference spectra of $Ce_{0.5}Zr_{0.5}O_{2-\delta}$ (see chapter 5) gave a standard deviation of $\pm 5 \cdot 10^{-2}$ eV, which corresponds to ± 1% Ce^{3+} concentration. This value for the precision represents an optimistic estimation of the total error of the measurement. A very cautious estimation of the total error in the determination of the Ce^{3+} concentration is a standard deviation of ± 5 % Ce^{3+}.

EXAFS analysis at relevant solar reactor temperature

The analysis of EXAFS data measured at high temperatures is very challenging due to very strong thermal damping and the resulting short data range. At 1073 K absorption minima and maxima distinguishable from noise are found only up to a few hundred eV above the edge. The extraction of the fine structure is complicated by the small data range close to the absorption edge. The EXAFS signal is extremely sensitive to minute variations of the background curve as well as the k-range and the window function used in the Fourier-transform.

Experimental details - in situ XAS

In situ XAS experiments were carried out at beamline BM01B of the Swiss-Norwegian Beamlines (SNBL) at the ESRF. An unusually small gap between the first and the second monochromator crystal enables measurements from the Ti K to the Au K edges in one single Bragg rotation using a Si (111) crystal. The divergence of the beam is approximately twice as large as the Darwin width. Taking into account both the intrinsic contribution of the Si-111 monochromator crystal and the divergence,[238] the energy resolution ΔE of the instrument at 40 keV is better or equal to 6.0 eV.

Experimental details ceria-hafnia (Chapter 4)

The incident and transmitted intensities were monitored with ionization chambers filled with 1 bar krypton/argon (20/80%) and 1.2 bar krypton that were in front of and behind the in situ cell, respectively. A pellet of ceria in cellulose was placed between the second and third ionization chamber as a reference. The storage ring (6 GeV) was operated in 16 bunch filling mode at 90 mA intensity and 10 h life-time. Measurements were carried out in transmission mode at the cerium K edge (40.433 keV) with a step width of 1 eV and 100 ms step time. The monochromator was detuned to suppress higher-order harmonics. Spectra of the XANES region (40.2 to 41 keV) with a step width of 1 eV were recorded with a time resolution of 0.676 min^{-1}. Spectra of the EXAFS region (40.2 to 42 keV) were recorded at room temperature with a step width of 1 eV. A 10 mg pellet (diameter 5 mm) was introduced into the cell. Samples were exposed to reducing conditions (1 atm argon or 2% H_2 in helium) and oxidising conditions (1 atm CO_2) at a gas flow rate of 100 mL min^{-1}. The rate of heating was 50 K·min^{-1}, cooling to 1073 K - 100 K·min^{-1}; cooling from 1073 K to room temperature was achieved by switching off the furnace. Gases used were; Ar (BIP, Air Products, $O_2 < 10$ ppb water < 20 ppb CO

+ CO_2 < 100 ppb THC (as CH_4) < 100 ppb N_2 < 1 ppm), CO_2 4.5, 2% H_2 5.0 in He 5.0 (Messer France SAS). The noise level in the reference spectra did not allow for the correction of possible energy drifts by alignment of reference spectra.

Experimental details ceria-zirconia (Chapter 5)

The incident and transmitted intensities were monitored with ionization chambers filled with 1.0 bar krypton/argon (20/80%) and 1.2 bar krypton, respectively. As a reference, a pellet of ceria or cerium acetate in cellulose was placed between the second and third ionization chamber. The storage ring was operated in uniform filling mode at 200 mA intensity and 60 h lifetime. Measurements at the cerium K edge (40.433 keV) were carried out in transmission mode with a step width of 1 eV and 100 ms dwell time. The monochromator was not detuned. For energies of ca 40 keV and a Si-111 monochromator, the first through-coming harmonic lies at ca. 120 keV where the flux from the source as well as the response of the ion-chambers is negligible. Spectra of the XANES region were recorded (40.2 to 41.2 keV) with a step size of 1 eV. Zr K edge spectra in the XANES region were recorded from 17.5 to 18.8 keV with a step size of 1 eV and 50 ms dwell time. A zirconium foil served as the reference. The monochromator was detuned to 60% intensity to reject higher-order harmonics. A pellet (diameter ca. 5 mm) was mounted on an alumina sample holder and introduced into a high-temperature alumina flow cell with kapton windows. Samples were exposed to reducing conditions (1 atm argon) and oxidizing conditions (1 atm carbon dioxide and 0.5 atm carbon dioxide/argon) at a gas flow rate of 100 mL/min. The rate of heating was 50 K/min, the cooling rate was -100 K/min from 1773 K to 1073 K. Cooling from 1073 K to room temperature was achieved by switching off the furnace. The gases were: argon (Air Products, BIP, oxygen < 10 ppb, water < 20 ppb, carbon monoxide + carbon dioxide < 100 ppb and THC (as methane) < 100 ppb, nitrogen < 1 ppm), carbon dioxide (Air Products, UltraPure, oxygen <0.5 ppm, water < 2 ppm, carbon monoxide < 0.5 ppm, THC (as methane) < 0.1 ppm, nitrogen < 2 ppm). Data processing and analysis were performed using MATLAB and the ATHENA program, which is part of the Demeter software package.[241]

Experimental details ceria-hafnia (Chapter 6)

The storage ring was operated in 7/8 multibunch filling mode at a maximum ring current of 200 mA. Measurements were performed in transmission mode. 31 mg fresh ceria-hafnia powder were pressed at 1 ton to obtain a thin pellet with a diameter of 5 mm. X-ray intensities were monitored with ionization chambers filed with 1 bar krypton/argon

(20/80 vol%) and 1.2 bar krypton before and after the in situ cell, respectively. Between the second and third ionization chamber a ceria or hafnia/cellulose pellet was placed as a reference. At both the Ce K and Hf K edges, the Si-111 monochromator was tuned to maximum intensity because rejection of higher order harmonics is not necessary. Owing to their high energy (ca. 125 keV at the Ce K edge) and their low intensities in the spectrum of the source, a bending magnet with critical energy of 20 keV, their interaction with the ion chambers are negligible. Energy scans were carried out with a step size of 1 eV. Ce K edge XANES and EXAFS scans were carried out with 50 ms and 200 ms dwell time, respectively. Hf K edge EXAFS scans with 200 ms and 100 ms dwell time, respectively and 3-5 scans were merged (in $\mu(E)$) for EXAFS analysis. Argon 6.0 (BIP, Air Products) was used at a flow rate of 100 mL/min.
The absolute value of the Hf K edge energy (tabulated value: 65.351 keV) was not determined because Hf metal was not available as a standard. About 25% of the incoming intensity was absorbed at 65 keV in the ion chambers that were filled with Kr at 1.1 bar. Hf K edge spectra were normalized by fitting a linear background in the pre-edge range and a second order polynomial in the post-edge region -230 to -150 and 70 to 350 (XANES) or 1500 eV (EXAFS) relative to the maximum of the first derivative, respectively. HfO_2 (Alfa Aesar, 99.95%, see SI) was used as reference material.
Data processing and analysis was performed using MATLAB code and the Athena and Artemis software packages.[241] Fitting of Hf K edge EXAFS data was performed by exchanging Zr by Hf in the feff6 input file which was generated using the 'atoms' code of Demeter 0.9.21. Crystallographic data of $Ce_2Zr_2O_7$ determined by neutron diffraction by Raison et al. (ICSD collection code 168595).[221] Fitting was performed in R-space in the range 1.15 to 4.4 Å and a Hanning window function for the Fourier-transform. Gases used for in situ XRD and combined in situ XAS/XRD experiments: Argon 6.0 (BIP, Air Products), 5% H_2 5.0 in He 5.0 (Messer gases); CO_2 4.8, ($O_2 \leq 2$ vpm, CO ≤ 1 vpm, $H_2O \leq 3$ vpm, $CH_4 \leq 2$ vpm, $N_2 \leq 8$ vpm). The flow rates of Ar and H_2/He were 200 mL/min and the flow rate of CO_2 was 100 mL/min.

2.3 X-ray diffraction

Diffraction is based on elastic scattering and occurs at slits or structures with a characteristic size roughly comparable to the wavelength of a wave. The angles and intensities of reflections in an X-ray diffraction pattern provide information on the electron density of a material and thus the arrangement of atoms. X-ray diffraction is the most important

tool for the determination of crystal structures and provides insights into the arrangement of chemical bonds, the nature of thermal and structural disorder and various other structural information.

The scattering vector q is the vectorial difference between the wave vectors of the incident and elastically scattered wave. The magnitude of the scattering vector q of a wave relates to the scattering angle θ and the wavelength of the radiation λ. The wavevector k has a magnitude of $\frac{2\pi}{\lambda}$.

$$|q| = 2k \sin\theta = \frac{4\pi}{\lambda} \sin\theta \tag{2.25}$$

The Bragg and Laue conditions for diffraction

Bragg's law describes the condition for positive interference of X-rays of wavelength λ that are reflected at an angle of incidence θ from mirror-like parallel crystal lattice planes with spacing d. It can be inferred from simple geometry of the crystal lattice in real space.

$$n\lambda = 2dsin\theta \tag{2.26}$$

Introducing the reciprocal lattice, which is the Fourier-transform of the direct lattice allows a very powerful mathematical description of diffraction. Points on the reciprocal lattice are described by the Miller indices h, k, l and reciprocal lattice vectors a_1^*, a_2^* and a_3^*, which fulfill $a_i a_j^* = 2\pi\delta_{i,j}$ with $\delta_{i,j}$ the Kronecker delta. The Bragg condition is equivalent to the Laue condition, which states that diffraction from a crystal occurs only if the scattering vector q coincides with a reciprocal lattice vector g of the crystal.

$$k - k' = q = g = ha_1^* + ka_2^* + la_3^* \tag{2.27}$$

The incident and scattered wavevectors k and k' can be visualized as a sphere with radius $|k|$ spanned by k and k', with k ending at the origin of the reciprocal lattice. The so-called Ewald sphere indicates the distinct points in reciprocal space diffraction from a crystal is confined to at a certain angle of incidence. Only reciprocal lattice points that lie on the Ewald sphere fulfill the Laue criterion and thus constructive interference of the scattered intensities, which leads to the observation of a diffraction peak. Figure 2.6 shows the construction of the Ewald sphere. For the determination of the space group of single crystals, polychromatic radiation is used to maximize the number of reflections. In order to determine the crystal structure, the crystal needs to be rotated. A large Ewald sphere and polychromatic radiation gives access to more diffraction peaks.

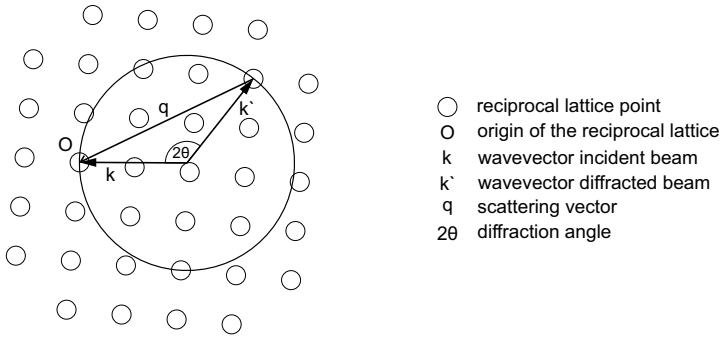

Figure 2.6 The incident wave-vector k and scattered wave-vector k' span the Ewald circle in two dimensions in reciprocal space. If q coincides with a reciprocal lattice vector, the Laue condition is fulfilled and a diffraction peak observed in the direction of k'.

Powder X-ray diffraction

In the case of randomly oriented crystallites, the angularily separated information that is accessible in single-crystal diffraction is lost and all reflections are projected to one dimension, which can lead to the overlap of reflections. Only if the orientation of a crystallite relative to the incident beam fulfills the diffraction condition, it contributes to the signal, which consists of concentric cones with an opening angle of 2θ for each symmetry-allowed lattice plane d_{hkl}. The powder diffraction pattern can then be obtained by azimuthal integration of the diffracted intensity of the concentric rings of the diffracted X-ray beams on a two-dimensional planar detector. The shape and intensity of the peaks in a diffraction pattern depends on the texture and crystallite size of the powder and also reflects the presence of strain. The Scherrer Equation relates the width D (FWHM) of a reflection hkl with the mean size of the crystalline domains τ. A typical value for the form factor K in Equation 2.28 is 0.9.

$$\tau = \frac{K\lambda}{2D\cos\theta_{hkl}} \tag{2.28}$$

X-ray diffraction at high temperature

Apart from zero-point fluctuations which arise from the uncertainty principle and are explained by quantum mechanics, structural defects or thermal motion cause deviations from the ideal positions of atoms arranged in a perfect, rigid crystal. These thermal vibrations affect the scattered intensity which is observed in two distinguished effects. Firstly, a decrease in the intensity of Bragg peaks with increasing wave-vector q, described by an exponential term, the Debye-Waller factor. Secondly, diffuse thermal

scattering (DTS), which appears as a scattering background with reflections of much larger width than those of Bragg peaks.

The position of an atoms can be described as the sum of their time-averaged mean position and displacement $R_n + u_n$, due to thermal vibrations with the average of the displacement $\langle u_n \rangle = 0$, with angular brackets denoting thermal averages. The structure factor F of a crystal that contains one type of atom on each lattice point is

$$F = \sum_n f(q)^{iqR_n} \tag{2.29}$$

Evaluation of the timely average of the scattered intensity, which is the product of the scattering amplitude with its complex conjugate gives

$$\begin{aligned} I =& \langle \sum_m f(q) e^{iq(R_m+u_m)} \sum_n f^*(q) e^{-iq(R_n+u_n)} \\ =& \sum_m \sum_n f(q) f^*(q) e^{iq(R_m-R_n)} \langle e^{iq(u_m-u_n)} \rangle \end{aligned} \tag{2.30}$$

$$\langle e^{ix} \rangle = e^{-\frac{1}{2}\langle x^2 \rangle} \tag{2.31}$$

The Baker-Hausdorff theorem (Equation 2.31) can be applied and translational symmetry with the identity of $\langle u_{q_m}^2 \rangle = \langle u_{q_n}^2 \rangle$, with both terms rewritten as $\langle u_q^2 \rangle$, allows to describe the scattered intensity with an an expression that is the sum of two terms:[232]

$$\begin{aligned} I =& \sum_m \sum_n f(q) e^{-M} e^{iqR_m} f^*(q) e^{-M} e^{-iqR_n} \\ &+ \sum_m \sum_n f(q) e^{-M} e^{iqR_m} f^*(q) e^{-M} e^{-iqR_n} \cdot \{ e^{q^2 \langle u_{q_m} u_{q_n} \rangle} - 1 \} \end{aligned} \tag{2.32}$$

The first component is the description of elastic scattering from a lattice but with the atomic form factor multiplied by an exponential term, the Debye-Waller factor e^{-M}.

$$f^{atom} = f(q) e^{-\frac{1}{2} q^2 \langle u_q^2 \rangle} \equiv f(q) e^{-M} \tag{2.33}$$

The intensity of elastic Bragg scattering is reduced, however the width of reflections is not affected by vibrations of the atoms. The second term describes thermal diffuse scattering (TDS), which leads to a background signal. TDS exhibits much broader features than the Bragg peaks because it depends on the correlation of the movements, $\langle u_{q_m} u_{q_n} \rangle$. The thermal diffuse scattering signal depends on the lattice dynamics and can provide information on structural features such as statical and lattice defects. Lattice dynamics and temperature-dependent material properties such as heat capacity have been described by the Einstein model and the Debye models. The scattered intensity of

a reflection can be described by multiplying the atomic form factor $f(q)$ with an exponential term. In the case of isotropic disorder, $\langle u^2 \rangle = \left\langle u_x^2 + u_y^2 + u_z^2 \right\rangle = 3 \left\langle u_q^2 \right\rangle$. Combining Equations 2.25 and 2.33 gives

$$M = \frac{8\pi^2}{3} \langle u^2 \rangle \frac{\sin^2 \theta}{\lambda^2} \tag{2.34}$$

Thus, in the isotropic case, the intensity of a Bragg peak decreases exponentially, with the exponent M proportional to the mean average square displacement (mean square vibrational amplitude), the square of the scattering angle and the square of the X-ray energy. Displacements from the equilibrium position of an atom can be interpreted as a Gaussian distribution in the case of isotropic displacements. In the more common anisotropic case, the positions of atoms are described as a vibrational ellipsoid with three principal axes of different magnitude.

Debye-Waller factors in EXAFS and XRD

In the expression of the Debye-Waller factor in the EXAFS Equation, $M = k^2\sigma^2(T)$, with $\sigma^2(T)$ is the mean square relative displacement (MSRD) of the absorber atom a and the scattering atom s. In the expression of the Debye-Waller factor of XRD, $\langle u_q^2 \rangle$ is the the mean spuare displacement (MSD), or mean square atomic vibrational amplitude. $\hat{R}$ is a unit vector.

$$\sigma^2 = \langle [(u_s - u_a) \cdot \hat{R}]^2 \rangle \tag{2.35}$$

$$\langle u_q^2 \rangle = \langle (u_i \cdot \hat{R})^2 \rangle \tag{2.36}$$

The MRSD can be decomposed into the MSD and the displacement correlation function (DCF)[242–245] for the contributions parallel to the bond of atoms a and b. $\langle (u_a \cdot \hat{R})^2 \rangle$ and $\langle (u_b \cdot \hat{R})^2 \rangle$ are the isotropic mean square displacements, which can be obtained from refining XRD data.

$$\sigma^2 = \langle (u_a \cdot \hat{R})^2 \rangle + \langle (u_b \cdot \hat{R})^2 \rangle - 2\langle (u_a \cdot \hat{R})(u_b \cdot \hat{R}) \rangle \tag{2.37}$$

Experimental aspects

At beamline BM01B[236,237] two pairs of Si(111) monochromator crystal pairs were available for diffraction experiments: a double-crystal pair for XAS, that could also be used for XRD in combined experiments, and a another crystal pair with a focusing second crystal with a fixed radius for diffraction experiments at 41.5 keV. The monochromator crystal pairs were mounted on slides inside the monochromator cage and were movable horizontally, which made it possible to switch between focusing and non-focusing

geometry. For combined experiments, the monochromator for XAS was also used for diffraction experiments. The switch from absorption to diffraction measurements and vice versa in that configuration took less than one minute.

Focused X-ray Beam

Focusing was achieved by means of a bent cylindrical-concave Si(111) crystal (waver) that served as the second crystal of the crystal pair for diffraction. The Bragg angle and radius R of the bent Si (111) crystal are related to the distance p from the source, its distance q from the sample (≈ distance to the 2D detector). The distance between the detector and sample is small compared to their distance to the focusing crystal.

$$\frac{1}{p} + \frac{1}{q} = \frac{2 \cdot sin\theta}{R} \tag{2.38}$$

The bent focusing Si(111) crystal had a length of 200 mm, and was attached to a concave cylindrical support made of pyrex by anodic bonding with a radius of 0.56 m. The photon energy of the focused beam at this radius is 41.5 keV. In this arrangement higher harmonics with n = 3 were not rejected and diffraction peaks of photons with an energy of 125 keV were detected.

Experimental details: in situ XRD and combined XAS/XRD measurements (Chapters 3 and 6)

During in situ XRD, and combined XAS/XRD measurements, the storage ring was operated in 16-bunch mode with a ring current of 90 mA and a half life of 10 h. XANES measurements at the Ce K edge were carried out with a time resolution of 1.2 min^{-1} in 725 steps with a step width of 1 eV and a dwell time of 50 ms. Intensity was monitored by means of three ion chambers, 30 cm long, and by applying 1 kV voltage. The ion chamber that monitored the incident intensity I_0 was filled with a mixture of 80/20 vol% argon/krypton, and the ion chambers monitoring I_1 and I_2 were filled with pure krypton. In the diffraction-only configuration, the beam was focused at a photon energy of 41.507 keV, which corresponds to a wavelength of 0.2987 Å. The wavelength was calibrated against a Si NIST standard using the beamline's high-resolution diffractometer. In the combined diffraction/absorption experiment, the beam size was adjusted by slits, resulting in a beam size of approximately 400 x 400 μm^2 (vertical x horizontal) for diffraction measurements and 800 x 400 μm^2 (vertical x horizontal) for absorption measurements. Diffraction measurements in the combined experiments were performed at a photon energy of 64.786 and 55.855 keV, which correspond to wavelengths of 0.1914 and 0.2220 Å,

respectively. Diffraction data were collected by a Dexela 2923 CMOS 2D pixel detector. In this configuration, a resolution of typically 0.005° 2θ is achievable. Sets of five dark and five exposed images with an exposure time of four seconds were recorded with a fast shutter. From each set, one background-corrected diffraction pattern was obtained at a time resolution of 0.876 min^{-1}. The 2D pixel detector was moved in and out of the beam by means of a step motor in less than a minute. The position of the sample relative to the pixel detector was determined by means of a LaB_6 660c NIST standard in a 0.3-mm quartz capillary mounted on top of the inner ceramic tube. To account for the exact position of the sample, 3 mm inside the tube, the whole device was moved towards the source for calibration. Data reduction by azimuthal integration was performed with PyFAI software[246] and background subtraction was carried out by MATLAB and the baseline estimation and denoising by the sparsity (BEADS) algorithm.[247]

2.4 (Laboratory) Powder X-ray diffraction

X-ray diffraction patterns recorded after calcination and sintering, respectively (chapters 5 6) were recorded on a Bruker D8 (Parallel Beam) using Cu-Kα radiation (2θ range of 10-110° step size 0.014° scan speed 1° min^{-1}). For X-ray diffraction measurements after TGA (chapter 6), the pellets were ground in a mortar and a powder-ethanol slurry was deposited on a sample holder. Coupled two-theta-theta scans were performed on a Bruker D8 instrument with a Cu source on a 280 mm measurement cycle, 2.5° axial Soller slits, a Ni Filter and a Lynx-eye detector. The step size was 0.0296° 2θ and dwell times were 96 (Hf10 and Hf20) and 384 ms (Hf50). The Kα_2 signal was stripped. The X-ray diffraction patterns presented in chapter 7 were recorded with a PANalytical X'Pert X-ray powder diffractometer The diffractometer was operated at 45 kV and 20 mA in continuous scanning mode with Cu K_α radiation (λ = 1.5405 Å) as the X-ray source. An integration time of 10 s and a step size of 0.05° were chosen. For sample preparation, the materials after reaction were finely ground in ethanol and the slurry was manually deposited on clean glass substrates.

2.5 Synthesis of ceria-based materials for solar thermochemical looping

The determination of changes in the intrinsic material properties requires well-defined materials. Typical concentrations of hetero-cations in ceria-based single-phase solid solution with a random distribution of the hetero-cation range up to 20 mol%. Only in exceptional cases, compositions with up to or more than 50% hetero-cations are of interest. In many cases it was reported that the synthesis method had an influence on the thermochemical looping performance of ceria-based materials. The synthesis method determines the morphology of materials, which can cause kinetic limitations and apparent differences in the oxygen storage properties[153] because equilibria are not reached. Thermochemical cycling conditions provide high mobility of cations in the bulk and thus, if thermodynamically favorable, solid solutions with evenly distributed hetero-cations will form and the segregation of secondary phases occurs after a certain number of cycles. In order to avoid distortions by heterogeneity of experiments based on a small number of cycles, it is convenient to prepare materials with a uniform distribution of hetero-cations. In this work, the materials investigated were prepared by the ceramic method, polymerized-complex synthesis, co-precipitation and wet impregnation.

Ceramic method

Metal oxide powders are mixed in the desired composition and form a solid solution in a solid state reaction. In order to complete the reaction and obtain phase-pure materials, the reaction mixture is exposed to high temperatures of typically 1873 K in air for several few hours. The ceramic method is important for the production porous monoliths on the kg scale, such as reticulated porous structures for cavity-receiver-type solar thermochemical looping reactors. Bonk et al. synthesized the material used in chapter 4: $Ce_{0.9}Hf_{0.1}O_{2-\delta}$ was synthesized using ceria (Sigma Aldrich, 99.9%, $< 5\mu m$) and HfO_2 (Alfa Aesar, 99.95%). De-agglomeration and mixing were carried out by ball milling on a roller mill (ZO, RM1) for 24 h in polypropylene bottles using YSZ balls 5 mm in diameter (Tosoh). After 24 h the slurry was separated from the YSZ balls and dried at 358 K for 12 h. Samples of 15 mg were pressed uni-axially at 5 kN in a 6 mm pressing tool. The pellets were fired in a furnace (Carbolite HTF 17/10) at 1873 K for 5 h in air on a ceria powder to avoid contamination.

Polymerized-complex (Pecchini-type) method

The polymerized-complex method is based on the synthesis of a solid, carbon-containing precursor polymer from a solution containing metal salts. The polymer acts as a complexing agent in the precursor material, which subsequently calcined to obtain metal-oxide particles. Typically, an esterification reaction is used to link complexing agents with many carboxylic acid groups. The random distribution of the metal ions in the solution can be maintained in the precursor material and the metal oxide. Bonk et al.[157] used the following procedure: $(NH_4)_2Ce(NO_3)_6$ (Alfa Aesar, 99.9%) and $ZrO(NO_3)_2$, (Alfa Aesar, 99.9%) or $HfCl_4$, (Alfa Aesar, 99.9%) were dissolved in deionized water. Anhydrous citric acid (CA, Sigma Aldrich, 99.5%) was added to 1,4-butanediol (BD) (Sigma Aldrich, 99%) in a 1:4 molar ratio (with [CA]:[M^{4+}] = 4:1) and stirred at 373 K until all citric acid was dissolved. The aqueous solution containing the dissolved metal salts was added to the CABD mixture and heated to 423 K to promote the esterification reactions. The resulting highly viscous polymer was dried at 353 K for 4 h and fired for 10 h at 973 K in a constant air flow to remove organic matter. Sintering of samples was performed in a Carbolite HTF 17/10 furnace at 1873 K for 5 h in air.

Co-precipitation

The solid solution is obtained by precipitation from an aqueous solution of metal salts. The pH is increased by adding a base such as $NH_4(OH)$ and the precipitate is subsequently filtered, dried and calcined. Cerium nitrate and cerium acetate are well suited because the anion can be removed fairly easily by calcination. Lin et al. used the synthesis:[248] 1 mol% rhodium-doped ceria and 10 mol% nickel-doped ceria ($x_{Rh} = 0.01$ and $x_{Ni} = 0.1$, balance cerium) were synthesized by a simple co-precipitation method as described earlier.[159] Cerium(III) nitrate hydrate and rhodium(III) nitrate hydrate and nickel(II)nitrage hydrate, respectively (Sigma Aldrich) were used as precursors. Appropriate amounts of the nitrate salts were dissolved in excess amount of de-ionized water. Aqueous ammonia solution (28 vol%) was added drop-wise to the precursor solution under vigorous stirring. After the pH was stabilized at 9, the precipitates were aged for 24 h under stirring, followed by settling for another 24 h. The precipitates were filtered, rinsed, and dried before they were crushed into fine powders and calcined at 773 K for 5 h.

Wet impregnation

Reduced Hf50 pellets were decorated with platinum by dipping them into hydrogen hexachloroplatinate ($H_2PtCl_6(6\,H_2O)$, 99.9%, (38-40% Pt), Acros).

2.6 Thermochemical activity tests (Chapter 7)

Thermochemical cycling experiments with rhodium-doped and nickel-doped ceria were carried out with the setup for in situ XAS (see section 3.2 and Figure 3.2). A pellet prepared from 150 mg material was placed in the reactor on an alumina sample holder. The materials were auto-reduced at 1673 K or 1773 K in a flow of 100 mL/min argon and re-oxidised at 773 K. The oxidation gas condition was varied by mixing argon (100 NmL/min) with carbon dioxide at 6.2 NmL/min and/or water at 0.6 g/h (12.4 NmL/min). The molar ratio of water to carbon dioxide was two. The concentrations of hydrogen (m/z = 2), oxygen (m/z = 32), carbon dioxide (m/z = 44), carbon monoxide (m/z = 28 and 12) and methane (m/z = 15) in the effluent gas were monitored by MS. For preliminary tests involving reduction with hydrogen, a similar setup with a Heraeus Thermicon P furnace and an Pfeiffer Vacuum D-35614 Asslar GSD 301 O1 was used. Ceria was chemically reduced at 873 K in a flow of 100 mL/min 10 mol% H_2/Ar. The re-oxidation was carried out in a gas mixture of argon (70 mL/min), carbon dioxide (10 mL/min) and water (1 g/h). The mixture of 500 mg of ceria powder and 1000 mg sea sand formed a packed-bed in a quartz tube.

2.7 Thermogravimetric analysis (chapter 6)

Thermogravimetric analysis (TGA) experiments were carried out using a Netzsch STA 449F3 thermogravimetric analyzer. Samples were placed in an alumina crucible supported by an alumina rod which houses a thermocouple. After oxidation at 973 K in air, and the gas flow in the analyzer was changed to argon 5.0 at 573 K. The heating and cooling rates were 30 K/min. A blank run was used to correct buoyancy effects. Before XRD measurements samples were ground in a mortar and stored for five months at ambient conditions.

Thermochemical cycles (Chapter 7)

Experiments were carried out using a TGA (thermogravimetric analysis) reactor (Netzsch TA409). Approximately 400 mg of fresh rhodium-ceria powder was placed inside an alumina crucible supported by an alumina rod, which houses a thermocouple and is atop the balance. Reduction was carried out at 1723 K in argon and oxidation at 773 K at a gas flow rate of 100 mL/min. The partial pressures of carbon dioxide and water were adjusted by changing the flow rate of carbon dioxide, the flow rate of argon passing through a bubbler (temperature 283, 291 or 295 K), and the flow rate of the balancing argon. Three cycles were measured for each fresh sample for each water/ carbon dioxide ratio.

2.8 X-ray fluorescence (Chapter 7)

X-ray fluorescence (XRF) data were obtained using an EDAX ORBIS micro X-ray fluorescence analyzer. The details can be found elsewhere.[160]

Chapter 3

In situ Flow Cells for XAS and Combined XAS/XRD Under Solar Thermochemical Looping Conditions

based on:
Rothensteiner, M., Sala, S., Bonk, A., Vogt, U., Emerich, H., and van Bokhoven, J. A. (2015). Phys. Chem. Chem. Phys., 17(40), 26988-26996. http://doi.org/10.1039/C5CP03179F

Rothensteiner, M., Jenni, J., Emerich, H., Bonk, A., Vogt, U. F., van Bokhoven, J. A. (2017). Rev. Sci. Instrum., 88(8), 83116. http://doi.org/10.1063/1.4994890

M.R. contributions: designed the setup and in situ-cells, assembled, tested and optimized the setup, wrote LabView code for setup automation and data logging; applied for beam time, planned and performed in situ XAS, XRD and XAS/XRD experiments, processed and analyzed the data, wrote the manuscripts.

3.1 Introduction

The temperatures required for solar-driven thermochemical looping present a complex engineering problem and a significant challenge for in situ structural characterization. First, the choice of material for the walls and windows of the reactor as well as their geometry are limited and a suitable, reliable system of heating and temperature measurement must be found for the proposed technique. Second, due to high reactivity at elevated temperature, samples cannot be diluted, for example to adjust transmission in an absorption experiment, and contact with other materials usually leads to contamination. Last but not least, thermal disorder of the oxygen storage material dramatically limits access to structural information because of thermal damping and broadening of scattered intensities and spectral features. Owing to their considerable depth of penetration, synchrotron X-ray and neutron-based techniques are the most promising for in situ characterization at high temperature in the reactive environment of both sub-steps of the solar thermochemical cycle. X-ray absorption spectroscopy (XAS) is a powerful technique for determining the electronic and geometric structure of functional materials under relevant operating conditions.[210,249] XES is very sensitive to the electronic structure and enables the determination of the ligand environment of specific elements.[250] The challenge faced in construction of a high temperature in situ cell capable of mimicking conditions in a solar thermochemical looping reactor, is to guarantee the access of photons of the required energies to a sample with an appropriate stable geometry in a well-known environment of uniform temperature and under a controlled gas flow.

Figure 3.1 shows the two-step thermochemical dissociation of water and/or carbon dioxide and the typical process conditions. It visualizes important aspects of the design of an in situ flow cell for XAS and XRD. The option of performing XAS in fluorescence mode or X-ray emission spectroscopy (XES) is illustrated.

There are large number of cells for in situ characterization by synchrotron X-ray technology.[251–262] Most cells are optimized with respect to specific requirements of the characterization technique, a limited photon energy range and specific reaction conditions. Some cells enable simultaneous measurements by means of two or more X-ray techniques or other methods such as infrared and Raman spectroscopy. Most cells do not function at temperatures up to 1773 K and devices that were designed for this extreme temperature are usually inoperable in presence of steam and reactive gases such as hydrogen and carbon monoxide.

Equipment for in situ XAS up to 1273 K is readily available and cell designs for cat-

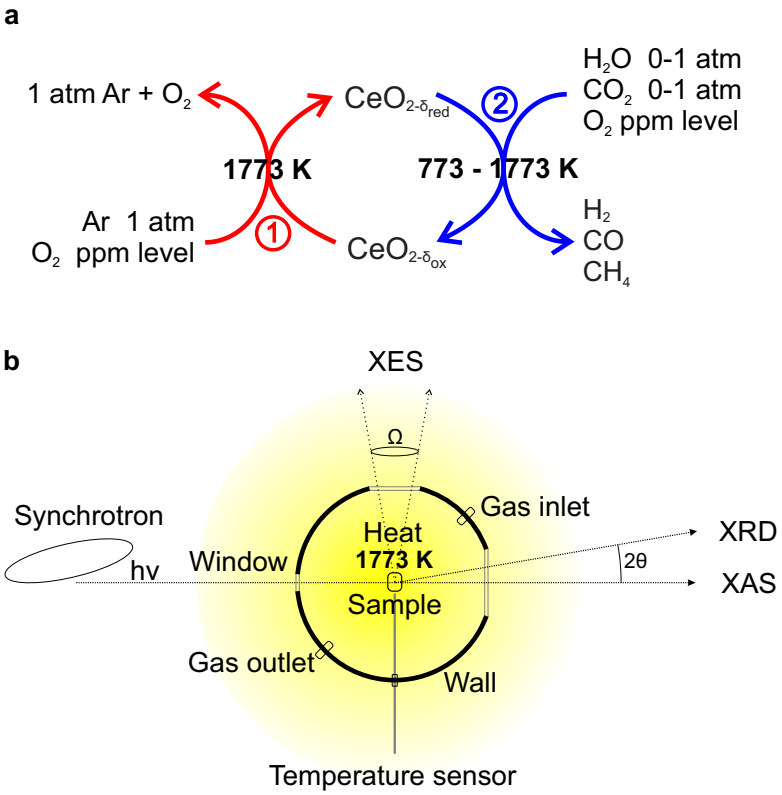

Figure 3.1 The two-step thermochemical cycle using ceria and typical process conditions during (1) the auto-reduction and (2) the oxidation sub-steps of solar thermochemical looping (a). Components and important parameters for the design of an in situ flow cell, that can be operated under these conditions (b). Requirements of the geometrical arrangement of the incident, emitted and diffracted X-ray beam and the sample depend on the technique and the required/available incident photon energy $h\nu$. Transmission experiments require an accurate sample geometry. Critical parameters are the transmission of windows and gases, the geometry of the sample, the solid angle Ω for XES as well as the accessible range of the Bragg-angle 2θ in XRD.

alytic systems are helpfully reviewed by Bare and Ressler.[257] Guilera et al.[258] described cells for transmittance and fluorescence where reactive gases are employed, Huwe et al.[254] and An et al.[261] described cells for temperatures up to 1273 K. Above this temperature, however, in situ XAS data are hardly available because mechanically stable and inert materials that are permeable to X-rays are very limited. This is also the case for advanced techniques based on X-ray emission detection with more demanding X-ray optics, such as high energy resolution fluorescence detection (HERFD),[263] high energy resolution off-resonant spectroscopy (HEROS),[264] or resonant inelastic X-ray scattering (RIXS).[265] Approaches to performing spectroscopic measurements at significantly higher temperatures have been reported. A small sample may be placed on a resistive

heating wire (e.g. Richet et al.,[266] Neuville et al.[267]), which is limited by the melting point of the wire material. Another approach overcomes this limitation by heating an aerodynamically levitated sample with a laser (Landron et al.,[268,269] Hennet et al.[270]).

Contact-free heating facilitates cell design with regard to the control and reproducibility of the sample temperature. Placing the sample in a container is required to achieve low oxygen concentrations. Thus, a reactor material through which X-rays can penetrate, or alternatively, a cell with an X-ray window that can be actively cooled or that withstands the high temperature must be developed. Element-specific characterization of materials under reaction conditions by X-ray spectroscopy is primarily restricted by the photon energy of the absorption edges of the chemical element, the emitted photon energy and the transmission of window materials of the in situ cell. In many oxygen storage materials, e.g. ferrites and perovskites for solar-driven thermochemical looping, the redox-active species are period-four transition-metal ions. The highest photon energy for probing these atoms is at the absorption K edge. This range is 5.0 keV (titanium) to 9.7 keV (zinc). Important absorption edges in perovskites of the La-Sr clan[209,271–273] are the La L_{III} edge at 5.5 keV, the La K edge at 38.9 keV, and the Sr K edge at 16.1 keV. In ceria-based materials, relevant absorption edges are the Ce L_{III} edge at 5.7 keV, the Ce K edge (40.4 keV), and absorption edges of hetero-cations such as the Zr K edge (18.0 keV), the Hf L_{III} edge (9.6 keV), and the Hf K edge (65.4 keV).

The requirements of an in situ flow cell with a controlled atmosphere (inert gas, water and/or carbon dioxide) that may be used up to 1773 K, strongly restrict the choice of materials and geometry. Moreover, it is preferable to measure pure samples as preparation of pellets with diluent (for adjusting the absorption edge jump and transmission) will probably result in contamination. XAS measurements in transmission mode thus require thin, homogeneous, and mechanically stable samples. Typically, at a photon energy below about 15 keV, the sample must be a few microns thin. Pellets that meet these requirements are not easy to prepare and are prone to breakage during the experiment. If a reasonable compromise between total absorption and the size of the edge jump cannot be found, then fluorescence detection can give access to elements at low photon energies or of low concentration. Thin reactor walls (a few hundreds of microns) of ceramic materials composed of low-Z elements such as B_4C, Si_3N_4, (hexagonal) BN, polycrystalline alumina (corundum), and sapphire Al_2O_3 can be used with a suitable heating system. Considering the low transmission of potential wall materials of such an in situ cell, and the small unit edge step absorption length of ceria of $\approx 5\ \mu m$ at the cerium L_{III} edge (5.723 keV), it is more promising to perform in situ XAS measurements

in transmission mode at the cerium K edge (40.443 eV) because there, the unit edge step absorption length of ceria is $\approx 80\ \mu m$. Uniform, self-supporting pellets of this thickness are fairly easy to prepare. Access to high-energy photons facilitates the design of in situ cells which enable operation under solar thermochemical looping conditions.

3.2 In situ XAS cell

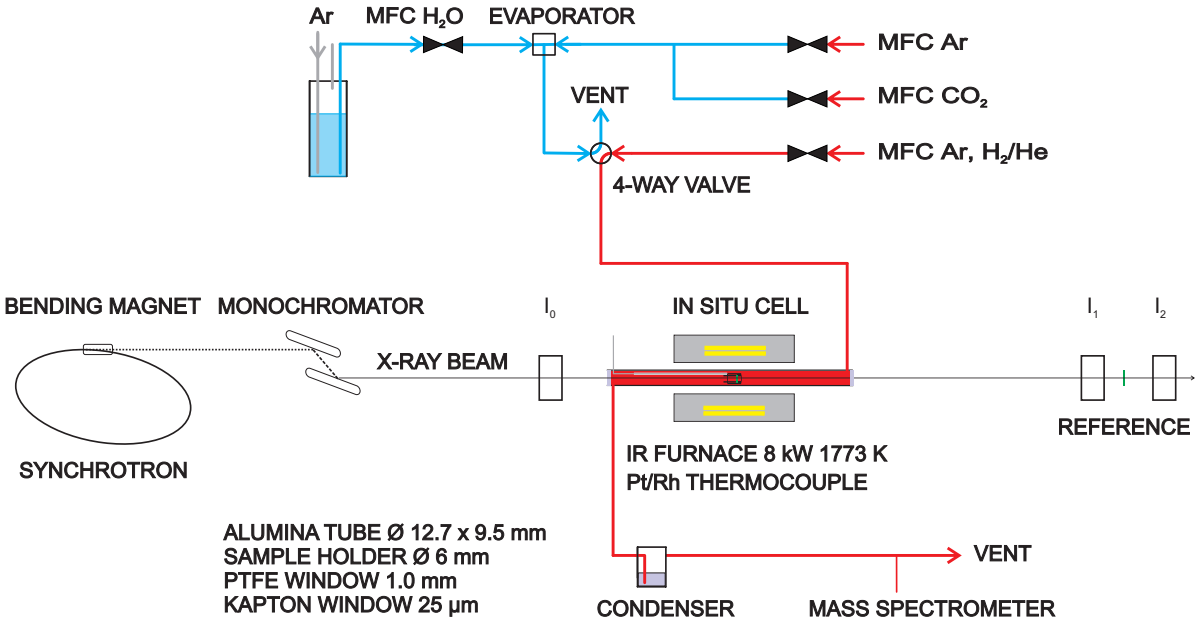

Figure 3.2 Setup for in situ XAS under realistic two-step solar thermochemical water and carbon dioxide splitting conditions. The same equipment (gas and vapor dosing system, high temperature reactor, condenser and mass spectrometer) was also used in the home laboratory at ETH Zurich for thermochemical looping experiments (see Chapter 7).

Figure 3.2 shows a schematic representation of the setup for XAS measurements in transmission mode. Figure 3.3 depicts the in situ cell with open furnace at the beamline. An alumina sample holder is shown in Figure 3.5. The main components of the setup were a unit for dosing gases and water vapor (mass flow controllers and a controlled-evaporation-mixing system, Bronkhorst), a four-way valve (Vici) with an electric actuator that enabled a fast switch between two gas streams, the in situ cell, a condenser immersed in an ice bath and a mass spectrometer (Pfeiffer GSD 320). Flow rates of the mass-flow controllers and the position of the four-way valve were controlled and logged on a computer by our own LabVIEW application. The composition of the products in the gas stream was monitored by means of a quadrupole mass spectrometer.

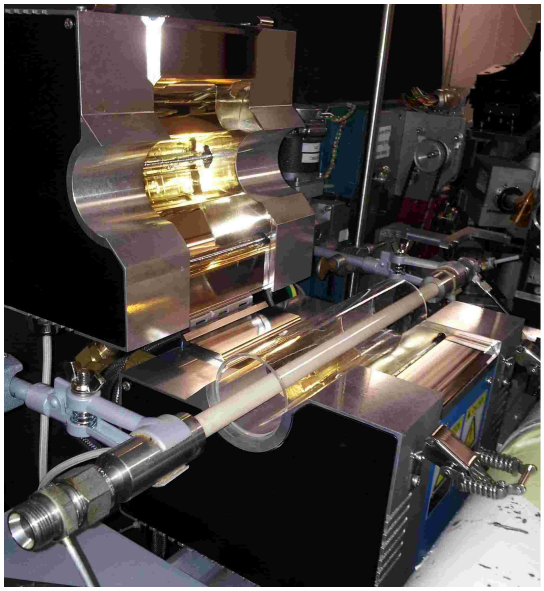

Figure 3.3 The in situ XAS cell with open furnace mounted at the beamline BM01B. The cell was also used for thermochemical activity tests in the laboratory (ETH Zurich).

The in situ cell consisted of an alumina tube (99.7 Alsint, Haldenwanger Ceramics, 9.5 mm x 12.7 mm x 400 mm). The ends of the tube were connected to steel adapters for 12 mm swagelok tubes. The inlet and the outlet were manufactured by modifying 12 mm swagelok linear connectors. In the cell, the temperature in the hot zone (100 mm) was measured at the position of the sample with an S-type (Pt/Rh) thermocouple covered by an alumina sheath. The conditions that could be reached in the cell are given in Table 3.1. Samples were introduced on an alumina sample holder consisting of two cylindrical parts (see Figure 3.5 c)). The inner diameter (3.5 mm) of the sample holder determined the maximum cross section of the X-ray beam on the sample. The X-ray beam was parallel to the axis of the in situ cell and passed through removable, thin windows (1 mm thin PTFE or 25 μm kapton) at the inlet and outlet. The cell withstood isothermal carbon dioxide and water splitting conditions as well as reducing atmospheres (5% hydrogen/helium) and allowed fast cycling between reducing and oxidizing conditions at high rates of heating and cooling and temperatures from room temperature up to at least 1773 K. Heating and cooling rates of several hundred $K \cdot min^{-1}$ could be reached due to the power of the IR furnace and the small thermal mass of the cell. Rates of heating and cooling were primarily limited by resistance to thermal shock. The total inner volume of the cell was 35 mL. Given the small amount of sample of typically 10 to 15 mg, the rather large dead volume represented a drawback, but might be compensated for using high gas flows. The in situ cell was placed between the

first (I_0) and second (I_1) ionization chambers. A reference material exposed to ambient conditions and located between the second and third ionization chamber was measured simultaneously.

Table 3.1: Characteristics of the setup for in situ XAS under realistic two-step solar thermochemical water- and carbon dioxide-splitting conditions.

Parameter	value
Temperature range	room temperature to at least 1773 K
Inner diameter (cell)	9.5 mm
Volume	35 mL
Cross sectional diameter of beam on sample	< 3.4 mm

3.3 In situ cell for XRD and combined XAS/XRD

Element-specific information about the changes in the local structure, such as the electronic structure and oxygen coordination of the elements involved in the redox reactions is obtained by means of XAS using the cell described above (chapters 4,5 and 6).[240,274] Here, we present the reaction cell suitable for XAS and XRD measurements under relevant solar-reactor conditions which combines both techniques in a single experiment under identical conditions. The initial design of the cell was based on our in situ cell for XAS in transmission mode.

Cell description

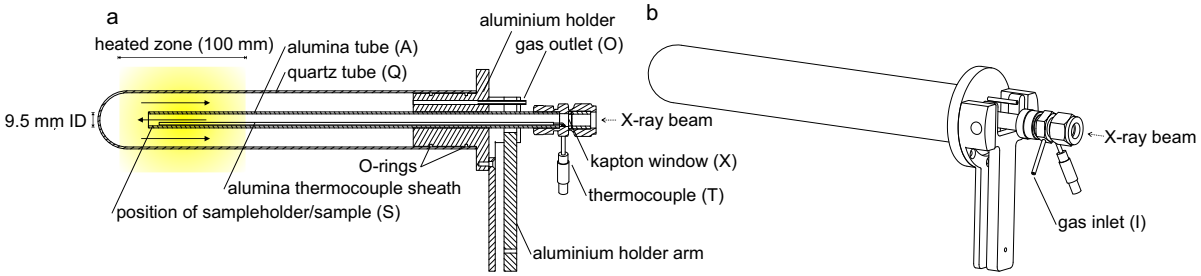

Figure 3.4 Sectional (a) and three-dimensional (b) views of the in situ XAS/XRD cell with holder arms. The length of the heated zone was 100 mm. Arrows indicate the direction of the gas flow. See also Figure 3.5.

Figure 3.4 presents a crosssection and three-dimensional view of the cell. Figure 3.5 shows pictures of the apparatus mounted at the beamline and a close-up of the alumina

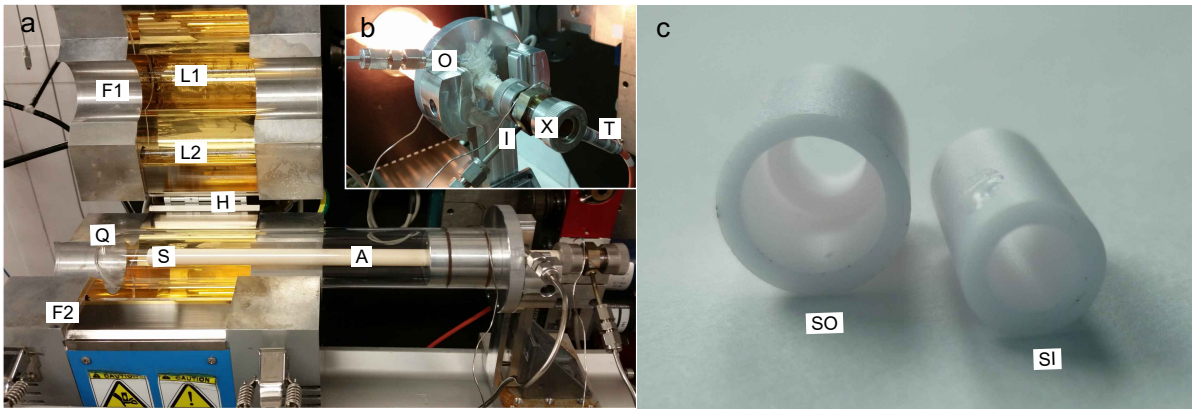

Figure 3.5 The high-temperature in situ XAS/XRD cell inside the opened focusing infrared furnace at the Swiss-Norwegian Beamline BM01B. a) Open furnace consisting of two parts (F1,F2) that are connected by a hinge (H). The lamps (L1, L2) and the gold-coated mirrors are in the upper part of the picture. The removable, quartz tube with a semi-spherical closed end (Q) and the inner alumina tube (A) bearing the sample holder (S) and a thermocouple. b) The closed furnace in operation: aluminium holder with the gas outlet (O) and the X-ray-transparent kapton window (X), gas inlet (I) and the thermocouple feedthrough (T) at the cold end of the alumina tube. c) Alumina sample holder, outer part (SO) and inner part(SI).

sample holder. The cell consisted of two coaxial tubes made of quartz and alumina, respectively, mounted onto a cylindrical aluminium holder hinged to a rotatable arm. The hemispherical shape of the closed end of the outer quartz tube (46 x 43 x 300 mm) served as a diffraction dome. The samples were mounted on an alumina sample holder at the open end of the inner alumina tube (12.7 x 9.5 x 326 mm, 99.7 Alsint, Haldenwanger Ceramics). The removable quartz tube was sealed by two viton O-rings. The alumina tube was glued to the aluminium holder with a silicon sealant (Dow Corning 736). Samples were mounted on an alumina sample holder that was placed in the hot zone at the end of the alumina tube (length 100 mm, diameter 10 mm) of an infrared focusing furnace with four lamps, gold-coated mirrors, 8 kW rated power and the maximum temperature 1973 K (VHT E-44, Ulvac-Riko). The casing of the furnace was water-cooled, and the lamps were cooled by pressurized air, which also cooled the quartz tube. The diameter of the furnace casing was 52 mm. The temperature was measured in the immediate vicinity of the sample by means of a Pt/Rh thermocouple (type S, diameter 0.5 or 1 mm) inside an alumina sheath, which also fixed the position of the sample holder. The cold end of the alumina tube was sealed with a modified linear 1/2 inch Swagelok Ultra-Torr fitting with an X-ray window (25 μm kapton), a thermocouple feedthrough, and an 1/8" gas inlet. Gases were introduced into the alumina tube through this gas

inlet and flowed in reverse direction between the two tubes to the gas outlet in the aluminium holder. The total gas volume in the cell was 327 mL. The X-ray beam was oriented on axis and entered the cell through the kapton window at the cold end of the alumina tube. Sample holders were made of pieces of alumina tubes (99.7 Alsint, Haldenwanger Ceramics). A short piece of the thin tube (5.5 x 3.5 x 3 mm) was glued flush with the outer tube (8.0 x 6.0 x 10 mm) using alumina-filled high-temperature adhesive (Aremco Ceramabond 503). The sample, a pellet of typically 5 mm diameter and less than 200 μm thick was introduced and the second alumina tube kept the pellet in vertical position. Pellets of 5 mm in diameter were made with a pellet press (1 ton) (msschentific Chromatographie-Handel GmbH) and consisted of 30 mg $Ce_{0.5}Hf_{0.5}O_{2-\delta}$ (Hf50) powder and 17 mg ceria prepared by Pechini-type synthesis and calcination at 973 K.[157,164]

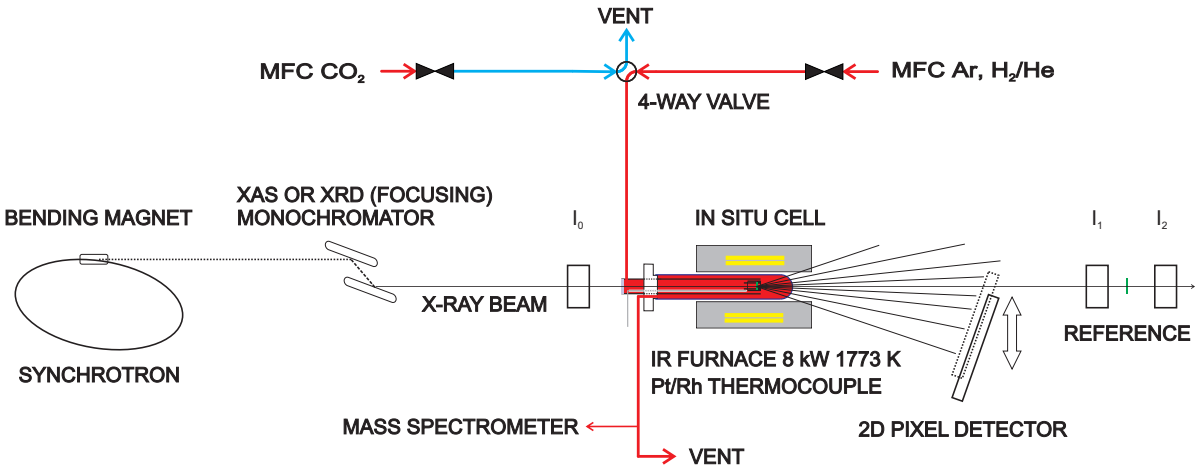

Figure 3.6 Scheme of the equipment used for testing the in situ cell for XRD using a focused beam at 41.5 keV and for performing combined XAS/XRD experiments in transmission mode under realistic solar thermochemical carbon dioxide-splitting conditions up to 1773 K.

Figure 3.6 is a scheme of the setup for in situ XAS, XRD, and combined XAS/XRD experiments. At the beamline, the in situ cell and the IR furnace were mounted to an aluminum profile on an xyz sample stage. The inner tube of the cell was aligned and was placed in the center of the hot zone of the furnace. Subsequently the apparatus was aligned to a visible laser beam, which was, in turn, co-axially aligned with the X-ray beam. The transmitted and scattered photons passed through the wall of the quartz tube and their intensity was detected by means of ion chambers and a 2D pixel detector, respectively. Above 40 keV, only a small fraction of the transmitted or scattered intensity, less than 10%, was absorbed by the 1.5-mm thin wall of the quartz tube. The

maximal detectable scattering angle was limited by the diameter of the furnace opening (52 mm).

Combined in situ XAS/XRD

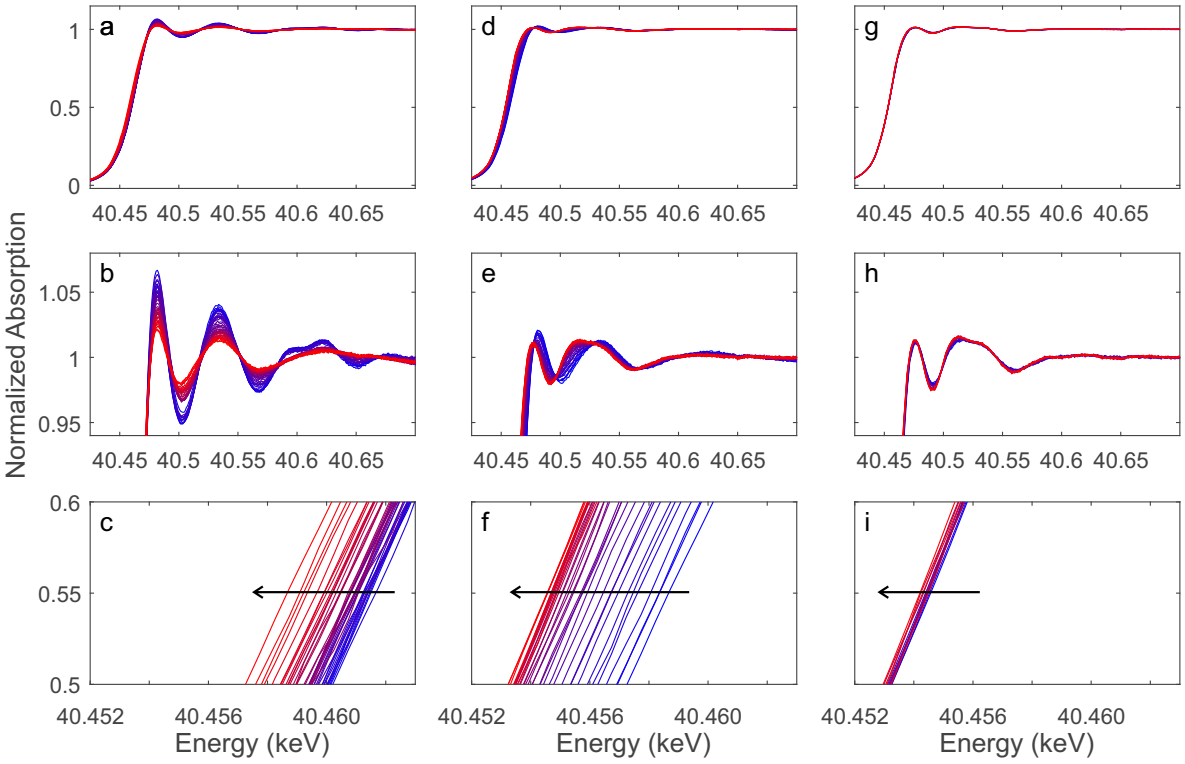

Figure 3.7 Ce K edge XAS spectra of $Ce_{0.5}Hf_{0.5}O_{2-\delta}$ during thermal auto-reduction by heating in a flow of argon from room temperature to 1773 K (a-c), subsequent exposure to a constant temperature of 1773 K (d-f) and during cooling from 1773 K to 1073 K (g-i). The first spectrum in each series is in blue and the last spectrum in red. Arrows indicate the direction of the shift in the edge energy.

Figure 3.7 shows Ce K edge XAS spectra, recorded during thermal auto-reduction of $Ce_{0.5}Hf_{0.5}O_{2-\delta}$ (Hf50) by heating from room temperature to 1773 K at a rate of 50 K/min in a flow of 200 mL/min argon, subsequent exposure to a constant temperature of 1773 K for 30 min and cooling to 1073 K. The Ce K edge XANES changed significantly during heating from room temperature to 1773 K, indicating changes in the electronic and geometric structures. The amplitude of the absorption fine structure decreased with increasing temperature. The intensity of the white line dropped sharply during heating and concomitant release of oxygen. An additional absorption maximum appeared at

an energy higher than that of the second absorption maximum. The third and fourth absorption maxima of the pristine Hf50 disappeared after auto-reduction at 1773 K and cooling to 1073 K. The intensity of the white line remained constant during cooling from 1773 K to 1073 K. Very strong thermal damping affected the EXAFS, which was essentially a flat line at the highest temperature. The EXAFS consisted of only few very weak features at 1073 K. The energy of the absorption edge decreased clearly during auto-reduction during heating and at 1773 K but only exhibited a small shift during cooling, from 1773 to 1073 K. During heating from room temperature to 1773 K, at about 573 K, a discontinuous change in the intensity of the first absorption minimum and the third and fourth absorption maxima occurred. All the other changes in the spectra were gradual.

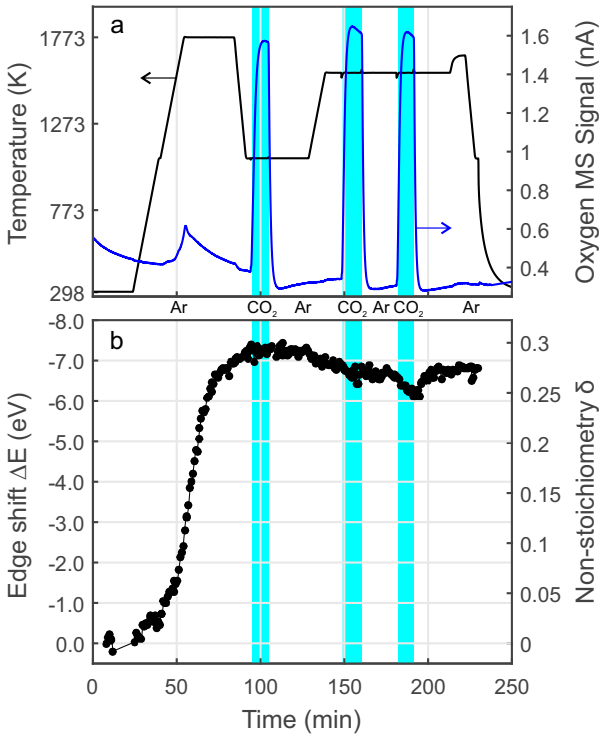

Figure 3.8 Thermal auto-reduction of $Ce_{0.5}Hf_{0.5}O_{2-\delta}$ in a flow of 200 mL/min argon and exposure to a flow of 100 ml/min carbon dioxide. a) Furnace profile and MS signal of oxygen (m/z = 32) b) shift in the Ce K edge energy determined by interpolation at a constant normalized absorption of 0.56.

The temperature profile in Figure 3.8 a) shows that the temperature around sample was very similar to the temperature throughout the experiment. The PID controller parameters were the same as in our in situ XAS cell,[240] and only a slightly higher furnace power was required for the temperature to reach 1773 K. The release of oxygen,

as observed in the MS, started at about 1073 K and peaked after reaching 1773 K. At first, there was a rapid and then a slower decrease in the oxygen signal. Upon cooling to 1073 K after auto-reduction at 1773 K, the oxygen signal decreased only slightly to its baseline level, indicating that, at this point, oxygen release from the sample was almost complete. During subsequent heating from 1073 K to 1570 K there was no detectable oxygen release. In the last part of the experiment, only a very small amount of oxygen was released from the material during heating in a flow of argon. Figure 3.8 b) presents the changes in the Ce K edge energy that were determined from the time-resolved XAS spectra. The shift in the edge energy is proportional to the concentration of Ce^{3+} in the material and the non-stoichiometry parameter δ in $Ce_{0.5}Hf_{0.5}O_{2-\delta}$.[240] The trend in the edge shift was in good agreement with the MS oxygen signal. However, during heating from room temperature δ increased already below 1073 K, before an increase in the MS oxygen signal was detected. At 1773 K, the rate of the change in δ peaked at $\delta \approx 0.12$, which is half that of the theoretically expected total change. The shift in the edge energy leveled out, but increased slightly to a non-stoichiometry δ of 0.29 during cooling to 1073 K. Exposure to a flow of 100 mL/min carbon dioxide did not change δ. Subsequently, isothermal switches between a flow of 200 ml/min argon and 100 ml/min carbon dioxide were performed at 1570 K. The value of δ gradually decreased when the temperature was increased to 1570 K. During the first exposure to carbon dioxide and subsequent exposure to argon, δ remained virtually the same. In the second switch to carbon dioxide, δ decreased slightly, by about 0.025, and, in line with the detection of oxygen release by MS, it increased by the same value when the gas feed was switched back to argon. The change in the oxidation state of cerium was followed quantitatively.

In the course of the auto-reduction at elevated temperature, the green pellet, consisting of compacted powder, was transformed into a dense ceramic body and significant changes in its density, geometry, and composition affected its X-ray transmission and scattering. The changes in the pellet can be traced by plotting the initial and transmitted intensity at a constant photon energy below the absorption edge. Figure 3.9 gives the incident intensity I_0 and the transmitted intensity I_1 during the thermal auto-reduction experiment described above (see Figures 3.7 and 3.8). Both intensities reflect the slow, exponential decrease in the ring current. In addition, a slow drift in the relative position of the monochromator crystals may have also contributed to changes in the photon flux. During the experiment, the intensity of the transmitted beam was not parallel to that of the incident beam but first increased slightly and then dropped dramatically until 1773 K was reached. Subsequently, the trend in the transmitted intensity was similar

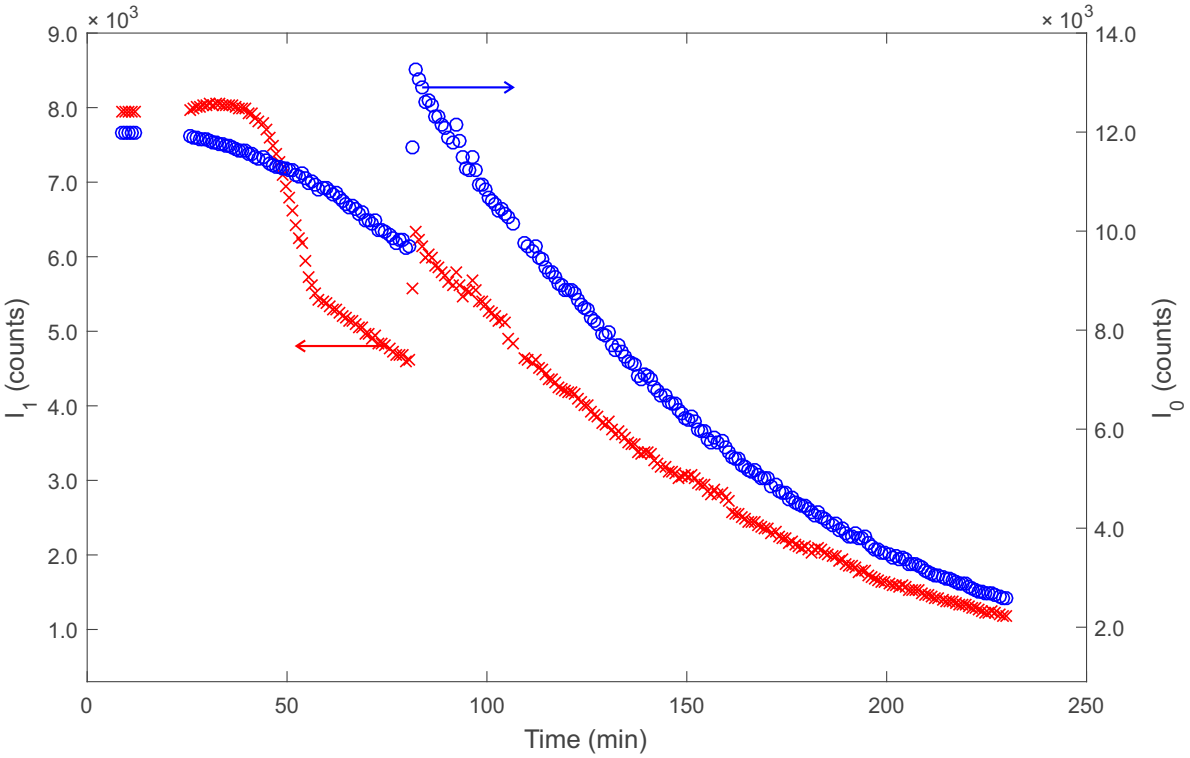

Figure 3.9 Trends in the incident intensity I_0 (blue) and transmitted intensity I_1 (red) at 350 eV below the energy of the Ce K edge of the first spectrum during thermal auto-reduction (Figures 3.7 and 3.8). In contrast to the incident intensity I_0, the transmitted intensity I_1 remained constant at first and then gradually decreased during thermal auto-reduction, indicating the sintering process leading to densification and an increase in the thickness of the pellet. The jump in intensity at 80 minutes resulted from the refilling of the storage ring.

to that of the incident intensity. Refilling the storage ring had only a minute effect on the spectra and did not disturb the quantification of the shift in the energy of the edge position.

Figure 3.10 shows XRD patterns recorded at a photon energy of 64.786 keV at room temperature before and after the above-mentioned thermal auto-reduction. Because the furnace opening limited the 2θ range, above approximately 15° 2θ, the scattered intensity decreased due to absorption in the furnace casing. The intensity of the background was significantly lower after the thermal treatment. The intensity of the broad background peak at 2.4° 2θ was assigned to scattering in the wall of the quartz tube. Sintering and solidification of the pellet reduced the transmitted intensity and the scattering contribution of the quartz tube, which contributes to the background in the diffraction pattern. Because the sample was not placed in the center of the semi-sphere of the quartz

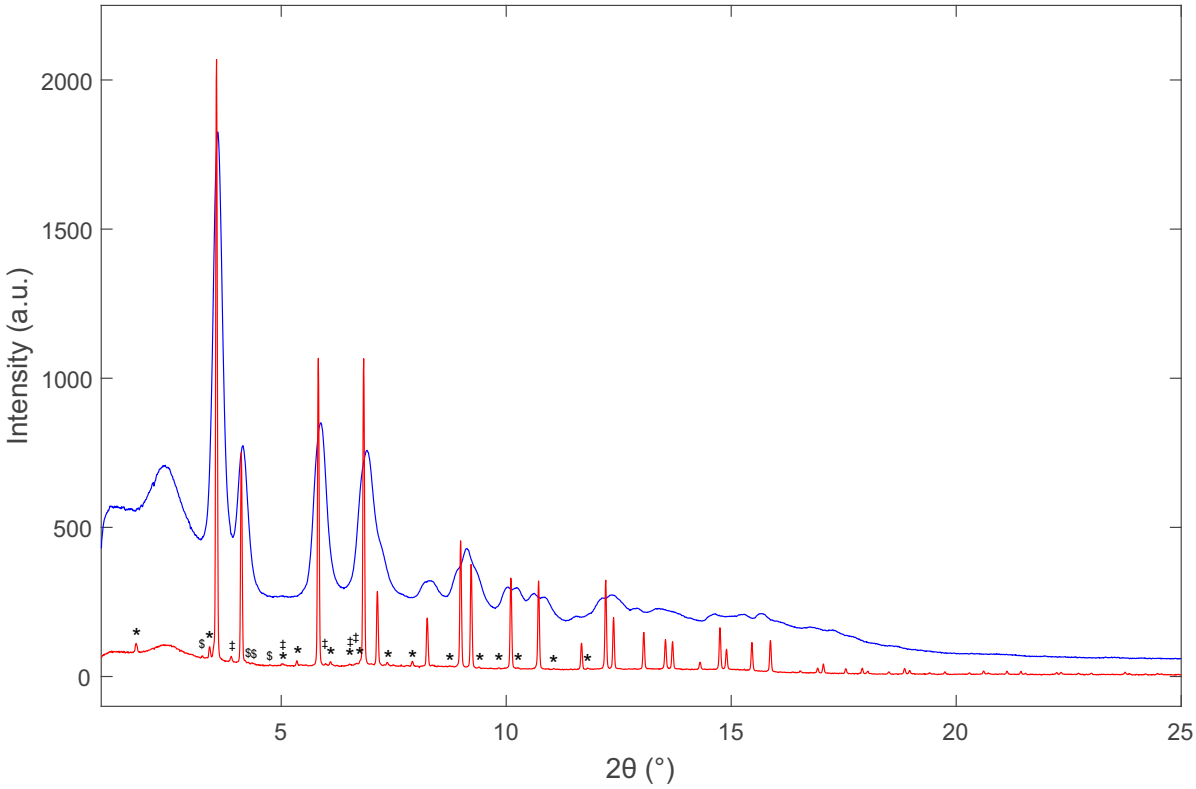

Figure 3.10 XRD patterns of Hf50 recorded at room temperature at 64.786 keV before (blue) and after (red) the thermal auto-reduction and exposure to carbon dioxide (see Figures 3.7 and 3.8). Asterisks (*) indicate weak reflections indicative of the cation-ordered pyrochlore structure, diesis (‡) reflections of monoclinic hafnia, and the dollar sign ($) unknown reflections and reflections that could not be definitely assigned.

tube, the intensity and broadening of individual reflections depended on the scattering angle. The detection of reflections with relative intensities below 5 % indicated the high sensitivity that was achieved at a time resolution of 0.876 min^{-1}. Many of the very weak peaks were be tentatively assigned to a cation-ordered structure equivalent to the ceria-zirconia pyrochlore.[176,221] In addition to $Ce_{0.5}Hf_{0.5}O_{1.75}$, there was a small amount of monoclinic hafnia.

Relevant solar reactor temperatures of 1773 K were easily reached in a flow of argon or carbon dioxide. The rather large gas volume between the hot alumina tube and the quartz tube limited the maximum attainable temperature due to conductive and convective heat transfer. Because the thermal conductivity of helium[275] is significantly higher than that of argon[276] and carbon dioxide,[166] the maximum attainable temperature was about 1650 ± 50 K when the cell was flushed with 5% hydrogen in helium at 200 mL/min.

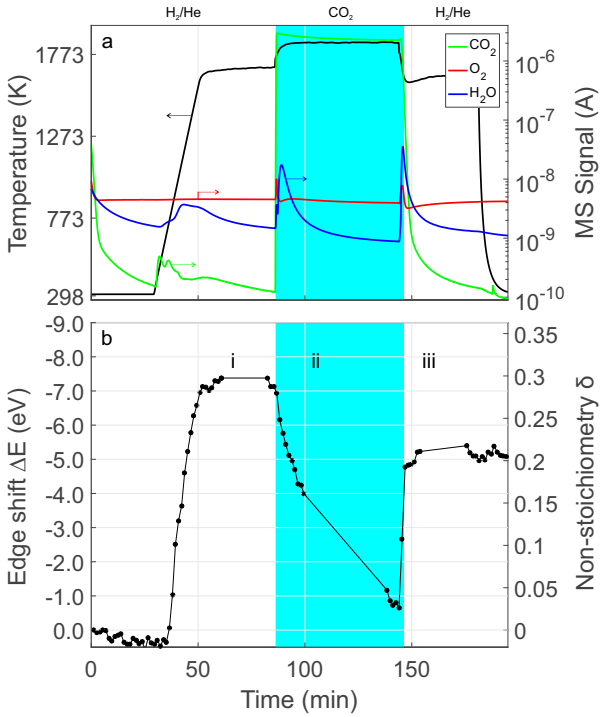

Figure 3.11 Temperature-programmed reduction of Hf50 in a flow of hydrogen/helium and subsequent switch to a flow of carbon dioxide. a) Temperature profile and MS signals of carbon dioxide (m/z = 44), oxygen (m/z = 32), and water (m/z = 18). b) Non-stoichiometry δ in $Ce_{0.5}Hf_{0.5}O_{2-\delta}$ determined in situ by quantification of the energy shift in the energy of the absorption edge of time-resolved Ce K edge spectra. The indices i) to iii) indicate the collection of XRD patterns (see Figure 3.12 a-c)).

Figure 3.11 shows the experimental conditions, including the furnace temperature and MS signals and the shift in the energy of the Ce K edge determined in a combined XAS/XRD experiment with a flow of hydrogen/helium and carbon dioxide. A pellet of 30 mg pristine Hf50 was mounted in the in situ cell, the temperature was increased to about 1650 K at 50 K/min in a flow of hydrogen/helium. After 30 min the gas feed was switched to 200 mL/min carbon dioxide for 60 min, which led to an increase in temperature to about 1800 K. Subsequently the gas feed was switched back to hydrogen/helium and the temperature decreased and leveled out at about 1610 K at full power in the furnace. The MS signals clearly indicated the formation of water from Hf50 when the temperature was increased from room temperature, indicating the removal of oxygen from the sample. Switching between hydrogen/helium and carbon dioxide also led to the formation of water from carbon dioxide and hydrogen. A small peak in the dioxygen signal occurred during the switch. Following the acquisition of Ce K edge X-ray absorption spectra during the switch, X-ray diffraction patterns were recorded at 55.855 keV.

The indices i) to iii) in Figure 3.11 indicate the acquisition of series of time-resolved X-ray diffraction patterns. The release of water during heating in hydrogen/helium was in line with an increase in δ, determined from the time-resolved Ce K edge XANES spectra. XAS indicated that oxygen release from the sample was completed by 1650 K. The maximum in the energy shift of the Ce K edge absorption edge was 7.2 eV, suggesting full conversion of Ce^{4+} to Ce^{3+}. The quality of the reference spectra did not enable correction of energy drifts. When the beamline settings were switched from XRD back to XAS in i), δ dropped by about 0.1. This shift, which is probably related to temperature changes in the monochromator crystals, was corrected for by assuming that structural changes did not occur during XRD measurements in a flow of hydrogen/helium. During XRD acquisition in region ii), structural changes in the XRD were detected (see Figure 3.12 b)). Thus, the absolute values of the non-stoichiometry δ, determined by XAS after ii) were unreliable. The relative change in δ indicated a concentration of Ce^{3+} slightly below its theoretical maximum of 0.25. After XRD measurements at point iii), there was no jump in the energy shift at the Ce K edge.

Figure 3.12 presents details of the time-resolved XRD patterns that were recorded in the combined XAS/XRD experiment (Figure 3.11). At high temperature, the (111),(311) and (333)(511) reflections of the pyrochlore structure were present in a flow of hydrogen/helium. In line with the above-mentioned results, it was not possible to clearly assign peaks close to the expected 2θ values of the (331) and (422) reflections of the potentially isostructural ceria-zirconia compound. Upon exposure to carbon dioxide, the normalized intensity of the (111) and (311) reflections and the peak assigned to the (333)(511) reflections decreased. A shoulder of the (440) reflection of the pyrochlore emerged. Exposure to carbon dioxide at 1800 K for one hour led to an increase in the monoclinic phase. The reflections indicating cation ordering persisted, but their normalized intensities decreased significantly.

After switching back to hydrogen/helium, the normalized intensities of the reflections indicating cation ordering were slightly lower. During data acquisition (point iii) after the feed gas was switched to hydrogen/helium, the diffraction patterns were the same, indicating fast structural changes during the switch. After exposure to hydrogen/helium, the intensity of the peaks assigned to the cation-ordered pyrochlore structure did not return to the initial intensity before exposure to carbon dioxide.

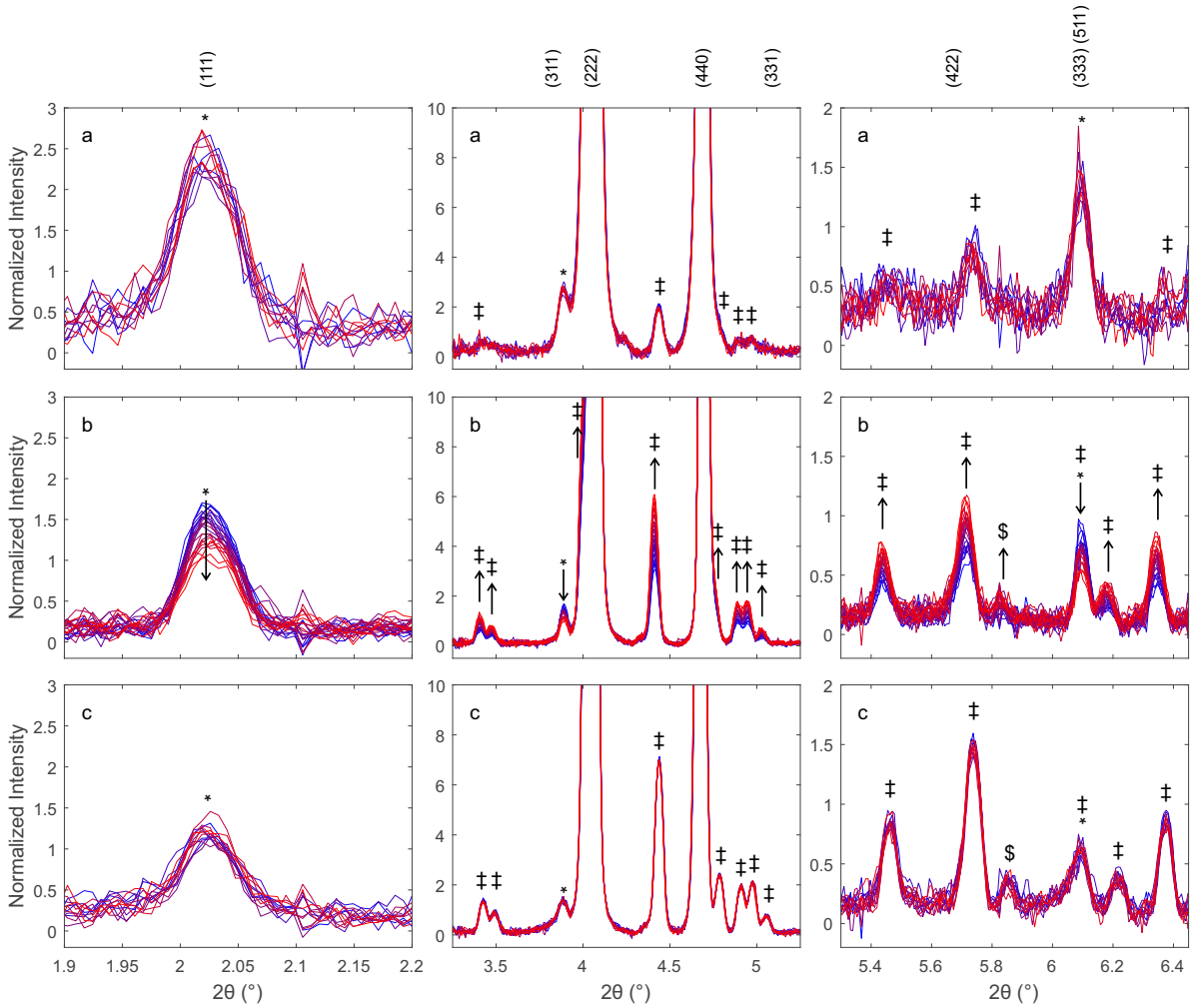

Figure 3.12 Diffraction patterns of chemically reduced Hf50 highlighting reflections related to cation ordering during the combined XAS/XRD experiment. Diffraction patterns were recorded at a photon energy of 55.855 keV at points i)-iii) (Figure 3.11). a) at point i) in a flow of hydrogen/helium, b) at point ii) after switching to a flow of carbon dioxide, and c) at point iii) after switching back to a flow of hydrogen/helium. Asterisks (*) indicate weak reflections indicative of the cation-ordered pyrochlore structure and diesis (‡) reflections of monoclinic hafnia. Arrows indicate direction of changes in the normalized intensity of the reflections and (hkl) indices the positions of reflections of the pyrochlore structure.

In situ XRD with a focused beam

Figure 3.13 presents time-resolved X-ray diffraction patterns, recorded with a focused beam at 41.5 keV during thermal treatment of ceria by heating from room temperature to 1773 K in a flow of argon. The time-resolved diffraction patterns reflected structural changes in the material and effects due to thermal disorder. In the diffraction pattern

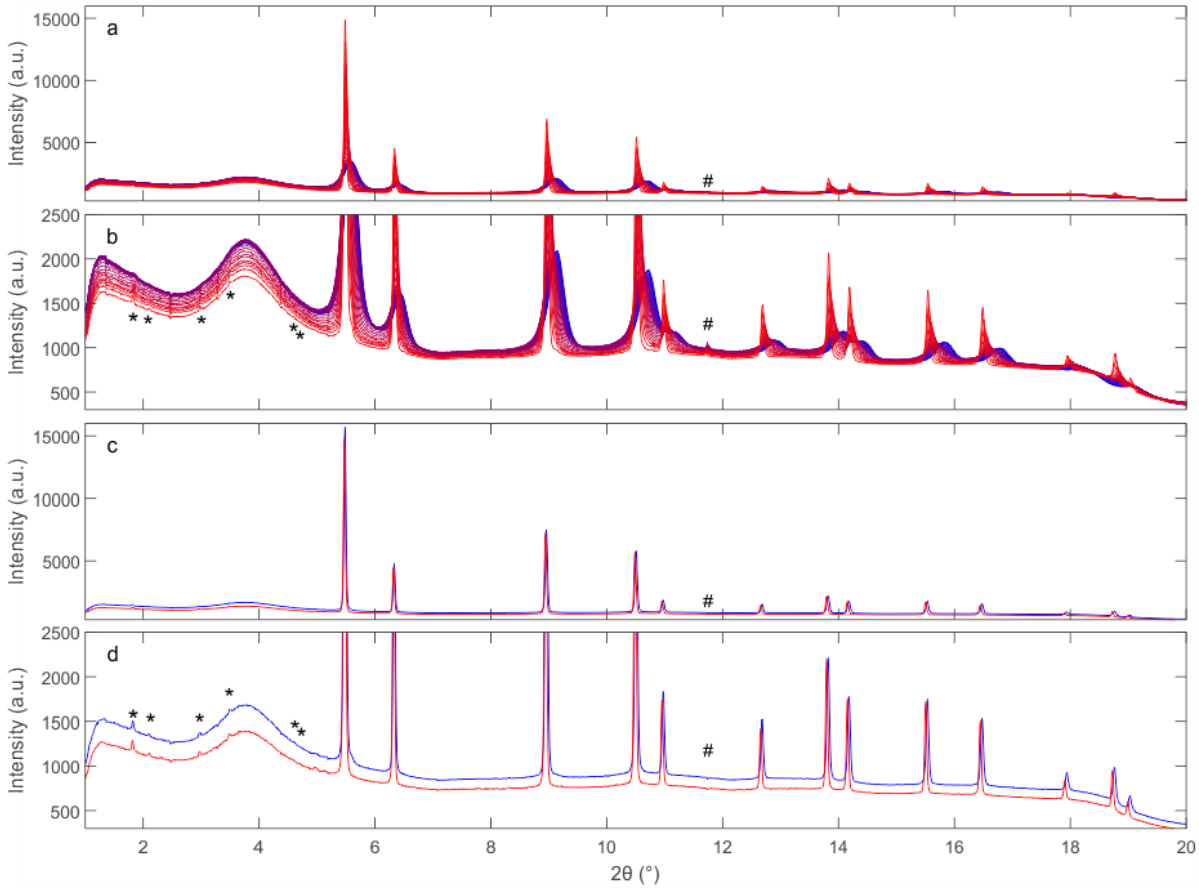

Figure 3.13 XRD patterns of ceria recorded with a focused beam at 41.507 keV during heating in a flow of argon from room temperature to 1773 K (a,b) at 50 K/min right after reaching 1773 K and after 25 minutes at 1773 K (c,d). The first patterns of the time series are in blue and the last in red. Octothorps (#) indicate an artifact originating from differences in the temperature during acquisition of the dark and exposed detector images. Asterisks (*) indicate reflections originating from higher harmonics with a photon energy of 124.5 keV.

of the pristine compressed powder, the reflections were very broad due to the small size of the crystallite. An increase in temperature caused sintering and to an increase in the crystallinity and the crystallite size of the material, leading to narrower diffraction peaks with a higher intensity. On the other hand, thermal disorder brought about lower scattered intensity and thermal expansion of the crystal lattice caused a substantial shift in the diffraction peaks to lower scattering angles. Ceria forms solid solutions of the fluorite-type structure and tetragonal and monoclinic phases with zirconia and hafnia.[157,164,171,192] There were no observable reflections indicating secondary phases. In contrast to the diffraction patterns recorded with an unfocused beam, the diffraction

patterns recorded with a focused beam (Figure 3.13) contained very weak reflections due to the presence of higher harmonics with the triple photon energy (124.5 keV) of the fundamental. The intensity of these peaks increased parallel to the diffraction peaks of the fundamental photon energy during heating. At a constant temperature of 1773 K, changes in the diffraction patterns were small compared to changes observed during heating. By 1773 K, the intensity of the background decreased further, the intensity of the reflections increased and their positions shifted shightly to lower scattering angles. Thermal expansion as well as the release of oxygen and the formation of oxygen vacancies led to an expansion of the fluorite-type crystal lattice.[164]

Performance of the in situ XAS/XRD cell

The cell for high photon energy XAS and XRD in transmission mode functions under the extreme conditions required for solar thermochemical looping. Coupling of a mass spectrometer to the cell enables quantitative gas analysis. The robust design gives access to information about the working structure of oxygen storage materials during both the reduction and oxidation sub-steps of the dissociation of carbon dioxide from room temperature up to at least 1773 K. If thermal disorder masks the structure, the cell allows exposure to reaction conditions at high temperature and measurements at room temperature without exposure to air.

A crucial factor in in situ XAS and XRD experiments in transmission mode is the quality of the sample, i.e. the homogeneity, uniformity and mechanical stability of the pellet throughout the experiment upon heating and cooling as well as changes in the feed gas. Minute cracks or pinholes negatively affect the quality of XAS data. XRD is not as sensitive to pinholes as XAS, but requires a precise, reproducible position of the sample. The cell ensured good control of the temperature because the sample was placed in a large heated zone and the temperature was measured in the immediate vicinity of the sample. Radiative, non-contact heating led to a sufficiently good distribution of temperature in the sample, and mechanical failure, probably caused by temperature gradients during heating was infrequent, even at heating rates up to 50 K/min. Careful preparation of the pellets allowed reliable operation and the failure rate was less than 10 %. Contamination of the sample due to contact with the alumina sample holder cannot be excluded, but is highly unlikely to affect the spot hit by the X-ray beam in the center of the pellet. There was no observable formation of a tetragonal $CeAlO_3$ phase. The energy of the focusing device is just above the Ce K edge, and there were significant absorption effects. In the combined XAS/XRD experiment, a photon energy below the

Hf K edge was chosen for XRD to avoid absorption effects. The size of the sample is sufficient to reach concentrations of the product gases suitable for quantification by means of online quadrupole mass spectrometry. The gas flow rates can be adjusted to reach concentrations of oxygen or carbon monoxide, respectively, of typically a few hundred ppm. The enormous power of the furnace and the small thermal mass of the alumina tube bearing the thermocouple, sample holder and the sample enable heating and cooling rates up to several hundred K/min. The rapid change of samples at room temperature is very convenient with regard to the time pressure in experiments at a synchrotron beam line.

The cell design enables detailed modification and optimization of samples, reaction conditions and X-ray-based characterization techniques. The reproducibility of the sample position, the calibration of the detector position and the movement of the sample during the experiment are of great importance in XRD experiments. This might be improved by a key lock mechanism. The change in the sample position due to thermal expansion of the alumina tube was not corrected. The use of an internal standard might help to improve the reproducibility and precision of the measurements, for example by attaching a thin platinum foil to the pellet. In addition, an internal standard might provide a alternative measure of temperature. The (dead)volume of the cell can be significantly reduced by adjusting the shape of the quartz tube for time-resolved transient experiments such as the modulation-excitation method with phase-sensitive detection.[277,278] Under static conditions, the background contribution of the quartz tube might be eliminated by using an open quartz tube and a kapton window. The requirement for higher Bragg angles can be met by modifying the casing of the furnace.

Complementarity of in situ XAS and XRD at high temperature and advantages of high photon energy

The combination of XAS at the Ce K edge and XRD provides complementary information about structural changes in ceria-based oxygen storage materials. As shown in Figure 3.7, despite strong thermal damping effects leading to insurmountable difficulty in the extraction and evaluation of the EXAFS signal, features in the XANES region of Ce K edge X-ray absorption spectra are very sensitive to structural changes. It is advantageous to combine many techniques because signals may be weak and ambiguous at high temperature. Accurate data of the average oxidation state of cerium and information about the local geometric structure, determined by Ce K edge XAS, can be

combined with structural data of the long-range structure as determined by XRD to obtain an unprecedented comprehensive, detailed and precise picture. While information about the short-range order is given by Ce K edge XAS, XRD gives detailed insight into the long-range order, as shown by the ordered arrangement of the cerium and hafnium cations. While the average oxidation state is difficult to extract from XRD data, it is determined from the Ce K edge XANES. Unlike XAS, XRD enables the facile detection of the formation of other phases such as the monoclinic hafnia phase. Structural changes were rather slow during the oxidation of the oxygen-deficient materials due to the limited surface area of the dense ceramic body and limited reaction rate of the surface. The time resolution of both XAS and XRD is sufficient to study the dynamics of structural changes and gain in-depth knowledge of the role of oxygen vacancies in the dynamics of phase transition. In the case of ceria-hafnia materials, XAS at the Hf K edge, gives information about the electronic structure of hafnium and the hafnium-oxygen coordination geometry (see Chapter 6). While XAS at absorption edges at lower photon energy is desirable , XRD data collected at high photon energy open up the possibility of analyzing the pair distribution function.

Potential application of the analysis of the pair distribution function

The analysis of the pair distribution function (PDF) is a powerful tool for determining the structural short-and long range ordering, which depends on the total scattered intensity. It enables the determination of local, short-range structural features, which are not reflected in the long-range average crystal structure.[279–282] PDF has been successfully applied to synchrotron X-ray scattering data of ceria-based materials.[224,283–285] PDF analysis requires a scattering intensity up to a very large momentum transfer $q = 4\pi \sin\theta/\lambda$ with the scattering angle θ and the wavelength λ. A typical Q-range greater than 30 $Å^{-1}$ is required to minimize termination effects in the Fourier-transform of the total scattered intensity. Thus, the scattering data for PDF analysis are collected preferably in transmission experiments at high photon energy. The in situ cell for XAS and XRD in a solar thermochemical reactor enabled a maximum Bragg angle of about 18° 2θ, which corresponds to an upper limit of the q range of 10.3 $Å^{-1}$ at 64.8 keV and 6.6 $Å^{-1}$ at 41.4 keV. A greater q range might be accessible if modifications are undertaken to enable larger scattering angles and/or by increasing the photon energy. At 64.8 keV and 40° 2θ, the maximum wave vector q is 22.5 $Å^{-1}$ and at 100 keV and 40° 2θ, it is 34.7

$Å^{-1}$, respectively. Both the scattering angles and the photon energy are accessible. PDF can lead to a better understanding of the properties of defect interactions[96,163,165] and the influence of inhomogeneity[145] on the performance of materials for the generation of fuels by means of solar-driven thermochemical cycles.

Conclusions

A robust device was developed and tested for combined in situ XAS and XRD measurements of oxygen storage materials and quantitative online mass spectrometry under the extreme conditions of thermochemical looping for the generation of solar fuels. The combination of in situ XAS and XRD provides reliable structural high-quality data. The local and global structural features, such as the average oxidation state of cerium and the ordered arrangement of cations, can be determined under identical and relevant conditions.

Chapter 4

Ce K Edge XAS of Ceria-based Redox Materials Under Realistic Conditions for the Two-step Solar Thermochemical Dissociation of Water and/or CO_2

based on:
Rothensteiner, M., Sala, S., Bonk, A., Vogt, U., Emerich, H., and van Bokhoven, J. A. (2015). Phys. Chem. Chem. Phys., 17(40), 26988–26996. http://doi.org/10.1039/C5CP03179F
http://doi.org/10.1039/C5CP03179F

M.R. contributions: applied for beam time, planned and performed XAS experiments, processed and analyzed the data, wrote the manuscript.

4.1 Introduction

The setup and in situ XAS cell suitable for measurements in transmission mode at the cerium K edge from room temperature up to 1773 K presented in Chapter 3 was used to characterize ceria-based materials under realistic conditions of solar thermochemical two-step carbon dioxide splitting. Time-resolved X-ray absorption near-edge structure (XANES) data, collected for a 10 mol% hafnium-doped ceria sample $Ce_{0.9}Hf_{0.1}O_{2-\delta}$ during reduction at 1773 K in a flow of inert gas and during re-oxidation by carbon dioxide at 1073 K, enabled the quantitative determination of the non-stoichiometry δ of the fluorite-type structure. XANES analysis suggests the formation of the hexagonal Ce_2O_3 phase upon reduction in 2% hydrogen/helium at 1773 K. We discuss the experimental limitations and possibilities of high-temperature in situ XAS at edges of lower energy as well as the importance of the technique for understanding and improving the properties of ceria-based fluorite-type oxygen storage materials for thermochemical solar energy conversion. At high temperature substantial damping of the EXAFS signal significantly limits the access to structural information. In the case of a flat EXAFS region, however, the preferred strategy is to exploit spectral features in the XANES which are less affected by thermal damping. In contrast to the cerium L_{III} near edge region, which has more complex and oxidation-state-dependent spectral features, the shift in the edge position at the cerium K edge only indicates the oxidation state.

4.2 Results and discussion

Figure 4.1(a) illustrates normalised cerium K edge spectra of $Ce_{0.9}Hf_{0.1}O_{2-\delta}$ at 298, 1073 and 1773 K at three different levels of non-stoichiometry δ. Spectra were recorded during two-step carbon dioxide-splitting with a temperature swing between 1773 and 1073 K, under isothermal conditions for carbon dioxide splitting at 1773 K and after reduction with hydrogen at 1773 K. After reduction a shift in the edge position to lower photon energy was found at all temperatures, indicating the accessibility of structural information related to the near edge region of the spectra up to 1773 K. As indicated by the data in Table 2.1, the expected edge shift is small after reduction in a flow of argon and larger after reduction in hydrogen.

In normalised spectra, damping leads to an apparent shift in the edge position to lower energies. Despite temperature differences of 1575 K, the accuracy of the edge position is remarkably good without any correction for temperature. Below is a discus-

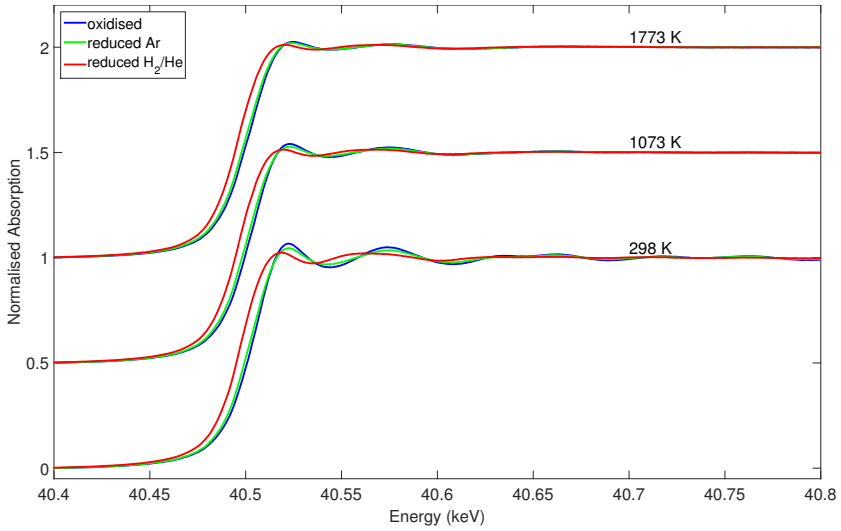

(a)

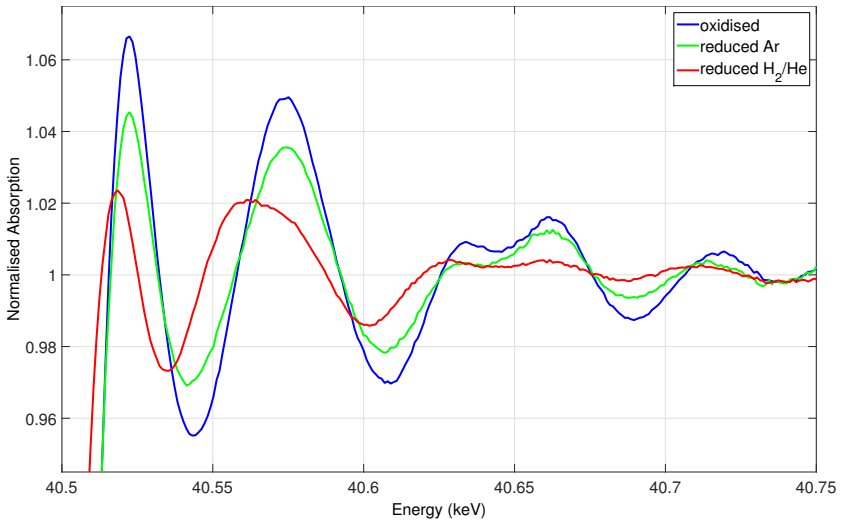

(b)

Figure 4.1 a) Normalised cerium K edge spectra of $Ce_{0.9}Hf_{0.1}O_{2-\delta}$, recorded at 298, 1073, and 1773 K. 'Oxidised' (298 K) is the spectrum of the as-prepared pellet after introduction into the XAS cell. 'Oxidised' (1073) and 'oxidised' (1773) were recorded after oxidation in 1 atm carbon dioxide. 'Reduced Ar' denotes spectra recorded after reducing the sample in a flow of argon at 1773 K and 'reduced H_2/He' spectra recorded after reducing the sample in a flow of 2% hydrogen/helium at 1773 K. b) Close-up of spectra recorded at 298 K. 'Oxidised' denotes the spectrum of the as-prepared pellet after introduction into the XAS cell. 'Reduced Ar' denotes spectra recorded after reducing the sample in a flow of argon at 1773 K and 'reduced H_2' spectra recorded after reduction in a flow of 2% hydrogen/helium at 1773 K.

sion of the effect of temperature on the shift in the edge position. The amplitude of the extended X-ray absorption fine structure is strongly affected by damping because of thermal and structural disorder. Figure 4.2 compares the Ce K edge EXAFS of the pristine sample collected at room temperature with spectra recorded after oxidation in carbon dioxide at 1073 K and 1773 K. As the temperature increases, the useful range for EXAFS analysis becomes smaller, as the energy range in which oscillations are distinguishable from noise moves close to the absorption edge. While oscillatory features are still visible at 1073 K, the post edge region contains only very weak oscillations at 1773 K. Figure 4.3 presents EXAFS data of ceria and ceria-hafnia recorded at room

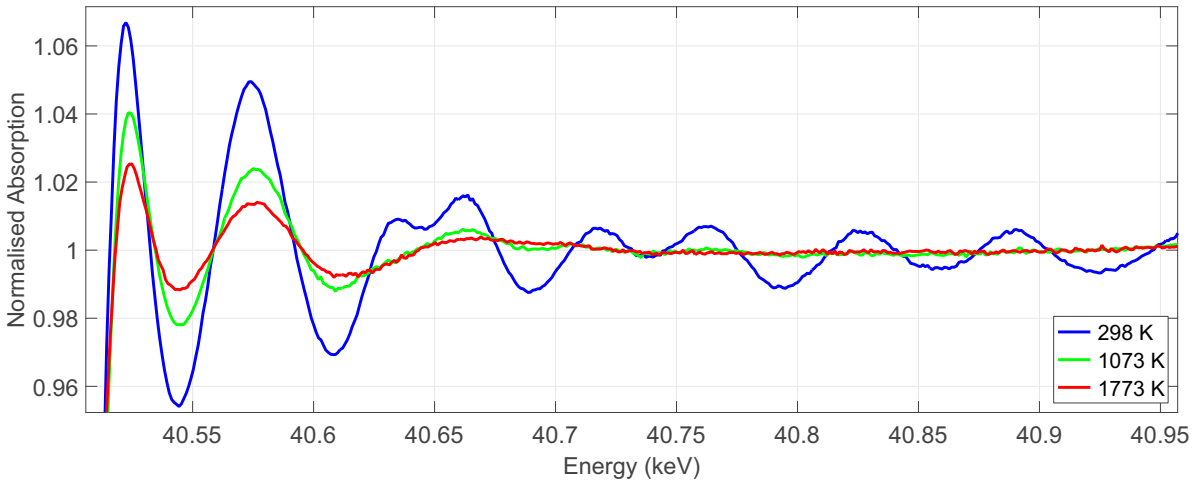

Figure 4.2 EXAFS of $Ce_{0.9}Hf_{0.1}O_{2-\delta}$ of the pristine sample at room temperature (blue), after re-oxidation in carbon dioxide at 1073 (green) and 1773 K (red).

temperature. Thermal reduction in a flow of argon caused a decrease in the amplitude of the EXAFS of ceria and $Ce_{0.9}Hf_{0.1}O_{2-\delta}$, which might be due to increased disorder. Exposure to the temperature range relevant for solar thermochemical cycles can affects the quality of the pellet. A degradation of the pellet cannot be excluded, in particular in the spectrum recorded after reduction in hydrogen/helium, which led to substantial changes in the structure. After reduction in hydrogen/helium, the amplitude of the EXAFS signal decreased significantly and the shape of the first maximum in the Fourier-transform broadened. It is very likely that a glitch at k = 9.3 $Å^{-1}$ (see chapter 6) affects the EXAFS signal. Experimental difficulties and thermal damping complicate comparison and EXAFS analysis. Furthermore, anharmonic oscillations hinder a detailed EXAFS analysis.[286,287] Therefore, we did not attempt to fit EXAFS at high temperature. After reduction in hydrogen, both the shift in the edge position and the spectral features suggest the formation of the hexagonal Ce_2O_3 phase. In this crystal

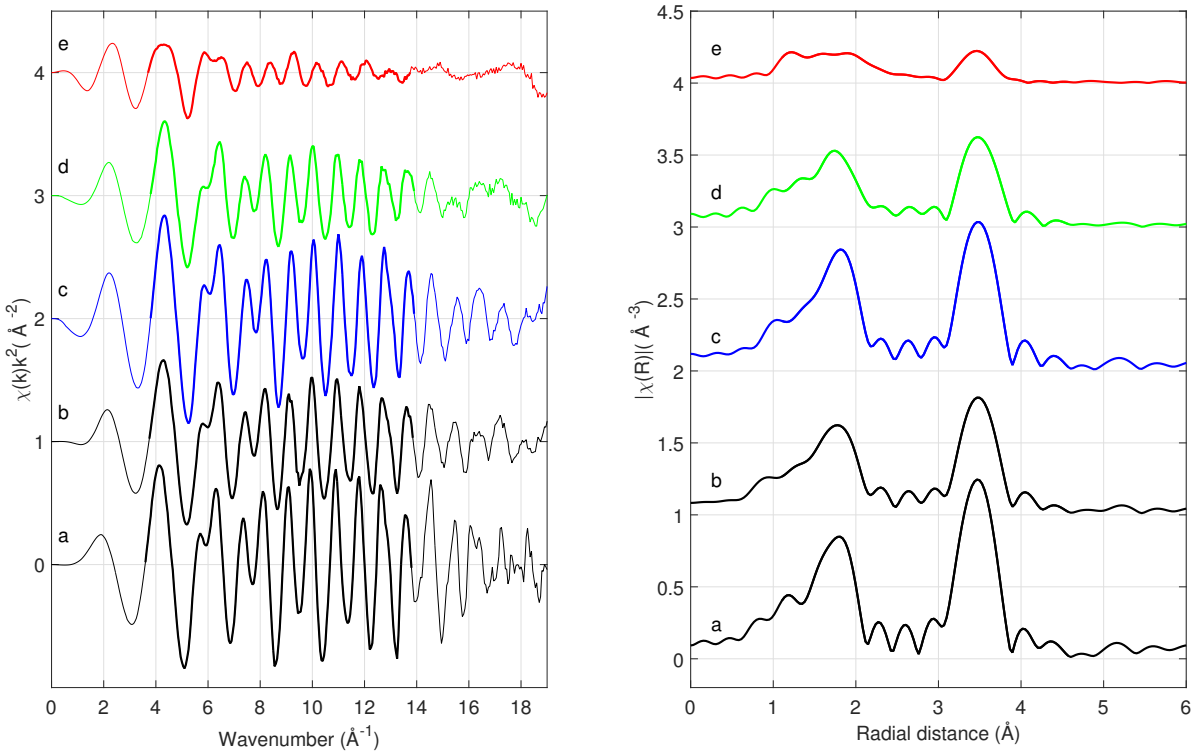

Figure 4.3 Extended X-ray absorption fine structure (EXAFS) of a) CeO_2 (as prepared) b) $CeO_{1.93}$ (reduced Ar) c) $Ce_{0.9}Hf_{0.1}O_2$ (as prepared) d) $Ce_{0.9}Hf_{0.1}O_{1.92}$ and e) $Ce_{0.9}Hf_{0.1}O_{1.55}$ (reduced H_2) recorded at RT. The bold lines indicate the data range used for Fourier-transformation of $\chi(k)$ to obtain the pseudo-radial distribution functions $\chi(R)$. The k-weight was two.

structure, cerium is surrounded by seven oxygen atoms. The relationship between non-stoichiometry and coordination number given in Table 2.1 is valid only for the cubic, fluorite-type phase of ceria. Figure 4.4 displays the results of the completed experiment. It gives the temperature in the reactor, the gas atmosphere, and the mass spectrometer signals for oxygen (m/z = 32) and water (m/z = 18) which form under reducing conditions in a flow of argon and 2% hydrogen/helium, respectively. Furthermore, Figure 4.4 shows the non-stoichiometry δ in $Ce_{0.9}Hf_{0.1}O_{2-\delta}$ and the corresponding energy of the edge shift obtained at constant normalised absorption. In addition, a contour plot of normalised difference spectra highlights minute spectral changes. A spectrum recorded at 1073 K after thermal reduction in a flow of argon at 1773 K was subtracted to obtain these difference spectra.

In the first part of the experiment, two redox cycles with a temperature swing were performed, consisting of a reduction step at 1773 K in a flow of argon followed by an oxidation step at 1073 K in a flow of carbon dioxide. The MS signal shows that in the first

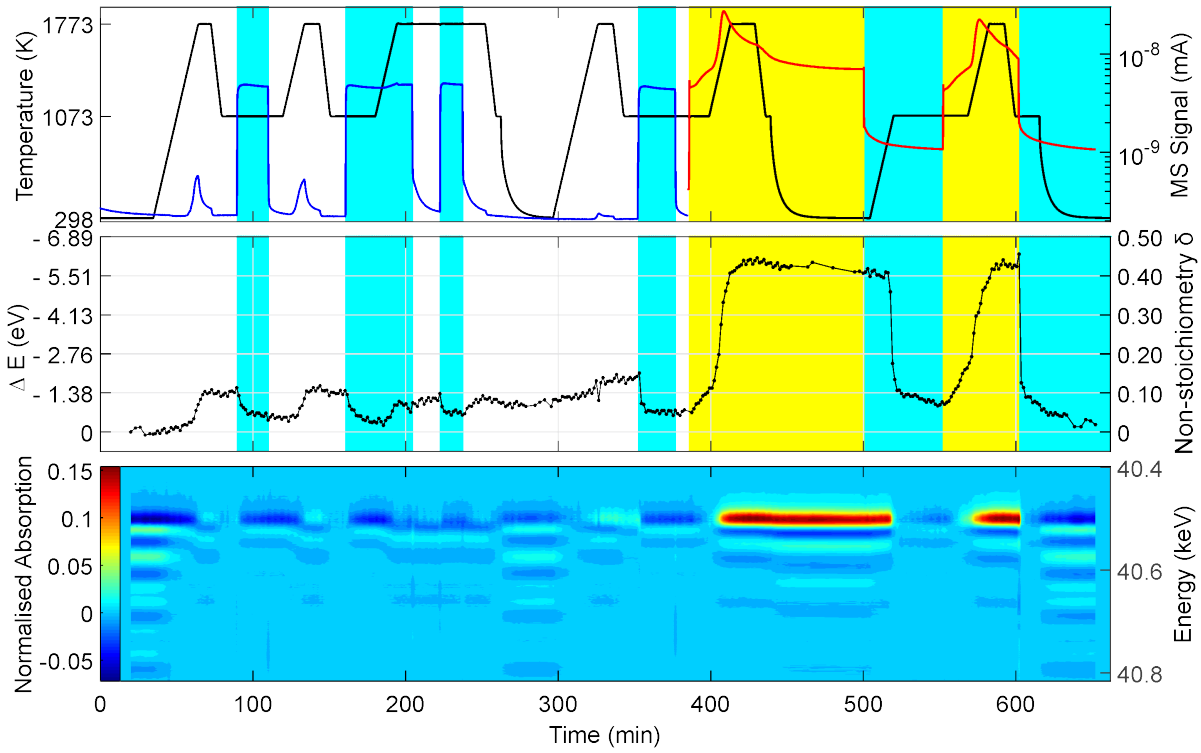

Figure 4.4 Top: Experimental conditions: furnace profile, gas atmosphere (white = argon, blue = carbon dioxide, yellow = 2 % hydrogen/helium), MS signals for oxygen (blue) and water (red). Middle: Non-stoichiometry δ and corresponding shift of the edge energy, determined by interpolation at the absorption value corresponding to the edge position of the first spectrum Bottom: Contour plot of normalised difference spectra obtained by subtraction of a spectrum recorded at 1073 K after the first reduction by flushing the reactor with argon at 1773 K. See Figures 4.1 4.2, and 4.3 for selected spectra.

cycle, while heating from room temperature, oxygen release starts at about 1323 K and peaks when the temperature reaches 1773 K. After cooling to 1073 K and re-oxidation in a flow of carbon dioxide at 1073 K, the same amount of oxygen is released from the material in the second cycle, indicated by an oxygen MS signal peak area ratio of 1.00, which suggests complete re-oxidation. The onset of the second oxygen peak occurs at the same temperature as in the first cycle but has a different peak shape, indicating that oxygen release is slower. The maximum oxygen concentration in the flush gas is lower and the peak broader. After the second re-oxidation at 1073 K, isothermal redox cycles were performed by heating up in carbon dioxide and switching between argon and carbon dioxide at 1773 K. When the temperature reached 1773 K, the oxygen signal presented as a small peak. After switching from carbon dioxide to argon the oxygen release from the sample was revealed by comparison with the MS signal obtained when the same

switch was performed at 1073 K. The sample was then cooled to 298 K and another redox cycle with a temperature swing carried out. During heating 12% of the oxygen released in the first cycle was detected, confirming that this fraction of Ce^{3+} is oxidised to Ce^{4+} by residual oxygen.

In the second part of the experiment, the sample was reduced by heating from 1073 to 1773 K in a flow of 2% hydrogen in He. After cooling to 298 K, the temperature was increased to 1073 K in carbon dioxide followed by reduction at 1773 K in a flow of 2% hydrogen in helium and oxidation at 1073 K in carbon dioxide. The MS signal for water clearly indicates that reduction of the sample begins to take place at 1073 K. A similar amount of water forms in the second reduction treatment with hydrogen. Heating from room temperature to 1073 K in carbon dioxide leads to re-oxidation, as proved by the formation of a carbon monoxide peak at 28 m/z (not shown).

It is evident that the non-stoichiometry δ determined from XAS spectra is in good agreement with the MS signals reported above. The precision and noise of δ obtained from XAS can be estimated from the first six spectra of the pristine sample taken in a flow of argon at 298 K and the average of which is $6.886 \cdot 10^{-4}$ and a standard deviation of $8.6 \cdot 10^{-3}$. The maximum value of δ in $Ce_{0.9}Hf_{0.1}O_{2-\delta}$ is 0.45 based on the assumption that hafnium is always present as Hf^{4+}.

The non-stoichiometry δ reaches a maximum value of 0.10 in the first reduction step. In the second reduction step, a slightly higher value (about 0.11) is reached. Prior to release of oxygen, as indicated by MS, δ rises to an apparent value of about 0.015, a behaviour that we ascribe to the effects of temperature. However, based on the non-stoichiometry after the second reduction step and the oxygen peak area ratio of 1.00 0.35 is assumed for this apparent δ. Results for δ of the second re-oxidation step are very similar and in line with the MS signals. Re-oxidation at 1073K leads to a decrease in δ by 0.065 in the first and 0.08 in the second cycle. During cooling from 1773 K to 1073 K δ does not change significantly in the first two redox cycles. Upon switching to carbon dioxide at 1073 K the temporal evolution of the non-stoichiometry during re-oxidation is visible.

The general trends of the non-stoichiometry agree with the experimental conditions while heating to 1773 K in carbon dioxide and switching under isothermal conditions at 1773 K. However, lower values for δ are found in argon despite a similar amount of oxygen, shorter reduction times and probably higher carbon dioxide levels. The switch from argon to carbon dioxide at 1773 K leads to a decrease in δ by about 0.043 and increases by about the same value in the subsequent reduction step. Decreasing the

temperature of the reduced sample in argon from 1773 K to 1073 K leads to 0.008 decrease in δ and a further decrease by 0.06 to 0.066 as the temperature reaches 298 K. These edge shifts are not caused by temperature changes and play only a small role. Subsequent heating leads to oxygen release, starting at about 1623 K, and is accompanied by a 0.035 increase in δ. This increase in δ was twice as high as expected based on oxygen peak area ratios and corresponding values for δ obtained earlier in the experiment and coinciding with a change in beam intensity due to refilling of the storage ring. During the last cooling step in argon to 1073 K δ further increases and eventually plateaus at 0.14. This value drops by 0.1 during re-oxidation in carbon dioxide at 1073 K.

Reduction in hydrogen leads to a clear increase in δ under isothermal conditions at 1073 K and after heating to 1773 K, reaching a maximum value of 0.44. The theoretical maximum of δ is 0.45. Cooling from 1773 K to room temperature under reducing conditions lead to a decrease in δ from 0.44 to 0.40, as a result of temperature. This observation suggests that the extraction of the non-stoichiometry from XAS spectra recorded in the same gas environment at two temperatures separated by 1475 K, leads to an error of less than 10% without correcting for temperature effects. Re-oxidation is fast when heating from room temperature in carbon dioxide, starting at approximately 873 K, and it is approximately 75% complete when the temperature in the reactor reaches 1073 K. The second reduction step in hydrogen is similar to the first. Upon re-oxidation after switching to carbon dioxide at 1073 K the change from a hexagonal to a cubic structure is very fast. However, re-oxidation is probably not completed when the heating of the furnace is stopped. At the end of the experiment, and under oxidizing conditions at room temperature, δ reaches an average value of 0.018. Apart from temperature effects and incomplete re-oxidation, this derivation might be explained by significant structural changes, such as the segregation of a hafnium-rich phase upon complete reduction in hydrogen.

Temperature effects are also evident in the XANES region, which complicates the determination of non-stoichiometry. Interpolation at constant absorption is less affected by these influences than using the position of the maximum of the first derivative, but depends on the pre-and post-edge region for subtracting the background. The noise level related to the non-stoichiometry indicates that the experiment is highly dependent on the stability of the incoming X-ray beam and the mechanical movement of the monochromator crystals. The rocking curve is extremely narrow and the stability and reproducibility of the beam after detuning is limiting at a photon energy of 40 keV. An

energy scan from 40 to 41 keV requires a mere 0.07 ° change in the Si(111) Bragg angle. On the other hand, the energy of the beam can be changed quickly, leading to better time resolution. XAS data measured at the $L_{II,III}$ edges, show more complex features

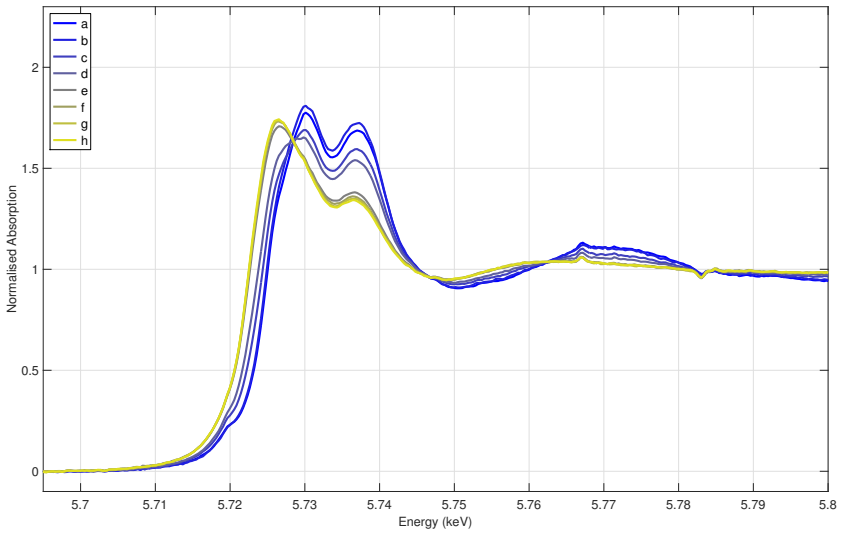

Figure 4.5 Normalised Ce L_{III} edge absorption spectra recorded during reduction of $Ce_{0.9}Hf_{0.1}O_{2-\delta}$ powder diluted with BN by heating with a rate of 50 $Kmin^{-1}$ from RT (a) to 1073 K (f,g,h) in a flow of helium. Kapton windows were used.

related to the electronic structure of cerium. These features might be advantageous at high temperature, at which relevant features are observable only in the XANES region, but do require the use of a diluent such as boron nitride. Measurements in transmission mode restrict XAS at the absorption edges of dopant elements due to their low concentrations (typically < 20 mol%) and the high absorption cross section of cerium.

Preliminary experiments showed the possibility of measuring the cerium L_{III} edge in transmission mode, but chemical stability was not achieved at high temperatures. Figure 4.5 presents cerium L_{III} XANES during reduction of a boron nitride pellet containing $Ce_{0.9}Hf_{0.1}O_{2-\delta}$ powder prepared by polymerized-complex method. While only minute changes in the spectra were expected up to 1073 K, spectral changes suggest much larger structural changes, which are most likely due to the small particle size of the material or interaction with boron nitride. The ceria-hafnia system has been considerably less explored than the ceria-zirconia system. High-temperature structural or thermodynamic data are available,[195] however little work on non-stoichiometric compounds has been done. Zhou and Gorte et al.[192,288] reported on ceria-hafnia and found the separation of $Ce_{0.8}Hf_{0.2}O_2$ into $Ce_{0.81}Hf_{0.19}O_2$ and $Ce_{0.85}Hf_{0.15}O_2$ when calcined in air at 1323 K.

In a study on doped ceria compounds for thermochemical cycling,[153] it was found

that hafnium increases the non-stoichiometry less than zirconium. This is in line with work by Baidya et al.[191] who found that in equimolar composition ceria-hafnia is less reducible than ceria-zirconia. The catalytic properties of ceria-hafnia materials were investigated by Reddy et al.[289] who found higher catalytic activity in soot oxidation compared to ceria-zirconia materials.

The possibility to measure XAS at high photon energies such as the Hf K edge (65.351 keV) could provide complementary structural information. Combined with in situ XRD, our approach can contribute to a better understanding of ceria-based systems under extreme conditions.

Unlike well-established laboratory methods to determine the amounts of reduction and oxidation products, XAS provides element-specific electronic and geometric structural information and gives greater insight into redox chemistry. Several effects must be considered when working at high temperature. Radiative heat transfer predominates and thus the absorbance of the sample plays a crucial role. Dark samples such as praseodymium-doped ceria might reach a higher temperature than bright samples such as pure ceria. The damping of the EXAFS signal, however, might offer the possibility of measuring the temperature of the sample. Temperatures of the sample in carbon dioxide might deviate from those in argon. Our ultimate goal is to characterize materials for the thermochemical dissociation of water and carbon dioxide. To achieve this it is necessary to determine the structural features that govern the formation, distribution, and reactivity of oxygen vacancies and, using this knowledge we hope to design materials with superior properties for the exchange and storage of oxygen. The cell described enables exposure of materials to relevant solar thermal conditions - in particular achieving desired temperature regimes for EXAFS measurements in their reduced state. A superior redox material must be able to store large amounts of oxygen by reacting with water or carbon dioxide with fast kinetics, high thermal stability and cyclability. An element-specific in situ method such as X-ray spectroscopy is necessary to determine structural changes during the production of solar fuels.

4.3 Conclusions

Overall, ceria-based redox materials can be characterized in situ under relevant conditions using cerium K-edge X-ray absorption spectroscopy in transmission mode. Using diluted samples, the absorption L_{III} edge of cerium can be accessed only at lower temperature. The high penetration depth of X-rays at the cerium K edge facilitates a

simple and robust cell design that can be operated under these harsh conditions. In the temperature range relevant to thermochemical looping the determination of structural properties is, to a large extent, limited to spectral features in the XANES region of the spectrum. The shift in the cerium K edge position enables accurate determination of the non-stoichiometry. By means of in situ XAS it is possible to determine the element-specific structural changes that occur during synthesis of solar fuel.

Chapter 5

Structural Changes in $Ce_{0.5}Zr_{0.5}O_{2-\delta}$ under Temperature-Swing and Isothermal Solar Thermochemical Looping Conditions Determined by in Situ Ce K and Zr K Edge X-ray Absorption Spectroscopy

based on:
Rothensteiner, M., Bonk, A., Vogt, U. F., Emerich, H., and van Bokhoven, J. A. (2016). J. Phys. Chem C, 120(26), 13931-13941. http://doi.org/10.1021/acs.jpcc.6b03367

M.R. contributions: concept, applied for beam time, planned and performed XAS experiments, processed and analyzed the data, wrote the manuscript.

5.1 Introduction

The shift in the Ce K absorption edge reveals quantitative information about changes in the electronic structure of cerium. Zr K edge XANES features are sensitive to the geometry of the zirconium-oxygen coordination. In situ XAS at both the Ce K and Zr K edges can be performed in transmission mode under the conditions of thermochemical carbon dioxide splitting and a temperature swing of 1773 to 1073 K and isothermal conditions at 1773 K. Structural changes in an equimolar ceria-zirconia solid solution were determined from room temperature to 1773 K under typical reducing and oxidizing conditions in a reactor for the solar thermochemical dissociation of water and/or carbon dioxide in a two-step redox cycle. The maximum extent of reduction at 1773 K was 53±5%; about 9±5% of the cerium atoms changed valence from 4+ to 3+ and vice versa during isothermal looping in a flow of argon and carbon dioxide, respectively. Zr K edge XANES indicated a transformation of the oxygen coordination of zirconia to a more centrosymmetric cubic geometry upon reduction. During isothermal cycling at 1773 K, there were no visible changes in the zirconium-oxygen coordination geometry. Zr K edge spectra recorded at room temperature of the equimolar composition were compared to those of $Ce_{0.8}Zr_{0.2}O_{2-\delta}$ materials. The non-stoichiometry determined by Ce K edge XAS allowed to relate the spectra to the cerium-zirconium-oxygen phase diagram at 1773 K.

5.2 Results

Figure 5.1 shows the XRD patterns of $CeO_{2-\delta}$ (Zr0), $Ce_{0.8}Zr_{0.2}O_{2-\delta}$ (Zr20), and $Ce_{0.5}Zr_{0.5}O_{2-\delta}$ (Zr50), a)-c) after calcination of the Pechini-type precursor polymer at 973 K for 10 hours and d)-f) the XRD patterns of Zr0CS, Zr20CS and Zr50CS after sintering pellets of Zr0C, Zr20C and Zr50C powders at 1873 K in air for five hours. The patterns of the calcined powders Zr0C, Zr20C and Zr50C showed the same reflections, which shifted to higher 2θ values with increasing zirconia content, revealing contraction of the lattice. All reflections showed significant broadening, increasing with zirconia content, indicative of smaller crystallites and/or enhanced structural disorder. Peak asymmetry was most pronounced in the reflection pattern of Zr20C. Zr50C showed the broadest reflections, indicating both disorder and/or a somewhat smaller mean crystallite size compared to Zr0C and Zr20C. In the patterns of Zr0CS, Zr20CS and Zr50CS all reflections became much narrower and there was lattice contraction by zirconium. Peak asymmetry was still present in the pattern of Zr20CS. In the diffraction pattern of Zr50CS new reflections

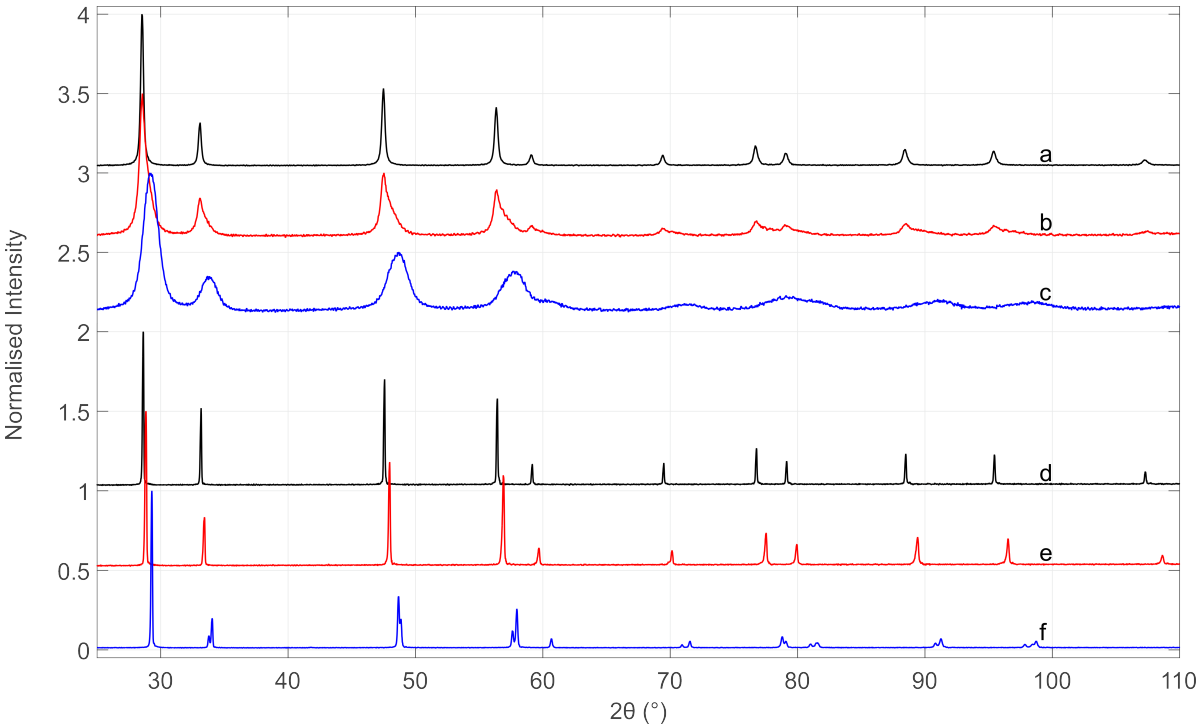

Figure 5.1 XRD patterns of $CeO_{2-\delta}$ (a,d) $Ce_{0.8}Zr_{0.2}O_{2-\delta}$ (b,e) and $Ce_{0.5}Zr_{0.5}O_{2-\delta}$ (c,f) after calcination of the Pechini-type precursor polymer at 973 K in air for ten hours (a-c) and after sintering at 1873 K in air for five hours (d-f).

appeared. Because of their arrangement in pairs, this effect is often referred to as 'peak splitting', indicating the formation of new tetragonal phases related to the fluorite-type structure[185,226] in Figure 1.8. Figure 5.2 shows a close-up of a very weak reflection at $2\theta = 41.79°$, which is characteristic of the tetragonal phase in Zr50CS. In the tetragonal phase, oxygen atoms are displaced from their positions in the fluorite-type lattice. Figure 5.3 presents the Ce K edge XANES of Zr50CS recorded during thermal reduction by heating from room temperature to 1773 K (a) and b)), during cooling from 1773 K to 1073 K after the second reduction step (c) and d)) in a flow of argon, and at 1073 K during exposure to a flow of carbon dioxide (e) and f)). Arrows indicate the direction of the spectral changes. The amplitude of the fine structure decreased drastically due to thermal damping as the temperature increased from room temperature to 1773 K. Above 1073 K, the oscillations disappeared a few hundred eV above the absorption edge. Figure 5.3 b), d) and f) highlight the shift in the photon energy at the inflection point of the absorption edge. In Figure 5.3 b) this shift is caused by changes in the formal oxidation state from Ce^{4+} to Ce^{3+} of a fraction of cerium atoms and concomitant release of oxygen.[240] There is a discontinuity in the Ce K edge XANES during heating at

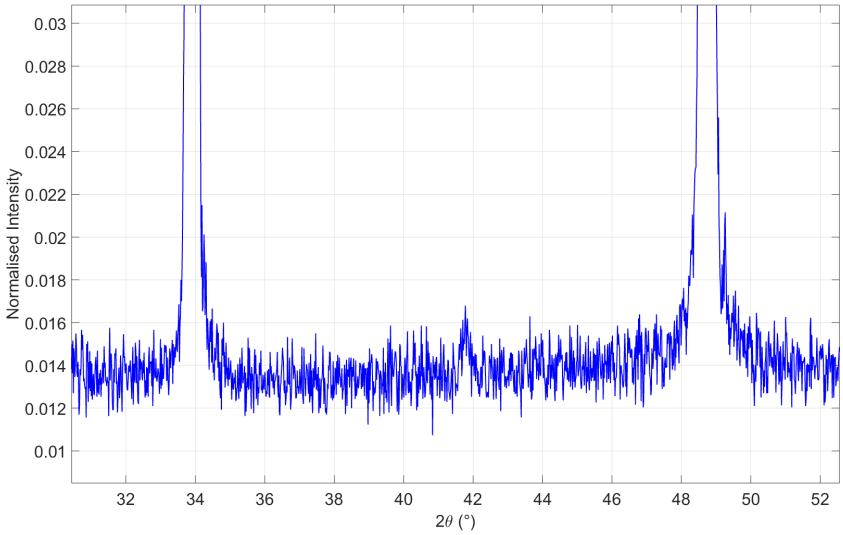

Figure 5.2 Detail of the XRD pattern indicating the presence of the tetragonal phase in Zr05CS at $2\theta = 41.79°$.

about 970 K in argon. Figure 5.3 c,d) shows that cooling from 1773 K to 1073 K led to an increase in the amplitude of the absorption fine structure due to decreased thermal damping. There is a slight shift in the edge position back to higher photon energy. The minima and maxima of the spectra measured at 1073 K were more pronounced during the heating compared to those after thermal reduction. This difference is due to the electronic and structural changes of the material during reduction at high temperature. The main effects during cooling from 1773 K to 1073 K were mainly due to temperature. Switching from argon to carbon dioxide at 1073 K resulted in minute spectral changes. After switching from argon to carbon dioxide the white line intensity increased slightly (Figure 5.3 e) accompanied by a very small edge shift (Figure 5.3 f). Thus, at this temperature, reoxidation of cerium by carbon dioxide did not occur. Figure 5.4 presents Ce K edge XANES of Zr50CS recorded during isothermal two-step carbon dioxide splitting at 1773 K. After reduction in the flow of argon, Zr50CS was exposed to alternating oxidizing and reducing conditions by switching between a flow of carbon dioxide and argon, respectively. Unlike at 1073 K, the Ce K edge shifted gradually to higher energy in a flow of carbon dioxide and back to lower energy in a flow of argon. Concurrently, the white line intensity increased slightly upon oxygen uptake and decreased upon oxygen release. These spectral changes are brought about by repeated and reversible oxidation of Ce^{3+} to Ce^{4+} and reduction of Ce^{4+} to Ce^{3+}, respectively. At 1773 K the rates of the oxidation reaction were higher than at 1073 K and a clear effect was found at 1773 K, while the reaction did not seem to occur at 1073 K despite a higher thermodynamic

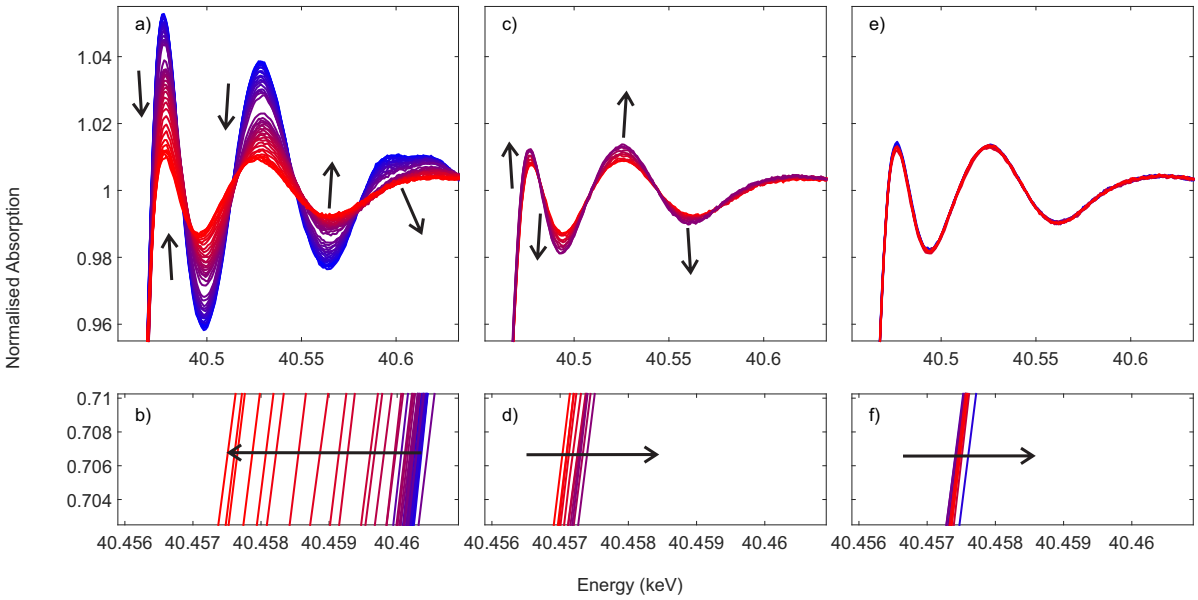

Figure 5.3 Series of Ce K-edge XANES of Zr50CS recorded during heating from room temperature to 1773 K (a) and b), during cooling down from 1773 K to 1073 K (c and d)) in a flow of argon. 295 K (blue), 1773 K (red). Panels e) and f) represent spectra recorded before (blue) and after (red) switching from argon to carbon dioxide at 1073 K.

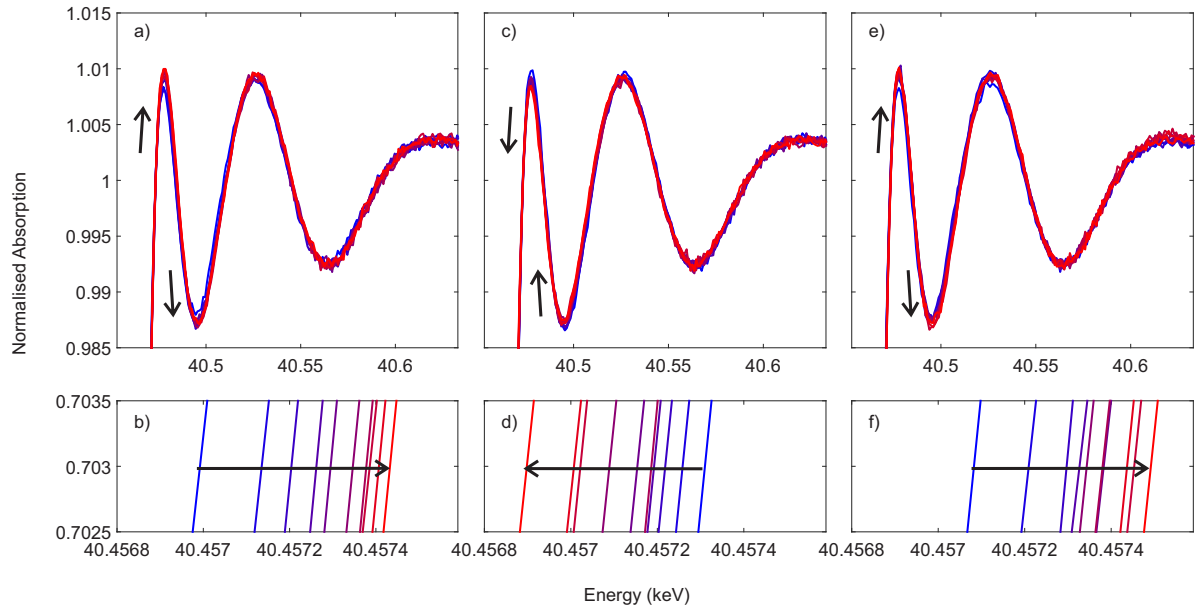

Figure 5.4 Series of Ce K-edge XANES of Zr50CS recorded during switches from a flow of argon to a flow of carbon dioxide at 1773 K. Spectra in (a) and b)) and (e) and f)) were recorded in carbon dioxide and spectra in panels (c) and d)) in argon. The shift of the edge position is shown in b), d) and f), first spectrum (blue) and last spectrum (red).

driving force at the lower temperature. Figure 5.5 relates the thermochemical looping conditions to the shift in the edge energy and the non-stoichiometry δ in $Ce_{0.5}Zr_{0.5}O_{2-\delta}$ obtained from time resolved Ce K edge XAS using the interpolation method described above. Figure 5.5 a) shows the reduction of fresh Zr05CS by heating from room temperature to 1773 K in a flow of argon and subsequent carbon dioxide splitting by means of a temperature swing. During heating, oxygen release was first detected in the MS at about 1173 K, which coincided with changes in the energy of the Ce K absorption edge. At 1773 K, the edge shifted by 3.0 eV to a lower photon energy, which is indicative of 48±5% Ce^{3+} (Equation 2.24). Cooling to 1073 K led to a 0.1 eV increase in photon energy to 2.9 eV and 47±5% Ce^{3+}, respectively. Switching from argon to carbon dioxide at 1073 K did not significantly alter the edge position. As evident from the oxygen MS signal, reduction was not complete in the first reduction step. In the second reduction step, further release of oxygen and a shift in the edge occurred, leading to a shift by -3.25 eV, corresponding to 52±5% Ce^{3+} at 1773 K. When the sample was cooled to 1073 K the edge position changed back to higher photon energy, reaching -3.05 eV, which is equivalent to 49±5% Ce^{3+}. Switching from argon to carbon dioxide for 10 min at 1073 K did not affect the spectra, indicating that the redox reaction of reduced Zr50CS with carbon dioxide to form carbon monoxide and oxidized $Ce_{0.5}Zr_{0.5}O_{2-\delta}$ was very slow. Figure 5.6 b) shows isothermal carbon dioxide splitting at 1773 K in a half period of 10 minutes. Heating from 1073 to 1773 K in a flow of argon led to the maximum recorded edge shift, -3.3 eV (53±5% Ce^{3+}) after 20 min at 1773 K. The reversible energy shift during isothermal switches between argon and carbon dioxide amounted to approximately 0.6 eV, indicating oxygen uptake and concomitant formation of carbon monoxide in the oxidation step as well as oxygen release in the reduction step. About 9±5% of the cerium atoms changed valence from 4+ to 3+ and vice versa during isothermal looping. After three cycles there was only a slight drift to lower non-stoichiometry. Figure 5.6 gives the temperature, feed gas and oxygen MS signal during the Zr K edge XAS measurements performed on the same sample directly after the Ce K edge measurements. Zr50CS was already in a highly reduced state before measurements at the Zr K edge, which was also reflected in the negligible amount of oxygen released during heating from room temperature to 1773 K in a flow of argon. Figure 5.7 a) and b) shows spectral changes upon heating the reduced Zr50CS in a flow of argon, which led to higher intensity of the pre-edge feature A, lower intensity of features B and C and higher intensity of feature D. Figure 5.7 c) and d) shows spectra recorded during cooling from 1773 to 1073 K, indicating that these changes were reversible and originated from temperature effects.

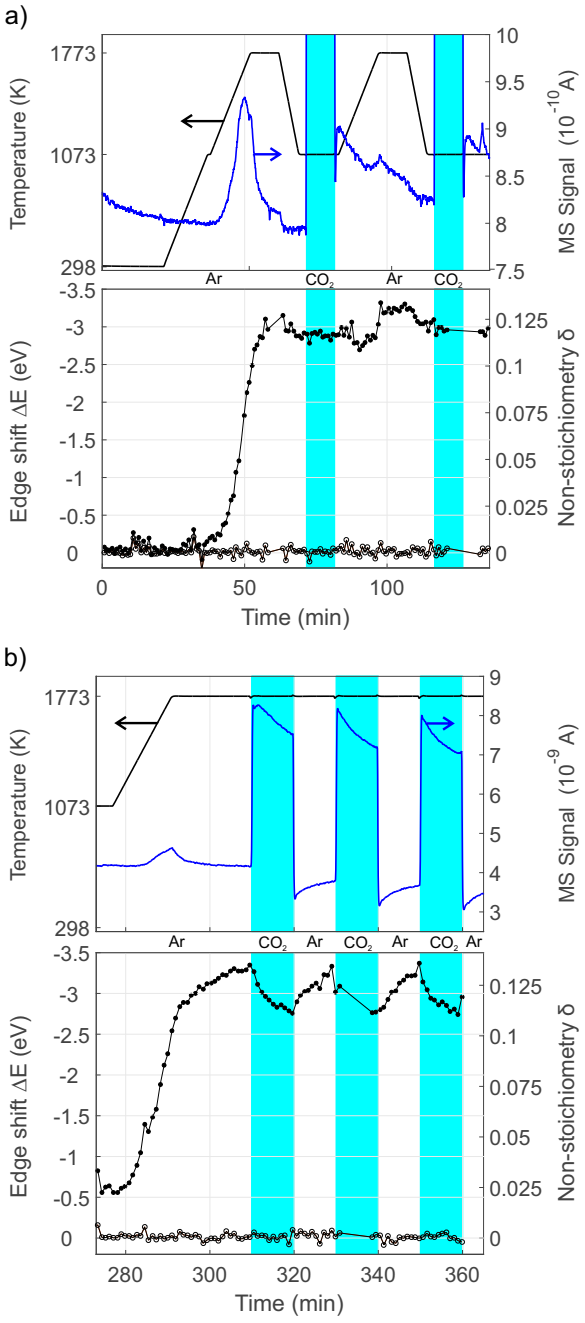

Figure 5.5 Quantification of the Ce K edge shift during carbon dioxide splitting, a) temperature swing from 1773 K to 1073 K and b) isothermally at 1773 K. Top panels show the thermochemical looping conditions: the furnace temperature, MS signal of oxygen (m/z =32), and feed gas (argon (white), carbon dioxide (blue)). The bottom panels show the shift in the Ce K edge energy and related non-stoichiometry in $Ce_{0.5}Zr_{0.5}O_{2-\delta}$. Filled symbols: Zr50CS, open symbols: ceria reference spectra after energy alignment.

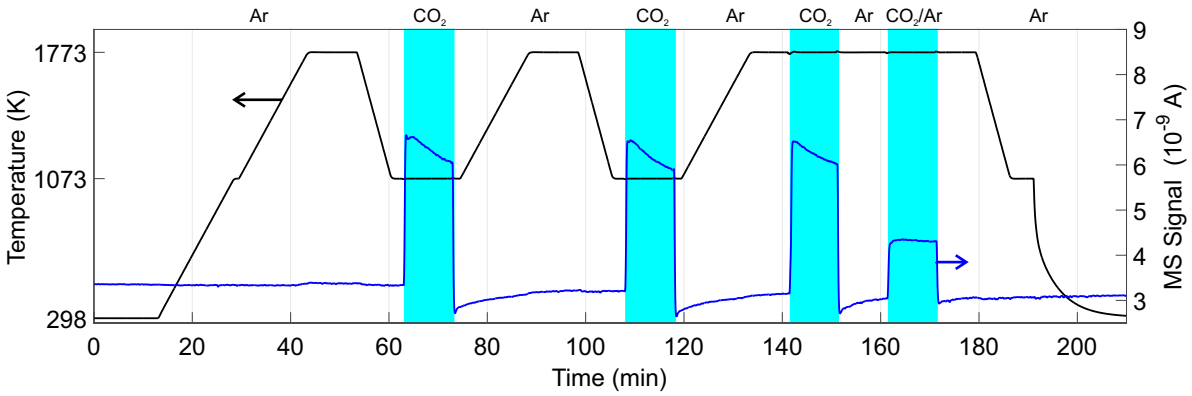

Figure 5.6 Thermochemical cycling while measuring Zr K edge in situ XAS of Zr50CS: furnace temperature, MS signal of oxygen (m/z = 32), and gas atmosphere (argon (white), carbon dioxide (blue)). In the last oxidation step at 1773 K the composition of the feed gas was 50% carbon dioxide/argon.

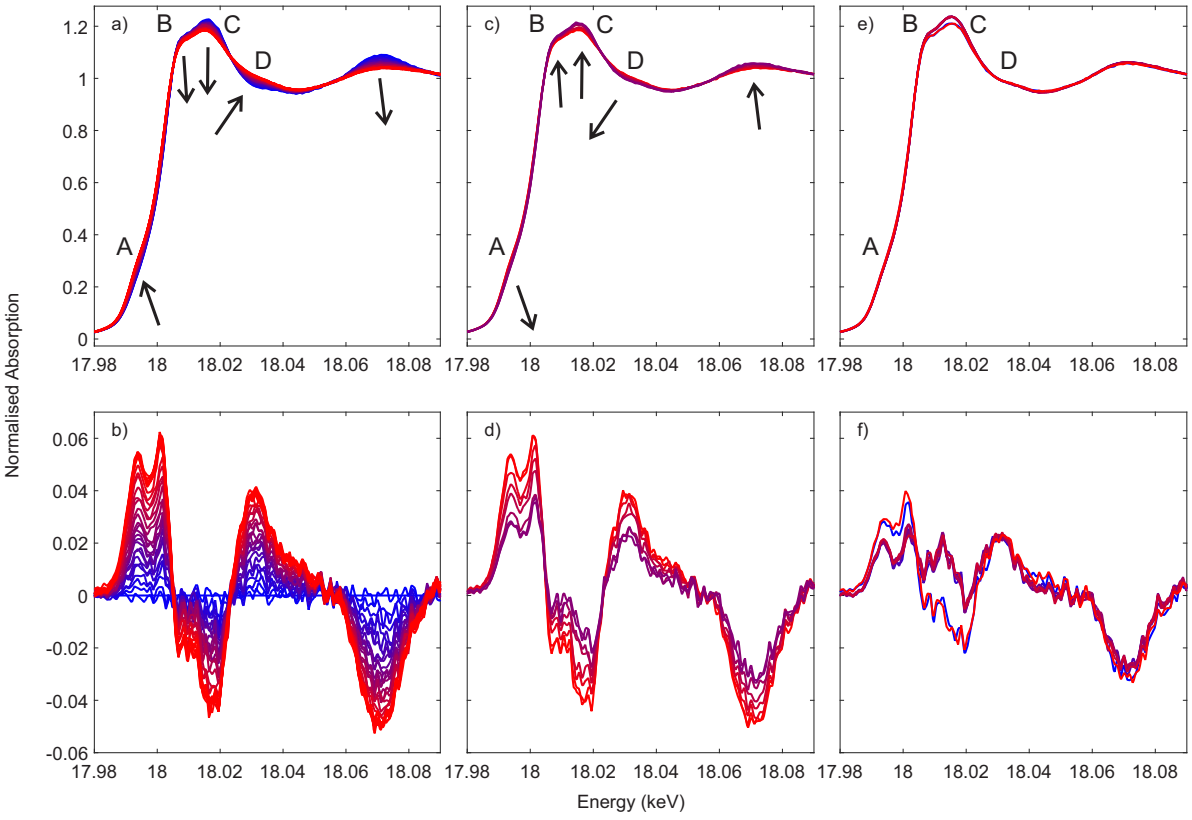

Figure 5.7 Zr K edge XANES of reduced Zr50CS recorded in a flow of argon during heating from room temperature to 1773 K (a) and b)), cooling from 1773 to 1073 K (c) and d)) and switching from argon to carbon dioxide and back at 1073 K (e) and f)). The bottom panels show difference spectra obtained by subtracting the first spectrum recorded at room temperature. Colors: see Figure 5.3. A-D identify spectral features.

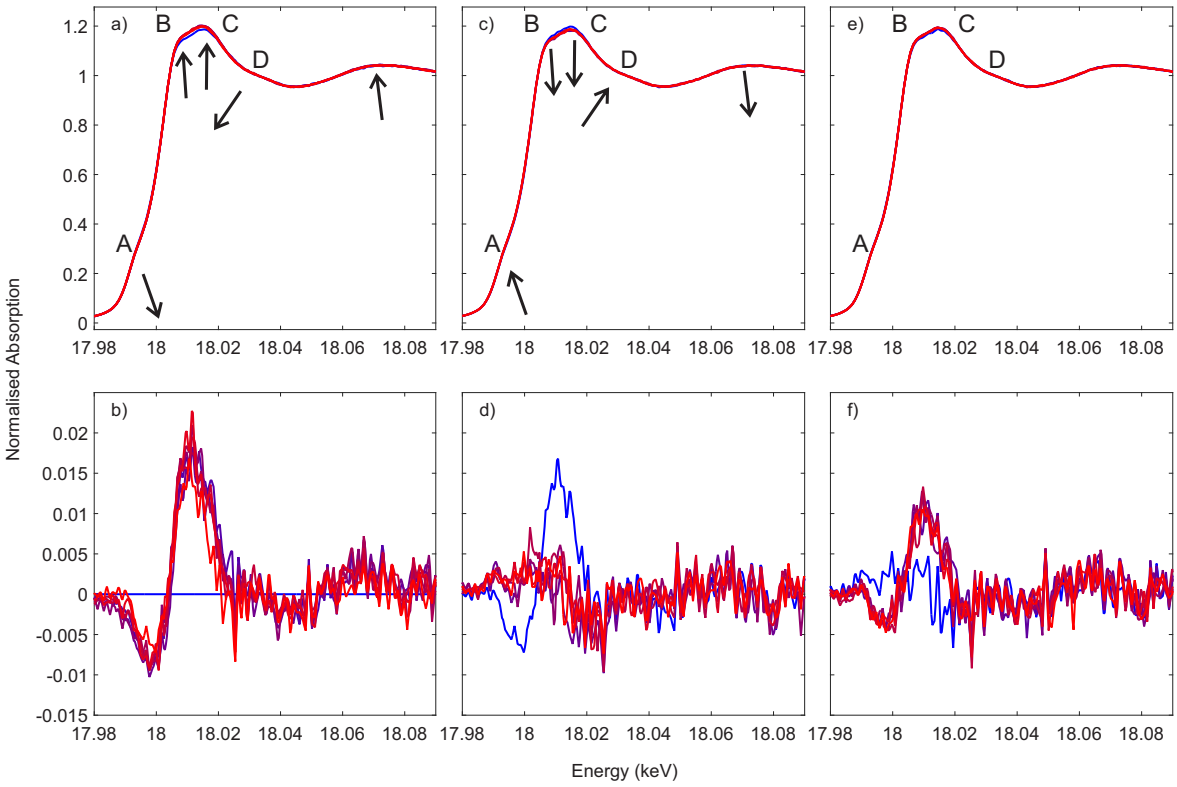

Figure 5.8 Zr K edge XANES of Zr50CS recorded during isothermal switches to a flow of carbon dioxide (a) and b)), a flow of argon (c) and d)) and a flow of 50% carbon dioxide/argon (e) and f)) at 1773 K. b) d) and f) show difference spectra obtained by subtracting a spectrum recorded in a flow of argon at 1773 K before the first switch of the feed gas to carbon dioxide. To highlight changes due to total absorption effects, the spectrum measured before switching the gas was included as the first in a series (blue). Capital letters A-D identify spectral features.

The Zr K edge spectra were strongly affected by the difference in the total absorption of argon and carbon dioxide. Figure 5.7 e) and f) shows a series of spectra recorded in carbon dioxide, including the first (blue) and last (red) spectra recorded in argon before and after exposure to carbon dioxide. Spectra recorded in argon were almost identical, indicating that after exposure to carbon dioxide at 1073 K for 10 min there were no structural changes. Spectra recorded in carbon dioxide were essentially the same and showed only minute changes in the intensity of features A, B and C. The oxidation at 1073 K did not change the valence of cerium. Therefore, the differences between spectra recorded at 1073 K in argon and carbon dioxide shown in Figure 5.7 e) and f) are likely to be artefacts. Figure 5.8 a) c) and e) shows Zr K edge spectra of Zr50CS recorded during isothermal carbon dioxide splitting at 1773 K. Figure 8 b) d) and f) show difference spectra that were obtained by subtraction of a spectrum recorded in argon after

reduction and highlight the minute differences upon changing the gas feed. The first spectrum of each series was recorded before the switch (blue). Figure 5.8 a) and b) shows the switch from a flow of argon to a flow of carbon dioxide, Figure 5.8 c) and d) the switch from a flow of carbon dioxide to a flow of argon and Figure 5.8 e) and f) the subsequent switch from a flow of argon to a flow of 50% carbon dioxide/argon. Contrary to Ce K edge XANES, there were no significant gradual changes upon exposure to carbon dioxide. There was no clear trend due to noise in the spectra collected in carbon dioxide and argon. Furthermore, in a 50% mixture of carbon dioxide and argon there were no gradual changes indicating structural changes linked to the cerium redox process. Comparison of the spectra in Figure 5.8 a) and b) that were recorded in 100% carbon dioxide with those in Figure 5.8 e) and f) that were recorded in 50% carbon dioxide reveal similar trends. This suggests the presence of total absorption effects. The absence of a shift in the Zr K edge energy indicates that unlike cerium, all zirconium remains in a formal 4+ oxidation state and that the local structure of zirconium hardly changes. At the Ce K edge, the differences in total absorption between a reactor filled with argon or carbon dioxide was negligible at 1773 K. The shifts in the edge position were not related to total absorption: MS shows that 98% of the gas was exchanged within less than one hot minute. Furthermore, there were no visible changes between spectra recorded in argon and carbon dioxide at 1073 K. Ce K edge XAS data confirm that the sample was already reduced at the beginning of measurements at the Zr K edge and, thus, spectral features linked to structural changes related to the valence of cerium are absent. Figure 5.9 displays Zr K edge XANES spectra and their first derivatives of Zr50CS and Zr20CS recorded at room temperature, before and after thermal reduction in a flow of argon at 1773 K. The spectra of reduced Zr50CS were taken after the Ce K edge measurements in the in situ experiment (vide supra). Zr20CS was reduced for 1 min at 1773K, and spectra after cooling to approximately 353 K were available. Feature A was more pronounced in the spectra of oxidized Zr50CS than in the spectra of reduced Zr50CS. Spectra of the latter two exhibited lower intensity in feature A when compared to spectra of both reduced and oxidized Zr20CS. After oxidation, feature B decreased and feature C shifted to higher photon energies higher intensity. The intensity of feature D was lower in the spectra of reduced than in the spectra of oxidized materials.

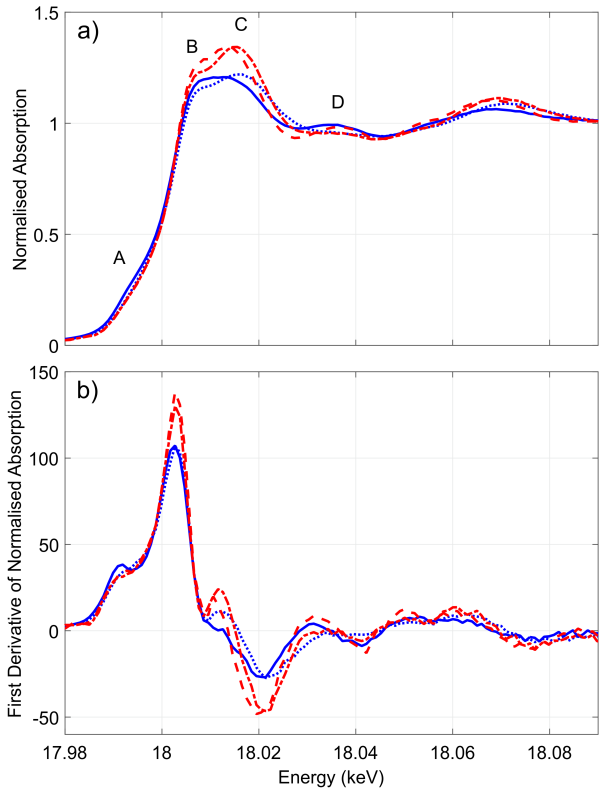

Figure 5.9 Zr K edge XANES a) and first derivatives b) spectra of Zr50CS and Zr20CS collected at room temperature before and after reduction at 1773 K in a flow of argon.: Zr50CS oxidized (solid blue line); Zr50CS reduced (dotted blue line); Zr20CS oxidized (dashed red line),: Zr20CS reduced (dash-dotted red line). A-D identify spectral features.

5.3 Discussion

Comparison of the diffraction patterns of Zr20C and Zr50C with Zr0C in Figure 5.1 a), b) and c) shows that the peaks in the diffraction pattern of Zr20 and Zr50 are broader and asymmetric. The shift in the first reflection to higher scattering angles with increasing zirconium content as well as the absence of reflections of other phases show that the calcined powders consist of a well-mixed homogeneous solid solution. The Zr50C patterns are more symmetric than the Zr20C peaks, which might be due to the less homogeneous phase composition in Zr20C. Broader peaks in Zr50C compared to Zr20C indicate a smaller particle size in Zr50C. The detection of tetragonal phases is hampered by the broadening of reflexes due to small crystallites20. In Zr20CS, the reflections are symmetric, indicating the formation of a single, homogeneous, fluorite-type phase. The pattern of Zr50CS shows features characteristic of tetragonal symmetry.

The tetragonal t" type can be derived from the fluorite type structure by a displacement of oxygen atoms in the c-direction of the cubic unit cell. By elongation of the cubic unit cell in the c direction, the t' tetragonal type is derived. The displacement of oxygen atoms causes a very weak reflection due to the relatively low scattering cross section of oxygen. It corresponds to the 112 lattice plane in the pseudocubic lattice and the 102 lattice plane in the tetragonal lattice[183] and its intensity increases with increasing zirconia content.[290] Figure 5.2 is a close-up of the pattern of Zr50CS and shows that the reflection was detected at $2\theta = 41.79°$. In contrast, in the pattern of Zr20CS, the reflection is absent. The apparent splitting of reflections into two peaks is evident in the pattern of Zr50CS. Acunas et al.39 investigated compositionally homogeneous 50/50 ceria-zirconia nanopowders and reported one asymmetric peak of the 004 and 400 pseudo-fluorite reflections. The pattern of Zr50CS shows clearly separated peaks at $2\theta = 70.93°$ and 71.55°, respectively. Lamas et al. reported clearly separated peaks in a 15/85 ceria-zirconia nanopowder.[290] The oxygen displacement and c/a ratio in a pseudocubic lattice are larger in bulk compared to nanosized materials.[171] Reflections in the XRD pattern of the $\kappa - Ce_2Zr_2O_8$ phase ($Ce_{0.5}Zr_{0.5}O_{2-\delta}$,$\delta = 0$) that were assigned to cation ordering[179,291] are absent. Sintering in air, an oxidizing environment, prevented formation of the pyrochlore $Ce_2Zr_2O_7$. The ordered pyrochlore superstructure transforms to a disordered fluorite-type structure when exposed to oxygen at 1373 K.[292] Based on in-depth knowledge of the preparation method the initial non-stoichiometry δ of the sintered pellet at the beginning of the in situ experiment is assumed zero. The extent of the changes in Ce K edge XAS spectra are linked primarily to the amount of oxygen that is released upon thermal reduction at 1773 K in a flow of argon.[240] Figure 5.10 illustrates the isothermal section of the $Ce_{1-x}Zr_xO_{2-\delta}$ system at 1773 K represented in the ternary CeO_2-$CeO_{1.5}$-ZrO_2 phase diagram calculated based on CALPHAD.[172] The red dotted line indicates the possible compositions of Zr50CS during oxygen release and uptake. During isothermal thermochemical carbon dioxide splitting at 1773 K the most reduced state of Zr50CS is located in the two-phase region indicating the presence of the fluorite-type and pyrochlore phases, while the most oxidized state falls into the single cubic phase region. The phase diagram predicts the presence of a single cubic phase for the Zr20CS at 1773 K during thermochemical looping. At lower temperatures, the cubic, single-phase regime is considerably smaller.[172] The attempt to oxidize the sample at 1073 K in carbon dioxide was unsuccessful due to the unfavorable geometry of the pellet with a low surface area and the surface reaction rate combined with lower thermodynamic driving forces and potential diffusion limitation. There is an obvious

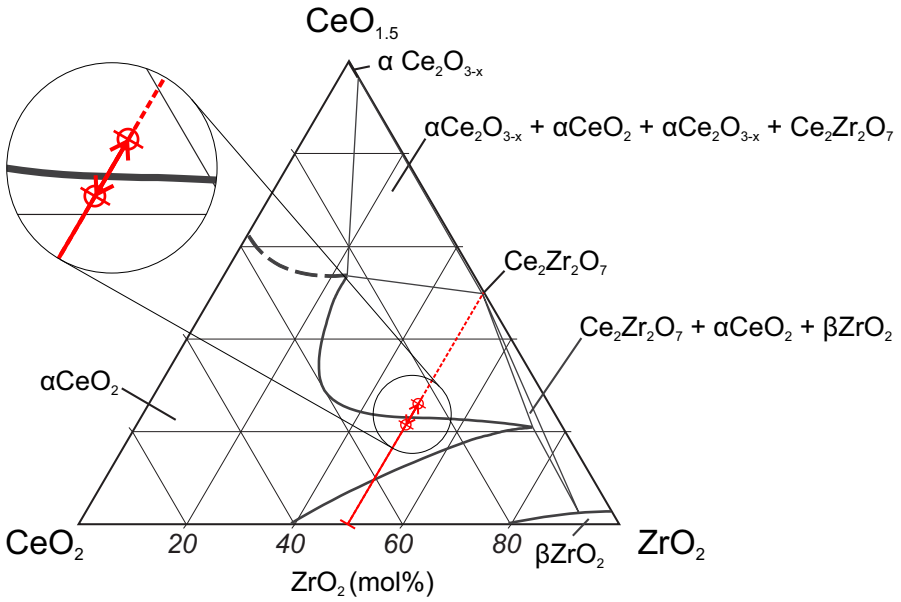

Figure 5.10 Isothermal section of the $Ce_{1-x}Zr_xO_{2-\delta}$ system at 1773 K reproduced from Lebrun and Perrot.[173] The dashed red line indicates $Ce_{0.5}Zr_{0.5}O_{2-\delta}$ for all compositions $0 \leq \delta \leq 0.25$. The solid red line represents the non-stoichiometry accessed in the in situ XAS experiment using Zr50CS. The red arrows indicate the path from the highest to the lowest oxygen uptake during isothermal thermochemical looping at 1773 K as determined by in situ XAS at the Ce K edge (see Figure 5.4 and Figure 5.5 b)).

relationship between the intensity of spectral features and the argon concentration (total absorption). This is also confirmed by a linear combination fit using two components, a spectrum of reduced Zr50CS collected at 1773 K after 10 min in a flow of argon and after oxidation in a flow of carbon dioxide, respectively (See Figure 5.11).

Evidence of gradual changes in the oxygen coordination of zirconium is absent in Zr K edge XANES recorded in both argon and carbon dioxide at 1773 K shown in Figure 7 and Figure 8. Differences in the spectra are due to temperature effects or artefacts related to changes in the total absorption. Changes in the oxygen coordination geometry by switching from a flow of argon to a flow of carbon dioxide were, therefore, not observed. At least four spectral features in the Zr K edge edge XANES (Figure 9) indicate differences between the structures of the oxidized and reduced materials. The pre-edge feature A on the rising absorption edge of the Zr K-edge is assigned to a 1s-4d transition[293] that is stronger when the oxygen coordination deviates from centrosymmetry, as is the case in tetragonal zirconia. In tetragonal $Ce_{0.5}Zr_{0.5}O_2$ feature A is pronounced and almost identical to the feature in 1 mol% Y_2O_3 doped zirconia.[204] In oxidized Zr50CS the intensity of feature A is higher than in reduced Zr50CS, oxidized

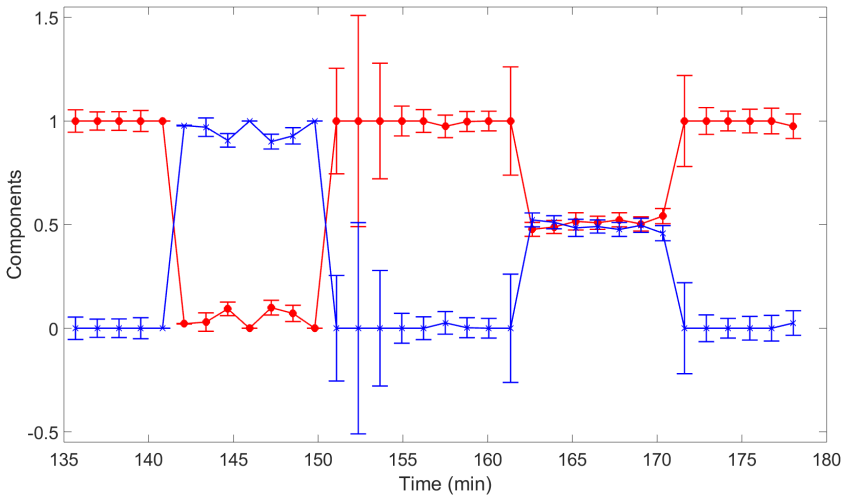

Figure 5.11 Linear combination fit of reduced (red) and oxidized (blue) Zr K edge XANES (data range -20 to 30 eV relative to the edge position). The most reduced state of the first reduction (at 139 min) and the most oxidizing conditions (at 150 min) serve as fitting standards. The weights were forced to sum to 1. There are no gradual changes upon oxidation, as observed in the Ce K edge data (edge shift). Reduction was performed in a flow of argon; the first oxidation was performed in a flow of 100% carbon dioxide and the second oxidation in 50% carbon dioxide/argon.

Zr20CS and reduced Zr20CS, indicating that the average crystal structure deviates from centrosymmetry. Upon the first release of oxygen, the feature is considerably smaller, similar to the Zr K XANES of fluorite-type $\kappa - Ce_2Zr_2O_8$ spectra reported by Yamamoto et al.[180] Contrary to Zr50CS, the spectra of Zr20CS shows a very weak feature A significant changes related to oxygen release, indicating only minute changes in the Zr-O coordination. Zr20CS is very similar to that of reduced Zr50CS. Characteristic XANES spectra[293] show differences in the main absorption peak of the Zr K XANES in zirconia polymorphs. Two peaks, B and C, reveal the split in the main absorption peak. The spectrum of the cubic structure with the absorption maximum in feature C clearly appears at higher energies. In contrast, in a structure deviating from centrosymmetry, feature B is more intense and observed at lower energies close to the absorption edge. This feature is clearly linked to spectra of reduced and oxidized Zr50CS and Zr20CS. The double-peak feature is more pronounced in Zr20CS both before and after oxygen release, indicating the cubic nature of the crystal lattice, in line with the XRD patterns of the oxidized materials. In addition, the intensity of feature D, reported by Li et al.[293] are in agreement with the intensity of features A, B and C. Thus, all features validate the tetragonal nature of the local environment of Zr in oxidized Zr50CS and they indicate the presence of a more cubic-like structure after exposure to reducing conditions

at 1773 K. XAS indicates that the average structure thus changes from that dominated by the structure depicted in Figure 1 b) to an average structure which is more a more centrosymmetric and cubic, as is the case in the model structures depicted in Figure 1 c) and d). XRD and Zr K-edge XANES suggest the presence of the tetragonal phase in the sintered Zr50CS before thermal reduction. Unlike cerium, zirconium remained in a formal +4 oxidation state, irrespective of oxygen uptake and release because there is no shift in the energy of the Zr K edge position upon reduction and oxidation. After thermal reduction and redox cycling under isothermal conditions at 1773 K, features in the Zr K edge XANES indicate a cubic structure. The maximum non-stoichiometry reached in argon at 1773 K corresponds to an intermediate phase with the composition $Ce_2Zr_2O_{7.5}$ ($\delta = 0.125$ in $Ce_{0.5}Zr_{0.5}O_{2-\delta}$).[180,291] The Zr K edge spectra did not show significant changes during thermochemical cycling at 1773 K, probably because the oxygen content was varied by only 9% of the theoretical maximum capacity of the pyrochlore-type κ phase. The difference in reactivity at 1073 K and 1773 K shows that the surface area of the sample was a limiting factor in the oxidation half-reaction. Once the material was reduced, the Zr K edge XANES did not show further changes related to structural properties. The phase diagram in Figure 10 suggests that fast cycling at 1773 K leads to a transition from the single-phase domain of the cubic fluorite-type structure to a two-phase region of cubic and pyrochlore-type phases. At lower non-stoichiometries, however, it is assumed that the formation of the tetragonal phase will form. It is unclear how fast cation ordering occurs in the material and whether those changes cause mechanical failure of $Ce_{0.5}Zr_{0.5}O_{2-\delta}$ structures in solar thermochemical looping reactors. It seems appropriate to use in situ XAS as well as in situ X-ray diffraction to determine ordering phenomena and structural changes in complex non-stoichiometric ceria-based systems at extreme temperatures.

5.4 Conclusions

Thermochemical looping entails complex structural changes in ceria-zirconia oxygen storage materials. We successfully collected time-resolved structural information about the electronic and local geometric structure of an equimolar ceria-zirconia solid solution $Ce_{0.5}Zr_{0.5}O_{2-\delta}$ using both Ce and Zr K edge XAS under realistic solar thermochemical reactor conditions. The Ce K edge XANES allows quantification of the oxygen storage capacity. The Zr K edge, by contrast, is rich in features characteristic of the nature of the zirconium-oxygen coordination geometry. Upon reduction by heating oxidized

$Ce_{0.5}Zr_{0.5}O_{2-\delta}$ from room temperature to 1773 K in a flow of argon the centrosymmetric and cubic contributions to the average structure increase. The zirconium-oxygen coordination geometry becomes more similar to that of $Ce_{0.8}Zr_{0.2}O_{2-\delta}$. Gradual shifts in the edge position of the Ce K absorption edge were evident in argon and carbon dioxide at 1773K, indicating a change in the oxidation state of cerium upon release and uptake of relatively small amounts of oxygen. In the Zr K edge spectra, there were no detectable changes in features characteristic of the oxygen coordination geometry. Reoxidation was not observed at 1073 K in a flow of carbon dioxide. Thermochemical cycling of$Ce_{0.5}Zr_{0.5}O_{2-\delta}$ at 1773 K did not lead to detectable structural changes in the oxygen coordination geometry around zirconium, indicative of the centrosymmetric geometry of the cubic structure.

Chapter 6

Structural Changes in Equimolar Ceria-hafnia Materials Under Solar Thermochemical Looping Conditions: Formation and Stability of the Pyrochlore Structure

based on:
Rothensteiner, M., Bonk, A., Vogt, U. F., Emerich, H., and van Bokhoven J.A. "Structural changes in equimolar ceria-hafnia materials under solar thermochemical looping conditions: cation ordering, formation and stability of the pyrochlore structure" (submitted)

M.R. contributions: concept, applied for beam time, planned and performed in situ XAS, XRD and XAS/XRD experiments, processed and analyzed the data, wrote the manuscript.

6.1 Introduction

In the previous chapter, the structural changes in equimolar ceria-zirconia materials with an initially random arrangement of cerium and zirconium cations were determined under solar thermochemical reaction conditions by in situ XAS. Mapping the composition determined by Ce K edge XAS in the phase diagram[172,173] suggests that the cubic structure is in equilibrium with the pyrochlore structure. Little is known about the pyrochlore phase of ceria-zirconia and ceria-hafnia at high temperature and its water and carbon dioxide splitting capability. Thermogravimetric analysis, in situ and ex situ XRD, in situ Ce K edge XANES and Hf K edge XANES and EXAFS analysis were carried out to determine the properties of cation-ordering in equimolar ceria-hafnia compounds and its potential application as oxygen storage material for two-step thermochemical fuel production.

6.2 Results

Sample preparation

Samples Hf10C ($Ce_{0.9}Hf_{0.1}O_2$), Hf20C ($Ce_{0.8}Hf_{0.2}O_2$) and Hf50C ($Ce_{0.5}Hf_{0.5}O_2$) were synthesized using the polymerized complex method and calcination (C) at 973 K in air. Figure 6.1 presents XRD patterns of samples that were collected after calcination (C) at 973 K as well as after sintering (S) pressed pellets in air at 1873 K. The XRD patterns of the calcined materials indicated the fluorite-type crystal structure of ceria. The peaks were substantially broadened due to the small crystallite size that is obtained with the polymerized-complex method. Reflections of phases other than the fluorite-type were not detected. In the diffraction pattern of calcined Hf10C and Hf20C, the positions of the peaks were very similar, while the peak positions in the diffraction pattern of calcined Hf50C were shifted to higher angles, indicating a contraction of the lattice with increasing hafnia content. The diffraction peaks of calcined Hf20C were more asymmetric than those of calcined Hf10C and Hf50C. Peak broadening was most pronounced in the diffraction pattern of calcined Hf50C. In the diffraction patterns of calcined Hf10C and Hf20C, the widths of the reflections were very similar. While all reflections of sintered Hf10CS and Hf20CS could be assigned to the fluorite-type crystal structure, a large number of weak reflections below 10 % normalized intensity were observed in the diffraction pattern of sintered Hf50CS, all of which could be assigned to monoclinic and ortorhombic hafnia. In the diffraction pattern of sintered Hf50CS, the

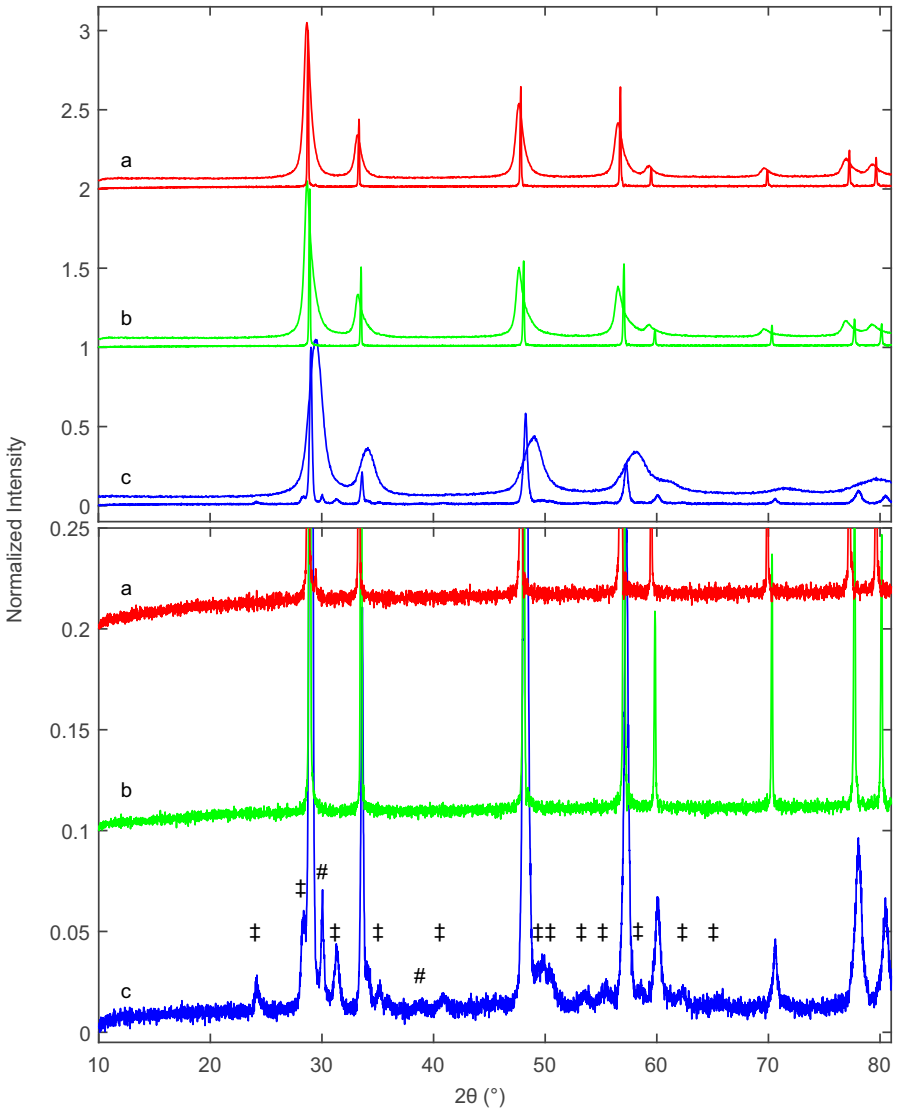

Figure 6.1 XRD patterns of a) Hf10C and Hf10CS, b) Hf20C and Hf20CS, c) Hf50C and Hf50CS prepared by polymerized complex method, calcination (C) at 973 K in air and after subsequent sintering (S) of a pressed pellet at 1873 K in air. Diesis (‡) indicate reflections of monoclinic HfO_2 and the octothorp (#) mark peaks assigned to monoclinic and/or orthorhombic HfO_2.

normalized intensity of the reflections indicating the cubic ceria lattice were asymmetric, smaller and significantly broader than those in the patterns of sintered Hf10CS and Hf20CS. Reflections indicating the pyrochlore structure were not detected.

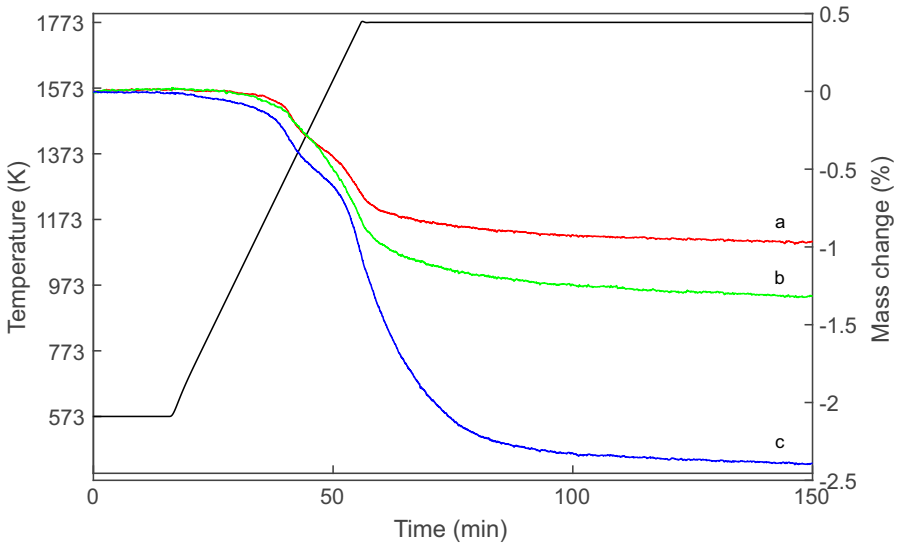

Figure 6.2 Relative mass change of a) Hf10 b) Hf20 and c) Hf50 by heating to 1773 K in a flow of argon. The samples were oxidized in air at 973 K before thermal auto-reduction. The mass losses leveled out after about 100 min at 1773 K.

Thermogravimetric analysis

Figure 6.2 shows the mass loss of the three samples determined by thermogravimetric analysis during heating to 1773 K in a flow of argon. The oxygen release profiles of Hf10C and Hf20C were very similar: auto-reduction started at about 1173 K and weight loss occurred in two steps. Before and at the first decrease of weight at intermediate temperature, the auto-reduction profiles of Hf10C and Hf20C overlapped. The mass change of Hf20C was higher than Hf10C at the second step at higher temperature. Hf50C also showed two steps in oxygen release, however, the onset of auto-reduction occurred already at about 573 K. The weight loss profile of Hf50C was similar to Hf10C and Hf20C at temperatures up to about 1173 K but at higher temperatures a substantially larger quantity of oxygen was released at a higher rate. The mass loss of all three samples leveled out when they were kept at 1773 K after about 100 minutes and remained unchanged during subsequent cooling to 573 K. Table 6.1 reports the weight changes and composition of the auto-reduced materials assuming 1) complete oxidation of the pristine material and 2) attribution of weight loss solely to the release of oxygen. While the composition of Hf10CT Hf20CT is typical of nonstoichiometeric fluorite-type ceria, that of Hf50CT suggests changes in the crystal structure and complete reduction of cerium from Ce^{4+} to Ce^{3+}.

Figure 6.3 displays XRD patterns of the ceria-hafnia materials after the thermal auto-

Sample after autoreduction (T)	weight change (%)	Composition
Hf10CT	-0.97	$Ce_{0.9}Hf_{0.1}O_{1.89}$
Hf20CT	-1.32	$Ce_{0.8}Hf_{0.2}O_{1.85}$
Hf50CT	-2.38	$Ce_{0.5}Hf_{0.5}O_{1.72}$

Table 6.1: Weight loss and composition after auto-reduction (T) in a flow of argon at 1773 K. The entire mass loss was attributed to the release of oxygen and complete oxidation of the pristine material was assumed.

reduction (T). Auto-reduced Hf10 showed only the reflections of the fluorite-type phase, which indicates that hafnium ions were well dispersed/randomly distributed and that they substitute cerium ions in the fluorite-type lattice. Thermal reduction of the materials with higher hafnium content gave rise to additional, very weak reflections with normalized intensities below 0.03, which indicate the ordering of cations in pyrochlore-type and pyrochlore-related crystal structures. The peak positions were located at slightly higher angles than that in literature data based on XRD[178] and neutron diffraction[221] of pyrochlore-type ceria-zirconia. The main component of Hf20CT is a fluorite-type solid solution, however also some reflections indicating the presence of a cation-ordered phase were found. The fluorite-type phase in Hf20CT had a slightly smaller lattice parameter than that of Hf10CT, indicated by a shift to higher angles. Reflections assigned to the cation-ordered phase of auto-reduced Hf20CT were less intense and appeared at lower angles than corresponding reflections in the diffraction pattern of Hf50CT. The reflections arising from cation ordering in the diffraction pattern of Hf50CT were sharp, and in contrast to the diffraction pattern of Hf20CT, most reflections of the pyrochlore crystal structure were observed. Peaks close to the (220), (620), (642), (733), (660)(822), (751)(555) reflections of $Ce_2Zr_2O_7$ reported[178] at 2θ = 23.39, 53.91, 64.86, 71.85, 74.9 and 76.73° could not be distinguished from noise. In the diffraction pattern of Hf50CT, the intensity of the (331) reflection was 90% more intense and the (331) reflection 98% less intense than the corresponding reflections[178] in the diffraction pattern of $Ce_2Zr_2O_7$. Reflections close to those of the $Ce_2Zr_2O_{7.5}$ phase at 2θ = 16.65 and 51.49° (the (200) and (600) reflections, respectively)[178] were not detected. However, the asymmetry of the reflections related to the cubic lattice planes suggests partial re-oxidation to $Ce_2Zr_2O_{7+x}$. Reflections of the hexagonal Ce_2O_3 phase were absent. Very weak reflections at $2\theta \approx 31°$ indicated the presence of a very small amount of monoclinic or orthorhombic hafnia. Corresponding reflections of cubic lattice planes of the cation-ordered structure appeared at higher angles relative to the fluorite-type lattice of Hf10CT and Hf20CT, indicative of a smaller lattice parameter in auto-reduced Hf50CT. Peaks in the pattern of Hf50CT

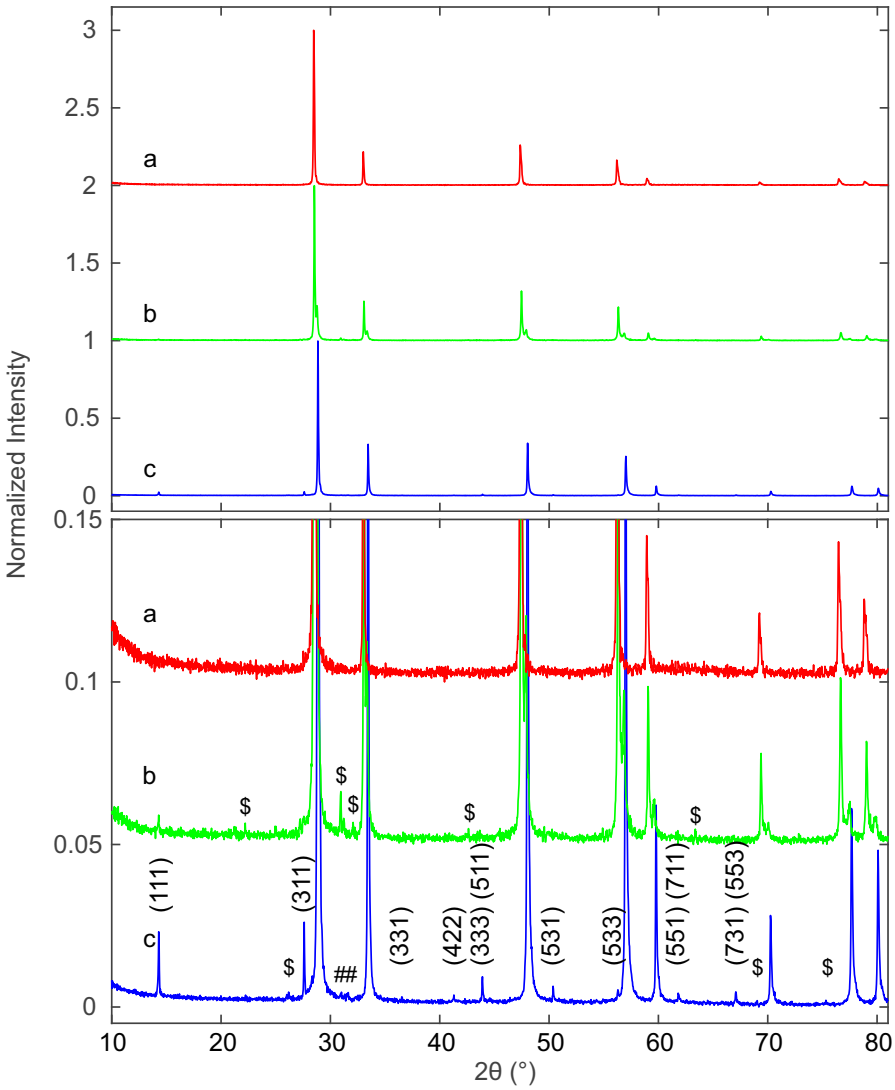

Figure 6.3 XRD patterns of a) Hf10CT b) Hf20CT and c) Hf50CT after thermal auto-reduction (T) of the calcined materials in a thermogravimetric analyzer at 1773 K. The close-up highlights weak reflections that could be assigned to lattice planes with Miller indices (hkl) of the pyrochlore phase, which were assigned based on crystal structure data of the ceria-zirconia system.[221] Octothorps (#) mark peaks close to the position of the (111) reflection of monoclinic and the (121) reflection of orthorhombic HfO_2. Dollar signs ($) indicate peaks without clear assignment.

were asymmetric with a tail at the higher 2θ side.

In situ XAS at the Ce K edge

Figure 6.4 shows time resolved Ce K edge XANES spectra that were collected during the auto-reduction (R) of Hf50C in a flow of argon. The temperature was first ramped to

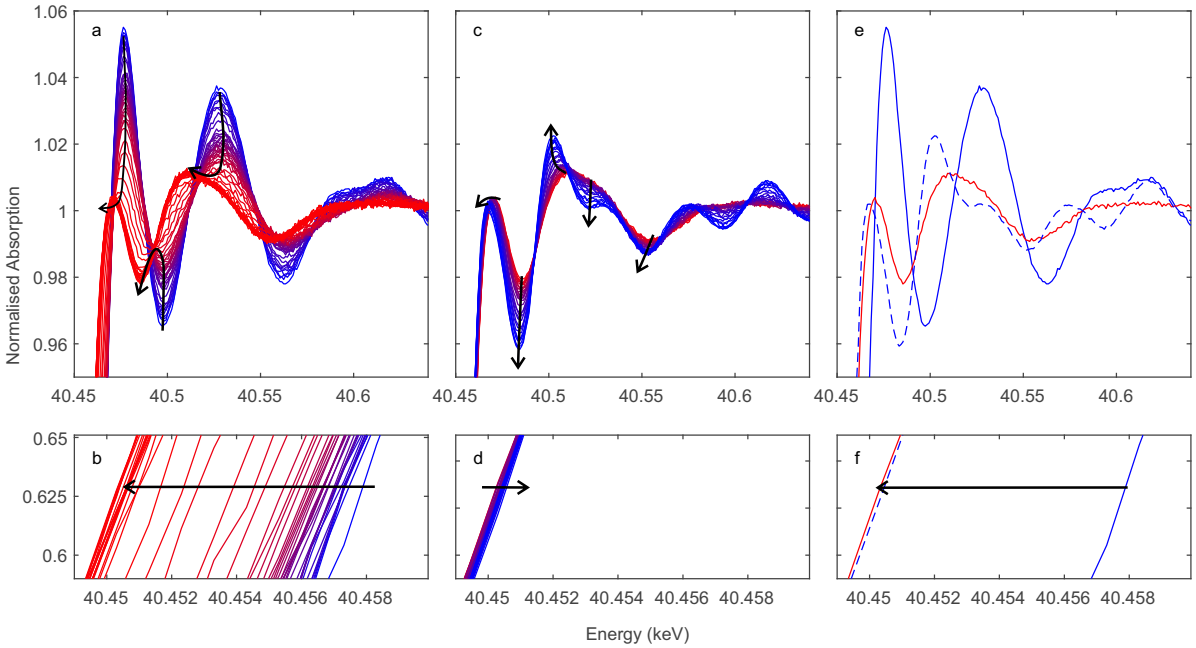

Figure 6.4 Time resolved, Ce K edge spectra recorded during auto-reduction of Hf50C by heating in a flow of argon (see Figure 6.5). Black arrows indicate changes of spectral features. Spectra in a) and b) were recorded during heating room temperature (blue) to 1773 K and at 1773 K (red); spectra in c) and d) during cooling from 1773 K (red) to room temperature (blue). Spectra in e) and f) were recorded at room temperature before (blue solid line) and after auto-reduction (blue dashed line) and at 1773 K before cooling (red). Correction by aligning reference spectra that were recorded simultaneously was not performed.

1773 K at 33.3 K/min, kept constant for 30 minutes before cooling to room temperature at the same rate, very similar to the TGA experiment presented above (see Figure 6.5 for more details). With increasing temperature, thermal damping lowered the amplitude of the absorption fine structure, which smeared spectral features related to structural changes. Except for a small discontinuity at ca. 873 K, the XANES features changed gradually. Figure 6.4 a) shows the drop in the intensity of the white line during heating. The white line intensity of the auto-reduced material changed only slightly upon cooling to room temperature, as depicted in Figure 6.4 c) and d). Only a minute shift in the energy of the Ce K edge position to higher energy was found during cooling. In the absorption fine structure, oscillation of higher frequencies compared to those in the spectrum of pristine, oxidised Hf50C emerged and the edge position was shifted to lower energy, indicating significant changes in the local geometrical and electronic structure of cerium in Hf50CR. Figure 6.5 presents the temperature profile and the mass spectrometer signals of oxygen and carbon dioxide of the temperature programmed auto-reduction of

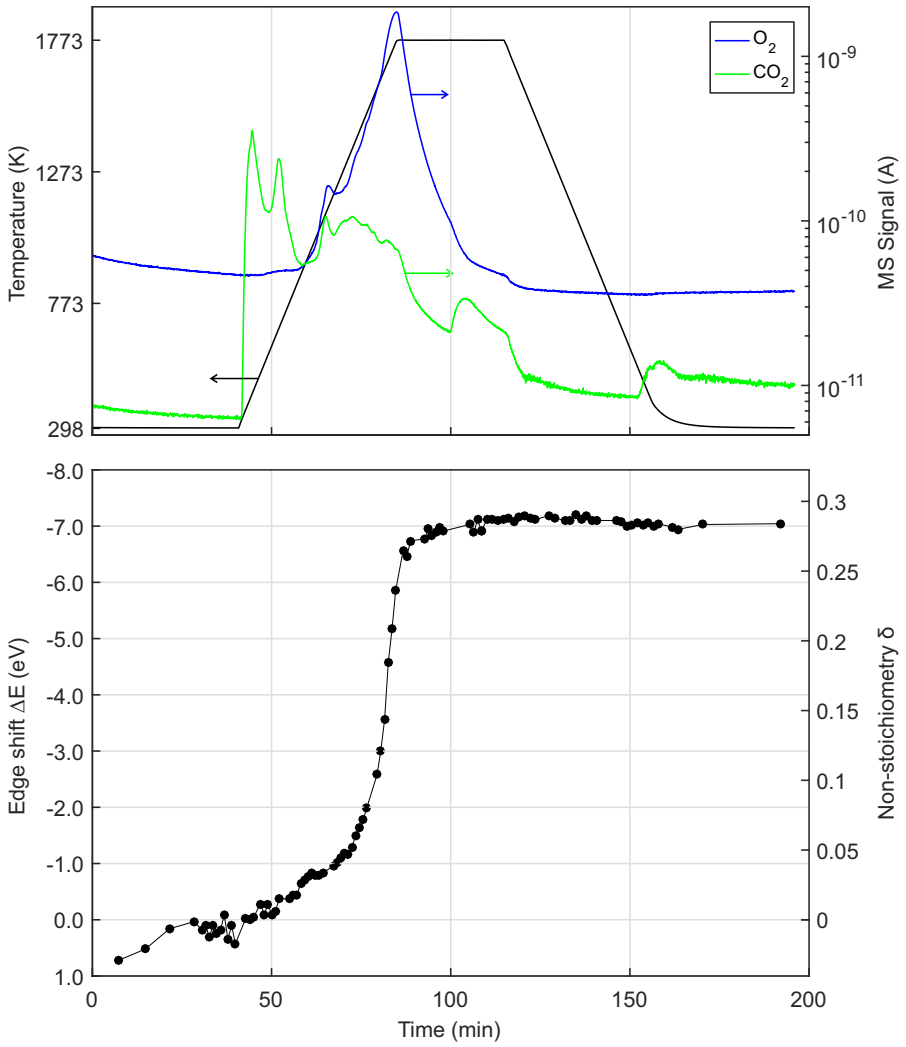

Figure 6.5 Time-resolved in situ XAS at the Ce K edge during temperature programmed auto-reduction of Hf50C in a flow of argon. a) temperature profile and the MS signals of oxygen (m/z = 32) and carbon dioxide (m/z = 44); b) Non-stoichiometry δ in $Ce_{0.5}Hf_{0.5}O_{2-\delta}$ determined by quantification of the shift in the energy of the edge position of Ce K edge spectra. Corrections by alignment of reference spectra was not performed.

Hf50 in the in situ XAS experiment. The oxygen trace (m/z = 32) was in good agreement with the derivative of the mass change in the TGA experiment presented in Figure 6.2. In both experiments, two maxima in the oxygen release rate were observed, the first maximum occurred at intermediate temperature and the second, absolute maximum when 1773 K was reached. The carbon dioxide signal indicated desorption from the sample and reactor walls, and to some extent also arose from carbon that was burned and thus obscured the release of oxygen. Unlike in the TGA experiment, a pre-treatment

of oxidation in air at 973 K and argon at 573 K before heating was not performed. Thus, the release or desorption of carbon dioxide from the sample and reactor started already at very low temperature. When the temperature was decreased, all oxygen released from the sample had been removed from the reactor because only a very small drop in the oxygen signal back to its baseline level occured. Figure 6.5 also shows the shift in the energy of the Ce K edge position that was quantified by interpolation at a constant normalized absorption of 0.633, and the corresponding value of the non-stoichiometry δ in $Ce_{0.5}Hf_{0.5}O_{2-\delta}$. In agreement with the MS signals, XAS indicated that auto-reduction to cerium(III) was virtually completed when the temperature reached 1773 K. The non-stoichiometry reached a maximum of 0.29 at 1773 K, and the mean value determined from the ten last spectra was 0.28 ± 0.04. This clearly indicated that during auto-reduction, cerium changed from Ce^{4+} to Ce^{3+}, which is required for the formation of the ceria-hafnia pyrochlore structure. The two peaks in the MS oxygen signal were not resolved as two inflection points in the curve of δ determined by XAS. The non-stoichiometry δ corresponds to the cumulative oxygen release and thus its temporal derivative gives the oxygen release rate, which is proportional to the oxygen MS signal.

Ce K edge EXAFS

EXAFS fitting of Ce K edge data collected at room temperature was complicated by a very strong and broad glitch that severely corrupted the signal. Figure 6.6 depicts the incident intensity I_0 as a function of the photon energy containing three strong glitches at 40.260, 40.578 and 40.787 keV. The glitch at 40.787 keV had a at FWHM of 12 eV. Figure 6.7 displays the Ce K edge EXAFS signals of pure ceria and ceria-hafnia that were recorded at different beam times. The main difference was the extent of monochromator detuning and the quality of the pellet. The glitch appears at k = 9.3 $Å^{-1}$ with different intensity. While the spectrum of Hf50C ($Ce_{0.5}Hf_{0.5}O_2$) appears normal, the contribution of the first oxygen shell of Hf50CR ($Ce_{0.5}Hf_{0.5}O_{1.75}$) consists of several peaks that are unusually broad and low in intensity. EXAFS analysis of the first oxygen shell of Hf50CR was not successful and might be related to the glitch. In the pyrochlore structure of ceria-zirconia,[221] the first cerium-oxygen coordination shell consists of eight atoms, six at a distance of 2.615 and two at a shorter distance of 2.326 Å. In pure ceria, the cerium-oxygen distance is 2.343 Å. The peak of the second coordination shell of cerium, consisting of cerium and hafnium atoms appears less affected by the glitch. Fitting the second peak was not attempted because of potential interference of the glitch. Truncating the data was not successful because the glitch is in the center of the EXAFS

range. In addition, thermal treatment often affects the quality of the pellets which is detrimental to the quality of the XAS signal. Thus, despite very good signal/noise ratios up to very high wave-numbers, reliable results from Ce K edge EXAFS were not accessible.

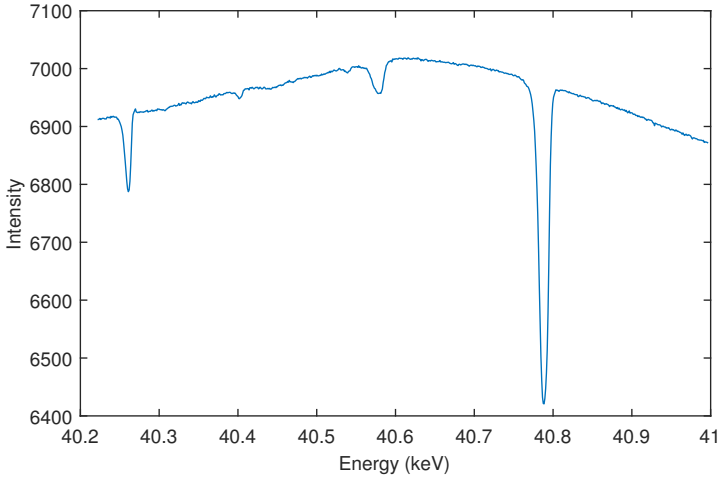

Figure 6.6 The incident photon intensity I_0 indicating a glitch above the Ce K edge that interfered with the Ce K edge EXAFS signal. The glitch was very broad and intense with a FWHM of 12 eV.

Hf K edge XANES

Immediately after measurements at the Ce K edge during auto-reduction of Hf50CR (see Figures 6.4 and 6.5), spectra were recorded at the Hf K edge at room temperature. Figure 6.8 presents Hf K edge spectra of Hf50C and Hf50CR, recorded before and after the in situ XAS auto-reduction experiment. In addition, it shows spectra of the reference material, hafnia powder that consisted of a mixture of monoclinic and orthorhombic phases. Spectral features were less pronounced in the spectrum of pristine Hf50C compared to the auto-reduced material mainly due to lower crystallinity and homogeneity of the powders compared to the dense ceramic body of auto-reduced Hf50CR. A spectral feature close to the absorption edge at a normalized absorption of 0.92 was most intense in hf50CR, less pronounced in the hafnia reference and even weaker in pristine Hf50C. The energy at the first maximum (white line) was the highest in the spectrum of Hf50CR. At energies higher than that of the white line, the largest amplitude of the fine structure was found in the spectrum of auto-reduced Hf50CR. The differences in the energy and intensity of the Hf K edge XANES features of Hf50C and Hf50CR suggest changes in the oxygen coordination geometry.

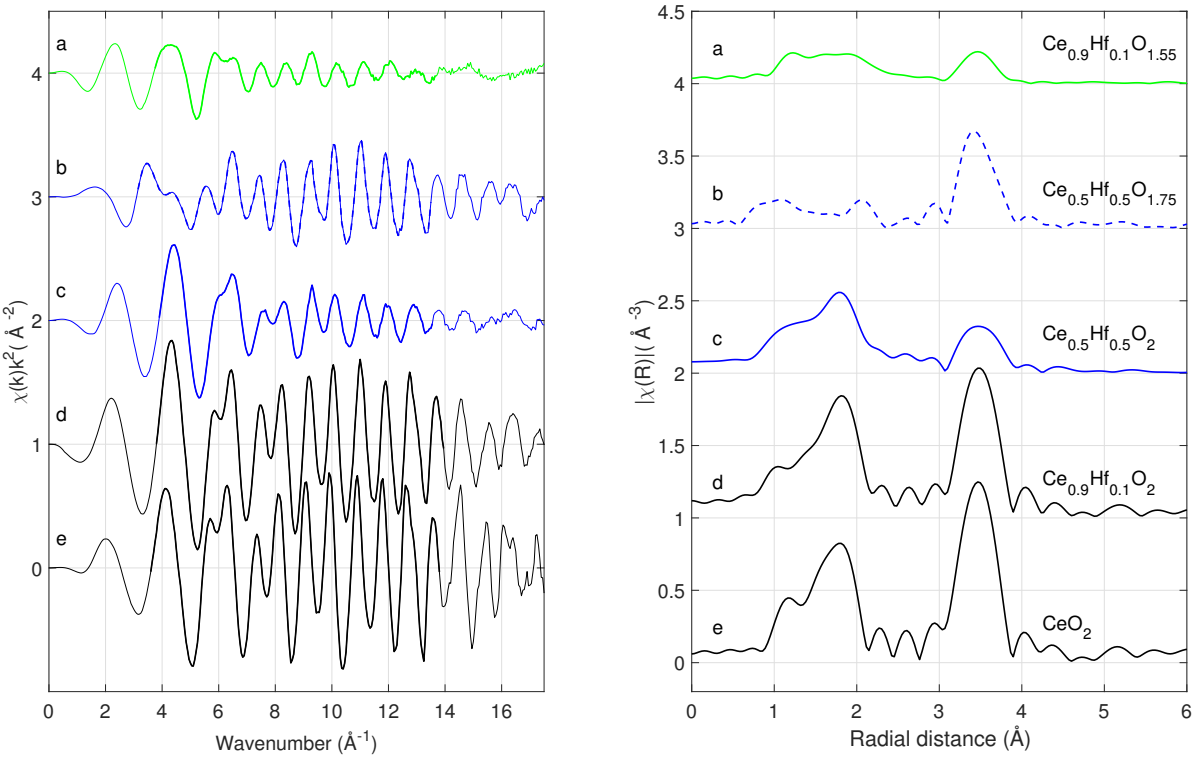

Figure 6.7 Ce K EXAFS of CeO_2, $Ce_{0.9}Hf_{0.1}O_2$, before and after reduction in a flow of hydrogen/helium ($Ce_{0.9}Hf_{0.1}O_{1.55}$, see Chapter 4), equimolar ceria-hafnia before and after thermal reduction at 1773 K in a flow of argon ($Ce_{0.5}Hf_{0.5}O_2$ and $Ce_{0.5}Hf_{0.5}O_{1.75}$). All spectra were recorded at RT. The bold lines indicate the data range used for Fourier-transformation of $\chi(k)$ to obtain the pseudo-radial distribution functions $\chi(R)$. The k-weight was two.

Hf K edge EXAFS

Figure 6.9 shows the Hf K edge EXAFS signals of Hf50C and Hf20C recorded before and after thermal reduction (see Figures 6.4 and 6.5). There were significant differences in the amplitude and the signal/noise ratio of the data. The EXAFS signal of auto-reduced Hf50C had the largest amplitude and the best signal/noise ratio. In the Fourier-transform of all spectra except that of calcined Hf50C, two main peaks could be identified, the first and most intense one originating from the first coordination shell of oxygen atoms and the second from the second coordination shell consisting of cerium and hafnium atoms at higher radial distance. Differences in the intensity of the peaks were caused by differnces in the crystallinity of the samples, which is much higher in the dense ceramic body of Hf50CR obtained after thermal treatment of Hf50C, which consisted of pressed powder. In the pyrochlore ceria-zirconia structure,[221] the first coordination shell

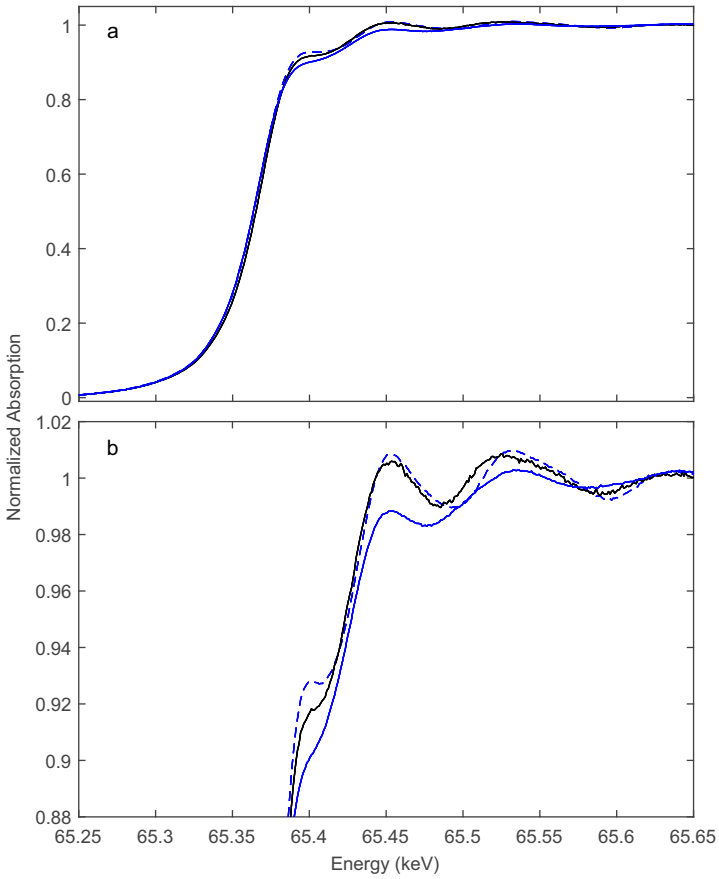

Figure 6.8 Hf K edge XANES recorded at room temperature. Hf50C (solid blue), auto-reduced Hf50CR (dashed blue) recorded in a flow of argon immediately after the experiment (see Figures 6.4 and 6.5), and hafnia reference (solid black). b) Close-up of the XANES region.

of zirconium consists of six oxygen atoms at a distance of 2.097 Å. Figure 6.10 presents a fit of the Hf K edge EXAFS of Hf50CR. The real part and the magnitude of the fit are in excellent agreement with the data, which is reflected in the excellent goodness-of-fit parameters (see Table 6.2). Deviations at low radial distance are small and due to low frequency component in the background. In the fit, a background function was not used to correct this effect. Results of the fit are in good agreement with the pyrochlore structure. The hafnium-oxygen distance is shorter than that of the zirconium-oxygen bond of the initial model, which is in agreement with the slightly smaller ion radius of Hf^{4+} compared to Zr^{4+} (0.72 and 0.71 Å) in six-fold coordination. S_0^2 was manually adjusted such that the Hf-O coordination number was 6.0. The Hf-Ce and Hf-Hf coordination numbers are in agreement with the expected theoretical value of 6.0. While the Hf-Ce coordination number is lower and bond length is shorter compared to the starting

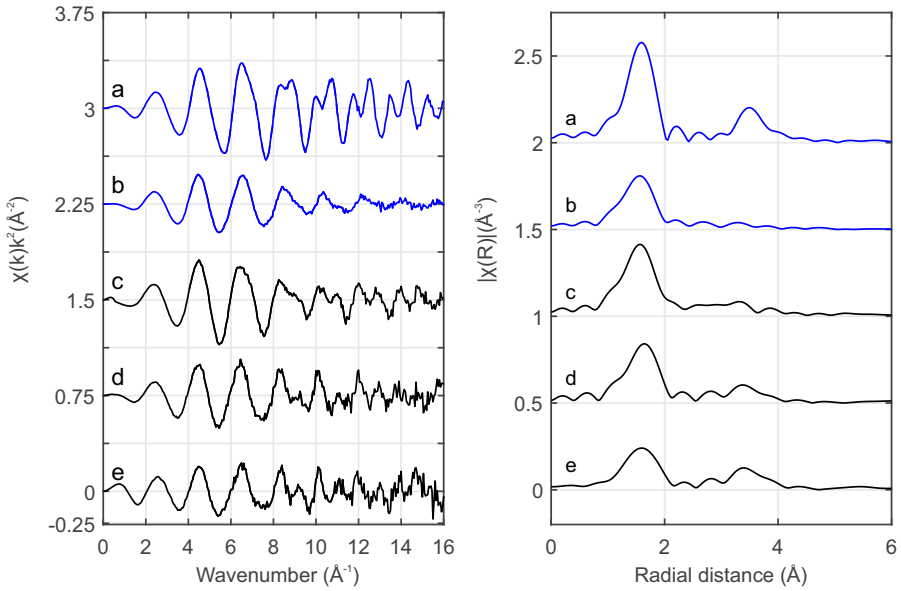

Figure 6.9 Hf K edge EXAFS recorded at room temperature. a) auto-reduced Hf50CR, b) calcined Hf50C, c) HfO_2 reference, d) auto-reduced Hf20CR and e) calcined Hf20C. The k-range used in the Fourier transform was 4.000 to 11.600 $Å^{-1}$.

value, the Hf-Hf coordination number is higher than that of Hf-Ce at a longer bond length. Consistent and very similar results, however with larger statistical uncertainty were obtained by fitting data in a smaller k-range (see Table 6.2).

Path	CN	$\sigma^2 \cdot 10^3$ (Å^2)	R (Å)	ΔE_0 (eV)	S_0^2
Hf50CR, k-range: 4.091 to 14.603 Å^{-1}, red.χ^2 = 194.3, Rf = 0.0073				-6.3 ± 0.93	0.945
Hf-O	6.0 ± 0.3	3.29 ± 0.38	2.09		
Hf-Ce	2.3 ± 2.8	2.64 ± 4.90	3.78		
Hf-Hf	5.6 ± 2.9	4.20 ± 2.09	3.81		
Hf50CR, k-range: 4.000 to 11.600 Å^{-1}, red.χ^2 = 462.6, Rf = 0.0063				-5.6 ± 1.37	0.930
Hf-O	6.0 ± 0.5	3.11 ± 0.68	2.09		
Hf-Ce	2.5 ± 4.3	2.23 ± 7.84	3.77		
Hf-Hf	5.2 ± 5.0	3.17 ± 5.29	3.83		

Table 6.2: Numeric details of Hf K edge EXAFS fits of auto-reduced Hf50CR to the pyrochlore structure[221] (see Figure 6.10) utilizing the Artemis software package.[241] The R-range of the fits was 1.1 to 4.4 Å. All parameters except S_0^2 were guess parameters. S_0^2 was manually adjusted such that the Hf-O coordination number was 6.0. For all scattering paths, one common parameter for ΔE_0 was used. The goodness of the fit is given by the parameters reduced χ^2 and the R-factor Rf. CN is the coordination number, σ^2 the Debye-Waller factor, ΔR is the change of the inter-atomic distance relative to the starting structure and R is the result for the inter-atomic distance.

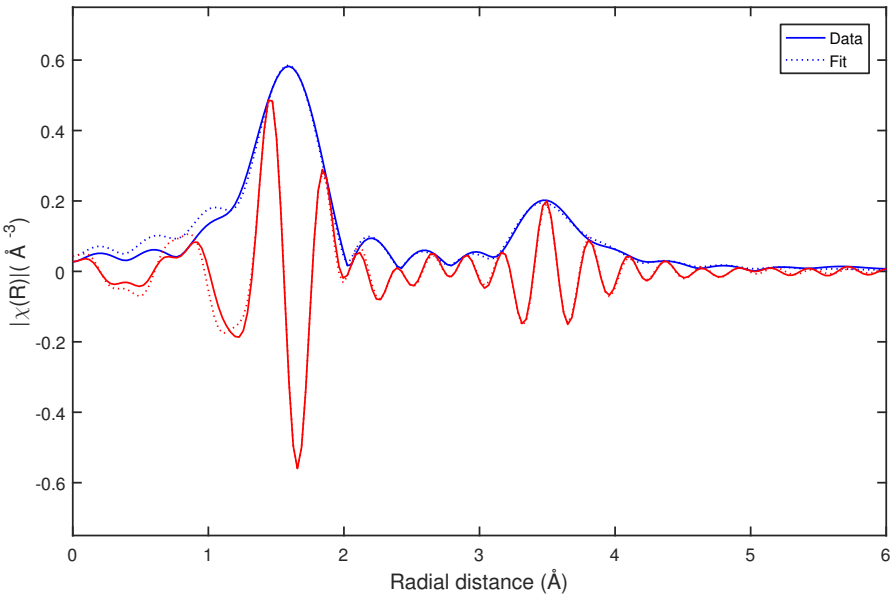

Figure 6.10 Fit of the Hf K edge EXAFS of auto-reduced Hf50CR to the pyrochlore structure. Magnitude (blue) and real part (red) of the data (solid lines) and the fit (dashed lines). The k-range used in the Fourier transform was 4.000 to 11.600 $Å^{-1}$. Numerical details are reported in Table 6.2.

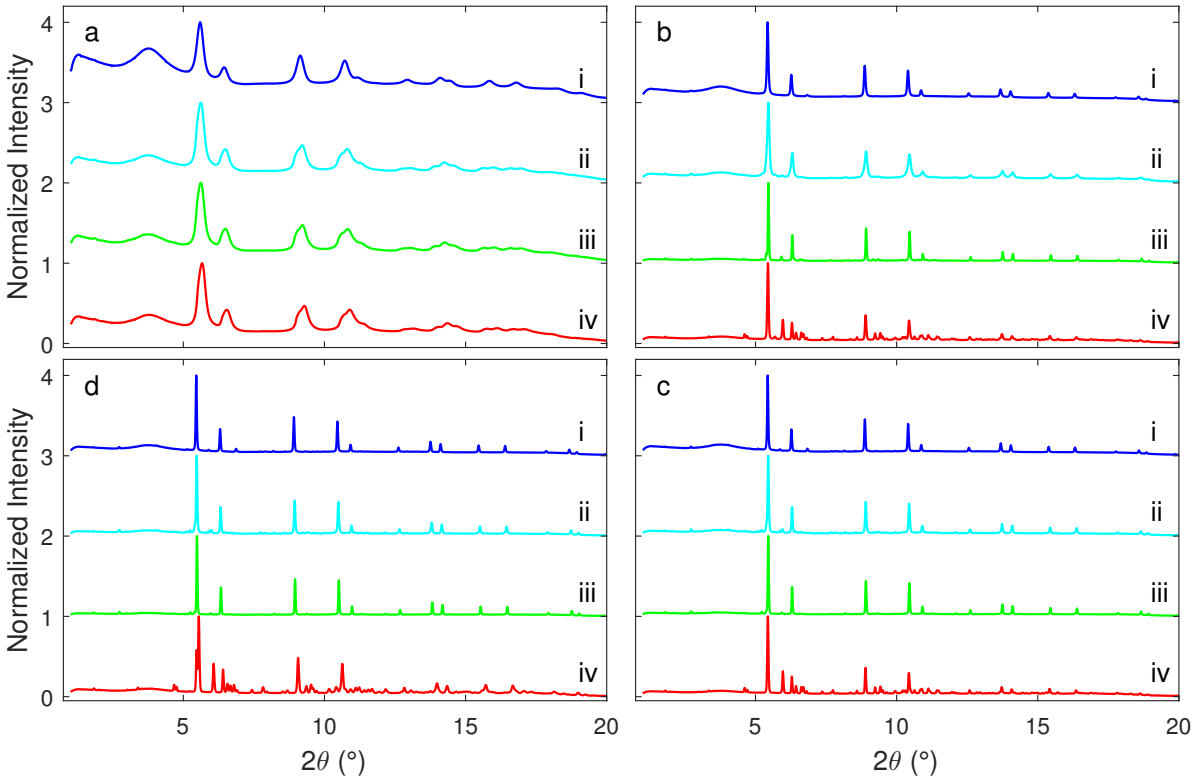

Figure 6.11 Normalized XRD patterns recorded with a focused beam before, during and after high temperature treatment of i) Zr50C in a flow of hydrogen/helium, ii) Hf50C in a flow of hydrogen/helium iii) Hf50C in a flow of argon and iv) Hf50C in air; a) at room temperature before heating b) at the end of the heating ramp, c) after 30 minutes at the maximum temperature (1623 ± 50 K in hydrogen/helium and 1823 ± 50 K in argon and air) before cooling and d) after the thermal treatment at room temperature.

In situ XRD

Chemical reduction and auto-reduction

Figure 6.11 shows selected normalized XRD patterns of Zr50C and Hf50C that were recorded during chemical reduction in a flow of hydrogen/helium, auto-reduction in a flow of argon and in air at high temperatures. The temperature was increased at a rate of about 50 K/min and 1823 ± 50 K were reached in argon and air, and about 1623 ± 50 K in hydrogen/helium. In hydrogen/helium the temperature was about 200 K lower due to the high heat conductivity of helium. The geometry of the in situ cell enabled recording a 2θ-range from 1 to about $2\theta \leq 18°$. The scattering contribution of the quartz tube appeared as a smooth background with a very broad peak at $2\theta = 3.8°$. The normalized intensity of the background was significantly higher in the pattern of Zr50C compared to that of Hf50C. Compared to XRD measurements of powder samples

in thin quartz capillaries, the peaks in the diffraction patterns obtained using the in situ setup were broadened. Several reasons for the broadening can be identified: First, the interaction volume was given by the beam size and not limited by the geometry of the sample, second the pellets used were thicker than a typical quartz capillary and third, the diffracted beam was additionally broadened by scattering when passing through the quartz tube. In addition, a significant fraction of the beam was absorbed because samples with a thickness optimized for XAS at the Ce K edge were used at a photon energy just above the Ce K edge (40.443 keV). In addition, the positions of the samples relative to the detector varied slightly, which complicated comparison of the positions of diffraction peaks. In the diffraction patterns of materials that were exposed to reducing conditions, the reflections of the cubic fluorite-type structure appeared at higher scattering angles than expected for pure ceria and they contained additional very weak reflections, some of which indicated the formation of the cation-ordered pyrochlore structure. At the end of the heating ramp the width of the peaks in the pattern of Hf50C that was heated in a flow of hydrogen/helium were larger compared to that in the pattern of Zr50C. During chemical reduction in a flow of hydrogen/helium, more peaks appeared in the diffraction pattern of Hf50C than in that of Zr50C. Many of these reflections were tentatively assigned to monoclinic and/or the orthorhombic hafnia phases. The patterns of Hf50C heated in air and the one recorded after sintering in air at 1873 K (shown in Figure 6.1) were very similar and differed slightly in the intensities of the reflections. In both diffraction patterns, reflections of hafnia were present and reflections indicating cation ordering were absent.

Figures 6.12 and 6.13 display selected reflections of the diffraction patterns of Zr50 and Hf50 recorded during reduction. Most reflections of the ceria-zirconia pyrochlore $Ce_2Zr_2O_7$ emerged during reduction of Zr50C in a flow of hydrogen/helium at a maximum temperature of 1623 ± 50 K: the (111), (331) and (333)(511) and more reflections could be clearly identified. The peak at the position of the very weak (442) reflection of the pyrochlore could not be clearly assigned due to potential overlap with a reflection of the monoclinic zirconia phase that emerged after the temperature ramp. In the patterns of Hf50C that were recorded during reduction in hydrogen/helium, a larger number of small peaks emerged, many of which were tentatively assigned to monoclinic and/or orthorhombic hafnia phases. The (111) reflection of the pyrochlore phases of chemically reduced Zr50C and Hf50C in a flow of hydrogen/helium emerged at a similar temperature. The (333)(511) diffraction peak of auto-reduced and chemically reduced Hf50C was clearly detected close to the position of that of reduced Zr50C. Compared

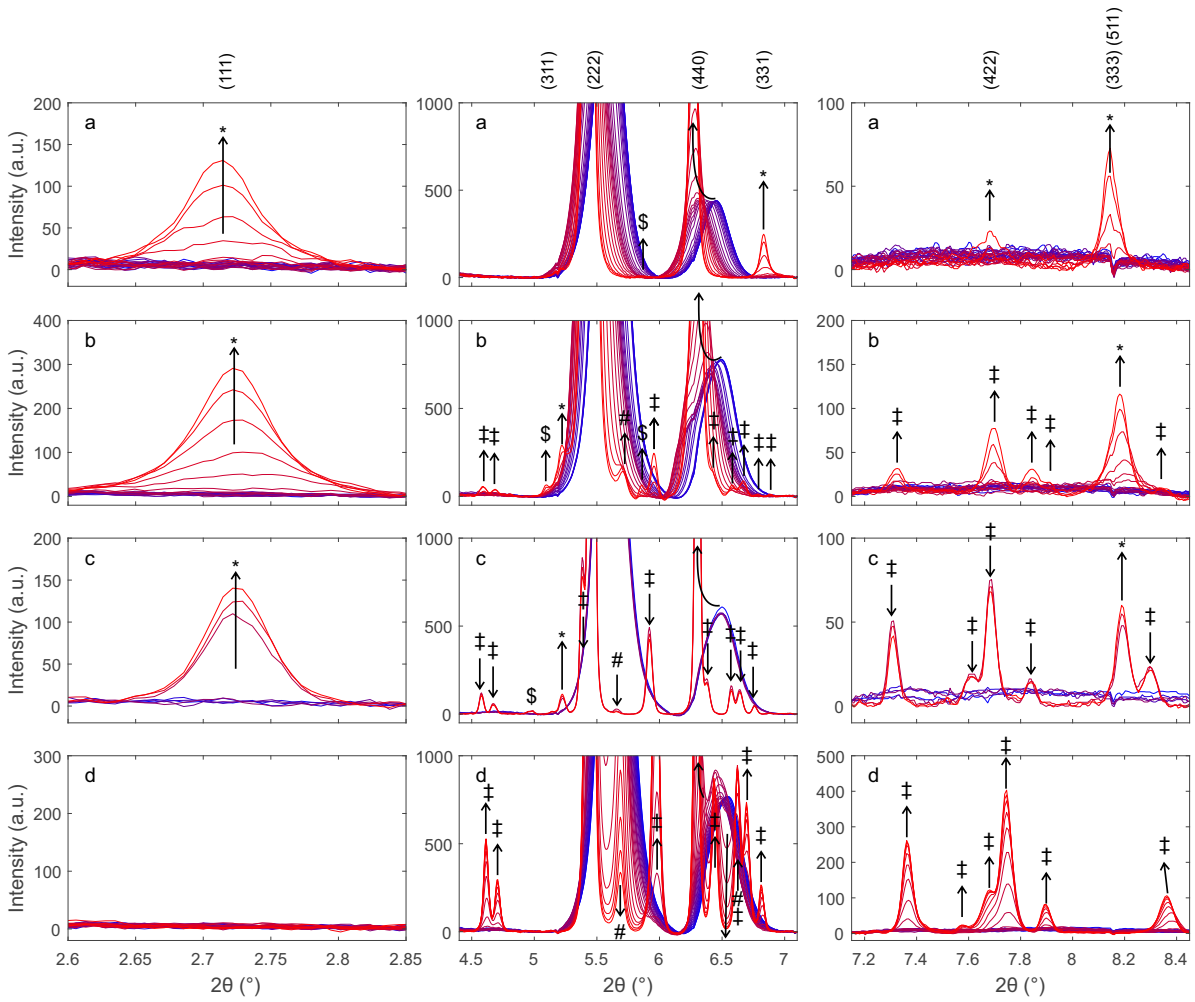

Figure 6.12 Details of diffraction patterns, highlighting reflections of the pyrochlore structure recorded during heating of a) Zr50C in hydrogen/helium, b) Hf50C in hydrogen/helium, c) Hf50C in argon and d) Hf50C in air at about 50 K/min from room temperature to 1623 ± 50 K in hydrogen/helium) and 1823 ± 50 K in argon and air. Blue indicates room temperature and red indicates high temperature. Arrows indicate directions of changes. Reflections were tentatively assigned to the pyrochlore ceria-hafnia phase (*), monoclinic hafnia (‡), orthorhombic hafnia (#). Some peaks could not be assigned unambiguously($).

to reduced Zr50C, its intensity relative to the (111) reflection was slightly weaker. By contrast, close to the position of the (311) reflection of the Zr50C pyrochlore three very small peaks were detected in the pattern of chemically reduced and auto-reduced Hf50C that could not be clearly assigned to the pyrochlore phase. During thermal reduction of Hf50C in a flow of argon, the (11-1) reflection at $2\theta = 5.9$ indicated the formation of monoclinic hafnia. The (222) peak of the pyrochlore corresponds to the (111) reflection

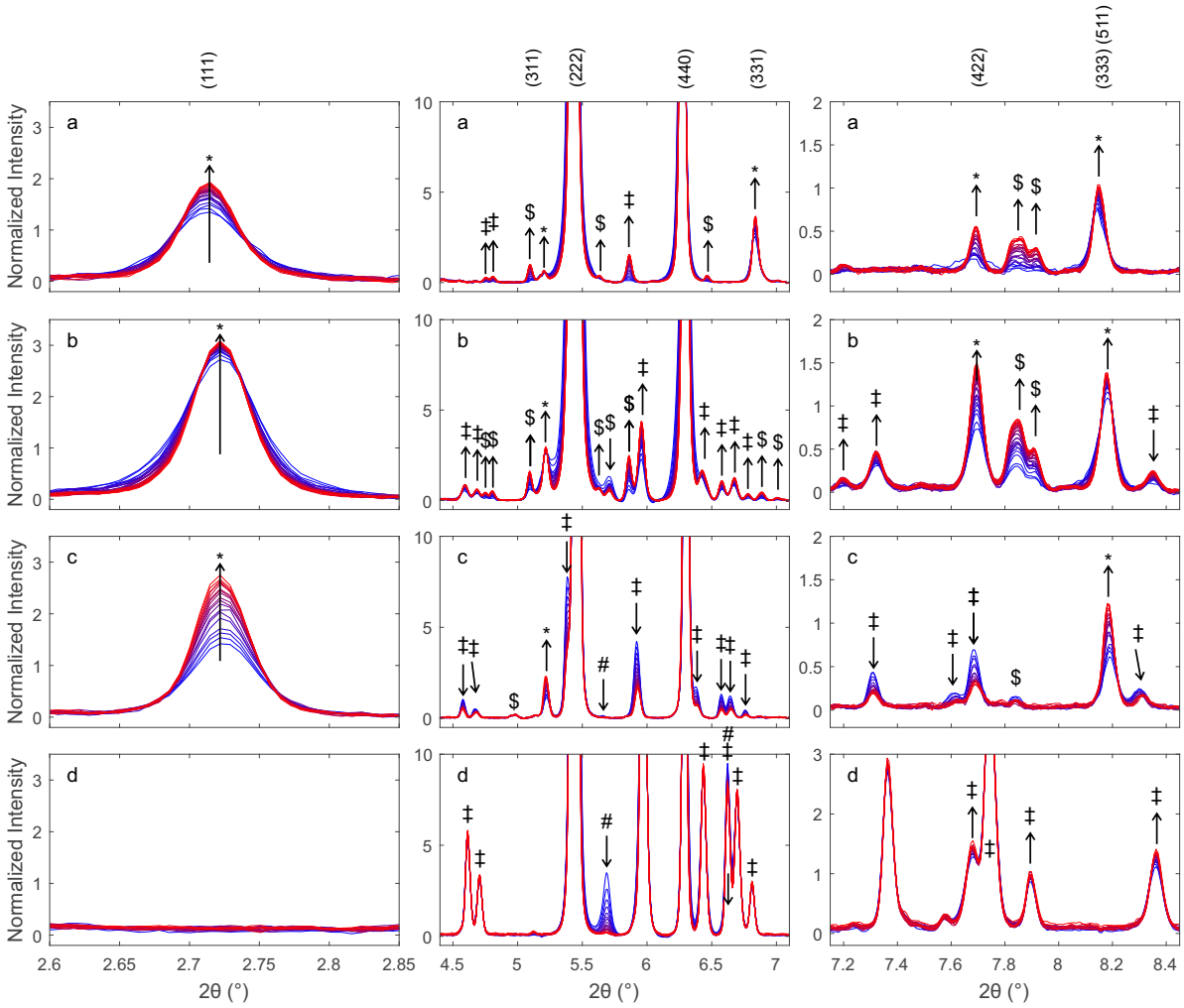

Figure 6.13 Details of normalized diffraction patterns highlighting reflections of the pyrochlore structure. Patterns were recorded during 30 min at constant temperature after heating a) Zr50C in hydrogen/helium, b) Hf50C in hydrogen/helium, c) Hf50C in argon and d) Hf50C in air at 50 K/min (see Figure 6.12). In hydrogen/helium the maximum temperature was 1623 ± 50 K and it was 1823 ± 50 K in argon and air. Blue indicates the first and red the last diffraction pattern. The background was subtracted prior to normalization. Arrows indicate changes in the intensities of reflections assigned to the pyrochlore phase.

of the fluorite-type structure. At higher temperature, the normalized intensities of the reflections of the monoclinic hafnia phase decreased, while the intensities of the peaks assigned to the pyrochlore further increased. In agreement with the pattern of Hf50C that was chemically reduced in hydrogen/helium, the (333)(511) reflection of Hf50C was clearly detected. There were fewer peaks of other phases compared to the reduction of Zr50C and Hf50C in hydrogen/helium at a lower temperature. At the position of the

notable (331) reflection of the ceria-zirconia pyrochlore, there was no peak with increasing intensity related to the pyrochlore phase. The reflections at low angles indicating cation ordering were not observed during heating in air. In the heating ramp both the monoclinic and a small amount of the orthorhombic hafnia phase were formed. The peak assigned to the (121) reflection, the most intense reflection of ortorhombic hafnia, was observed at 5.7 2θ and decreased below 0.2 % relative normalized intensity after 30 min at 1823 ± 50 K. A peak at a very similar position to that of the (331) reflection of the pyrochlore was also formed by heating in air. While the intensities of the (111),(331) and (333)(511) reflections associated with cation ordering increased in the pattern of reduced Zr50C, the corresponding intensities of the reflections of Hf50C decreased both in hydrogen/helium and argon. The intensities of the (311) reflections changed very little in the patterns of reduced Zr50C and reduced Hf50C. In reducing atmosphere, only minute changes in the intensities of the hafnia phases were detected. In air, by contrast, the intensity of the reflections of monoclinic hafnia increased and the most intense peak split into two peaks, indicating the presence of substantial amounts of monoclinic hafnia and a fluorite-type phase. Upon cooling, there was no significant change in the intensity of the (121) reflection indicating the presence of a small amount of orthorhombic hafnia.

Isothermal carbon dioxide splitting

Figure 6.14 reports the furnace profile and MS signals recorded during the in situ XRD experiment under isothermal carbon dioxide splitting conditions using a platinum-decorated Hf50C pellet that had been auto-reduced in a flow of argon. The temperature was increased at about 50 K/min to 1800 ± 50 K. Subsequently, the gas feed was alternated between a flow of argon and a flow of carbon dioxide at a half period of 30 min. The release of oxygen (m/z = 32) was not observed when the sample was heated in the first part of the experiment. The MS signal of 28 and 16 differed in the three oxidation steps, however the formation of CO from carbon dioxide due to re-oxidation of the auto-reduced Hf50C could not be inferred. Figure 6.15 presents diffraction patterns of auto-reduced (see Figure 6.12 c) and 6.13 c)), platinum-decorated Hf50 under isothermal carbon dioxide splitting conditions. During heating in argon to 1800 K (not shown) and during 30 minutes at 1800 ± 50 K in a flow of argon, there were no significant changes in the diffraction pattern. Switching from a flow of argon to a flow of carbon dioxide caused a gradual decrease in the intensities of the (111) and (311) reflections of the pyrochlore phase to less than a third of their initial intensities, while the intensity of the (333)(511) reflection increased. The normalized intensities of peaks of monoclinic hafnia increased

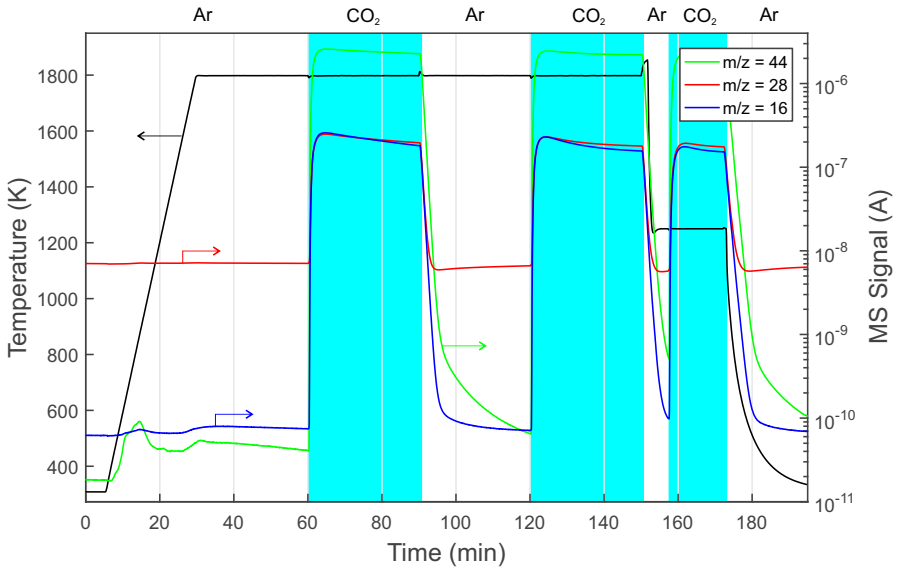

Figure 6.14 Temperature profile and MS signal of an in situ XRD experiment using a focused beam. Hf50C that was thermally auto-reduced in a flow of argon and subsequently decorated with platinum was exposed to isothermal carbon dioxide splitting conditions at 1800 ± 50 K. The gas feed was 200 mL/min argon and 100 ml/min carbon dioxide.

significantly during the oxidation step. Subsequent exposure to a flow of argon led to a slight increase of the intensities of the pyrochlore (111) and (311) reflections, while that of the (333)(511) reflection decreased. The intensity of the (333)(511) reflection increased dramatically at the time the gas feed was switched. After the second switch from a flow of argon to a flow of carbon dioxide, the (111) and (311) peaks decreased gradually and after about 15 min exposure to carbon dioxide they were no longer distinguishable from noise. The intensity of the peak assigned to the (333)(511) reflection gradually increased and then decreased again. Its intensity was significantly higher in the first pattern recorded in carbon dioxide compared to the last one recorded in argon before the second feed gas switch. A weak peak was observed at a slightly higher Bragg angle than the (440) reflection of the pyrochlore structure. Its intensity decreased slightly during heating and at 1800 K in a flow of argon. In a flow of carbon dioxide, its intensity increased and formed a shoulder on the (440) reflection. Its intensity went up during the first exposure to carbon dioxide, which led to the formation of a broad shoulder on the (440) peak. During subsequent exposure to a flow of argon, the shoulder changed to an individual peak with a higher intensity compared to that in the pattern recorded in argon after reaching isothermal conditions. During the second exposure to carbon dioxide, the intensity of the peak increased further, forming a broad shoulder of

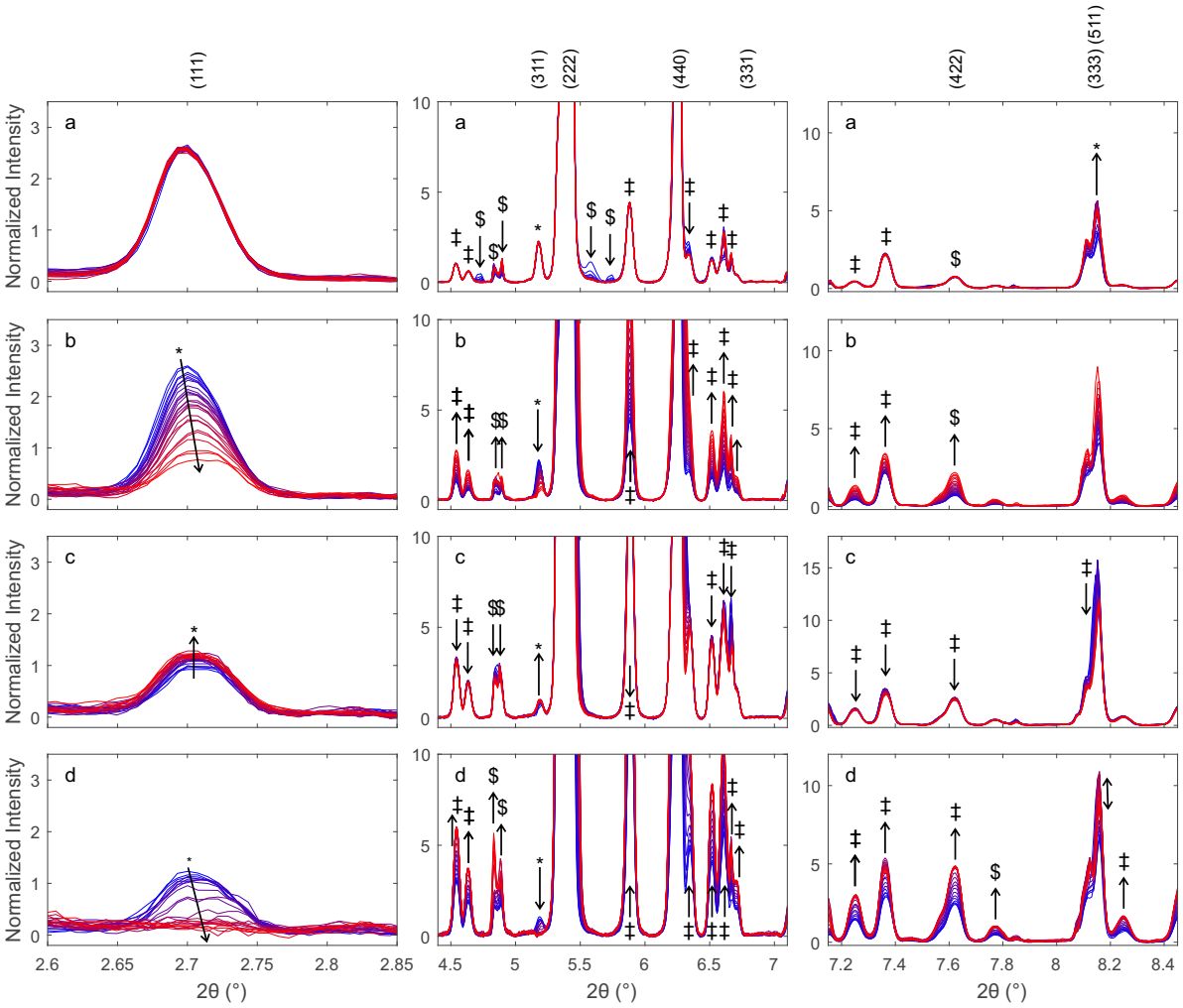

Figure 6.15 Normalized diffraction patterns of auto-reduced Hf50C, highlighting changes in the reflections of the pyrochlore structure under isothermal carbon dioxide splitting conditions. A pellet Hf50C was auto-reduced at 1823 K in a flow of argon and impregnated with platinum. Subsequently, it was heated to 1800 ±50 K in a flow of argon and the feed gas was switched at a half period of 30 min from a flow of a) argon to b) carbon dioxide, c) argon and d) carbon dioxide. Blue indicates the first and red the last diffraction pattern in a series. Arrows indicate changes in the intensities of the reflections assigned to the pyrochlore structure.

the peak assigned to the (400) reflection of the pyrochlore structure. The (400) peak of the $Ce_2Zr_2O_{7.5}$ phase was reported at a higher angle than that of the (400) reflection of the $Ce_2Zr_2O_7$ pyrochlore. However, the peak might also be the (002) reflection of monoclinic hafnia.

6.3 Discussion

XRD after auto-reduction in a thermogravimetric analyzer showed the formation of the ceria-hafnia pyrochlore in Hf50CT. The pyrochlore structure was stable for several months at ambient conditions. The release of oxygen from equimolar ceria-hafnia in the thermogravimeter indicates an average oxidation state of ceria in Hf50CT higher than +3.0, which is rather unusual. The reduction is more likely a systematic error - a drift of the thermobalance in the experiment of Hf50CT was corrected with a linear function. On the other hand, a ceria-zirconia pyrochlore-type structure with a composition of $Ce_2Zr_2O_{6.2}$ prepared by reduction in hydrogen/argon at 1023 K was reported by Baidya.[191] By contrast, under the same reaction conditions the formation of the ceria-hafnia pyrochlore was not observed, most likely because, at this temperature, the mobility of hafnium cations (M = 178.5 amu) is substantially lower compared to that of zirconium cations (M = 91.22 amu). The Ce K edge XANES of pristine Hf50C and reduced Hf50CR indicates structural changes, however the spectral features are diffuse at 1773 K and only after cooling to room temperature an oscillation indicating a different cerium-oxygen coordination geometry and cerium-oxygen bond length become visible. The edge shift and the drop in the intensity of the white line during thermal reduction are clear indications of changes in the electronic structure of cerium. In the acquisition of Hf K edge spectra at 65 keV, the accuracy of the movement of the monochromator is even more critical than at the Ce K edge. The differences in the energy and intensity of the XANES features of Hf50C and Hf50CR suggest changes in the oxygen coordination geometry. Improvements in data quality and measurements of phase-pure reference compounds are required. Unfortunately, no Hf K edge XANES spectra of reference compounds could be found in the literature. To the best of our knowledge, these are the first Hf K edge XAS spectra. In an attempt to confirm the pyrochlore structure, the amplitude reduction factor was varied as a set parameter in the fits until a Hf-O coordination number of 6.0 was obtained. Yamamoto et al. investigated the ceria-zirconia pyrochlore at 773 K and reported an error of ±0.7 for the Zr-O coordination number determined by Zr K edge EXAFS fitting.[180] The error for the coordination numbers of the second shell is similar to the coordination number, which might be caused by lattice distortions or the presence of a secondary hafnia-rich phase. Despite excellent statistics, the fit gives only vague indications of cation ordering. By contrast, compelling evidence of cation ordering was achieved by XRD of Hf50CT. A preliminary analysis of XRD data provides clear evidence of the ceria-hafnia pyrochlore structure, however a more detailed analysis

by Rietveld refinement is desirable. The uncertainty in the position of the sample and the temperature of the sample in some of the experiments might complicate refinement. Overall, in situ XRD is a powerful tool that provides detailed insights into the structure of the material and the dynamic changes at high temperature. It enables detection of a secondary monoclinic hafnia phase and provides valuable insights into the dynamics of structural changes of the pyrochlore-type structure under relevant thermochemical looping conditions. The ordered arrangement of cations disintegrated upon exposure to a flow of carbon dioxide at 1773 K. After thirty minutes in a flow of carbon dioxide, the normalized intensity of the (111) reflection of the pyrochlore decreased by about 60 % but increased by less than 10 % of the initial intensity after 30 min in a flow of argon. In the second cycle, the reflections of the pyrochlore structure disappeared. The reversibility of the order-disorder transformation is most likely possible under more reducing conditions. However, preparation of the pyrochlore from small particles that are not stable at high temperature lead to higher mobility of the cations compared to the oxidized bulk material that consists of at least two phases. It cannot be excluded that the conditions during the reduction step of isothermal carbon dioxide splitting were not reducing enough to reverse the decomposition of the pyrochlore phase. The ceria-hafnia pyrochlore is not stable in an oxidizing environment at 1773 K, which is in agreement with the work of Andrievskaya et al.[188,189] who determined the phase diagram of ceria-hafnia at 1773 K in air. It is not clear if there is a temperature range that allows the complete oxidation of the cation-ordered material analogous to $Ce_2Zr_2O_8$, the κ-phase of ceria-zirconia. Further experiments with better control of the oxygen partial pressure are required. The formation of the cation-ordered phase demonstrates the influence of the preparation method on material performance in thermochemical looping. Le Gal et al.[151,217] found substantial differences in the carbon monoxide yield obrtained from commercial materials (Rhodia, Solvay group) and materials prepared by co-precipitation and polymerized complex (Pechini-type) synthesis. Bonk et al.[157] compared materials prepared via the ceramic method and a polymerized complex method and eliminated any potential influence of the preparation method: sintering pressed pellets at 1873 K led to qualitatively equal materials in thermochemical carbon dioxide splitting. Deviations of material properties and changes of material properties upon exposure to reducing conditions over time were attributed to ordering phenomena of cations or oxygen vacancies. Oxidation at high temperature could reverse these effects in ceria-zirconia.[165] This is in agreement with the low stability of the cation-ordered ceria-hafnia structure under oxidizing conditions at 1773 K reported in Figure 6.15.

6.4 Conclusions

Thermogravimetric analysis and XRD identified the pyrochlore structure which forms during the reduction step of solar-driven thermochemical cycles. In situ Ce K edge XAS confirmed the complete reduction of cerium(IV) to cerium(III) during auto-reduction of equimolar ceria-hafnia powder. Hf K edge XANES indicated structural changes and Hf K edge EXAFS fitting supports the formation of the pyrochlore structure. Time-resolved in situ XRD confirmed the formation of the ceria-hafnia pyrochlore phase from powders and its stability in a flow of argon at 1773 K. In situ XRD was successfully performed at 1773 K under relevant reaction conditions of thermochemical carbon dioxide splitting. Exposure to a flow of carbon dioxide at 1773 K led to a decrease in the diffraction peaks of the pyrochlore phase, and they disappeared after two carbon dioxide splitting cycles. Cation ordering was not recovered during exposure to a flow of argon. The ceria-hafnia pyrochlore is an important structure that might form in thermochemical cycles also in inhomogeneous samples with lower than equimolar hafnia content. Therefore, it is important to prepare materials with a homogeneous distribution of the heterocation, for example by using a polymerized complex synthesis route (see Chapter 1). This work also highlights both the importance and opportunities of in situ characterization which combines spectroscopy and a diffraction technique. The stability of ceria-zirconia and ceria-hafnia materials under solar reactor conditions needs further investigation. Thermodynamic data of oxygen uptake and release in pyrochlore-type ceria-zirconia and ceria-hafnia materials have not yet been determined. Similar to fluorite-type ceria, the cation-ordered materials can be further modified and stabilized by heterocations and might make equimolar ceria-hafnia an interesting material for the storage, transport and activation of oxygen.

Chapter 7

First Demonstration of Direct Hydrocarbon Fuel Production from Water and Carbon Dioxide by Solar-driven Thermochemical Cycles Using Rhodium-ceria

based on:
Lin, F., Rothensteiner, M., Alxneit, I., van Bokhoven, J. A., and Wokaun, A. (2016). Energy Environ. Sci., 9(7), 2400-2409. http://doi.org/10.1039/C6EE00862C

M.R. contributions: setup for automated water and/or carbon dioxide splitting experiments with quantification of reaction products, co-designed cycling experiments, performed cycling experiments, processed measurement data and performed quantitative analysis, revised the manuscript.

7.1 Introduction

Syngas, a mixture of hydrogen and carbon monoxide produced by solar thermochemical dissociatin of H_2O and CO_2 can be converted to higher grade fuels such as methane and liquid hydrocarbons via methanation and Fischer-Tropsch processes. The entire production chain to renewable jet fuel from water and carbon dioxide by a two-stage conversion process, first solar thermochemical cycles (STC) and then the Fischer-Tropsch process, was recently demonstrated by the European consortium SOLARJET.[13] Most research efforts in designing redox materials for STCs are devoted to improving syngas production. This can be achieved by doping ceria with heterocations,[128,143,149,153,216] or by fabricating porous structures to facilitate mass/heat transfer and improve the redox kinetics.[123,127,145] A very attractive route is the direct production of hydrocarbon fuels from water and carbon dioxide by realistic STCs.[294] This new concept, if high selectivity for hydrocarbons is achieved, inherently bypasses a second stage conversion, such as methanation or Fischer-Tropsch processes. This could potentially make the solar fuel production chain much more economical. In addition, storage and transportation of syngas would not be required. Encouragingly, Chueh and Haile reported the direct formation of methane from water and carbon dioxide by thermochemical cycles using 10 wt% nickel supported on samarium-doped ceria.[295] However, ceria was chemically reduced with hydrogen at 1073 or 1173 K, a much lower temperature than required for the thermal reduction of ceria. With the aim to produce hydrocarbon fuels directly from water and carbon dioxide, we propose a strategy of incorporating a catalytic process into STCs by adding a catalyst to ceria. This study shows that direct methane production in STCs is possible. The primary role of the catalyst is to drive the formation of hydrocarbon molecules (Figure 7.1). The formation of these hydrocarbon fuels can be either from the conversion of the syngas generated by water and carbon dioxide splitting, or directly from water and carbon dioxide without the intermediate formation of syngas, or from a combination of both. In this study, we have prepared nickel-doped ceria and rhodium-doped ceria by incorporating cationic nickel and, respectively rhodium into the ceria lattice using a simple co-precipitation method. By incorporation instead of impregnation of the catalyst, a better dispersion of the catalyst on ceria can be achieved in the event of phase segregation potentially occurring during STCs. Nickel is well known as an active methanation catalyst due to its activity for carbon monoxide dissociation and hydrogenation.[296–298] Rhodium was chosen since oxide-supported rhodium is an active Fischer-Tropsch catalyst for the conversion of syngas to methane, methanol and

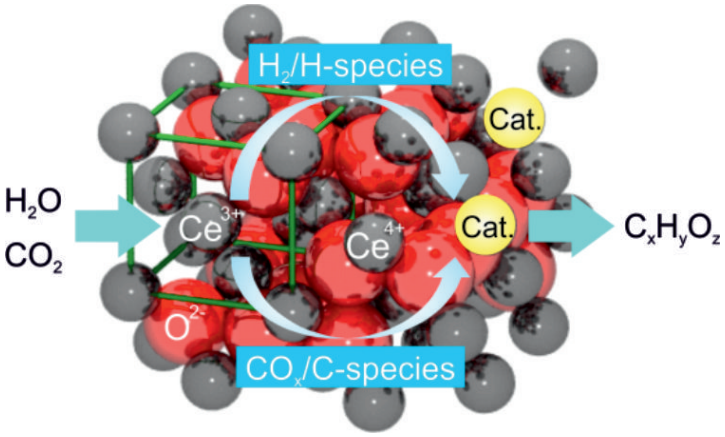

Figure 7.1 Schematic illustration of direct hydrocarbon ($C_xH_yO_z$) formation from water and carbon dioxide during the reoxidation of reduced ceria doped with a catalyst (Cat.).

other oxygenates.[299,300] Rhodium-doped ceria has been reported previously,[301–303] with advantages such as atomic dispersion and thus potentially large number of active reaction sites.[301,302] Atomically dispersed and nanosized rhodium particles supported on ceria-alumina are an active and stable catalyst for methane steam reforming.[304] Here, we demonstrate the concept of producing a hydrocarbon fuel directly from water and carbon dioxide during the reoxidation of thermally reduced rhodium-ceria under realistic conditions. Long-term activity of the material for 59 cycles is reported. In contrast, nickel-doped ceria is not active in producing methane when thermally activated.

7.2 Results and discussion

To screen ceria doped with various heterocations for their use in the thermochemical production of hydrocarbons directly from water and carbon dioxide under realistic conditions, preliminary studies were carried out. The materials were activated by reduction with a mixture of hydrogen and argon at 873 K. The reoxidation was carried out with a mixture of water, carbon dioxide and argon at 773 K. Figure 7.2 presents the results for 10 mol% nickel-doped ceria and 1 mol% rhodium-doped ceria. After reduction, hydrogen and methane are produced during the reoxidation steps by both materials. More methane is produced with rhodium-doped ceria than with nickel-doped ceria. However, for both materials, less methane is produced in the second cycle, likely due to sintering of the materials. Nonetheless, these preliminary results indicate the potential of nickel-, respectively rhodium-doped ceria for direct methane production from water and carbon dioxide during the reoxidation steps in realistic thermochemical cycles. Both materials

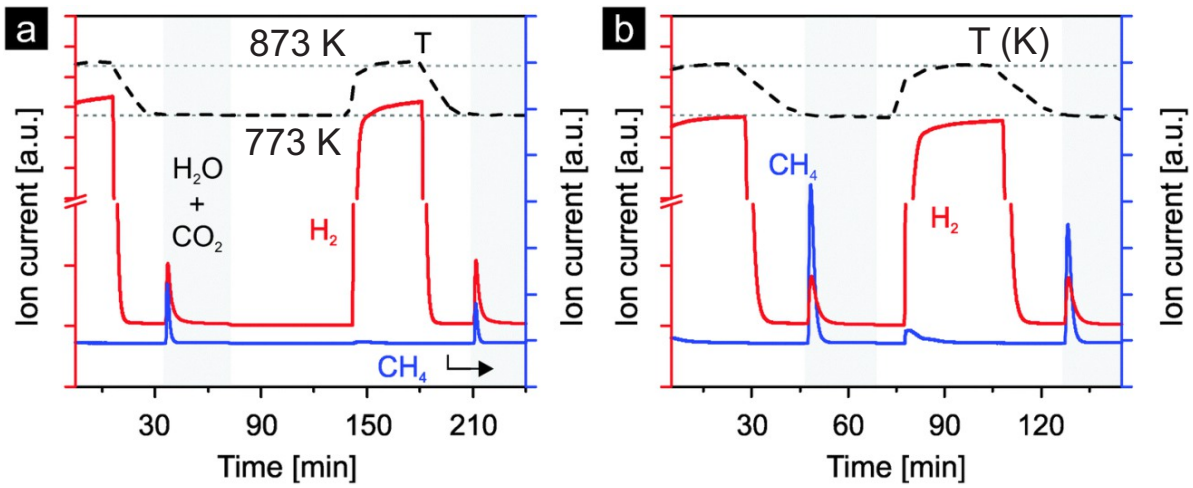

Figure 7.2 Formation of hydrogen and methane from water and carbon dioxide during the reoxidation of chemically reduced nickel-doped ceria (a) and rhodium-doped ceria (b). Chemical reduction was carried out at 873 K using a mixture of hydrogen and argon, and reoxidation at 773 K.

were further evaluated in realistic thermochemical cycles, in which they were activated by thermal reduction. The materials were reduced in argon at 1673 K and subsequently reoxidized by either water or carbon dioxide, or both at 773 K. In Figure 7.3 we report the first five cycles of 1 mol% rhodium-doped ceria. Very similar oxygen evolution profiles during thermal reduction are observed in all cycles except for the first (Figure 7.3a). The additional oxygen peak observed at about 1373 K is attributed to the irreversible reduction of the Rh^{3+} precursor during the first reduction step. Excluding the first cycle at 108.2 μmol O_2/g, the amount of oxygen released per cycle is in the range of 59 to 74 μmol/g (Table 7.1). With an estimated oxygen partial pressure of about 40 ppm during reduction, these values are in general agreement with the ceria non-stoichiometry established by Panlener et al.[71] A closer examination of the oxygen evolution profiles of cycles 2 to 5 reveals that oxygen evolution starts at a lower temperature in cycles 2 and 4 compared to cycles 3 and 5, leading to larger amounts of oxygen released (Table 7.1). Note that in cycles 3 and 5, the material was previously reoxidized by carbon dioxide only, while in cycles 2 and 4 water was present during the preceding reoxidation. This suggests that the reoxidation is more complete when water is present as oxidant. Thus, the true oxygen release capacity can be obtained by averaging the amounts of oxygen released during the reduction steps following complete reoxidation (i.e. by water). On average 72.6 μmol O_2/g can be released, based on cycles 2, 4 and 6. Looking at the reoxidation steps (Figure 7.3 b), when the reoxidation is performed with water as the

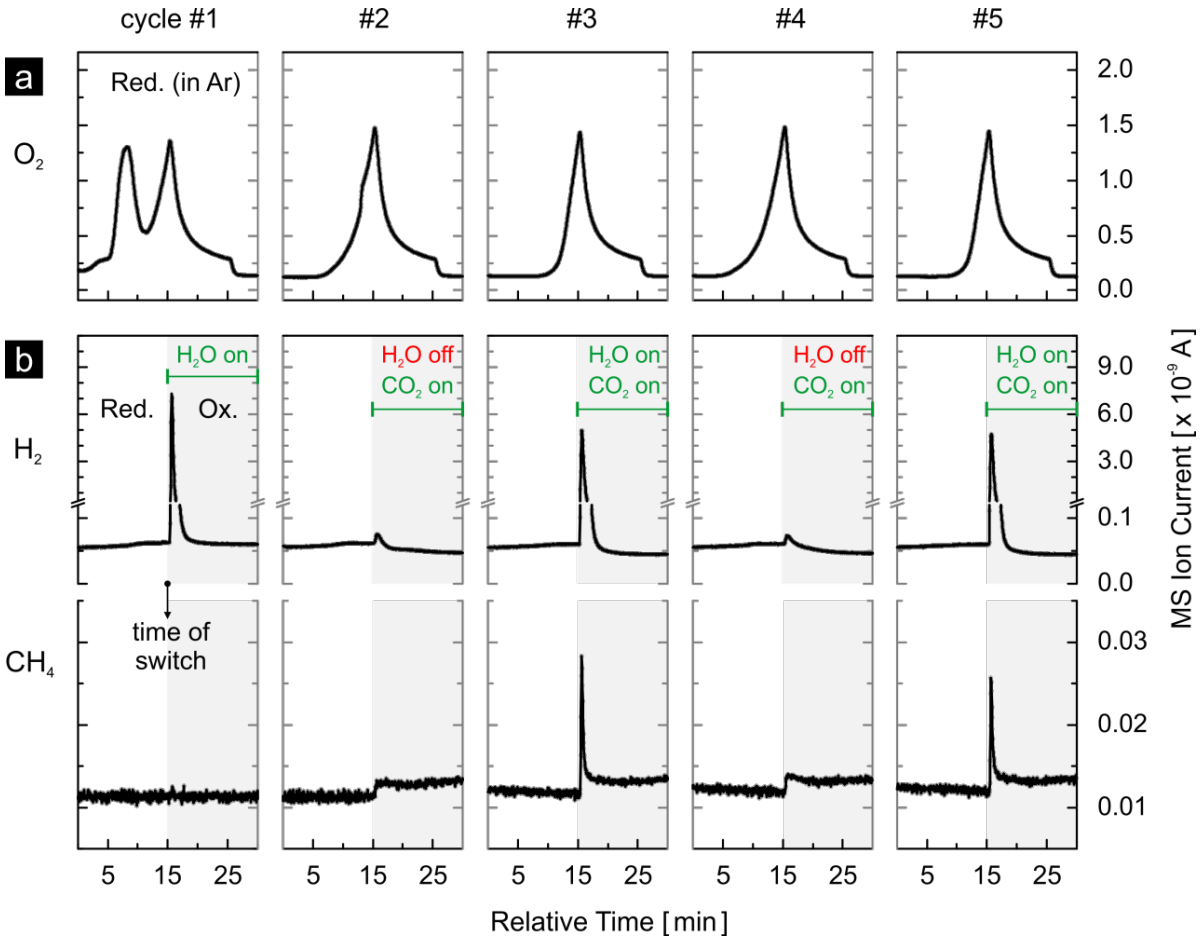

Figure 7.3 Five thermochemical cycles using rhodium-doped ceria with thermal reduction in argon at 1673 K and reoxidation by either water or carbon dioxide, or both at 773 K: a) oxygen evolution profiles during reduction, and b) hydrogen and methane evolution profiles during reoxidation. Methane is produced when water and carbon dioxide are used as oxidants (cycles 3 and 5).

oxidant such as in cycle 1, only hydrogen is produced (130 μmol H_2/g). A H_2/O_2 molar ratio of approximately 1.2 is observed in cycle 1. This value is much lower than 2 because Rh^{3+} is reduced during the first reduction but the reduced rhodium cannot be reoxidized by water. This suggests that the initially single-phased rhodium-doped ceria[294] is transformed into rhodium on ceria, which is confirmed later by X-ray powder diffraction. When carbon dioxide is used as the oxidant as in cycles 2 and 4, as expected essentially no hydrogen is produced (carbon dioxide splitting results discussed later). The very small hydrogen peaks observed are likely due to the reaction of ceria with traces of water from the previous cycle remaining in the gas-delivery system before the reactor. When both water and carbon dioxide are used as oxidants (cycles 3 and 5), in

addition to hydrogen, methane is produced. Compared to the average release of 72.6 μmol O_2/g, a H_2/O_2 molar ratio of approximately 1.85 is observed. Again this value is lower than 2, likely due to the presence of carbon dioxide as a second oxidant and the consumption of some of the produced hydrogen to form methane.[295] Indeed, based on the signal of m/z = 15 (methane), the formation of methane is clearly observed when both oxidants are used (cycles 3 and 5). The slightly larger background of the methane signal when carbon dioxide is introduced is due to traces of methane in the carbon dioxide feed. The methane signal is slightly smaller in cycle 5 compared to cycle 3, indicating some deactivation as the experiment progresses and consistent with the results of Figure 7.2.

Cycle	Oxidation	H_2 (μmol/g)	H_2 (mL/g)	O_2 (μmol/g)	O_2 (mL/g)	H_2/O_2*
1	H_2O	130.0	2.91	108.2	2.42	-
2	CO_2	-	-	70.6	1.58	-
3	CO_2 + H_2O	134.6	3.01	59.4	1.33	1.85
4	CO_2	-	-	73.0	1.64	-
5	CO_2 + H_2O	135.1	3.03	59.4	1.33	1.86
6	CO_2	-	-	74.1	1.66	-

Table 7.1: Amounts of hydrogen and oxygen produced per cycle using rhodium-doped ceria as the starting material. Reduction was carried out at 1673 K in argon, and reoxidation at 773 K in water, carbon dioxide, or both. * The amount of oxygen used in the calculation of the H_2/O_2 ratio is the average value (72.6 μmol O_2/g) of cycles 2, 4 and 6. In these reduction steps, the material is assumed to be fully reoxidized in the previous cycle by water.

Figure 7.4 shows the results of carbon dioxide splitting for three cycles (2, 3 and 4 as in Figure 7.3), in the presence and in the absence of water, with a, b and c representing the evolution profiles of m/z = 44 (CO_2^+), 28 (CO^+) and 12 (C^+), respectively. Nitrogen (N_2), also at m/z = 28, is excluded from discussion as constant and negligible contribution from the nitrogen background is expected. The abundance of nitrogen, estimated at about 150 ppm based on the level of background oxygen, is irrelevant as it only affects the baseline level of the m/z = 28 signal. It is not the baseline but the peak above it that matters. Note that in mass spectrometry, the ionization of carbon dioxide molecules results in smaller fragments of CO^+ and C^+ at lower relative abundance compared to the parent ion CO_2^+. Similarly, the ionization of carbon monoxide molecules results in the parent ion CO^+ and smaller fragments including C^+. When carbon dioxide is introduced to the reactor at room temperature and no carbon dioxide

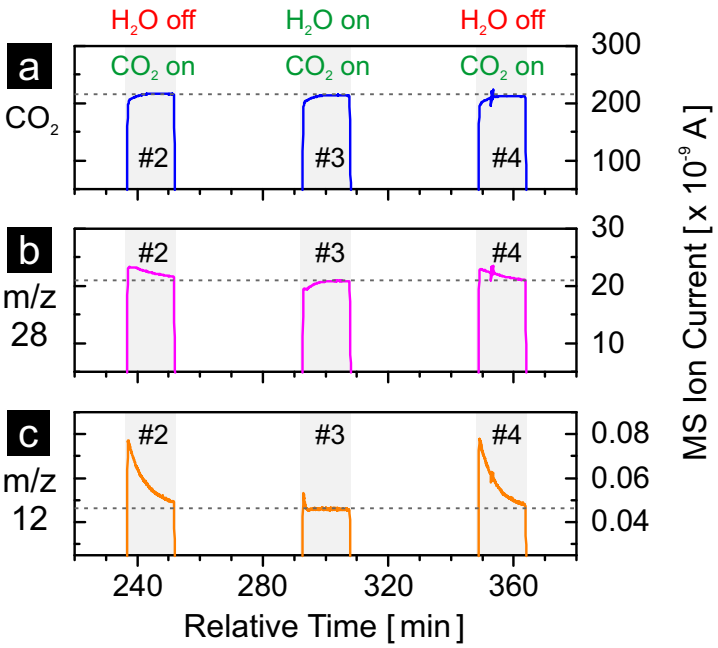

Figure 7.4 MS signals of m/z = 44 (CO_2^+), 28 (CO^+), and 12 (C^+) during the reoxidation steps cycles 2, 3 and 4 in Figure 7.3. The horizontal dashed lines indicate the levels of the signals once they have stabilized.

splitting occurs, the MS signals of m/z = 28 and m/z = 12 exhibit a step increase in a manner identical to the signal of m/z = 44. However, the signals of m/z = 28 and m/z = 12 during the reoxidation steps of cycles 2 to 4 as shown in Figure 7.4 b and c clearly differ from the one of m/z = 44 shown in Figure 7.4. In particular, when carbon dioxide is used as the sole oxidant (cycle 2 and 4), both the m/z = 28 and m/z = 12 signals rise to levels clearly exceeding the baseline values (stabilized ion currents as indicated by the horizontal dashed lines). These two dashed lines represent the contribution of CO_2 ionization to the current of CO^+ and C^+, respectively. A simple estimation reveals the cause of the difference between the signals of m/z = 44 (CO_2^+) and m/z = 28 (CO^+). The relative abundance of CO^+ from the ionization of carbon dioxide is about 11% of the parent ion CO_2^+, as calculated from data recorded at room temperature (no reaction) and from the dashed lines of Figures 7.4 a and b. Thus, the consumption of carbon dioxide by carbon dioxide splitting leading to 1 arbitrary unit (a.u.) decrease of the CO_2^+ signal would also result in 0.11 a.u. decrease of the CO^+ signal. However, the consumption of carbon dioxide produces carbon monoxide at 1 to 1 molar ratio, which leads to an increase of 1 a.u. of the CO^+ signal assuming that carbon monoxide has the same ionization probability as carbon dioxide. Thus, the result of combining these two effects is an increase by 0.89 a.u. of the CO+ (m/z = 28) signal. Thus, the difference

between the instantaneous CO^+ signal when carbon dioxide is introduced and its corresponding baseline value is due to the carbon monoxide produced by carbon dioxide splitting. A similar estimation can be made for the C^+ signal. In comparison to m/z = 28, the difference between the instantaneous signal and the baseline value observed for m/z = 12 is much more pronounced. This is due to a much smaller contribution to C^+ current from carbon dioxide ionization (less than 0.025% calculated from the dashed lines of Figures 7.4 a and c). Thus, the area beneath the instantaneous signal of m/z = 12 and above the baseline value is indicative of carbon monoxide production from carbon dioxide splitting. Comparing cycle 3 with cycles 2 and 4, it is clear that much less carbon monoxide is produced when water is present, indicating much faster oxidation with water although double the amount of water was used, and the consumption of carbon monoxide to form methane. The much higher reactivity of the material with water relative to carbon dioxide is further supported when one compares the hydrogen signals of cycles 1, 3 and 5 in Figure 7.3 to the m/z = 12 signals of cycles 2 and 4 in Figure 7.4c. The reoxidation is finished in about 3 min when water is present but not completely finished in 15 min (duration of the reoxidation step) when only carbon dioxide is used. This observation also explains the lower amount of oxygen released when water is not used as an oxidant in the previous cycle to reoxidize the material (Table 7.1). Figure 7.5 shows the results of 10 mol% nickel-doped ceria for the same experiment. No methane is produced during the reoxidation steps in cycles 3 and 5, during which both oxidants are used. However, during the heating up of the sample in argon after the reoxidation of cycle 3 (at about 240 min and 1473 K), hydrogen and methane peaks are observed. However, the same is not observed again after the fifth reoxidation, suggesting a rapid deactivation of the material. The deactivation is supported as less hydrogen is produced in cycle 5 than in cycle 3. Generally in this study, nickel-doped ceria exhibits poor dynamic redox capacity. While in the first cycle a relatively significant amount of oxygen is released, the following reoxidation with water produces a much smaller amount of hydrogen. This is confirmed when one compares cycles 1 and 3, which show similar amounts of hydrogen produced but very different amounts of oxygen released. In fact, only very small amounts of oxygen are released from the second cycle onwards. Part of the spent material was further tested for eleven thermochemical cycles, during which the thermal reduction was performed at 1773 K. Similarly, the material exhibits a relatively large amount of oxygen released during the first reduction step, while in the following cycles much less oxygen is observed (Figure 7.6). No methane is observed in any of the reoxidation steps. According to X-ray fluorescence measurements, the material after

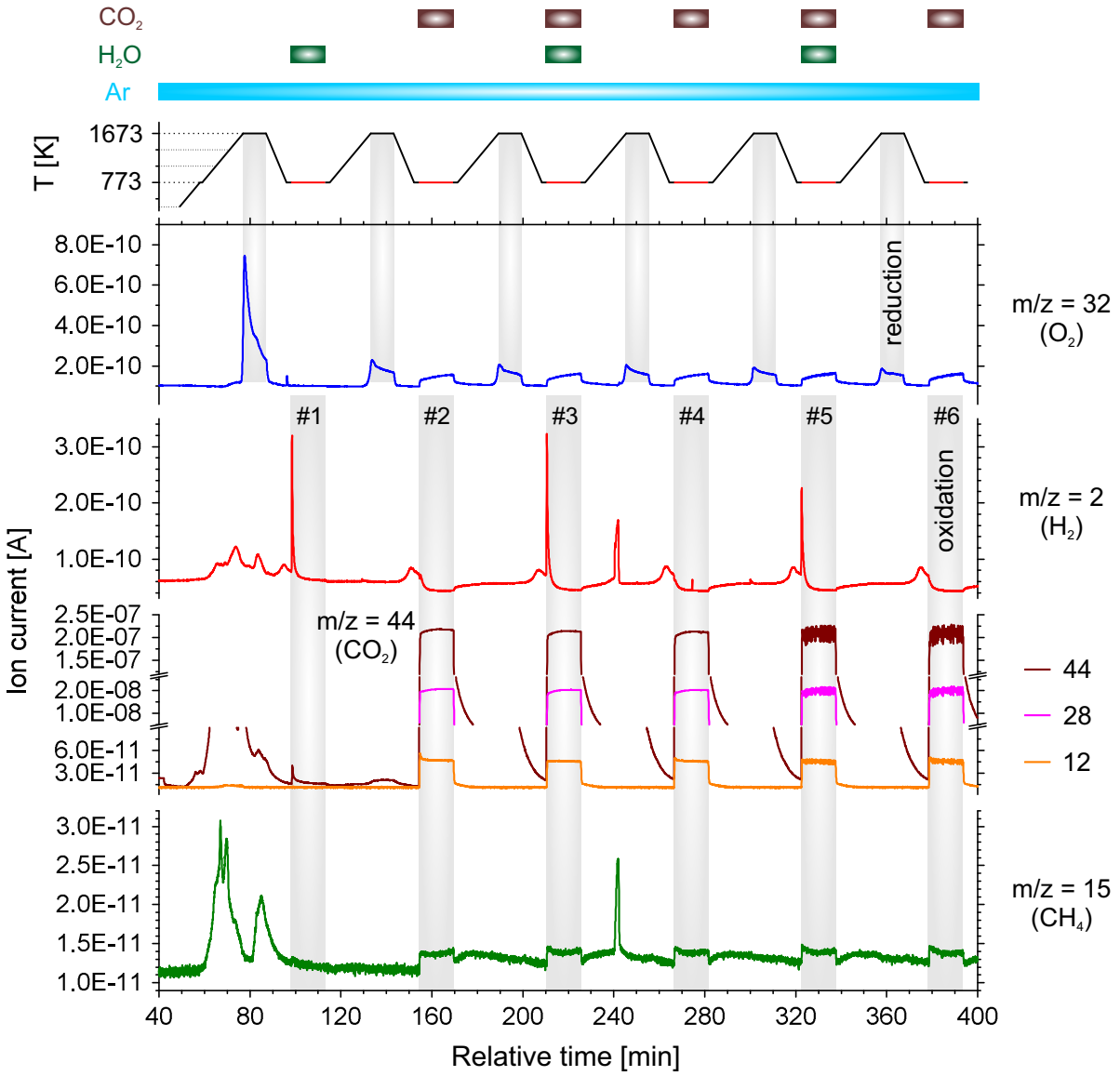

Figure 7.5 Six thermochemical cycles using 10 mol% nickel-doped ceria (ca. 90 mg) with thermal reduction in argon at 1673 K and reoxidation by either water or carbon dioxide, or both, at 773 K. Oxygen evolution profiles shows little reduction after the very first cycle. A very poor apparent redox capacity of nickel-doped ceria in the thermochemical cycles is observed. Methane is not produced when water and carbon dioxide are used simultaneously as the oxidants (cycles 3 and 5). However, after the third reoxidation at about 240 min and 1473 K (sample being heated in argon), hydrogen and methane peaks are observed. This could potentially come from the release of surface hydroxyl groups at the ceria surface and carbon groups at the nickel surface formed during the third reoxidation step. However this was not observed again after the 5th reoxidation step. The regions marked with grey areas indicated the isothermal segments of reduction and oxidation steps.

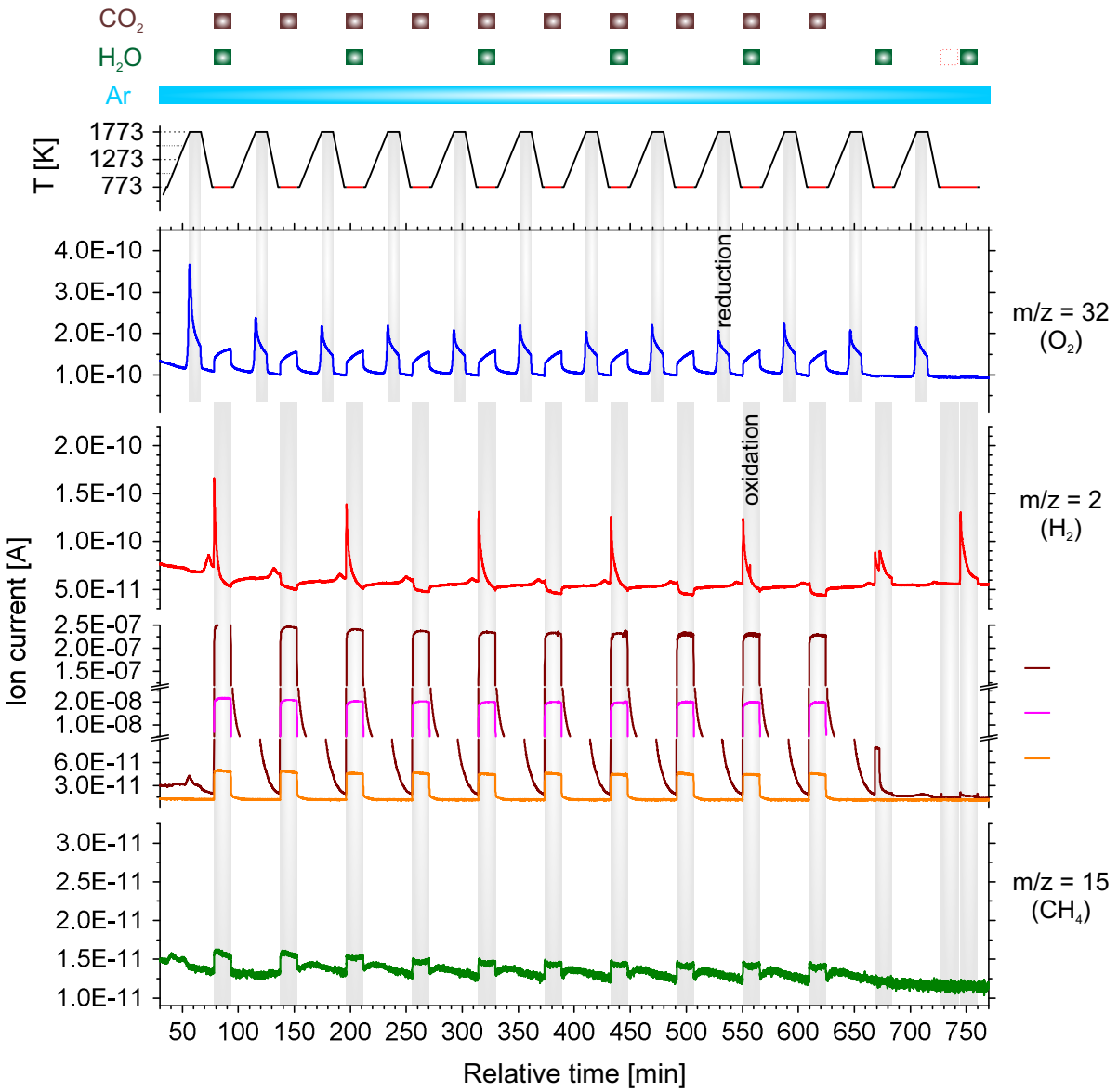

Figure 7.6 Eleven thermochemical cycles using 10 mol% nickel-doped ceria (ca 40 mg) with thermal reduction in argon at 1773 K and reoxidation by either water or carbon dioxide, or both, at 773 K. Oxygen evolution profiles also show little reduction after the first cycle. Again, no methane is produced when water and carbon dioxide are used simultaneously as the oxidants (cycle 1, 3, 5, 7 and 9). The materials used for this experiment firstly underwent six cycles at 1673|773 K.

this experiment contains no nickel while in the fresh material large amounts of nickel are present (Figure 7.12). Thus, essentially all nickel is lost after the eleven cycles. The loss of nickel is further supported by the observation that the alumina sample holder became blue after the experiment. Thus, it is concluded that nickel-doped ceria is not chemically stable at the extreme temperatures required for realistic STCs. This makes nickel-doped ceria unsuitable for direct hydrocarbon fuel production by STCs, although nickel-doped ceria and nickel supported by ceria are active for the formation of methane after they have been reduced by hydrogen at low temperatures, as shown in Figure 7.2 and as reported previously by Chueh and Haile,[295] respectively. Therefore, assessing the thermochemical activity of a redox material at low temperatures by chemical reduction is insufficient to predict its performance under the harsh conditions of realistic STCs. In addition, with pure ceria (without modification of a catalyst) as reactive medium, essentially no methane is produced when both water and carbon dioxide are used simultaneously as oxidants (Figure 7.13) If the thermochemical process based on rhodium-doped ceria is to become significant on an industrial scale, the activity of the material for hydrogen and methane production must be sustained over a large number of cycles. Activity here implies the fuel yield (i.e. the amount of fuel produced per cycle per unit mass of oxide used) and fuel yield per unit time (fuel production rate).

Figure 7.7 presents 59 thermochemical cycles of rhodium-doped ceria with reduction at 1673 K. Both water and carbon dioxide were used as oxidants for the first 58 cycles while only carbon dioxide was used in the last cycle. At first glance, rhodium-doped ceria exhibits a very stable oxygen release, and the peak hydrogen production rate decreases only very slightly during the experiment (Figure 7.7a). This is confirmed when one compares the oxygen as well as the hydrogen evolution profiles between the 5th, 15th, 25th, 35th, 45th, and 55th cycle (Figure 7.14a and b). The amounts of oxygen released, estimated from the area beneath the oxygen evolution curves, stay relatively constant. The oxygen evolution, however, shifts slightly towards the isothermal segments of 1673 K, indicating a slightly decreased rate of reduction. This could be due to the gradual loss of surface area cause by sintering that occurs as the thermochemical cycling progresses. The peak hydrogen ion current, proportional to peak hydrogen concentration and production rate, decreases only slightly as discussed earlier, and the decay of the hydrogen signal becomes slightly slower. Thus, the redox kinetics of the materials is stable during the 59 cycles. In comparison, the signals for methane (m/z = 15, Figure 7.7b) and carbon monoxide (m/z = 12, Figure 7.7c) appear rather different: the peak values decrease gradually and significantly with increasing number of cycles. However, a slow-

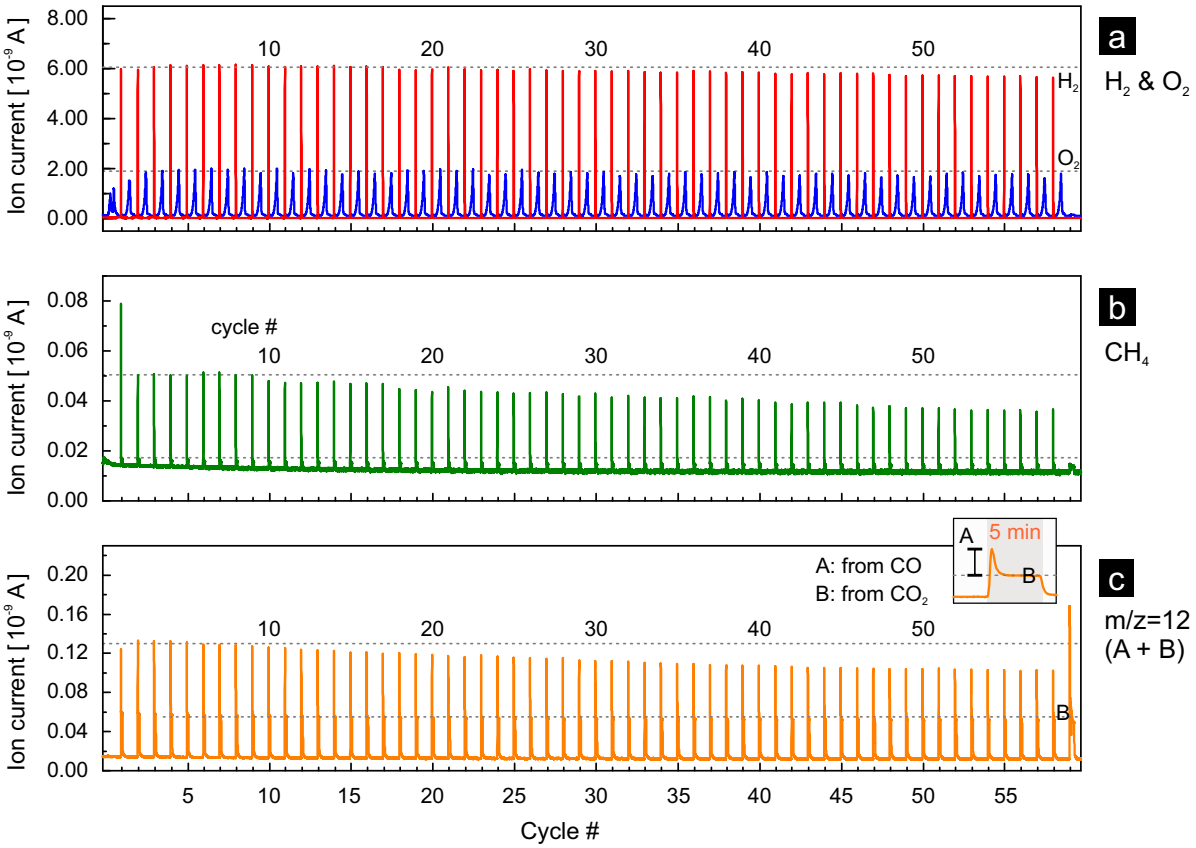

Figure 7.7 Rhodium-doped ceria during 59 thermochemical cycles: (a) hydrogen and oxygen evolution profiles, (b) methane evolution profiles and (c) the m/z = 12 signal. Both water and carbon dioxide were used as oxidants in all cycles except the last cycle, in which only carbon dioxide was used. The contribution of carbon dioxide (B) and carbon monoxide (A) to the MS signal of m/z = 12 is illustrated in the inset of (c). Dashed lines are a guide for the eyes.

ing of the reaction for carbon monoxide and methane production is not observed (Figs. 7.14c and d). Both signals decay to their background values within the same length of time in the fifth and in the 55th cycle. Decreasing amounts of carbon monoxide and methane are produced with increasing number of cycles. Figure 7.8 shows the amounts of hydrogen and oxygen produced per unit mass of oxide (including the H_2/O_2 molar ratio), and the relative carbon monoxide and methane productivities over 59 or 58 cycles. Quantification is based on the data presented in Figure 7.7. Integration of the signals is performed after subtraction of the background. The first cycle is excluded from the discussion as the amount of O_2 released also includes the irreversible reduction of Rh^{3+} (Figure 7.3). Consistent with the discussion earlier, the amount of oxygen released over all 59 cycles remains relatively constant at about 80 μmol O_2/g. The average amount

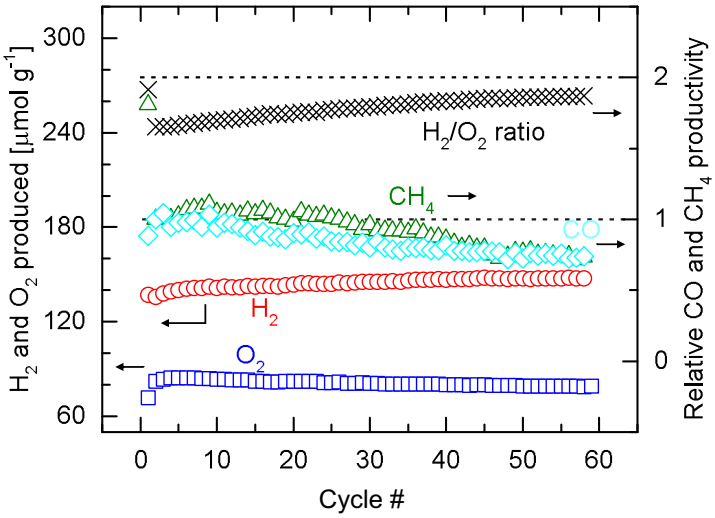

Figure 7.8 Amounts of hydrogen and oxygen evolved per gram of rhodium-ceria, and relative carbon monoxide and methane productivity over 59 or 58 cycles carried out at 1673|773 K. The H_2/O_2 molar ratio is also included.

of oxygen released of the first ten cycles is 83.8 μmol/g. This value slightly decreases to 79.1 μmol/g, the average of the last ten cycles. These values are, however, slightly higher the average value of 72.6 μmol/g reported in Table 7.1. This small difference is most likely due to the fact that different gas mixtures of oxygen and argon were used in the calibration for the two experiments. Despite that, the hydrogen production rate decreases very slightly as discussed earlier (Fig. S65b), increasing amounts of hydrogen are produced over the course of 58 cycles. The average amount of hydrogen produced in the first three cycles is about 136 μmol H_2/g, consistent with the values reported in Table 7.1. The amount of hydrogen produced stabilizes at about 147 μmol/g for the last twenty cycles. Combined with a relatively constant amount of oxygen evolved, the H_2/O_2 molar ratio increases from an initial value of about 1.6 to about 1.8 in the last cycle. The shift of the product selectivity of the reoxidation reaction towards hydrogen is reflected by the gradual decrease in the amounts of methane and carbon monoxide produced (Figure 7.8). The relative methane and carbon monoxide productivities were calculated by normalizing the integrated areas of the background-subtracted m/z = 15 and m/z = 12 signals by their corresponding values of the second cycle (the first cycle excluded from discussion). The methane and carbon monoxide productivities are relatively stable during approximately the first 10 cycles. After 59 cycles the productivities are at about 75% of their initial values. It is estimated based on the H_2/O_2 molar ratio that methane is produced at low quantities and hydrogen is the main product. However,

selectivity to methane can be enhanced significantly by simply adjusting the molar ratio of water to carbon dioxide in the reoxidation gas feed.

The average amount of methane produced increased by 227% when the molar ratio of water to carbon dioxide was decreased to 0.015 from 2.35, a value close to the ratio in the gas used in all previous experiments. Although this particular experiment was carried out in a thermogravimetric analyzer, the comparison was made within the same system, and thus the results are applicable to the main setup we used (Figure 3.2). It is not unrealistic to infer that carbon monoxide and hydrogen could be the intermediates for the formation of methane. However, to elucidate the reaction mechanism for methane formation, further studies with dedicated systems are required. As in the case of nickel-

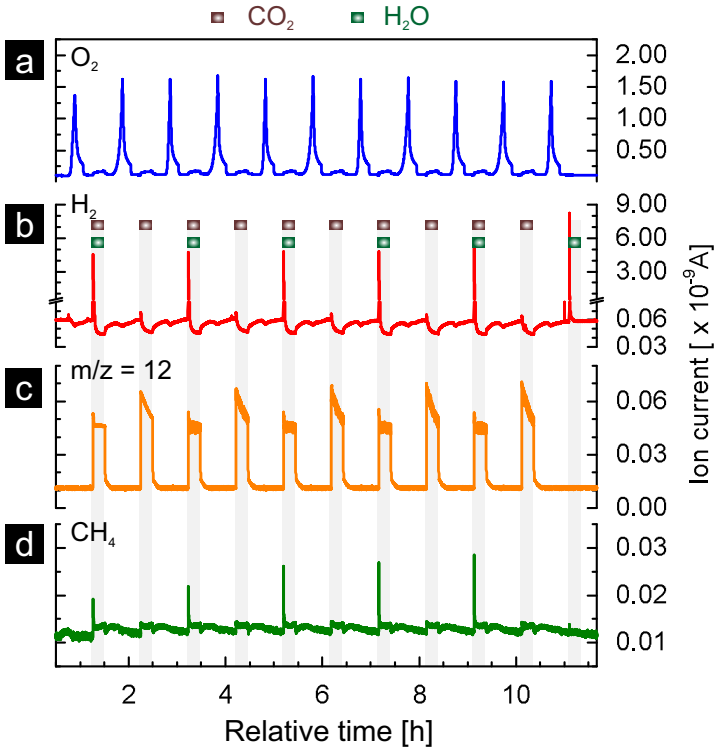

Figure 7.9 Eleven thermochemical cycles of rhodium-doped ceria (93.3 mg) with thermal reduction in argon at 1773 K and reoxidation by either water, carbon dioxide, or both at 773 K: (a) oxygen evolution profiles, (b) hydrogen evolution profiles, (c) the m/z = 12 signal and (d) methane evolution profiles. The reoxidation steps are marked as the grey areas. The sample used in this experiment firstly underwent six cycles at 1673|773 K.

doped ceria, part of the rhodium-doped ceria material used in the 1673|773 K cycles (results presented in Figure 7.3) was also further tested for additional eleven cycles, during which the reduction temperature was increased to 1773 K. Carbon dioxide was

used in the first ten reoxidation steps, while water was switched on and off in alternating cycles. In the last cycle, only water was used as oxidant. These results are presented in Figure 7.9. As clearly shown in Figure 7.9a and b, the oxygen evolution and hydrogen production are stable. This is consistent with the results obtained with the experiment at the lower reduction temperature (Figure 7.7). Unlike in the first cycle of Figure 7.3 and of Figure 7.7, where two peaks are observed in the oxygen evolution profile, only one peak is observed in the first cycle of Figure 7.9. This suggests that no further segregation of rhodium from the ceria lattice occurs at 1773 K during reduction after the material is first reacted at 1673|773 K. The m/z = 12 signal (Figure 7.9c, indicative of carbon monoxide) exhibits similar evolution profiles as the ones presented earlier (Figure 7.4, cycling at 1673|773 K). The methane signal exhibits a clear increase over the tested cycles. Figure 7.10 shows the quantitative results of the hydrogen and oxygen released

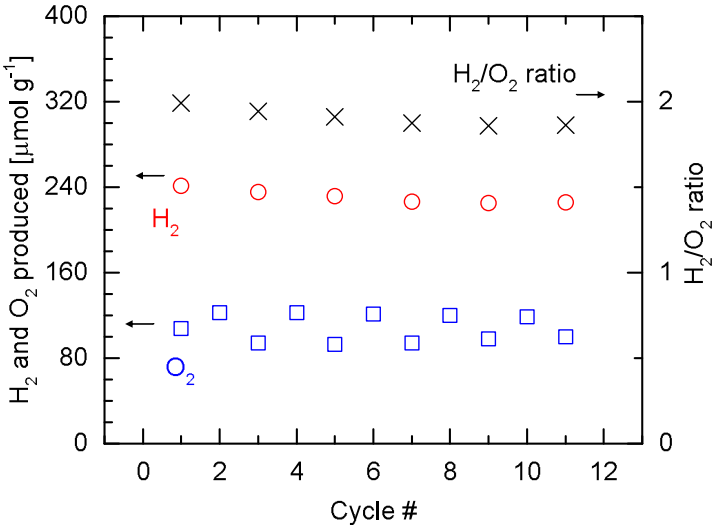

Figure 7.10 Amounts of hydrogen and oxygen evolved per gram of rhodium-doped ceria, and corresponding H2/O2 molar ratios during eleven cycles at 1773|773 K. As in Table 7.1, the amount of oxygen used in calculating the H_2/O_2 ratios is the average value of the amount of oxygen released in even-numbered cycles, during which the material is assumed to be fully reoxidized in the preceding cycles by water.

based on Figure 7.9. Relative carbon monoxide and methane productivities are not presented here as the results of Figures 7.7 and 7.8 suggest that the productivities can be indicated directly by the corresponding peak ion currents. Consistent with Figure 7.3 and Table 7.1, higher or lower amounts of oxygen are observed depending on whether water is switched on or off in the preceding reoxidation steps. Due to the incomplete reoxidation when only carbon dioxide is used as oxidant as discussed earlier, the true

oxygen release at 1773 K is calculated from the values of even-numbered cycles. During these cycles, the material is assumed to be completely reoxidized in the preceding cycles as water is present. On average about 121 μmol/g of oxygen (O_2) can be released. The amount of hydrogen (H_2) produced decreases from an initial value of 199 μmol/g to 186 μmol/g as cycling progresses. Since a constant amount of oxygen released is assumed, the H_2/O_2 ratio also decreases due to the decrease in the amount of hydrogen produced. The decrease in the amount of hydrogen produced is accompanied by an increase of the methane signal (Figure 7.9), illustrating the role of hydrogen as an intermediate towards methane formation. The phase composition of the rhodium-doped ceria after it

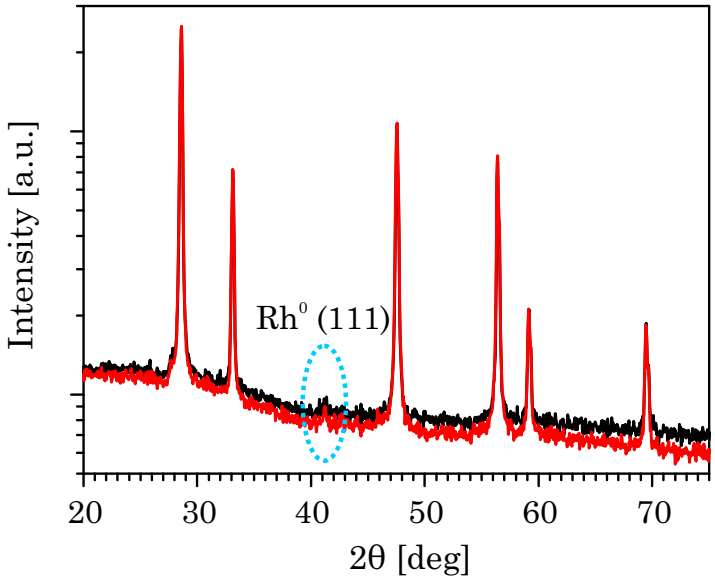

Figure 7.11 XRD diffraction patterns of rhodium-doped ceria samples after six cycles at 1673|773 K and after additional eleven cycles at 1773|773 K.

underwent thermochemical cycles was characterized by X-ray powder diffraction. Figure 7.11 shows that apart from the main phase of fluorite ceria, an additional peak was observed at about $2\theta = 41.6°$ in the sample that was subjected to six cycles at 1673|773 K, and in the sample after additional eleven cycles at 1773|773 K. The additional peak was identified as the (111) reflection of metallic rhodium, which is likely the active catalyst for methane formation. The relative intensity of this rhodium peak for the sample subjected to the additional cycles was essentially of the same magnitude as the one just subjected to the cycles at 1673|773 K. This suggests that, at 1773 K, sintering of the metallic rhodium originating from the irreversible reduction of Rh^{3+} was minimal. The XRD results are encouraging as they indicate thermal stability of the dispersed rhodium particles at extreme temperatures.

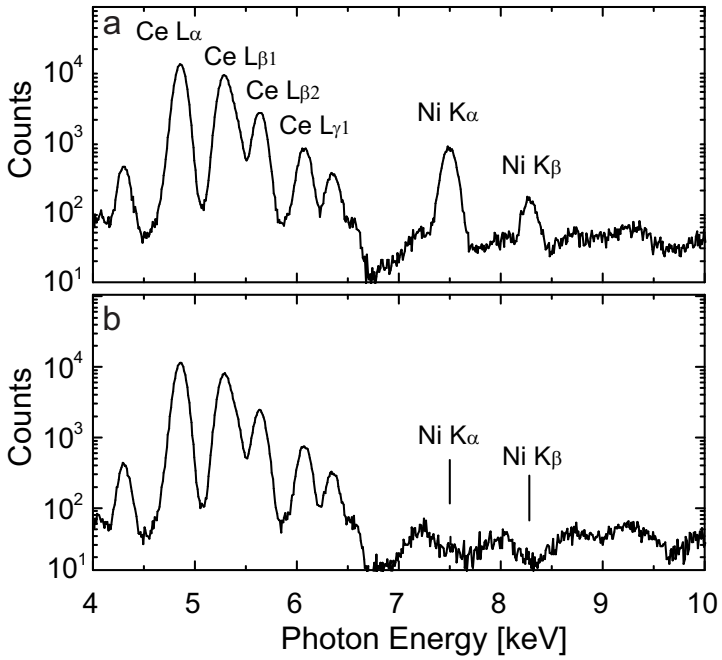

Figure 7.12 X-ray fluorescence spectra of 10 mol% nickel doped ceria a) as-prepared and b) after eleven cycles at 1673|773 K (see Figure 7.5). XRF suggests the complete loss of nickel.

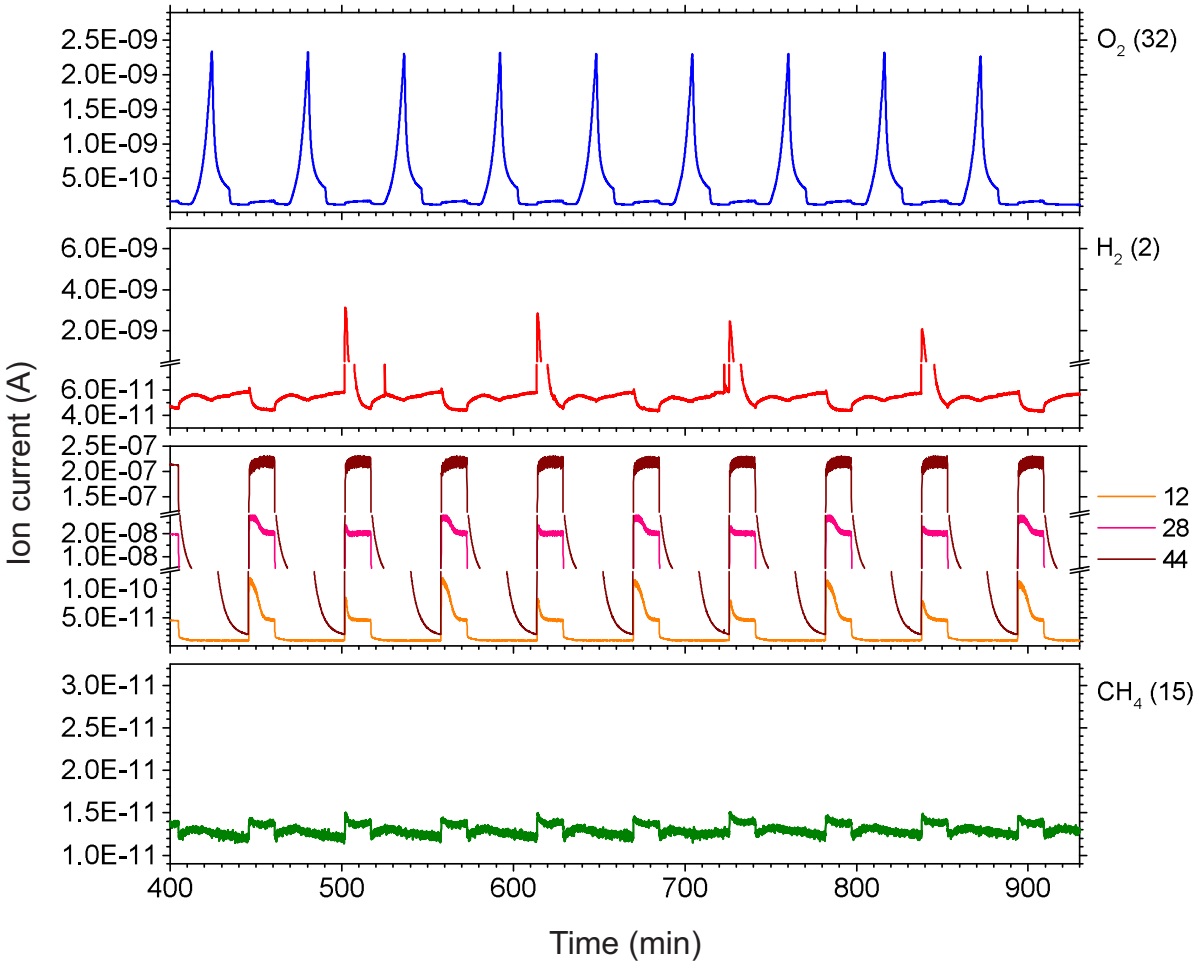

Figure 7.13 Nine thermochemical cycles using pure ceria (≈ 158 mg) with thermal reduction in argon at 1673 K and reoxidation either by only carbon dioxide or by carbon dioxide and water, at 773 K. Oxygen evolution profiles also show stable amounts of oxygen released. Essentially no methane is produced when water and carbon dioxide are used simultaneously as oxidants (even numbered cycles). Note that this experiment with pure ceria was carried out using the same alumina tube reactor after the experiments with rhodium-ceria (Figures 7.3 and 7.9) and nickel-ceria samples (Figure 7.5 and 7.6). The arguably very slight increase of methane signal when both oxidants are used compared to when only carbon dioxide is used, even if it is valid, could be due to the deposition of sublimated nickel (Figure 7.12) at downstream of the reactor during the nickel-ceria experiments. Nevertheless, essentially no methane is produced with pure ceria as reactive medium.

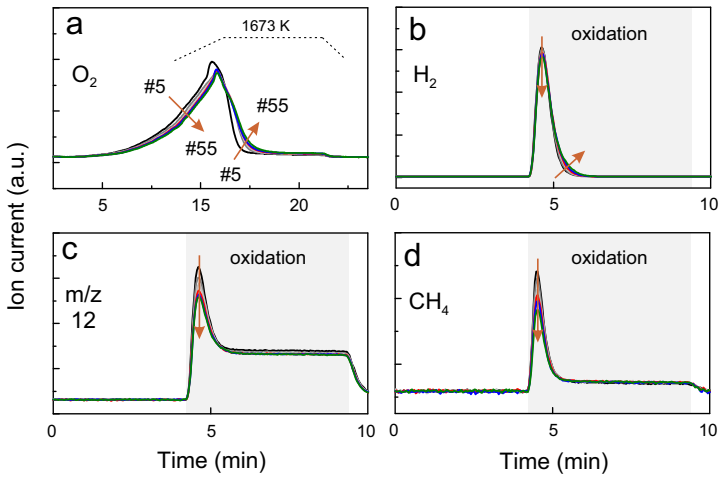

Figure 7.14 Comparison between cycles 5, 15, 25, 35, 45 and 55 during the long-term testing of rhodium-doped ceria at 1673|773 K (results presented in Fig. 7.7): evolution of signals (a) oxygen, (b) hydrogen, (c) m/z = 12 indicative of carbon monoxide, and (d) methane.

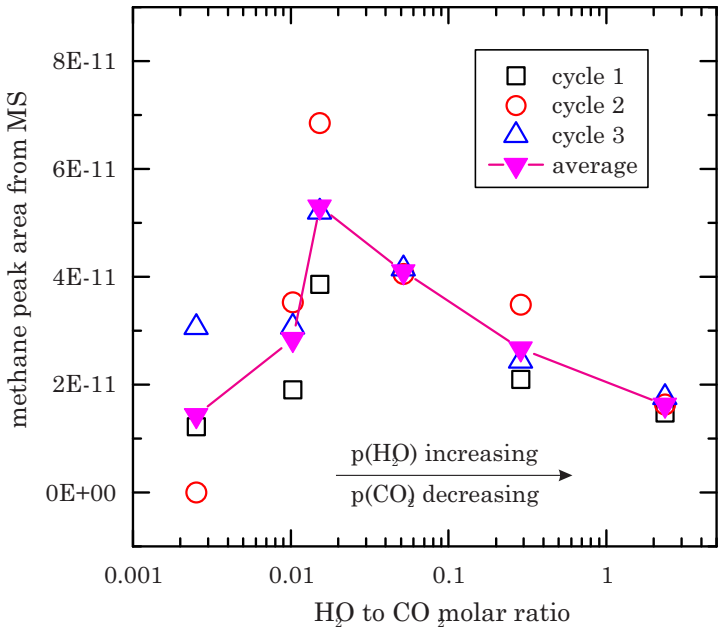

Figure 7.15 The relative amounts of methane produced (peak area beneath methane MS signal) over three consecutive thermochemical cycles using Rh- doped ceria depended on the molar ratio of water to carbon dioxide. The very first data point of the whole series of experiment (cycle 1 at molar ratio 0.0517) was excluded as the background signal of methane was not yet stabilized. For the second to forth ratios (counting from left), the water vapor partial pressures were kept same or very close.

7.3 Conclusions

This study proves the concept of producing hydrocarbon fuels directly from water and carbon dioxide with solar-driven thermochemical cycles. The strategy is to incorporate a catalytic process into the reoxidation steps of STCs. For this purpose, nickel-doped and rhodium-doped ceria have been synthesized by a simple co-precipitation method. Both materials are active in producing methane from water and carbon dioxide after being chemically reduced with hydrogen at 873 K. Nickel-doped ceria, however, is not active anymore in producing methane during reoxidation after being activated at extreme temperatures up to 1773 K. This is attributed to the loss of nickel by sublimation as revealed by X-ray fluorescence. These results with nickel-doped ceria underline the importance of evaluating potential changes of a material's physicochemical properties at extreme temperatures, when thermochemical activity results obtained at low temperatures are used to predict its performance during realistic STCs. With rhodium on ceria, this study demonstrates for the first time that direct and sustained production of methane from water and carbon dioxide by realistic STCs can be achieved. This material exhibits methane, hydrogen and carbon monoxide formation activity during 58 cycles with the activation of the material carried out at 1673 K. Under these conditions the material exhibits constant amounts of oxygen released during activation and stable hydrogen productivity during reoxidation. Some decrease in the carbon monoxide and methane productivity is observed. Encouragingly, the material exhibits steady increase of activity for methane production when activated at 1773 K. X-ray diffraction reveals the presence of metallic rhodium in the materials after cycling at 1673|773 K and after additional cycling at 1773|773 K, indicating metallic rhodium as the active catalyst for methane formation. This proof-of-principle study leaves significant room for improvement and may stimulate a new research area of solar thermochemical fuel production. Future research efforts shall be directed towards improving the product selectivity to methane and potentially to other hydrocarbons, preferably liquid hydrocarbons like oxygenates.

Chapter 8

Conclusions and Outlook

8.1 In situ characterization methods

In the oxygen-depleted state, vacancies can make up a large fraction of several percent of the regular oxygen lattice positions in the fluorite-type structure of ceria. Synchrotron X-ray based methods such as XAS and XRD are high-performance tools for the determination of structure-property relationships that meet the extreme demands of high-temperature in situ structure determination of functional oxides under relevant conditions in a solar thermochemical looping reactor.

X-ray absorption spectroscopy

Changes in the electronic structure of cerium from an oxidation state of 4+ to 3+ can be quantified using the XANES of an absorption edge of cerium, for example at the Ce K edge or the Ce L_{III} edge. The high penetration depth of X-rays at the energy of the Ce K edge facilitates the design of an in situ cell for measurements under the harsh conditions of solar thermochemical looping. The absence of complex spectral features in Ce K edge XANES spectra facilitates the accurate quantification of changes in the energy of the edge position, which is proportional to the non-stoichiometry. A simple but effective and robust method was developed which is only weakly affected by changes in temperature from 298-1773 K. A time resolution of approximately 1 min^{-1} was achieved. Using XAS in transmission mode, also edges of dopant elements such as the Zr K edge (see Chapter 5) or the Hf K edge (see Chapter 6) can be measured. The higher the concentration of a hetero-cation and the higher the energy of its absorption edge, the more favorable is the signal/noise ratio of the transmitted intensity. The setup for in situ XAS is versatile and not limited to ceria-based materials. Absorption edges of heavy atoms in perovskites for solar thermochemical looping, such as the La K edge of $La_{0.6}Sr_{0.4}Cr_{0.8}Co_{0.2}O_{3-\delta}$ can be readily measured in situ for the determination of structural changes in the lanthanum-oxygen coordination.

X-ray diffraction

Oxygen storage materials are highly crystalline materials containing elements with high X-ray scattering cross sections. XRD gives a separate, distinct signal for every structure in the sample with long-range order. The X-ray scattering cross section is proportional to the electron density. Thus, the diffracted intensity of cerium and other heavy elements such as zirconium and hafnium is high. The formation of Ce^{3+} gives rise to an expansion

of the crystal lattice often referred to as chemical expansion. In the diffraction pattern, both the thermal and the chemical expansion cause a shift to lower scattering angles. We followed the structural dynamics of cation ordering in equimolar ceria-zirconia and ceria-hafnia materials during auto-reduction and relevant isothermal carbon dioxide splitting conditions at 1773 K by time-resolved in situ XRD. XRD is less limited by the composition of the material and other types of solid oxygen storage materials such as perovskites or ferrites can be readily investigated.

Quasi-simultaneous in situ XAS and XRD in transmission mode

Chapter 3 presents a cutting-edge setup for combined, quasi-simultaneous in situ XAS, in situ XRD and on-line mass spectrometry. This unique setup is certainly among the most powerful characterization tools available for ceria-based oxygen storage materials under the extreme conditions in a solar thermochemical looping reactor. Ce K edge XAS provides valuable complementary information on the average oxidation state of cerium and enables direct determination of the oxygen storage capacity. XAS at other edges, such as the Zr K edge provides valuable additional information about the local structure of these elements. The measurement system is redundant - for example, the amount of oxygen released during the reduction of the material can be determined from the change in the electronic structure of cerium by XAS, by the chemical expansion of the crystal lattice (XRD) and quantification of the amount of oxygen in the product gas stream by mass spectrometry. In mixed oxides such as ceria-zirconia and ceria-hafnia with absorption edges that are accessible in transmission mode, the local structure of hetero-cations can be determined and EXAFS analysis of spectra collected at room temperature can readily be carried out. The main experimental difficulty is the reproducibility of the sample position in the measurement cell. There are three main approaches for the improvement of in situ XAS and XRD experiments in transmission mode under solar thermochemical reactor conditions: firstly higher accuracy of the monochromator movement will enable unparalleled precision and accuracy in the determination of the average oxidation state of cerium. Secondly, pellets with higher quality, homogeneity and mechanical stability for measurements in transmission geometry will improve data quality and substantially reduce time required for measurements. Thirdly, unprecedented accuracy in the determination of structure-property relationships can be achieved by enhancing the accuracy of of the oxygen partial pressure measurement in the in situ cell. In Chapter 3, further

highly promising modifications to increase the accuracy and precision of the in situ XRD measurements are highlighted.

8.2 Alternative characterization methods

A large number of characterization methods are available for measuring bulk and surface properties of ceria-based materials. A short description of three methods that might prove useful to detect and determine crystal structures, to verify and refine defect models and to elucidate the surface reaction mechanisms of non-stoichiometric oxygen storage materials under solar thermochemical looping conditions follows.

Neutron diffraction

In contrast to X-ray photons, the scattering cross section of an atom is not proportional to the number of electrons because neutrons interact with nuclei. In addition, the intensity of neutron diffraction peaks is independent of the scattering angle. The relative scattering power of oxygen is much higher for neutrons than for X-rays, which makes neutron scattering the method of choice for the precise determination of the position of oxygen atoms in complex materials such as oxide superconductors. Neutron diffraction of powders and single crystals was used to elucidate the crystal structure of non-stoichiometric ceria-based materials at ambient conditions,[174,222,223] and up to 1073 K at a pressure of 10^{-6} Torr,[219] at up to 1064 K in a sealed niobium container,[220] at 1823 K in air,[184] at 1273 K at a controlled oxygen partial pressure,[100] at up to 898 K sealed in a quartz tube with inert gas,[221] at up to 1701 K in air[183] and at 1123 K in air.[224] Neutron scattering is an excellent tool for the detection and determination of phases with an ordered arrangement of oxygen vacancies. The phase boundaries in the ceria-hafnia system are known in less detail than those of the ceria-zirconia system and can be determined by X-ray and neutron diffraction.

Positron annihilation lifetime spectroscopy

The positron is the antimatter counterpart of the electron. The annihilation of a positronium – a bound state consisting of a positron and an electron – occurs in different modes, but irrespective of the annihilation mode it creates two gamma rays of 0.511 MeV. PALS is based on the determination of the lifetime of positrons which depends on the electron density in a material. The lifetime of a positronium depends on the size, type and

concentration of defects. PALS can detect very low concentrations of defects down to the ppm level and has been successfully applied to characterize vacancies in ceria.[229,230] PALS might be a very powerful tool to better characterize the rather elusive vacancies and different types of vacancy clusters as a function of non-stoichiometry and temperature.

X-ray photoelectron spectroscopy

The kinetics of the surface reaction of the oxidation step of the thermochemical cycles is the rate-limiting step. The complex interplay of processes and the dynamic structures at the solid-gas interface are not yet well understood. XPS is a powerful surface-sensitive method that enables measurements at relevant oxygen partial pressure of solar thermochemical looping. Near ambient pressure XPS measurements of ceria at up to 923 K have been performed with a synchrotron X-ray source and differential pumping stages.[132,133] At the temperature required for ceria-based solar thermochemical cycles, XPS might be limited by thermionic emission of electrons. A better understanding of the structures and processes at the solid-gas interface during the re-oxidation of oxygen storage materials might be achieved by time-resolved XPS.

8.3 Materials

Although a large number of ceria-based mixed oxides have been investigated, a material that performs better than pure ceria has not yet been identified. Thermodynamic models suggest that modifying ceria with heterocations leads to less favorable water- and carbon dioxide splitting properties. Despite the rather small compositional space of fluorite-type, ceria-based materials, the 'right' combination of heterocations has not yet been found.

Pyrochlore-type materials

Isothermal carbon dioxide splitting experiments (Chapter 6) suggest that the ordered ceria-hafnia pyrochlore structure is not stable upon oxidation at high temperature. The stability, the thermodynamics and the diffusion coefficients of oxygen storage materials of the ceria-zirconia and ceria-hafnia pyrochlore type are not known. Thermogravimetric measurements could provide the required data.

Ceria-urania and ceria-thoria

The actinides uranium and thorium are among the few elements that have not yet been tested as dopants in ceria for high-temperature thermochemical reactions. Both elements form oxides with a fluorite-type structure. Radioactive materials are unlikely to be used for water splitting on an industrial scale, however they are very interesting from an academic perspective. Uranium dioxide forms a fluorite-type solid solution with ceria over the whole composition.[215] In air at high temperature other phases formed due to oxidation of uranium(IV) to uranium(VI) and formation of orthorhombic U_3O_8.[215,305] A high water-splitting activity of ceria-urania materials after reduction with hydrogen was found.[306] The average oxidation states of cerium and uranium in ceria-urania solid solutions can be determined by in situ XAS in transmission mode at the Ce K and U L_{III} edges in a single experiment. ESRF safety regulations do not permit changes in the temperature of radioactive materials.
The non-stoichiometry of thoria and ceria-thoria is unknown. Heavy elements are very likely to improve the stability of materials at high temperature.

Rhodium-ceria

The structure and stability of rhodium-ceria materials needs further investigation because it is not clear to what extent rhodium is incorporated in the lattice during both steps of the thermochemical cycle. Because of the low rhodium loading, XRD did not detect an increase in metallic Rh after thermochemical cycling. Depth-profiling using a surface-sensitive method such as XPS can give insights into the concentrations of rhodium on the surface and in the bulk. Due to the low loading, the Rh K edge (23.220 keV) edge cannot be accessed by in situ XAS experiments in transmission mode. XAS in fluorescence mode at the Rh K or the Rh L_{III} edge (3.004 keV) could give valuable insights into the structure of rhodium before and after thermochemical cycling. The average oxidation state of rhodium can also be determined by XPS. Little is known about the volatility of rhodium and rhodium oxides under these conditions. There is no evidence that the same amount of rhodium was present after the long-term stability tests. Sublimation of metal oxides are very common at high temperature – for example, sublimation of ceria[66,129,216] or tungsten oxide.[63]

8.4 Final thoughts

Synchrotron X-rays proved invaluable for the characterization of novel materials for two-step solar thermochemical fuel production. In situ XAS and XRD provided new insights into the electronic and local geometric structure of cerium and dopant elements as well as the symmetry and lattice parameters of relevant phases in ceria-based materials under relevant reaction conditions. Our approach is holistic and applicable to other oxygen storage materials such as perovskites or ferrites.

The accurate determination of thermodynamic quantities and the development of defect models are valuable contributions in the quest for better oxygen storage materials for the thermochemical conversion of solar energy. In any case, it is indispensable to validate these models with high-precision structural data measured under relevant reaction conditions.

Besides the improvement of in situ characterization using a combination of XRD, XES and XAS at high-temperature, future work should consider neutron diffraction, positron annihilation lifetime spectroscopy and X-ray photoelectron spectroscopy as characterization tools to increase our knowledge of materials with two-step solar thermochemical water or carbon dioxide splitting capability.

Publications

Journal Articles

- Rothensteiner, M., Bonk, A., Vogt, U. F., Emerich, H., and van Bokhoven J. A. "Structural changes in equimolar ceria-hafnia materials under solar thermochemical looping conditions: cation ordering, formation and stability of the pyrochlore structure" (submitted)

- Rothensteiner, M., Jenni, J., Emerich, H., Bonk, A., Vogt, U. F., van Bokhoven, J. A. (2017). "In situ flow cell for combined X-ray absorption spectroscopy, X-ray diffraction, and mass spectrometry at high photon energies under solar thermochemical looping conditions"'. Rev. Sci. Instrum., 88(8), 83116. http://doi.org/10.1063/1.4994890

- Lin, F., Rothensteiner, M., Alxneit, I., van Bokhoven, J. A., and Wokaun, A. (2016). "First demonstration of direct hydrocarbon fuel production from water and carbon dioxide by solar-driven thermochemical cycles using rhodium–ceria". Energy Environ. Sci., 9(7), 2400–2409. http://doi.org/10.1039/C6EE00862C

- Rothensteiner, M., Bonk, A., Vogt, U. F., Emerich, H., and van Bokhoven, J. A. (2016). "Structural changes in $Ce_{0.5}Zr_{0.5}O_{2-\delta}$ under temperature-swing and isothermal solar thermochemical looping conditions determined by in situ Ce K and Zr K edge X-ray absorption spectroscopy". The Journal of Physical Chemistry C, 120(26), 13931–13941. http://doi.org/10.1021/acs.jpcc.6b03367

- Rothensteiner M., Sala S., Bonk A., Vogt U. F., Emerich, H. and van Bokhoven J.A. (2015). "Ce K edge XAS of ceria-based redox materials under realistic conditions for the two-step solar thermochemical dissociation of water and/or CO_2." Phys. Chem. Chem. Phys., 17(40), 26988–26996. http://doi.org/10.1039/C5CP03179F

- Kato, S., Ammann, M., Huthwelker, T., Paun, C., Lampimäki, M., Lee, M.-T., Rothensteiner, M. and van Bokhoven, J. A. (2015). "Quantitative depth profiling of Ce^{3+} in Pt/CeO_2 by in situ high-energy XPS in a hydrogen atmosphere". Phys. Chem. Chem. Phys., 17(7), 5078–5083. http://doi.org/10.1039/C4CP05643D

Conference Contributions

Talks

- Rothensteiner M., Emerich H., van Bokhoven J.A. "Determination of the electronic and geometric structure of redox materials for solar thermochemical cycles using in situ XAS", 1st International Conference on Solar Fuels, Uppsala, Sweden, 29.4. 2015.

- Rothensteiner M., Sala S., Emerich H., van Bokhoven J.A. "In situ XAS of ceria materials for the thermochemical conversion and storage of concentrated solar thermal power". 249th ACS National Meeting & Exposition, Denver, CO, 23.3.2015.

- Rothensteiner M., Sala S., Emerich H., van Bokhoven J.A. "In situ XAS of ceria redox materials under relevant conditions for solar thermochemical fuel generation". Photon Tools for Physical Chemistry, Beatenberg, Switzerland, 1.10.2015.

- Rothensteiner M., Sala S., Bonk A., Vogt U., Emerich H., van Bokhoven J.A., "Performance and in situ characterization of ceria-based non-stoichiometric oxides for the conversion of solar energy using two-step thermochemical cycles". Fall Meeting of the Swiss Chemical Society, University of Zurich, Switzerland, 11.9.2014.

- Rothensteiner M., Emerich H., van Bokhoven J.A. "In situ XAS of ceria redox materials for two-step solar thermochemical H_2O and CO_2 splitting". Swiss Light Source (SLS) Symposium on Spectroscopy, PSI Villigen, Switzerland, 1.4.2014.

Poster presentations

- Rothensteiner M., Bonk A., Emerich H., van Bokhoven J.A. "In situ X-ray Absorption Spectroscopy of $Ce_{0.5}Zr_{0.5}O_{2-\delta}$ at 1773 K", Fall Meeting of the Swiss Chemical Society, Catalysis Engineering and Technology Poster Session, EPFL Lausanne, Switzerland, 4.9.2015.

- Rothensteiner M., Sala S., Emerich H., van Bokhoven J.A. "In situ XAS of ceria materials for the thermochemical conversion and storage of concentrated solar thermal power". Sci-Mix Poster session, 249th ACS National Meeting & Exposition, Denver, CO, 23.3.2015
- Rothensteiner M., Emerich H., van Bokhoven J.A. "In situ XAS of CeO_2-based materials for two-step solar thermochemical H_2O and CO_2 splitting". Fall Meeting of the Swiss Chemical Society, Catalysis Engineering and Technology Poster Session, EPFL Lausanne, Switzerland, 6.9.2013.

Acknowledgements

Looking back on the long and winding road of this PhD journey, I would like to thank many people I had the opportunity to meet and who supported my work at PSI, at ETH in Zürich and at the ESRF in Grenoble. Without their support and help, it would not have been possible to write this thesis.

I would like to thank Prof. Jeroen Anton van Bokhoven for giving me the opportunity to work on this project at ETH Hönggerberg. Thank you very much for your scientific guidance, the discussions about the project and research in general, your feedback and corrections in the writing process of the manuscripts and the thesis.

Bei Prof. Alexander Wokaun möchte ich mich für die Übernahme des Korreferats sowie für die Ermöglichung der Zusammenarbeit mit dem Solartechnologie-Labor am PSI bedanken.

The financial support by CCEM (Proposal #701) is greatly appreciated.

Prof. Aldo Steinfeld danke ich für die wissenschaftliche Leitung dieses interdisziplinären Forschungsprojektes, seine Unterstützung von Kollaborationen und den regen Informationsaustausch. Mein Dank gilt den Mitgliedern seiner Forschungsgruppe - Prof. Jonathan Scheffe, Dr. Simon Ackerman, Dr. Michael Takacs und Dr. Daniel Marxer für die wissenschaftlichen Diskussionen, u.a. bei den halbjährlichen Projektmeetings. Mein Dank gilt Prof. Ulrich Vogt für die unkomplizierte Zusammenarbeit, sowie für die Korrektur der Manuskripte. Alexander Bonk für die guten Gespräche über Wissenschaftliches und vieles mehr, die zuverlässige Unterstützung während Strahlzeiten, den Austausch von Proben aller Art und Durchführung von Messungen an der EMPA. Für ihre Beiträge in den Projektmeetings möchte ich Prof. Greta Patzke und Roger Jacot sowie Prof. Jennifer Rupp danken. Dr. Alexander H. Bork, thanks for the coffee and lunch breaks, the discussions about our work and the chance to forget about all that for a while on the soccer field. Dr. Fangjian Lin, thank you for a very exciting and fruitful collaboration, and good discussions. Vielen Dank auch an Dr. Ivo Alxneit für die Zusammenarbeit am PSI.

I'd like to thank Simone Sala and Sotiria Mostrou for the good work in their master thesis projects. Erich de Boni, Markus Mähr, Lukas Oberer und Thanh-Binh Truong am PSI, Jan Kovacovic, Joel Jenni, Fredy Mettler, Max Wohlwend und dem Team der ICB Werkstätte an der ETH danke ich für technische Unterstützung aller Art, insbesondere beim Bau der Apparatur und der Messzellen. Charlotte, Daniela and Doris, thanks for your support at PSI and ETH. I would like to thank Dr. Marco Ranocchiari for his support at PSI and for providing lab space in his research group. A very special thank you goes to Dr. Maarten Nachtegaal for his encouragement and constructive criticism, as well as his support with the interpretation of EXAFS data.

Eine grosse Herausforderung in diesem Projekt war die Durchführung von Messungen an der Strahllinie BM01B der Swiss-Norwegian Beamlines am ESRF in Grenoble. Mein Dank gilt Dr. Hermann Emerich: Vielen Dank für die technische Unterstützung bei der experimentellen Arbeit, die wissenschaftlichen Diskussionen und Deinen Beitrag zur Konstruktion der Hochtemperatur-XAS/XRD Messzelle sowie auch für Deine fundierte, konstruktive Kritik bei der Erstellung der Manuskripte. A big thank you to everybody who assisted me night and day at the beamlines: Dr. Alexander Bonk, Dr. Flavien Morel, Dr. Urs Hartfelder, René Kopelent, Simone Sala, Dr. Alexander H. Bork, Dr. Fangjian Lin, Dr. Kim Meyer, Petr Sot, Jerick Imbao, Jacinta Moraa Xto, Amy Jenelle Knorpp and Sotiria Mostrou.

I would like to thank all the members of the van Bokhoven group 2012-2016 who contributed to a good working environment. Thanks for the lunch and coffee breaks and activities outside the lab.

Ich danke allen Sängerinnen und Sängern im Akademischen Chor Zürich mit Dirigentin Anna Jelmorini und den krassä Zürcher Chorbuebe für die gemeinsame Freude an der Musik und die Freundschaft.

Ich danke meiner Tante Maridl für erholsame Wochenenden am Vierwaldstättersee. Besonderer Dank gilt meinen Eltern und Geschwistern und Alina.

Villigen - Grenoble - Zurich
(2012 - 2016)

References

[1] IEA, *Key World Energy Trends - Excerpt from: World energy balances*; 2016; p 4.

[2] IPCC, Climate Change 2013 - The Physical Science Basis. 2014; http://ebooks.cambridge.org/ref/id/CBO9781107415324.

[3] World Map Direct Normal Irradiation. 2016; http://geosun.co.za/wp-content/uploads/2014/10/DNI-Solar-map-World.png.

[4] Graetzel, M. *Accounts of Chemical Research* **1981**, *14*, 376–384.

[5] O'Regan, B.; Grätzel, M. *Nature* **1991**, *353*, 737–740.

[6] Nocera, D. G. *Accounts of Chemical Research* **2012**, *45*, 767–776.

[7] Mendelsohn, M.; Lowder, T.; Canavan, B. *National Renewable Energy Laboratory* **2012**, *303*, 275–3000.

[8] Meier, A.; Steinfeld, A. In *Solar Energy in Thermochemical Processing*; Richter, C., Lincot, D., Gueymard, C. A., Eds.; Springer New York: New York, NY, 2013; pp 521–552.

[9] Gil, A.; Medrano, M.; Martorell, I.; Lázaro, A.; Dolado, P.; Zalba, B.; Cabeza, L. F. *Renewable and Sustainable Energy Reviews* **2010**, *14*, 31–55.

[10] Medrano, M.; Gil, A.; Martorell, I.; Potau, X.; Cabeza, L. F. *Renewable and Sustainable Energy Reviews* **2010**, *14*, 56–72.

[11] Solucar, *10 MW Solar Thermal Power Plant for Southern Spain*; 2006; pp 1–10.

[12] Brightsource, Ivanpahsolar. 2013; http://www.ivanpahsolar.com/.

[13] Marxer, D.; Furler, P.; Scheffe, J.; Geerlings, H.; Falter, C.; Batteiger, V.; Sizmann, A.; Steinfeld, A. *Energy & Fuels* **2015**, *29*, 3241–3250.

[14] Haszeldine, R. S. *Science* **2009**, *325*, 1647–1652.

[15] Pires, J. C. M.; Martins, F. G.; Alvim-Ferraz, M. C. M.; Simões, M. *Chemical Engineering Research and Design* **2011**, *89*, 1446–1460.

[16] Steinfeld, A. *International Journal of Hydrogen Energy* **1998**, *23*, 767–774.

[17] Steinfeld, A.; Zurich, C.; Palumbo, R. SOLAR THERMOCHEMICAL PROCESS TECHNOLOGY. 2001.

[18] Steinfeld, A.; Meier, A. *Encyclopedia of Energy*; Elsevier, 2004; Vol. 5; pp 623–637.

[19] Perkins, C.; Weimer, A. W. *International Journal of Hydrogen Energy* **2004**, *29*, 1587–1599.

[20] Steinfeld, A. *Solar Energy* **2005**, *78*, 603–615.

[21] Kodama, T.; Gokon, N. *Chemical reviews* **2007**, *107*, 4048–77.

[22] Steinfeld, A.; Weimer, A. W. *Optics express* **2010**, *18*, A100–11.

[23] Petrasch, J.; Klausner, J. *Wiley Interdisciplinary Reviews: Energy and Environment* **2012**, *1*, 347–361.

[24] Roeb, M.; Neises, M.; Monnerie, N.; Call, F.; Simon, H.; Sattler, C.; Schmücker, M.; Pitz-Paal, R. *Materials* **2012**, *5*, 2015–2054.

[25] Smestad, G. P.; Steinfeld, A. *Industrial & Engineering Chemistry Research* **2012**, *51*, 11828–11840.

[26] Romero, M.; Steinfeld, A. *Energy & Environmental Science* **2012**, *5*, 9234.

[27] Xiao, L.; Wu, S.-Y.; Li, Y.-R. *Renewable Energy* **2012**, *41*, 1–12.

[28] D'Souza, L. *Materials for Renewable and Sustainable Energy* **2013**, *2*, 7.

[29] Agrafiotis, C.; Roeb, M.; Sattler, C. *Renewable and Sustainable Energy Reviews* **2015**, *42*, 254–285.

[30] Yadav, D.; Banerjee, R. *Renewable and Sustainable Energy Reviews* **2016**, *54*, 497–532.

[31] Roeb, M. et al. *Solar Energy* **2011**, *85*, 634–644.

[32] IEA, *Technology Roadmap: Concentrating Solar Power*; IEA Technology Roadmaps; OECD Publishing, 2010; Vol. 5; pp 1–52.

[33] Holladay, J.; Hu, J.; King, D.; Wang, Y. *Catalysis Today* **2009**, *139*, 244–260.

[34] Funk, J. E.; Reinstrom, R. M. *Industrial & Engineering Chemistry Process Design and Development* **1966**, *5*, 336–342.

[35] Fletcher, E. a.; Moen, R. L. *Science* **1977**, *197*, 1050–1056.

[36] Nakamura, T. *Solar Energy* **1977**, *19*, 467–475.

[37] Ihara, S. *International Journal of Hydrogen Energy* **1978**, *3*, 287–296.

[38] E. Funk, J. *International Journal of Hydrogen Energy* **2001**, *26*, 185–190.

[39] Nigara, Y.; Cales, B. *Bulletin of the Chemical Society of Japan* **1986**, *59*, 1997–2002.

[40] Bamberger, C. *Cryogenics* **1978**, *18*, 170–183.

[41] Yalçin, S. *International Journal of Hydrogen Energy* **1989**, *14*, 551–561.

[42] Abanades, S.; Charvin, P.; Flamant, G.; Neveu, P. *Energy* **2006**, *31*, 2805–2822.

[43] Liberatore, R.; Lanchi, M.; Giaconia, A.; Tarquini, P. *International Journal of Hydrogen Energy* **2012**, *37*, 9550–9565.

[44] Meredig, B.; Wolverton, C. *Physical Review B* **2009**, *80*, 1–8.

[45] Meredig, B.; Wolverton, C. *Physical Review B* **2011**, *83*, 239901.

[46] Miller, J. E.; Allendorf, M. D.; Diver, R. B.; Evans, L. R.; Siegel, N. P.; Stuecker, J. N. *Journal of Materials Science* **2008**, *43*, 4714–4728.

[47] Ermanoski, I.; Miller, J. E.; Allendorf, M. D. *Physical chemistry chemical physics : PCCP* **2014**,

[48] Muhich, C. L.; Ehrhart, B. D.; Al-Shankiti, I.; Ward, B. J.; Musgrave, C. B.; Weimer, A. W. *Wiley Interdisciplinary Reviews: Energy and Environment* **2016**, *5*, 261–287.

[49] Siegel, N. P.; Miller, J. E.; Ermanoski, I.; Diver, R. B.; Stechel, E. B. *Industrial & Engineering Chemistry Research* **2013**, *52*, 3276–3286.

[50] Muhich, C. L.; Ehrhart, B. D.; Witte, V. A.; Miller, S. L.; Coker, E. N.; Musgrave, C. B.; Weimer, A. W. *Energy Environ. Sci.* **2015**, *8*, 3687–3699.

[51] Roeb, M.; Sattler, C. *Science (New York, N.Y.)* **2013**, *341*, 470–1.

[52] Muhich, C. L.; Evanko, B. W.; Weston, K. C.; Lichty, P.; Liang, X.; Martinek, J.; Musgrave, C. B.; Weimer, A. W. *Science* **2013**, *341*, 540–542.

[53] Hao, Y.; Yang, C.-K.; Haile, S. M. *Physical chemistry chemical physics : PCCP* **2013**, *15*, 17084–92.

[54] Bader, R.; Venstrom, L. J.; Davidson, J. H.; Lipiński, W. *Energy & Fuels* **2013**, *27*, 5533–5544.

[55] Venstrom, L. J.; De Smith, R. M.; Hao, Y.; Haile, S. M.; Davidson, J. H. *Energy & Fuels* **2014**, *28*, 2732–2742.

[56] Hathaway, B. J.; Bala Chandran, R.; Gladen, A. C.; Chase, T. R.; Davidson, J. H. *Energy & Fuels* **2016**, *30*, 6654–6661.

[57] Davenport, T. C.; Yang, C.-k.; Kucharczyk, C. J.; Ignatowich, M. J.; Haile, S. M. **2016**, 1–8.

[58] Weidenkaff, A.; Steinfeld, A.; Wokaun, A.; Auer, P.; Eichler, B.; Reller, A. *Solar Energy* **1999**, *65*, 59–69.

[59] Weidenkaff, A.; Reller, A.; Wokaun, A.; Steinfeld, A. *Thermochimica Acta* **2000**, *359*, 69–75.

[60] Loutzenhiser, P. G.; Meier, A.; Steinfeld, A. *Materials* **2010**, *3*, 4922–4938.

[61] Levêque, G.; Abanades, S.; Jumas, J. C.; Olivier-Fourcade, J. *Industrial and Engineering Chemistry Research* **2014**, *53*, 5668–5677.

[62] Levêque, G.; Abanades, S. *Thermochimica Acta* **2015**, *605*, 86–94.

[63] Milshtein, J. D.; Gratz, E.; Basu, S. N.; Gopalan, S.; Pal, U. B. *Journal of Power Sources* **2013**, *236*, 95–102.

[64] Tamaura, Y.; Kuhn, P.; Ehrensberger, K. *Energy* **1995**, *20*, 325–330.

[65] Kaneko, H.; Miura, T.; Fuse, A.; Ishihara, H.; Taku, S.; Fukuzumi, H.; Naganuma, Y.; Tamaura, Y. *Energy & Fuels* **2007**, *21*, 2287–2293.

[66] Abanades, S.; Flamant, G. *Solar Energy* **2006**, *80*, 1611–1623.

[67] Chueh, W. C.; Falter, C.; Abbott, M.; Scipio, D.; Furler, P.; Haile, S. M.; Steinfeld, A. *Science (New York, N.Y.)* **2010**, *330*, 1797–801.

[68] McDaniel, A. H.; Miller, E. C.; Arifin, D.; Ambrosini, A.; Coker, E. N.; O'Hayre, R.; Chueh, W. C.; Tong, J. *Energy & Environmental Science* **2013**, *6*, 2424.

[69] Demont, A.; Abanades, S.; Beche, E. *Journal of Physical Chemistry C* **2014**, *118*, 12682–12692.

[70] Scheffe, J. R.; Steinfeld, A. *Materials Today* **2014**, *17*, 341–348.

[71] Panlener, R.; Blumenthal, R.; Garnier, J. *Journal of Physics and Chemistry of Solids* **1975**, *36*, 1213–1222.

[72] Ricken, M.; Nölting, J.; Riess, I. *Journal of Solid State Chemistry* **1984**, *54*, 89–99.

[73] Körner, R.; Ricken, M.; Nölting, J. *Journal of Solid State Chemistry 78* **1989**, *147*, 136–147.

[74] Kümmerle, E.; Heger, G. *Journal of Solid State Chemistry* **1999**, *147*, 485–500.

[75] Mogensen, M.; Sammes, N. M.; Tompsett, G. A. *Solid State Ionics* **2000**, *129*, 63–94.

[76] Zinkevich, M.; Djurovic, D.; Aldinger, F. *Solid State Ionics* **2006**, *177*, 989–1001.

[77] TROVARELLI, A. *Catalysis Reviews* **1996**, *38*, 439–520.

[78] Etsell, T. H.; Flengas, S. N. *Chemical Reviews* **1970**, *70*, 339–376.

[79] Inaba, Hideaki Tagawa, H. *Solid State Ionics* **1996**, *2738*, 1–16.

[80] Vernoux, P.; Lizarraga, L.; Tsampas, M. N.; Sapountzi, F. M.; De Lucas-Consuegra, A.; Valverde, J. L.; Souentie, S.; Vayenas, C. G.; Tsiplakides, D.; Balomenou, S.; Baranova, E. A. *Chemical Reviews* **2013**, *113*, 8192–8260.

[81] Minh, N. Q. *Journal of the American Ceramic Society* **1993**, *76*, 563–588.

[82] Haile, S. M. *Acta Materialia* **2003**, *51*, 5981–6000.

[83] Otsuka, K.; Hatano, M.; Morikawa, A. *Journal of Catalysis* **1983**, *79*, 493–496.

[84] Chueh, W. C.; Haile, S. M. *Philosophical transactions. Series A, Mathematical, physical, and engineering sciences* **2010**, *368*, 3269–94.

[85] Kröger, F. a.; Vink, H. J. *Solid State Physics - Advances in Research and Applications* **1956**, *3*, 307–435.

[86] Mullins, D. R.; Overbury, S. H.; Huntley, D. R. *Surface Science* **1998**, *409*, 307–319.

[87] Tuller, H. L.; Nowick, A. S. *Journal of Physics and Chemistry of Solids* **1977**, *38*, 859–867.

[88] Bevan, D.; Kordis, J. *Journal of Inorganic and Nuclear Chemistry* **1964**, *26*, 1509–1523.

[89] Panhans, M.; Blumenthal, R. *Solid State Ionics* **1993**, *60*, 279–298.

[90] Schneider, D.; Godickemeier, M.; Gauckler, L. J. *Journal Of Electroceramics* **1997**, *1*, 165–172.

[91] Lowe, A. J.; Keogh, K. A.; Murphy, B. E.; Krasnikov, S. a.; Shvets, I. V.; Bulfin, B.; Lowe, A. J.; Keogh, K. A.; Murphy, B. E.; Lübben, O.; Krasnikov, S. a.; Shvets, I. V. *The Journal of Physical Chemistry C* **2013**, *117*, 24129–24137.

[92] Sørensen, O. T. *Journal of Solid State Chemistry* **1976**, *18*, 217–233.

[93] Otake, T. *Solid State Ionics* **2003**, *161*, 181–186.

[94] Esch, F.; Fabris, S.; Zhou, L.; Montini, T.; Africh, C.; Fornasiero, P.; Comelli, G.; Rosei, R. *Science (New York, N.Y.)* **2005**, *309*, 752–5.

[95] Bishop, S.; Duncan, K.; Wachsman, E. *Electrochimica Acta* **2009**, *54*, 1436–1443.

[96] Scheffe, J. R.; Steinfeld, A. *Energy & Fuels* **2012**, *26*, 1928–1936.

[97] Takacs, M.; Scheffe, J. R.; Steinfeld, a. *Phys. Chem. Chem. Phys.* **2015**, *17*, 7813–7822.

[98] Bulfin, B.; Hoffmann, L.; de Oliveira, L.; Knoblauch, N.; Call, F.; Roeb, M.; Sattler, C.; Schmücker, M. *Phys. Chem. Chem. Phys.* **2016**, *18*, 23147–23154.

[99] Ray, S.; Cox, D. *Journal of Solid State Chemistry* **1975**, *15*, 333–343.

[100] Hull, S.; Norberg, S.; Ahmed, I.; Eriksson, S.; Marrocchelli, D.; Madden, P. *Journal of Solid State Chemistry* **2009**, *182*, 2815–2821.

[101] Lundberg, M. *International Journal of Hydrogen Energy* **1993**, *18*, 369–376.

[102] Rager, T. *Chemical Communications* **2012**, *48*, 10520–10522.

[103] Miller, J. E.; McDaniel, A. H.; Allendorf, M. D. *Advanced Energy Materials* **2014**, *4*, 1300469–1300469.

[104] Lange, M.; Roeb, M.; Sattler, C.; Pitz-Paal, R. *Energy* **2014**, *67*, 298–308.

[105] Falter, C. P.; Sizmann, A.; Pitz-Paal, R. *Solar Energy* **2015**, *122*, 1296–1308.

[106] Krenzke, P. T.; Davidson, J. H. *Energy & Fuels* **2015**, *29*, 1045–1054.

[107] Bala Chandran, R.; De Smith, R. M.; Davidson, J. H. *International Journal of Heat and Mass Transfer* **2015**, *81*, 404–414.

[108] Bulfin, B.; Lange, M.; de Oliveira, L.; Roeb, M.; Sattler, C. *International Journal of Hydrogen Energy* **2016**, *49*, 5–13.

[109] Jarrett, C.; Chueh, W.; Yuan, C.; Kawajiri, Y.; Sandhage, K. H.; Henry, A. *Solar Energy* **2016**, *123*, 57–73.

[110] Lin, M.; Haussener, S. *Energy* **2015**, *88*, 1–13.

[111] Ermanoski, I.; Miller, J. E.; Allendorf, M. D. *Physical chemistry chemical physics : PCCP* **2014**, *16*, 8418–27.

[112] Scheffe, J. R.; Welte, M.; Steinfeld, A. *Industrial & Engineering Chemistry Research* **2014**, *53*, 2175–2182.

[113] Welte, M.; Barhoumi, R.; Zbinden, A.; Scheffe, J. R.; Steinfeld, A. *Industrial & Engineering Chemistry Research* **2016**, acs.iecr.6b02853.

[114] Krenzke, P. T.; Davidson, J. H. *Energy and Fuels* **2014**, *28*, 4088–4095.

[115] Nair, M. M.; Abanades, S. *Energy & Fuels* **2016**, *30*, 6050–6058.

[116] Gao, X.; Vidal, A.; Bayon Sandoval, A.; Bader, R.; Hinkley, J. J. T. J.; Lipiński, W.; Tricoli, A.; Bayon, A.; Bader, R.; Hinkley, J. J. T. J.; Lipiski, W.; Tricoli, A. *Journal of Materials Chemistry A* **2016**, *4*, 9614–9624.

[117] Yuan, C.; Jarrett, C.; Chueh, W.; Kawajiri, Y.; Henry, A. *Solar Energy* **2015**, *122*, 547–561.

[118] Furler, P.; Scheffe, J.; Gorbar, M.; Moes, L.; Vogt, U.; Steinfeld, A. *Energy & Fuels* **2012**, 121024073702001.

[119] Ackermann, S.; Scheffe, J. R.; Steinfeld, A. *The Journal of Physical Chemistry C* **2014**, *118*, 5216–5225.

[120] Ackermann, S.; Scheffe, J. R.; Duss, J.; Steinfeld, A. *Materials* **2014**, *7*, 7173–7195.

[121] Furler, P.; Scheffe, J. R.; Steinfeld, A. *Energy & Environmental Science* **2012**, *5*, 6098.

[122] Gibbons, W. T.; Venstrom, L. J.; De Smith, R. M.; Davidson, J. H.; Jackson, G. S. *Physical chemistry chemical physics : PCCP* **2014**, *16*, 14271–80.

[123] Furler, P.; Scheffe, J.; Marxer, D.; Gorbar, M.; Bonk, A.; Vogt, U.; Steinfeld, A. *Physical chemistry chemical physics : PCCP* **2014**, *16*, 10503–11.

[124] Malonzo, C. D.; De Smith, R. M.; Rudisill, S. G.; Petkovich, N. D.; Davidson, J. H.; Stein, A. *The Journal of Physical Chemistry C* **2014**, *118*, 26172–26181.

[125] Call, F.; Roeb, M.; Schmücker, M.; Bru, H.; Curulla-ferre, D.; Sattler, C.; Pitz-paal, R. **2013**, *2013*, 37–45.

[126] Rhodes, N. R.; Bobek, M. M.; Allen, K. M.; Hahn, D. W. *Energy* **2015**, *89*, 924–931.

[127] Rudisill, S. G.; Venstrom, L. J.; Petkovich, N. D.; Quan, T.; Hein, N.; Boman, D. B.; Davidson, J. H.; Stein, A. *The Journal of Physical Chemistry C* **2013**, *117*, 1692–1700.

[128] Kang, M.; Wu, X.; Zhang, J.; Zhao, N.; Wei, W.; Sun, Y. *RSC Advances* **2013**, *4*, 5583–5590.

[129] Bonk, A. Synthesis, Modification and Characterization of Ceria Based Ceramics for Solar Thermochemical Fuel Production. Ph.D. thesis, University of Freiburg, 2015.

[130] Hansen, H. A.; Wolverton, C. *The Journal of Physical Chemistry C* **2014**, *118*, 27402–27414.

[131] Kullgren, J.; Wolf, M. J.; Castleton, C. W. M.; Mitev, P.; Briels, W. J.; Hermansson, K. *Physical Review Letters* **2014**, *112*, 156102.

[132] Chueh, W. C.; McDaniel, A. H.; Grass, M. E.; Hao, Y.; Jabeen, N.; Liu, Z.; Haile, S. M.; McCarty, K. F.; Bluhm, H.; El Gabaly, F. *Chemistry of Materials* **2012**, *24*, 1876–1882.

[133] Zhang, C.; Yu, Y.; Grass, M. E.; Dejoie, C.; Ding, W.; Gaskell, K.; Jabeen, N.; Hong, Y. P.; Shavorskiy, A.; Bluhm, H.; Li, W.-x.; Jackson, G. S.; Hussain, Z.; Liu, Z.; Eichhorn, B. W. *Journal of the American Ceramic Society* **2013**, *135*, 11572.

[134] Feng, Z. a.; El Gabaly, F.; Ye, X.; Shen, Z.-X.; Chueh, W. C. *Nature Communications* **2014**, *5*, 4374.

[135] Zhao, Z.; Uddi, M.; Tsvetkov, N.; Yildiz, B.; Ghoniem, A. F. *The Journal of Physical Chemistry C* **2016**, *120*, 16271–16289.

[136] Gopal, C. B.; Haile, S. M. *Journal of Materials Chemistry A* **2014**, *2*, 2405.

[137] Ji, H.-I.; Davenport, T. C.; Gopal, C. B.; Haile, S. M. *Phys. Chem. Chem. Phys.* **2016**, *18*, 21554–21561.

[138] Kaneko, H.; Taku, S.; Tamaura, Y. *Solar Energy* **2011**, *85*, 2321–2330.

[139] Meng, Q.-L.; Lee, C.-i.; Shigeta, S.; Kaneko, H.; Tamaura, Y. *Journal of Solid State Chemistry* **2012**, *194*, 343–351.

[140] Meng, Q.-L.; Lee, C.-i.; Kaneko, H.; Tamaura, Y. *Thermochimica Acta* **2012**, *532*, 134–138.

[141] Kaneko, H.; Ishihara, H.; Taku, S.; Naganuma, Y.; Hasegawa, N.; Tamaura, Y. *Journal of Materials Science* **2008**, *43*, 3153–3161.

[142] Lee, C.-i.; Meng, Q.-L.; Kaneko, H.; Tamaura, Y. *Journal of Solar Energy Engineering* **2012**, *135*, 011002.

[143] Kaneko, H.; Miura, T.; Ishihara, H.; Taku, S.; Yokoyama, T.; Nakajima, H.; Tamaura, Y. *Energy* **2007**, *32*, 656–663.

[144] Kaneko, H.; Tamaura, Y. *Journal of Physics and Chemistry of Solids* **2009**, *70*, 1008–1014.

[145] Petkovich, N. D.; Rudisill, S. G.; Venstrom, L. J.; Boman, D. B.; Davidson, J. H.; Stein, A. *The Journal of Physical Chemistry C* **2011**, *115*, 21022–21033.

[146] Le Gal, A.; Abanades, S.; Flamant, G. *Energy & Fuels* **2011**, *25*, 4836–4845.

[147] Le Gal, A.; Abanades, S.; Flamant, G. *Energy & Fuels* **2011**, *25*, 4836–4845.

[148] Meng, Q.-L.; Lee, C.-i.; Ishihara, T.; Kaneko, H.; Tamaura, Y. *International Journal of Hydrogen Energy* **2011**, *36*, 13435–13441.

[149] Le Gal, A.; Abanades, S. *The Journal of Physical Chemistry C* **2012**, *116*, 13516–13523.

[150] Abanades, S.; Le Gal, A. *Fuel* **2012**, 2–8.

[151] Le Gal, A.; Abanades, S.; Bion, N.; Le Mercier, T.; Harlé, V. *Energy & Fuels* **2013**, *27*, 6068–6078.

[152] Kang, M.; Zhang, J.; Wang, C.; Wang, F.; Zhao, N.; Xiao, F.; Wei, W.; Sun, Y. *RSC Advances* **2013**, *3*, 18878.

[153] Scheffe, J. R.; Jacot, R.; Patzke, G. R.; Steinfeld, A. *The Journal of Physical Chemistry C* **2013**, *117*, 24104–24114.

[154] Pappacena, A.; Boaro, M.; Šolcová, O.; Trovarelli, A. *Advances in Science and Technology* **2014**, *93*, 76–81.

[155] Jiang, Q.; Zhou, G.; Jiang, Z.; Li, C. *Solar Energy* **2014**, *99*, 55–66.

[156] Ramos-Fernandez, E. V.; Shiju, N. R.; Rothenberg, G. *RSC Advances* **2014**, *4*, 16456.

[157] Bonk, A.; Maier, A. C.; Schlupp, M. V.; Burnat, D.; Remhof, A.; Delmelle, R.; Steinfeld, A.; Vogt, U. F. *Journal of Power Sources* **2015**, *300*, 261–271.

[158] Lorentzou, S.; Karagiannakis, G.; Dimitrakis, D.; Pagkoura, C.; Zygogianni, a.; a.G. Konstandopoulos, *Energy Procedia* **2015**, *69*, 1800–1809.

[159] Lin, F.; Alxneit, I.; Wokaun, A. *CrystEngComm* **2015**, *17*, 1646–1653.

[160] Lin, F.; Delmelle, R.; Vinodkumar, T.; Reddy, B. M.; Wokaun, A.; Alxneit, I. *Catal. Sci. Technol.* **2015**, *5*, 3556–3567.

[161] Bishop, S. R.; Stefanik, T. S.; Tuller, H. L. *Journal of Materials Research* **2012**, *27*, 2009–2016.

[162] Heinzmann, R.; Issac, I.; Eufinger, J.-P.; Ulbrich, G.; Lerch, M.; Janek, J.; Indris, S. *The Journal of Physical Chemistry C* **2016**, *120*, 8568–8577.

[163] Bishop, S. R.; Tuller, H. L.; Kuru, Y.; Yildiz, B. *Journal of the European Ceramic Society* **2011**, *31*, 2351–2356.

[164] Bonk, A.; Remhof, A.; Maier, A. C.; Trottmann, M.; Schlupp, M. V. F.; Battaglia, C.; Vogt, U. F. *The Journal of Physical Chemistry C* **2016**, *120*, 118–125.

[165] Kuhn, M.; Bishop, S. R.; Rupp, J. L. M.; Tuller, H. L. *Acta Materialia* **2013**, *61*, 4277–4288.

[166] Haynes, W., Ed. *Handbook of Chemistry and Physics*, 92nd ed.; CRC Press/Taylor and Francis: Boca Raton, FL, 2012.

[167] Ruh, R.; Garrett, H. J.; Domagala, R. F.; Tallan, N. M. *Journal of the American Ceramic Society* **1968**, *51*, 23–28.

[168] Ruh, R.; Corfiels, W. R. *Journal of the American Ceramic Society* **1970**, *53*, 126.

[169] YOSHIMURA, M.; TANI, E.; SOMIYA, S. *Solid State Ionics* **1981**, *3-4*, 477–481.

[170] Tani, E.; Yoshimura, M.; Somiya, S. *Journal of the American Ceramic Society* **1983**, *66*, 506–510.

[171] Yashima, M. *Catalysis Today* **2015**, *253*, 3–19.

[172] Huang, S.; Li, L.; Van der Biest, O.; Vleugels, J. *Solid State Sciences* **2005**, *7*, 539–544.

[173] Materials Science International Team, T.; Lebrun, N.; Perrot, P. In *SpringerMaterials - The Landolt-Börnstein Database*; Effenberg, G., Ilyenko, S., Eds.; Landolt-Börnstein - Group IV Physical Chemistry; SpringerMaterials - The Landolt-Börnstein Database, Vol. 11E3; Chapter 11E3: Refr, pp 87–110.

[174] Mamontov, E.; Brezny, R.; Koranne, M.; Egami, T. *The Journal of Physical Chemistry B* **2003**, *107*, 13007–13014.

[175] Subramanian, M.; Aravamudan, G.; Subba Rao, G. *Progress in Solid State Chemistry* **1983**, *15*, 55–143.

[176] Achary, S. N.; Sali, S. K.; Kulkarni, N. K.; Krishna, P. S. R.; Shinde, A. B.; Tyagi, A. K. *Chemistry of Materials* **2009**, *21*, 5848–5859.

[177] Sasaki, T.; Ukyo, Y.; Suda, A.; Sugiura, M.; Kuroda, K.; Arai, S.; Saka, H. *Journal of the Ceramic Society of Japan* **2003**, *111*, 382–385.

[178] Sasaki, T.; Ukyo, Y.; Kuroda, K.; Arai, S.; Muto, S.; Saka, H. *Journal of the Ceramic Society of Japan* **2004**, *112*, 440–444.

[179] Otobe, H.; Nakamura, a.; Yamashita, T.; Minato, K. *Journal of Physics and Chemistry of Solids* **2005**, *66*, 329–334.

[180] Yamamoto, T.; Suzuki, A.; Nagai, Y.; Tanabe, T.; Dong, F.; Inada, Y.; Nomura, M.; Tada, M.; Iwasawa, Y. *Angewandte Chemie (International ed. in English)* **2007**, *46*, 9253–6.

[181] Wang, R.; Crozier, P. a.; Sharma, R. *The Journal of Physical Chemistry C* **2009**, *113*, 5700–5704.

[182] Wang, H. F.; Guo, Y. L.; Lu, G. Z.; Hu, P. *Angewandte Chemie - International Edition* **2009**, *48*, 8289–8292.

[183] Yashima, M.; Sekikawa, T.; Sato, D.; Nakano, H.; Omoto, K. *Crystal Growth & Design* **2013**, *13*, 829–837.

[184] Wakita, T.; Yashima, M. *Applied Physics Letters* **2008**, *92*, 101921.

[185] Zhang, F.; Chen, C.-H.; Hanson, J. C.; Robinson, R. D.; Herman, I. P.; Chan, S.-W. *Journal of the American Ceramic Society* **2006**, *89*, 1028–1036.

[186] Brisse, F.; Knop, O. *Canadian Journal of Chemistry* **1967**, *45*, 609.

[187] Kharton, V. V.; Naumovich, E. N.; Vecher, A. a. *Journal of Solid State Electrochemistry* **1999**, *3*, 61–81.

[188] Andrievskaya, E. R.; Redko, V. P.; Lopato, L. M. *Powder Metallurgy and Metal Ceramtcs* **2001**, *40*, 405–413.

[189] Andrievskaya, E. R.; Gerasimyuk, G. I.; Kornienko, O. A.; Samelyuk, A. V.; Lopato, L. M.; Redko, V. P. *Powder Metallurgy and Metal Ceramics* **2006**, *45*, 448–456.

[190] Stanek, C. R.; Grimes, R. W. *Journal of the American Ceramic Society* **2002**, *85*, 2139–2141.

[191] Baidya, T.; Hegde, M. S.; Gopalakrishnan, J. *The Journal of Physical Chemistry B* **2007**, *111*, 5149–5154.

[192] Zhou, G.; Gorte, R. J. *The journal of physical chemistry. B* **2008**, *112*, 9869–9875.

[193] Raitano, J. M.; Khalid, S.; Marinkovic, N.; Chan, S.-W. *Journal of Alloys and Compounds* **2015**, *644*, 996–1002.

[194] Sharma, A.; Varshney, M.; Shin, H.-J.; Park, Y. J.; Kim, M.-G.; Ha, T.-K.; Chae, K. H.; Gautam, S. *Physical Chemistry Chemical Physics* **2014**, *16*, 19909.

[195] Fujimori, H.; Yashima, M.; Sasaki, S.; Kakihana, M.; Mori, T.; Tanaka, M.; Yoshimura, M. *Physical Review B* **2001**, *64*, 1–5.

[196] Paun, C.; Safonova, O. V.; Szlachetko, J.; Abdala, P. M.; Nachtegaal, M.; Sa, J.; Kleymenov, E.; Cervellino, A.; Krumeich, F.; van Bokhoven, J. A. *The Journal of Physical Chemistry C* **2012**, *116*, 7312–7317.

[197] Rodriguez, J. A.; Hanson, J. C.; Kim, J.-y.; Liu, G.; Iglesias-Juez, A.; Fernández-García, M. *The Journal of Physical Chemistry B* **2003**, *107*, 3535–3543.

[198] Acuna, L.; Lamas, D.; Fuentes, R.; Fabregas, I.; Walsoe de Reca, N.; Prado, R.; Fantini, M.; Craievich, A. *LNLS 2007 Activity Report* **2007**, 1–2.

[199] Deguchi, H.; Yoshida, H.; Inagaki, T.; Horiuchi, M. *Solid State Ionics* **2005**, *176*, 1817–1825.

[200] Nitani, H.; Nakagawa, T.; Yamanouchi, M.; Osuki, T.; Yuya, M.; Yamamoto, T. a. *Materials Letters* **2004**, *58*, 2076–2081.

[201] Lee, J.; Tang, M.; Shih, W.; Liu, R. *Materials research bulletin* **2002**, *37*, 555–562.

[202] Zhang, F.; Wang, P.; Koberstein, J.; Khalid, S.; Chan, S.-W. *Surface Science* **2004**, *563*, 74–82.

[203] Fornasiero, P.; Fonda, E.; Di Monte, R.; Vlaic, G.; Kašpar, J.; Graziani, M. *Journal of Catalysis* **1999**, *187*, 177–185.

[204] Lemaux, S.; Bensaddik, A.; van der Eerden, A. M. J.; Bitter, J. H.; Koningsberger, D. C. *The Journal of Physical Chemistry B* **2001**, *105*, 4810–4815.

[205] Kopelent, R. R.; van Bokhoven, J. A.; Szlachetko, J.; Edebeli, J.; Paun, C.; Nachtegaal, M.; Safonova, O. V.; Bokhoven, J. A. V.; Szlachetko, J.; Edebeli, J.; Paun, C. *Angewandte Chemie* **2015**, *127*, 8852–8855.

[206] Duarte, R. B.; Safonova, O. V.; Krumeich, F.; Makosch, M.; van Bokhoven, J. A. *ACS Catalysis* **2013**, *3*, 1956–1964.

[207] Acuña, L. M.; Fuentes, R. O.; Lamas, D. G.; Fábregas, I. O.; Walsöe de Reca, N. E.; Craievich, a. F. *Powder Diffraction* **2008**, *23*, 70–74.

[208] Acuña, L. M.; Fuentes, R. O.; Fantini, M. C. A.; Lamas, D. G. *The Journal of Physical Chemistry C* **2014**, *118*, 11445–11453.

[209] Bork, a. H.; Kubicek, M.; Struzik, M.; Rupp, J. L. M. *J. Mater. Chem. A* **2015**, *3*, 15546–15557.

[210] Bordiga, S.; Groppo, E.; Agostini, G.; van Bokhoven, J. A.; Lamberti, C. *Chemical reviews* **2013**, *113*, 1736–850.

[211] Holgado, J. P.; Alvarez, R.; Munuera, G. **2000**, 301–315.

[212] Singh, P.; Hegde, M. S. *Chemistry of Materials* **2010**, *22*, 762–768.

[213] Matolín, V.; Cabala, M.; Cháb, V.; Matolínová, I.; Prince, K. C.; Škoda, M.; Šutara, F.; Skála, T.; Veltruská, K. *Surface and Interface Analysis* **2008**, *40*, 225–230.

[214] Kato, S.; Ammann, M.; Huthwelker, T.; Paun, C.; Lampimäki, M.; Lee, M.-T.; Rothensteiner, M.; van Bokhoven, J. a. *Phys. Chem. Chem. Phys.* **2015**, *17*, 5078–5083.

[215] Rajagopalan, S. *Journal of Nuclear Materials* **1986**, *139*, 19–26.

[216] Abanades, S.; Legal, A.; Cordier, A.; Peraudeau, G.; Flamant, G.; Julbe, A. *Journal of Materials Science* **2010**, *45*, 4163–4173.

[217] Le Gal, A.; Abanades, S. *International Journal of Hydrogen Energy* **2011**, *36*, 4739–4748.

[218] Bhosale, R. R.; Kumar, A.; AlMomani, F.; Alxneit, I. *Ceramics International* **2016**, *42*, 6728–6737.

[219] Mamontov, E.; Egami, T. *The Journal of Physical Chemistry B* **2000**, *104*, 11110–11116.

[220] Kümmerle, E. A.; Güthoff, F.; Schweika, W.; Heger, G. *Journal of Solid State Chemistry* **2000**, *153*, 218–230.

[221] Raison, P. E.; Pavel, C. C.; Jardin, R.; Suard, E.; Haire, R. G.; Popa, K. *Physics and Chemistry of Minerals* **2010**, *37*, 555–559.

[222] Playford, H. Y.; Modeshia, D. R.; Barney, E. R.; Hannon, A. C.; Wright, C. S.; Fisher, J. M.; Amieiro-Fonseca, A.; Thompsett, D.; O'Dell, L. a.; Rees, G. J.; Smith, M. E.; Hanna, J. V.; Walton, R. I. *Chemistry of Materials* **2011**, *23*, 5464–5473.

[223] Jimenez, R.; Bucheli, W.; Varez, A.; Sanz, J. *Fuel Cells* **2011**, *11*, 642–653.

[224] Coduri, M.; Scavini, M.; Brunelli, M.; Masala, P. *Physical chemistry chemical physics : PCCP* **2013**, *15*, 8495–505.

[225] Fornasiero, P.; Balducci, G.; Di Monte, R.; Kašpar, J.; Sergo, V.; Gubitosa, G.; Ferrero, a.; Graziani, M. *Journal of Catalysis* **1996**, *164*, 173–183.

[226] Omata, T.; Kishimoto, H.; Otsuka-Yao-Matsuo, S.; Ohtori, N.; Umesaki, N. *Journal of Solid State Chemistry* **1999**, *147*, 573–583.

[227] An, Y.; Shen, M.; Wang, J. *Journal of Alloys and Compounds* **2007**, *441*, 305–310.

[228] Riess, I.; Ricken, M.; NoÂ¨lting, J. *Journal of Solid State Chemistry* **1985**, *57*, 314–322.

[229] Sachdeva, A.; Chavan, S. V.; Goswami, A.; Tyagi, A. K.; Pujari, P. K. *Journal of Solid State Chemistry* **2005**, *178*, 2062–2066.

[230] Thorat, A. V.; Ghoshal, T.; Holmes, J. D.; Nambissan, P. M. G.; Morris, M. A. *Nanoscale* **2014**, *6*, 608–615.

[231] Willmott, P. *An Introduction to Synchrotron Radiation*; John Wiley & Sons, Ltd: Chichester, UK, 2011.

[232] Als-Nielsen, J.; McMorrow, D. *Elements of Modern X-ray Physics*; John Wiley & Sons, Inc.: Hoboken, NJ, USA, 2011; pp 1–28.

[233] Van Bokhoven, J. A., Lamberti, C., Eds. *X-Ray Absorption and X-Ray Emission Spectroscopy*; John Wiley & Sons, Ltd: Chichester, UK, 2016; p 60.

[234] Henning, C.; Funke, H.; Scheinost, A. *Temperature dependency of the EXAFS Debye-Waller factors of H[UO2AsO4]4H2O*; 2004; p 61.

[235] Krause, M. O.; Oliver, J. H. *Journal of Physical and Chemical Reference Data* **1979**, *8*, 329.

[236] Abdala, P. M.; Safonova, O. V.; Wiker, G.; van Beek, W.; Emerich, H.; van Bokhoven, J. a.; Sá, J.; Szlachetko, J.; Nachtegaal, M. *Chimia* **2012**, *66*, 699–705.

[237] van Beek, W.; Safonova, O. V.; Wiker, G.; Emerich, H. *Phase Transitions* **2011**, *84*, 726–732.

[238] Sanchez del Rio, M.; Mathon, O. *Advances in computational methods for x-ray and neutron optics* **2004**, *5536*, 157–164.

[239] Braglia, L.; Bugaev, A. L.; Lomachenko, K. A.; Soldatov, A. V.; Lamberti, C.; Guda, A. A. *Journal of Physics: Conference Series* **2016**, *712*, 012064.

[240] Rothensteiner, M.; Sala, S.; Bonk, A.; Vogt, U.; Emerich, H.; van Bokhoven, J. A. *Phys. Chem. Chem. Phys.* **2015**, *17*, 26988–26996.

[241] Ravel, B.; Newville, M. *Journal of Synchrotron Radiation* **2005**, *12*, 537–541.

[242] Beni, G.; Platzman, P. M. *Physical Review B* **1976**, *14*, 1514–1518.

[243] Sevillano, E.; Meuth, H.; Rehr, J. J. *Physical Review B* **1979**, *20*, 4908–4911.

[244] Van Hung, N.; Rehr, J. *Physical Review B* **1997**, *56*, 43–46.

[245] Fornasini, P.; Grisenti, R. *Journal of Synchrotron Radiation* **2015**, *22*, 1242–1257.

[246] Ashiotis, G.; Deschildre, A.; Nawaz, Z.; Wright, J. P.; Karkoulis, D.; Picca, F. E.; Kieffer, J. *Journal of Applied Crystallography* **2015**, *48*, 510–519.

[247] Ning, X.; Selesnick, I. W.; Duval, L. *Chemometrics and Intelligent Laboratory Systems* **2014**, *139*, 156–167.

[248] Lin, F.; Rothensteiner, M.; Alxneit, I.; van Bokhoven, J. A.; Wokaun, A. *Energy Environ. Sci.* **2016**, *9*, 2400–2409.

[249] Garino, C.; Borfecchia, E.; Gobetto, R.; van Bokhoven, J. A.; Lamberti, C. *Coordination Chemistry Reviews* **2014**, *277-278*, 130–186.

[250] van Bokhoven, J. A.; Lamberti, C. In *X-Ray Absorption and X-Ray Emission Spectroscopy: Theory and Applications*; van Bokhoven, J. A., Lamberti, C., Eds.; Wiley, 2016.

[251] Clausen, B. S.; Steffensen, G.; Fabius, B.; Villadsen, J.; Feidenhans'l, R.; Topsøe, H. *Journal of Catalysis* **1991**, *132*, 524–535.

[252] Jackson, W. E.; de Leon, J. M.; Brown, G. E.; Waychunas, G. a.; Conradson, S. D.; Combes, J. M. *Science (New York, N.Y.)* **1993**, *262*, 229–33.

[253] Rollet, A.-L.; Bessada, C.; Auger, Y.; Melin, P.; Gailhanou, M.; Thiaudiere, D. *Nuclear Instruments and Methods in Physics Research Section B: Beam Interactions with Materials and Atoms* **2004**, *226*, 447–452.

[254] Huwe, H.; Fröba, M. *Journal of synchrotron radiation* **2004**, *11*, 363–5.

[255] Girardon, J. S.; Khodakov, a. Y.; Capron, M.; Cristol, S.; Dujardin, C.; Dhainaut, F.; Nikitenko, S.; Meneau, F.; Bras, W.; Payen, E. *Journal of synchrotron radiation* **2005**, *12*, 680–4.

[256] Kawai, T.; Chun, W.-J.; Asakura, K.; Koike, Y.; Nomura, M.; Bando, K. K.; Ted Oyama, S.; Sumiya, H. *The Review of scientific instruments* **2008**, *79*, 014101.

[257] Bare, S. R.; Ressler, T. *Advances in Catalysis*, 1st ed.; Elsevier Inc., 2009; Vol. 52; pp 339–465.

[258] Guilera, G.; Gorges, B.; Pascarelli, S.; Vitoux, H.; Newton, M. A.; Prestipino, C.; Nagai, Y.; Hara, N. *Journal of synchrotron radiation* **2009**, *16*, 628–34.

[259] Dreher, M.; De Boni, E.; Nachtegaal, M.; Wambach, J.; Vogel, F. *The Review of scientific instruments* **2012**, *83*, 054101.

[260] Centomo, P.; Meneghini, C.; Zecca, M. *Review of Scientific Instruments* **2013**, *84*.

[261] An, P.; Hong, C.; Zhang, J.; Xu, W.; Hu, T. *Journal of synchrotron radiation* **2014**, *21*, 165–9.

[262] Chiarello, G. L.; Nachtegaal, M.; Marchionni, V.; Quaroni, L.; Ferri, D. *Review of Scientific Instruments* **2014**, *85*.

[263] Singh, J.; Alayon, E. M. C.; Tromp, M.; Safonova, O. V.; Glatzel, P.; Nachtegaal, M.; Frahm, R.; van Bokhoven, J. A. *Angewandte Chemie (International ed. in English)* **2008**, *47*, 9260–4.

[264] Szlachetko, J. et al. *Structural Dynamics* **2014**, *1*, 021101.

[265] Szlachetko, J.; Sá, J.; Safonova, O.; Smolentsev, G.; Szlachetko, M.; van Bokhoven, J. A.; Nachtegaal, M. *Journal of Electron Spectroscopy and Related Phenomena* **2013**, *188*, 161–165.

[266] Richet, P.; Gillet, P.; Pierre, A.; Bouhifd, M. A.; Daniel, I.; Fiquet, G. *Journal of Applied Physics* **1993**, *74*, 5451.

[267] Neuville, D.; Cormier, L.; de Ligny, D.; Roux, J.; a M. Flank,; Lagarde, P. *American Mineralogist* **2008**, *93*, 228–234.

[268] Landron, C.; Launay, X.; Rifflet, J.; Echegut, P.; Auger, Y.; Ruffier, D.; Coutures, J.; Lemonier, M.; Gailhanou, M.; Bessiere, M.; Bazin, D.; Dexpert, H. *Nuclear Instruments and Methods in Physics Research Section B: Beam Interactions with Materials and Atoms* **1997**, *124*, 627–632.

[269] Landron, C.; Hennet, L.; Coutures, J.-P.; Jenkins, T.; Alétru, C.; Greaves, N.; Soper, A.; Derbyshire, G. *Review of Scientific Instruments* **2000**, *71*, 1745.

[270] Hennet, L. et al. *The European Physical Journal Special Topics* **2011**, *196*, 151–165.

[271] Scheffe, J. R.; Weibel, D.; Steinfeld, A. *Energy & Fuels* **2013**, *27*, 4250–4257.

[272] Yang, C.-k.; Yamazaki, Y.; Aydin, A.; Haile, S. M. *Journal of Materials Chemistry A* **2014**, *2*, 13612.

[273] Demont, A.; Abanades, S. *RSC Adv.* **2014**, *4*, 54885–54891.

[274] Rothensteiner, M.; Bonk, A.; Vogt, U. F.; Emerich, H.; van Bokhoven, J. A. *The Journal of Physical Chemistry C* **2016**, *120*, 13931–13941.

[275] Faubert, F. M. *The Journal of Chemical Physics* **1973**, *58*, 4080.

[276] Lemmon, E. W.; Jacobsen, R. T. *International Journal of Thermophysics* **2004**, *25*, 21–69.

[277] Baurecht, D.; Fringeli, U. P. *Review of Scientific Instruments* **2001**, *72*, 3782–3792.

[278] Ferri, D.; Newton, M. a.; Di Michiel, M.; Yoon, S.; Chiarello, G. L.; Marchionni, V.; Matam, S. K.; Aguirre, M. H.; Weidenkaff, A.; Wen, F.; Gieshoff, J. *Physical chemistry chemical physics : PCCP* **2013**, *15*, 8629–39.

[279] Egami, T. *Journal of Physics and Chemistry of Solids* **1995**, *56*, 1407–1413.

[280] Proffen, T.; Billinge, S. J. L.; Egami, T.; Louca, D. *Zeitschrift für Kristallographie* **2003**, *218*, 132–143.

[281] Billinge, S. J. L.; Kanatzidis, M. G. *Chemical Communications* **2004**, 749.

[282] Newton, M. A.; Chapman, K. W.; Thompsett, D.; Chupas, P. J. *Journal of the American Chemical Society* **2012**, 2–5.

[283] Allieta, M.; Brunelli, M.; Coduri, M.; Scavini, M.; Ferrero, C.; Fisica, C. *Z. Kristallogr. Proc.* **2011**, *1*, 15–20.

[284] Tyrsted, C.; Ørnsbjerg Jensen, K. M.; Bøjesen, E. D.; Lock, N.; Christensen, M.; Billinge, S. J. L.; Brummerstedt Iversen, B. *Angewandte Chemie International Edition* **2012**, *51*, 9030–9033.

[285] Checchia, S.; Scavini, M.; Allieta, M.; Brunelli, M.; Ferrero, C.; Coduri, M. *Powder Diffraction* **2015**, *30*, S119–S126.

[286] Filipponi, A. *Journal of Physics: Condensed Matter* **2001**, *13*, R23–R60.

[287] Bus, E.; Miller, J. T.; Kropf, a. J.; Prins, R.; van Bokhoven, J. A. *Physical chemistry chemical physics : PCCP* **2006**, *8*, 3248–58.

[288] Zhou, G.; Shah, P. R.; Montini, T.; Fornasiero, P.; Gorte, R. J. *Surface Science* **2007**, *601*, 2512–2519.

[289] Reddy, B. M.; Reddy, G. K.; Reddy, L. H.; Ganesh, I. *The Open Physical Chemistry Journal* **2009**, *3*, 24–29.

[290] Lamas, D. G.; Fuentes, R. O.; Fábregas, I. O.; Fernández De Rapp, M. E.; Lascalea, G. E.; Casanova, J. R.; Walsöe De Reca, N. E.; Craievich, a. F. *Journal of Applied Crystallography* **2005**, *38*, 867–873.

[291] Nagai, Y.; Nonaka, T.; Suda, A.; Sugiura, M. *R&D Review of Toyota CRDL 37*, 20–27.

[292] Morikawa, A.; Yamamura, K.; Suda, A.; Tanabe, T.; Nobukawa, T.; Chiba, A.; Takahashi, N. *Journal of the American Ceramic Society* **2015**, *98*, 659–662.

[293] Li, P.; Chen, I. W.; Penner-Hahn, J. E. *Physical Review B* **1993**, *48*, 10063–10073.

[294] Lin, F.; Wokaun, a.; Alxneit, I. *Energy Procedia* **2015**, *69*, 1790–1799.

[295] Chueh, W. C.; Haile, S. M. *ChemSusChem* **2009**, *2*, 735–9.

[296] Goodman, D.; Kelley, R.; Madey, T.; Yates, J. J. *Journal of Catalysis* **1980**, *63*, 226–234.

[297] Bartholomew, C. H.; Pannell, R. B.; Butler, J. L. *Journal of Catalysis* **1980**, *65*, 335–347.

[298] Soong, Y.; Krishna, K.; Biloen, P. *Journal of Catalysis* **1986**, *97*, 330–343.

[299] Chuang, S. S. C.; Stevens, R. W.; Khatri, R. *Topics in Catalysis* **2005**, *32*, 225–232.

[300] Spivey, J. J.; Egbebi, A. *Chemical Society Reviews* **2007**, *36*, 1514.

[301] Gayen, A.; Priolkar, K. R.; Sarode, P. R.; Jayaram, V.; Hegde, M. S.; Subbanna, G. N.; Emura, S. *Chemistry of Materials* **2004**, *16*, 2317–2328.

[302] Hegde, M. S.; Madras, G.; Patil, K. C. *Accounts of Chemical Research* **2009**, *42*, 704–712.

[303] Kurnatowska, M.; Kepinski, L. *Materials Research Bulletin* **2013**, *48*, 852–862.

[304] Duarte, R. B.; Krumeich, F.; Van Bokhoven, J. A. *ACS Catalysis* **2014**, *4*, 1279–1286.

[305] Suresh Kumar, K.; Mathews, T.; Nawada, H.; Bhat, N. *Journal of Nuclear Materials* **2004**, *324*, 177–182.

[306] Al-Shankiti, I.; Al-Otaibi, F.; Al-Salik, Y.; Idriss, H. *Topics in Catalysis* **2013**, *56*, 1129–1138.